

2016

A Study of Manufacturable Rib-to-Floor Beam Connections in Steel Orthotropic Bridge Decks

Katelyn Jeanine Kitner
Lehigh University

Follow this and additional works at: <http://preserve.lehigh.edu/etd>



Part of the [Structural Engineering Commons](#)

Recommended Citation

Kitner, Katelyn Jeanine, "A Study of Manufacturable Rib-to-Floor Beam Connections in Steel Orthotropic Bridge Decks" (2016).
Theses and Dissertations. 2662.
<http://preserve.lehigh.edu/etd/2662>

This Thesis is brought to you for free and open access by Lehigh Preserve. It has been accepted for inclusion in Theses and Dissertations by an authorized administrator of Lehigh Preserve. For more information, please contact preserve@lehigh.edu.

**A Study of Manufacturable Rib-to-Floor Beam Connections in Steel Orthotropic
Bridge Decks**

by

Katelyn Kitner

A Thesis

Presented to the Graduate and Research Committee
of Lehigh University
in Candidacy for the Degree of
Master of Science

in

Structural Engineering

Lehigh University

May 2016

This thesis is accepted and approved in partial fulfillment of the requirements for the Master of Science.

Date

Dr. Sougata Roy
Thesis Advisor
Former Principal Research Scientist
ATLSS Engineering Research Center,
Lehigh University

Dr. Richard Sause
Thesis Advisor
Department of Civil and Environmental
Engineering, Lehigh University

Dr. Panayiotis (Panos) Diplas
Chairperson
Department of Civil and Environmental
Engineering, Lehigh University

ACKNOWLEDGEMENT

The author would like to express her sincere gratitude to her thesis advisors, Dr. Sougata Roy and Dr. Richard Sause, for their valuable guidance and insight of this research. The author especially appreciates the effort put forward by Dr. Roy in defining the primary research direction and helping her to complete her thesis. The author thanks Mr. Soham Mukherjee for sharing the Finite Element Analysis models. The author would also like to thank Mr. Peter Bryan for providing his technical support for performing the Finite Element Analyses. The author gratefully acknowledges the funding provided by Lehigh University and FHWA. Finally, the author would like to thank her family, fiancé, and friends for all the support they provided throughout her graduate studies.

CONTENTS

LIST OF TABLES	vi
LIST OF FIGURES	vii
ABSTRACT	1
1 INTRODUCTION	3
1.1 Background.....	3
1.2 Objective of Current Study.....	6
1.3 Study Approach	6
1.4 Outline	7
2 LITERATURE REVIEW OF THE RIB-TO-FLOOR BEAM DETAIL	9
2.1 Connection Details	10
2.2 Fatigue Testing	14
2.3 Fabrication	25
2.4 Performance Review.....	35
3 PARAMETER EVALUATION AND CONNECTION TYPES	37
3.1 Database Evaluation	37
3.2 Connection Type Identification	38
3.3 Connection Type Manufacturability.....	40
4 FINITE ELEMENT ANALYSIS	46
4.1 Analysis Plan	46
4.2 Summary of Global Model Analysis	47
4.3 Details of Submodels.....	48
4.4 Details of Element Type and Meshing for Submodels.....	52

4.5	Boundary Conditions	53
4.6	Loading	54
4.7	Material Properties	55
4.8	Analysis	55
5	FINITE ELEMENT ANALYSIS RESULTS	57
5.1	Discussion of FEA Results	57
5.2	Behavior of the Rib-to-Floor Beam Connection	59
5.3	Critical Location for a Given Connection Type	65
5.4	FEA Result Comparison	66
6	CONCLUSIONS AND RECOMMENDATIONS	70
6.1	Conclusions	70
6.2	Recommendations	72
	TABLES	73
	FIGURES	86
	REFERENCES	174
	VITA	183

LIST OF TABLES

Table 1	Steel Orthotropic Bridge Deck Parameters	73
Table 2	Database of North American Steel Orthotropic Bridge Decks	74
Table 3	Database of International Steel Orthotropic Bridge Decks	80
Table 4	Performance of Existing Steel Orthotropic Bridge Decks	82
Table 5	Limits of Steel Orthotropic Bridge Deck Parameters per FHWA Manual and AASHTO LRFD BDS	82
Table 6	Range of Existing Steel Orthotropic Bridge Deck Parameters	83
Table 7	Evaluation of Histograms	83
Table 8	Submodel Analysis Matrix	84
Table 9	Details of FEA Models	85

LIST OF FIGURES

Figure 1	Closed rib orthotropic deck	86
Figure 2	Torsionally stiff closed rib profiles: (a) Round-bottom; (b) Trapezoidal	86
Figure 3	Parameters of a steel orthotropic bridge deck with rounded bottom rib profile	87
Figure 4	Parameter of an orthotropic deck with trapezoidal rib profile	87
Figure 5	Common parameters of steel orthotropic bridge deck for all rib-to-floor beam connection types	88
Figure 6	Parameters of the extended cutout in the rib-to-floor beam connection with trapezoidal rib profile	88
Figure 7	Rib-to-floor beam connection with continuous ribs passing through cutout in the floor beam	89
Figure 8	Weld throat failure in rib-to-floor beam connection with ribs fitted between floor beams (reproduced from Kolstein 2007)	89
Figure 9	Rib-to-floor beam connection with discontinuous ribs fitted between floor beams	90
Figure 10	Fatigue crack at extended cutout termination in the rib wall (reproduced from Dexter and Fisher 1997)	90
Figure 11	Triangular rib profile	91

Figure 12	Cross section of experimental arrangement (reproduced from Haibach and Plasil 1983)	91
Figure 13	Rib dimensions	92
Figure 14	Preliminary forms of extended cutout: (a) Form I.1; (b) Form I.2 (reproduced from Haibach and Plasil 1983)	92
Figure 15	Form I (reproduced from Haibach and Plasil 1983)	93
Figure 16	Form II (reproduced from Haibach and Plasil 1983)	93
Figure 17	Dimensions of the Williamsburg Bridge rib-to-floor beam connection	94
Figure 18	Weld options for the rib-to-floor beam connection in the Williamsburg Bridge fatigue testing: (a) Weld Option A; (b) Weld Option B; (c) Weld Option C (reproduced from Tsakopoulos and Fisher 2003)	95
Figure 19	Dimensions of the Bronx Whitestone Bridge rib-to-floor beam connection	96
Figure 20	Dimensions of the Verrazano Narrows Bridge rib-to-floor beam connection	96
Figure 21	Dimensions of the rib-to-floor beam connection of SOBD for unnamed lift bridge	97
Figure 22	Welding terminology (reproduced from Linnert 1994)	97
Figure 23	Port Mann Bridge Cross Section	98

Figure 24	Concordia Bridge Cross Section	98
Figure 25	Poplar Street Bridge Cross Section	99
Figure 26	Mission Bridge Cross Section	99
Figure 27	Burning of rib profiles in floor beam web (reproduced from Gerritt Hardenberg)	100
Figure 28	Cutting rib profile in floor beam web to produce pair of floor beams (reproduced from Smylie, 1966)	100
Figure 29	Horizontal rotator (reproduced from Gill and Dozzi, 1966)	101
Figure 30	Assembly of the floor beams and deck units (reproduced from Shields and Schmidt, 1969)	102
Figure 31	Welding work angle (reproduced from Linnert 1994)	103
Figure 32	Welding travel angle (reproduced from Linnert 1994)	103
Figure 33	Existing deck plate thickness	104
Figure 34	Existing rib plate thickness	104
Figure 35	Existing rib spacing	105
Figure 36	Existing floor beam spacing	106
Figure 37	Existing floor beam web thickness	107
Figure 38	Existing cutout-to-rib depth	107
Figure 39	Existing rib depth-to-floor beam depth	108
Figure 40	Existing portion of floor beam depth-to-floor beam thickness	108

Figure 41	Existing rib-to-floor beam connection types	109
Figure 42	Type 1 rib-to-floor beam connection: (a) Type 1A with trapezoidal rib; (b) Type 1B with round-bottom rib	109
Figure 43	Type 1 rib-to-floor beam connection with alternate weld detail: (a) Type 1A with trapezoidal rib; (b) Type 1B with round-bottom rib	110
Figure 44	Type 2A rib-to-floor beam connection	110
Figure 45	Type 3A rib-to-floor beam connection	111
Figure 46	Type 4A rib-to-floor beam connection	111
Figure 47	Type 4B weld detail	112
Figure 48	Type 5A rib-to-floor beam connection	113
Figure 49	Type 5B weld detail	114
Figure 50	Assembly of ribs and deck plate in the inverted position	115
Figure 51	Assembly of floor beam, ribs, and deck plate in the inverted position	115
Figure 52	Manual welding rib-to-floor beam connection (reproduced from Mukherjee 2016)	116
Figure 53	Possible robotic floor beam welding sequence	117
Figure 54	Top view of the Global Model showing extent of Submodel A and Submodel B	118

Figure 55	Bottom view of the GM showing extent of Submodel A and Submodel B and global details	119
Figure 56	Cross section of the deck (reproduced from Mukherjee 2016)	120
Figure 57	Details of global model: (a) rib; (b) floor beam (reproduced from Mukherjee 2016)	121
Figure 58	Details of Global Model: (a) Box Girder; (b) End Floor Beam (reproduced from Mukherjee 2016)	122
Figure 59	Underside view of the GM showing the boundary conditions specified at the soffit of the end floor beams at locations identified as dots (reproduced Mukherjee 2016)	123
Figure 60	Longitudinal position of AASHTO tandem axles (reproduced from Mukherjee 2016)	124
Figure 61	Transverse load position considered for FEA of bridge deck (reproduced from Mukherjee 2016)	125
Figure 62	Top view of deformed global model (reproduced from Mukherjee 2016)	126
Figure 63	Bottom view of deformed global model (reproduced from Mukherjee 2016)	126
Figure 64	Deformed global model due to critical load position (reproduced from Mukherjee 2016)	127
Figure 65	Top view showing the extent of Submodel A and Submodel B	128

Figure 66	Partial cross section with parameters and dimensions applicable to all submodels	129
Figure 67	Cross section of Submodel A with floor beam FB2	130
Figure 68	Extent of Submodel A	131
Figure 69	Cross section of Submodel A with floor beam FB1	132
Figure 70	Extended cutout details of connection Type 5B used in FEA	133
Figure 71	Extended cutout details of connection Type 4B used in FEA	133
Figure 72	Extent of Submodel B	134
Figure 73	Cross section of Submodel B with connection Type 1B looking east	135
Figure 74	Cross section of Submodel B with connection Type 5B looking east	136
Figure 75	Solid Element, C3D20R, and degrees of freedom (reproduced from Dassault Systemes 2013)	137
Figure 76	Face of solid element showing DOF and integration points: (a) C3D20; (b) C3D20R (reproduced from Dassault Systemes 2013)	137
Figure 77	Submodeling progression with floor beam FB1	138
Figure 78	Submodeling progression with floor beam FB2	139
Figure 79	Shell-to-solid submodeling of the Global model to Submodel A	140
Figure 80	Shell-to-solid submodeling	140

Figure 81	Solid-to-solid submodeling of Submodel A to Submodel B	141
Figure 82	Uniformly distributed load on top surface of load patch	141
Figure 83	Vertical displacement of floor beam 14 due to symmetric loading (SL)	142
Figure 84	Vertical displacement of floor beam 14 due to longitudinally eccentric loading (EL)	143
Figure 85	Principal stress contour on the west face of floor beam 14 for Submodel B with floor beam FB1 and connection Type 1B: (a) symmetric loading (SL) (b) longitudinally eccentric loading (EL)	144
Figure 86	Principal stress contour on the west face of floor beam 14 for Submodel B with floor beam FB2 and connection Type 1B: (a) symmetric loading (SL) (b) longitudinally eccentric loading (EL)	145
Figure 87	Principal stress contour on the west face of floor beam 14 for Submodel B with floor beam FB1 and connection Type 5B: (a) symmetric loading (SL) (b) longitudinally eccentric loading (EL)	146
Figure 88	Principal stress contour on the west face of floor beam 14 for Submodel B with floor beam FB2 and connection Type 5B: (a) symmetric loading (SL) (b) longitudinally eccentric loading (EL)	147
Figure 89	Principal stress contour on the west face of floor beam 14 for Submodel B with floor beam FB1 and connection Type 4B due to symmetric loading (SL)	148

Figure 90	Comparison of principal stress contour in floor beam 14 with floor beam FB2 and connection Type 1B due to symmetric loading: (a) Submodel A; (b) Submodel B	149
Figure 91	Direction of maximum principal stress in floor beam 14 for Submodel B with connection Type 1B for symmetric loading (SL): (a) floor beam FB1; (b) floor beam FB2	150
Figure 92	Direction of maximum principal stress in floor beam 14 for Submodel B with connection Type 5B for symmetric loading (SL): (a) floor beam FB1; (b) floor beam FB2	151
Figure 93	Direction of maximum principal stress in floor beam 14 for submodel B with connection Type 4B for symmetric loading (SL) with floor beam FB1	152
Figure 94	Stress distribution at the extended cutout termination for FB1 and connection Type 5B due to symmetric loading (SL)	153
Figure 95	Stress distribution at the extended cutout termination for FB2 and connection Type 5B due to symmetric loading (SL)	153
Figure 96	Stress distribution at the extended cutout termination for FB1 and connection Type 4B due to symmetric loading (SL)	154
Figure 97	Elevation view of a section of rib-to-floor beam connection due to: (a) symmetric loading (SL); (b) longitudinally eccentric loading (EL)	155

Figure 98	Potential modes of toe cracking shown on a cross section of a typical rib-to-floor beam connection	156
Figure 99	Potential modes of root cracking shown on typical rib-to-floor beam connections	157
Figure 100	Comparison of tensile stress normal to the weld toe on floor beam 14 web due to symmetric loading (SL)	158
Figure 101	Comparison of tensile stress normal to the weld toe on the west face of floor beam 14 due to longitudinally eccentric loading (EL)	158
Figure 102	Comparison of tensile stress normal to the weld toe on the east face of floor beam 14 due to longitudinally eccentric loading (EL)	159
Figure 103	Comparison of radial stress in floor beam 14 along the critical path due to symmetric loading (SL)	159
Figure 104	Radial stress showing out-of-plane bending of floor beam 14 web with floor beam FB1 due to longitudinally eccentric loading (EL)	160
Figure 105	Radial stress showing out-of-plane bending of floor beam 14 web with floor beam FB2 due to longitudinally eccentric loading (EL)	160
Figure 106	Comparison of tensile stress normal to the weld toe in rib 10 due to symmetric loading (SL)	161
Figure 107	Comparison of stress normal to the weld toe on the west face of rib 10 due to longitudinally eccentric loading (EL)	161

Figure 108	Comparison of tensile stress normal to the weld toe on the east face of rib 10 due to longitudinally eccentric loading (EL)	162
Figure 109	Comparison of radial stress in rib 10 along the critical path due to symmetric loading (SL)	162
Figure 110	Comparison of radial stress on the west side of floor beam 14 in rib 10 along the critical path due to longitudinally eccentric loading (EL)	163
Figure 111	Comparison of radial stress range on the east side of floor beam 14 in rib 10 along the critical path due to longitudinally eccentric loading (EL)	163
Figure 112	Comparison of tensile stress tangential to the rib-to-floor beam connection at the weld root in floor beam 14 due to symmetric loading (SL)	164
Figure 113	Comparison of tensile stress tangential to the rib-to-floor beam connection at the weld root on the west face of floor beam 14 due to longitudinally eccentric loading (EL)	164
Figure 114	Comparison of tensile stress tangential to the rib-to-floor beam connection at the weld root on the east face of floor beam 14 due to longitudinally eccentric loading (EL)	165
Figure 115	Comparison of tensile stress tangential to lower radius of extended cutout in floor beam 14 with connection Type 5B due to symmetric loading (SL)	165

Figure 116	Comparison of tensile stress tangential to lower radius of extended cutout in floor beam 14 with connection Type 4B due to symmetric loading (SL)	166
Figure 117	Comparison of tensile stress tangential to upper radius of extended cutout in floor beam 14 with connection Type 5B due to symmetric loading (SL)	166
Figure 118	Comparison of tensile stress tangential to upper radius of extended cutout in floor beam 14 with connection Type 4B due to symmetric loading (SL)	167
Figure 119	Comparison of stress normal to the weld toe in floor beam 14 for with connection Type 5B due to symmetric loading (SL)	167
Figure 120	Comparison of stress normal to the weld toe in floor beam 14 with connection Type 4B due to symmetric loading (SL)	168
Figure 121	Comparison of tensile stress normal to rib-to-floor beam connection at the weld toe of the extended cutout on the face of rib 10 with connection Type 5B due to symmetric loading (SL)	168
Figure 122	Tensile stress normal to rib-to-floor beam connection at extended cutout termination on the face of rib 10 with connection Type 4B due to symmetric loading (SL)	169
Figure 123	Stress normal to extended cutout termination in rib 10 with connection Type 5B due to symmetric loading (SL)	169

Figure 124	Stress normal to extended cutout termination in rib 10 with connection Type 4B due to symmetric loading (SL)	170
Figure 125	Comparison of stress normal to weld toe in rib 10 with connection Type 5B due to symmetric loading (SL)	170
Figure 126	Comparison of stress normal to weld toe in rib 10 with connection type 4B due to symmetric loading (SL)	171
Figure 127	Potential modes of cracking for connection Type 1B	171
Figure 128	Potential modes of cracking for connection Type 5B	172
Figure 129	Location of critical tangential stress for extended cutout lower radius for: (a) connection Type 5B; (b) connection Type 4B	172
Figure 130	Location of critical tangential stress for extended cutout upper radius with: (a) connection Type 5B; (b) connection Type 4B	173

ABBREVIATIONS

CJP	Complete Joint Penetration (weld)
EC	Extended Cutout
FB	Floor Beam
FEA	Finite Element Analysis
LOF	Lack-of-fusion
SOBD	Steel Orthotropic Bridge Deck
PJP	Partial Joint Penetration (weld)
RDP	Rib-to-Deck Plate
RFB	Rib-to-Floor Beam

ABSTRACT

Implementation of steel orthotropic bridge decks is limited due to fatigue performance concerns and high initial cost owing to fabrication demands brought on by elaborate designs and detailing to achieve acceptable fatigue resistance of the welded connections in the deck. Simpler details that provide acceptable fatigue performance can result in improved manufacturability, reduced fabrication cost, and increased implementation of orthotropic steel decks. Modern orthotropic decks are designed with ribs that pass continuously through matching cutouts in the floor beam, often with an extended cutout in the floor below the rib, and with or without internal bulkhead plates or stiffeners. The rib-to-floor beam welded connection is the most labor intensive and fatigue sensitive. Accordingly, existing generalized rib-to-floor beam connection types that are in-service in North America were identified and assessed for manufacturability. The connection types that appeared promising in terms of fatigue performance and potential for automated fabrication were further analyzed.

Multi-level 3D linear elastic finite element analyses (FEA) were performed using a model of a steel orthotropic deck integrated with steel box girders developed in a previous study. Additional submodels were developed with variations of the rib-to-floor beam connections and floor beam depths. The response of the critical rib-to-floor beam connection, under critical symmetric and eccentric loading conditions, with respect to the FB, was analyzed under the rear axle loads of an AASHTO fatigue truck to assess the fatigue performance of the critical rib-to-floor beam connection.

The study showed that the stresses in the floor beam were primarily in-plane, and the contribution of the out-of-plane stress component was negligible. For the depth of the

floor beams considered in this study, no appreciable effect of the floor beam depth could be discerned. The rib-to-floor beam connections within the shear span of the floor beam adjacent to the primary load carrying component. The load bearing floor beams, both with and without an extended cutout, experienced significant stress concentrations at the floor beam cutouts. Without an internal stiffening, the connection with an extended cutout that terminates square on the rib wall and having wrapped-around fillet welds, although promising for automated fabrication, exhibited greater stress concentration compared to a connection that employed a complete joint penetration groove welded detail and tangential termination on the rib wall.

No evidence of rib-to-floor beam connection automation could be found in the published literature or in the anecdotal information. The literature review identified that continuous welding of RFB connections would be a challenge due to welding against and with gravity. Welding against gravity would be the preferable method for depositing welds of acceptable profile and shape. For continuous welding, the deck may have to be manipulated either by standing vertically up or by rotating about an axis. For fitted floor beams, match cutting would be necessary if a tight fit-up is specified. Alternatively, a larger fit-up gap along with PJP welded connection would be more cost-effective.

1 INTRODUCTION

1.1 Background

Typical steel orthotropic bridge decks (SOBD) are composed of an orthogonally stiffened steel deck plate, with closely spaced ribs in the longitudinal direction and discrete floor beams (FBs) in the transverse direction, as shown Figure 1. Due to the different stiffness characteristics in the longitudinal and transverse direction as well as the orthogonal placement of the ribs and FBs, this type of deck was termed as “orthotropic” from orthogonally anisotropic. Although the term orthotropic deck was coined by German engineers for these composite and efficient deck systems developed after the world war to overcome material shortages, a similar welded system composed of structural beams and steel plates, known as the battle deck floor, was proposed by American Institute of Steel Construction in the 1930s (Troitsky 1987).

The SOBD has several advantages including: light weight, modular construction, minimized traffic disturbance, increased life span, minimal maintenance, enhanced structural efficiency due to inherent redundancy, and decreased life-cycle cost. In addition, in-service performance and laboratory tests of these decks suggest that if adequately designed, detailed, and fabricated, the SOBD is likely to provide a 100 year service life (Fisher and Roy 2011) with minimal maintenance. These significant advantages make the orthotropic deck system ideal for both new construction and replacement decks, however two primary concerns exist with increased implementation of SOBD.

One of the concerns is the fatigue performance of a SOBD in service, which must be carefully considered due to the large number of welded joints. Weld toes and weld roots are obvious stress concentrations from which fatigue cracking can precipitate due to weld

discontinuities, such as slag inclusion or undercut at the weld toe, or lack-of-fusion (LOF) or porosity at the weld root. Propagation of these fatigue cracks under live load is promoted by the high tensile residual stresses due to welding processes. Early SOBDS experienced premature fatigue cracks due to deficient designs that did not consider the fatigue limit state and the local stress effects under wheel loads due to complex behavior of the deck system. These decks used $\frac{1}{2}$ in. (13 mm) or less thick deck plates, torsionally soft open ribs or ribs with triangular profile, discontinuous ribs fitted between FBs and fillet welded, fillet welds for closed rib-to-deck plate (RDP) connections, and inadequate welding practices in general. As a result, these SOBDS experienced significant fatigue cracking after a few years of service. This fatigue cracking occurred primarily through the deck plate and the weld throat of the RDP connection due to large localized transverse bending of the deck plate, and through the throat of the discontinuous RFB welds, and other undesirable details such as the welded rib splices. Costly repair and retrofit measures were incurred by the premature fatigue cracking (Nunn 1974a, Nunn 1974b, Cunninghame 1987, de Jong et al 2004, Kolstein 2007).

The other concern, related to the previous concern, is the high initial cost owing to fabrication effort required by elaborate designs and detailing to achieve acceptable fatigue resistance of the welded connections in the deck. Modern SOBDS employ ribs passing continuously through matching cutouts in the FBs. In some cases, extended cutouts (ECs) are included. Modern SOBDS are fabricated by continuously welding the RDP connection, then fitting FBs with cutouts to the ribs and deck plate. Torsionally stiff closed ribs with round-bottom or trapezoidal profile, as shown in Figure 2, enable efficient transverse distribution of wheel loads and reduce demands on individual ribs. Thicker deck plate is

also used to reduce the stress demands from transverse bending. The ribs are typically welded to the deck plate with a greater fusion than provided by a fillet weld, often by a specified minimum 75~80% partial joint penetration (PJP) groove weld. The RFB connection may be designed with or without an EC in the FB below the rib, and with or without internal stiffening of the rib walls by bulkhead plates or stiffeners.

In SOBDs, the rib-to-floor beam (RFB) connection is the most labor intensive and fatigue sensitive, being subjected to complex in-plane and out-of-plane deformations under passing wheel loads (Grundy et al. 1994, Gajer et al. 1996). When the depth of FB is sufficient below the rib soffit, an EC is not required to produce an adequate design, as long as the out-of-plane flexibility of the FB web is provided by the combination of the FB web thickness, the FB depth, and the FB spacing. When sufficient FB depth is not available and/or the FB spacing and resulting rib rotations are larger (which occurs mostly in the case of a replacement deck), an EC is provided below the rib soffit in the FB web to alleviate the out-of-plane stress component. A RFB connection that require an EC may also require internal stiffening in the form of bulkhead plates or stiffeners. The connection becomes more complex when an EC is used, and a complete joint penetration (CJP) groove weld at the EC termination transitioning to fillet or PJP welds in the upper regions is often used. The fabrication of the RFB connection with EC requires significant cutting, trimming, grinding, nondestructive inspection, and joint preparations, as well as fabrication of a carefully designed EC geometry, all of which are labor intensive. When an EC is not used, the RFB connection can be made with back-to-back fillet welds which may require match cutting or grinding of the FB web to achieve the required fit-up to control the inherent LOF.

Successful implementation of SOBD requires reduced initial cost, which can be achieved by details that require less fabrication effort while providing the desired fatigue performance and can be easily, consistently repeated. Automated fabrication of the RDP connection has been implemented, which allows for easy, consistent production, however such automated fabrication has not been developed for the RFB connection. By standardizing a less labor-intensive and fatigue resistant RFB connection that is amenable to automation, manufacturability of SOBD would improve and ultimately increase implementation.

1.2 Objective of Current Study

The objectives of this study were:

- i. to investigate the manufacturability of RFB connection details, with or without an EC in the FB web below the rib soffit, for SOBD;
- ii. to investigate automated (robotic) and cost-effective fabrication processes for the RFB connection;
- iii. to investigate RFB connection details that are fatigue resistant, cost-effective, and amenable to robotic fabrication to improve manufacturability.

1.3 Study Approach

The study objectives were achieved by the following approach. An extensive literature review was performed to gather published information on different RFB connection details in modern SOBDs and their fabrication details, both manual and automated. Unpublished literature, such as personal correspondence with fabricators, was also pursued due to the limited published literature providing sufficient detail concerning the fabrication of the RFB connections. Information concerning welding processes in

general and their suitability towards robotic fabrication were also reviewed to assess their possible application for automated fabrication of RFB connections in modern SOBD.

To understand the evolution of the RFB connections, key geometric parameters of existing SOBD were identified, defined, collected, and tabulated. Databases containing this information for North American and International SOBDs were developed and analyzed to understand the evolution of the RFB connection. From these databases, primary types of RFB connections were identified and the promising connection types that are amenable to cost-effective automated fabrication were identified. Multi-level three dimensional (3D) linear elastic finite element analysis (FEA) of the selected connections were performed based on the model developed for a recent study (Roy and Mukherjee 2015) to evaluate the connections based on their stress responses.

1.4 Outline

This thesis contains 5 chapters. The first (current) chapter introduces the background of SOBD, presents the study objectives, provides an overview of the study approach, and outlines the thesis.

The second chapter presents a review of relevant literature, including connection details and their fabrication. The parameters of SOBDs are defined, and these parameters are collected from existing bridges, including RFB connection details, and tabulated in this chapter. The performance of existing SOBD in North America is discussed and tabulated.

The third chapter presents an evaluation of the database and generalized RFB connection types identified based on the tabulated information. Advantages and disadvantages of manual and automated fabrication of these RFB connection types are discussed.

The fourth chapter discusses the finite element analyses (FEA) of RFB connections that were identified as manufacturable in the previous chapter.

The fifth chapter presents and discusses the results of the FEA. The global and local behavior of each evaluated connection type is discussed and compared.

The sixth and final chapter discusses the conclusions, recommendations, and requirements for further research.

2 LITERATURE REVIEW OF THE RIB-TO-FLOOR BEAM DETAIL

A preliminary search revealed more than 250 publications on SOBD from domestic and foreign sources. These publications cover a wide range of topics including: design and application for new or replacement decks; case studies for general application of SOBD; geometry and in-service performance of orthotropic deck bridges in North America; in-service fatigue cracking and fatigue assessment; retrofit for in-service fatigue cracking; experimental evaluation of fatigue resistance; analytical techniques for evaluation of fatigue resistance including FEA; orthotropic plate theory; fabrication procedures and inherent issues; welding processes in general and whether they are amenable to robotic welding; design and fabrication of RDP connection; design of different types of RFB connections and manufacturability of these connections; application of automated welding processes to the RFB connection; construction of bridges with orthotropic steel deck; wearing surface design and performance. Of these publications, those pertaining to the RFB connections were of primary interest, particularly: design and application for new or replacement decks; case studies for general application of SOBD; geometry and in-service performance of orthotropic deck bridges in North America; experimental evaluation of fatigue resistance; analytical techniques for evaluation of fatigue resistance including FEA; fabrication procedures and inherent issues; welding processes in general and whether they are amenable to robotic welding; design of different types of RFB connections and manufacturability of these connections; application of automated welding processes to the RFB connection. Unpublished information were used to supplement the literature review where published literature was limited, particularly with respect to plans and design documents for the geometry of SOBD in North America. Unpublished, anecdotal

information were also used to supplement the literature review, particularly with respect to: in-service performance of orthotropic deck bridges in North America; implemented fabrication procedures, successes and challenges, and lessons learned; and expert opinion regarding manufacturability of RFB connections. Review of the relevant literature are presented in the following summarized under three major areas, connection details, fatigue testing, and fabrication.

2.1 Connection Details

An extensive literature review was performed to identify the various RFB connection details implemented for SOBDS in North America (both in the United States and Canada) and around the world and their design evolution:

Hilton and Hardenberg (1964), Smylie (1966), Troitsky (1987), and Wolchuk (1968) presented the design of the SOBDD for the Port Mann Bridge, particularly focusing on the deck type selection process for significant reduction of steel weight, as well as the innovative fabrication process. Bouwkamp and Powell (1967) presented the theoretical and experimental investigation of the Dublin Test Bridges to understand the behavior of orthotropic steel deck systems and compare theoretical and experimental results to best assess orthotropic steel decks in the future. Gill and Dozzi (1966) provided a detailed discussion of the fabrication and construction of the Concordia Bridge. Shields (1964), Shields (1966), Shields and Schmidt (1969), and Troitsky (1987) presented the design of the SOBDD for the Poplar Street Bridge as well the fabrication and erection of the steel superstructure performed by Bethlehem Steel Corporation. Wolchuk and Lally (1979) and Bouwkamp (1967) discussed SOBDD design and use of the Bethlehem Steel Company's design aid for rib dimensions and spacing of the San Diego-Coronado Bridge. Also

discussed was the analysis performed at UC Berkeley prior to its construction, which built off the analytical and theoretical analysis of the Dublin Test Bridges. Brief summaries of the orthotropic deck geometry were given by Troitsky (1987) and Mangus and Sun (2000) for the Papineau Bridge, by Troitsky (1987) for the A. Murray McKay Bridge, by Mangus (2005) for the Queensway Twin Bridges, and by Mangus (2005) and Mangus (2014) for the Bay Area Rapid Transit (BART) Bridges. Cunningham et al (1968) and Mangus and Sun (2000) outlined the design, construction, and erection process for the Fremont Bridge, the fifth major orthotropic bridge deck in the United States. Manniche and Ward-Hall (1975) discussed the design, innovative fabrication developed by Canron Limited, Western Bridge Division, and construction for the Mission Bridge. Nottingham (1980), Troitsky (1987), and Mangus and Sun (2000) provide general geometry information for the Patton Yukon River Bridge. Buckland (1981) described the replacement of the Lion's Gate Approach Spans, providing information on the design development and fabrication processes, which were similar to the Mission Bridge since Canron Limited, Western Bridge Division performed the fabrication and erection. Significant focus, however, was placed on the replacement process and resulting issues. Brief summaries of the orthotropic deck geometry were given by Wolchuk (1999) for the McNaughton Bridge, and by Mangus and Sun (2000) for the Luling Bridge. Troitsky (1987), Stahl (1990), Wolchuk (1992), and Mangus and Sun (2000) provided design, fabrication (particularly the RDP connection), and construction for the Golden Gate Bridge. Stahl (1990) and Haight et al (2005) described the design of the replacement orthotropic bridge deck for the Throgs Neck Viaduct. Wolchuk (1992) and Carlin and Mirza (1996) discussed the replacement deck alternatives and design of the SOBD of the Champlain Bridge, particularly the RFB EC

detail, as well as some fabrication details for the rib formation and automation of the RDP connection. Marquez et al (1998) and Roberts et al (2000) presented the design, fabrication, and erection of the Maritime Off-Ramp SOBD, with additional information on the foundation design and seismic design requirements. Kaczinski et al (1997), Tsakopoulos and Fisher (1999), Connor and Fisher (2000), and Tsakopoulos and Fisher (2003) presented the phases of full-scale fatigue testing for the Williamsburg Bridge replacement SOBD. Wolchuk (2001) and Abdou et al (2003) provided design development, finite element analysis of EC geometry of the RFB connection, and results of monitoring a prototype deck panel in service for the orthotropic replacement deck for the Triborough Bridge. Matson (2000) and Matson (2001) provided design, fabrication, and construction information for the replacement deck of the suspended span of the Lion's Gate Bridge, with great focus placed on the fabrication and construction methods for replacing the deck in modular fashion. Spoth et al (2000), Yanagihara et al (2006), and Uang and Sim (2007) discussed fabrication, particularly the RDP connection, of Alfred Zampa Memorial Bridge, also known as the New Carquinez Bridge, as well as the influence of the Williamsburg Bridge with respect to the RFB detail, specifically the internal bulkhead plate and EC geometry. Finite element analysis calibrated to the Williamsburg Bridge laboratory test data was also performed to assess the orthotropic deck for strength and fatigue. Tsakopoulos and Fisher (2002), Connor and Fisher (2004), and Tsakopoulos and Fisher (2005) presented the full-scale fatigue testing for the Bronx-Whitestone Bridge replacement SOBD. Spoth et al (2005) and Serzan and Spoth (2008) discussed the automation of the RDP connection, the influence of the Williamsburg Bridge testing on the RFB connection, and the global design of the new bridge of the Third Tacoma Narrows Bridge. Roy et al (2012a) and Roy et al

(2012b) presented the two phases of full-scale fatigue testing for the Verrazano-Narrows Bridge replacement SOBD. Radojevic et al (2014) provided a general overview of the replacement deck of the Angus L. Macdonald Bridge as well as the modular construction and challenges.

The information on existing SOBD were synthesized in terms of the key geometric parameters of the deck namely, the rib geometry, the EC geometry, and the FB sectional dimensions, as well as the global orthotropic deck dimensions, such as rib and FB spacing, and the deck plate thickness. The key geometric parameters are defined in Table 1 and in Figures 3 through 6. The parameter nomenclature used in this study is consistent with the current AASHTO LRFD Bridge Design Specifications (AASHTO LRFD BDS) and the FHWA Manual for Design, Construction, and Maintenance of Orthotropic Steel Deck Bridges (Connor et al. 2012), hereafter denoted as the FHWA Manual. The information on existing SOBD in North America including year of construction, key dimensions of the decks (consistent with the defined nomenclature), and types of connections (both RDP and RFB) are tabulated in Table 2 in chronological sequence of year built. The bridge names are not included in the table since some information in the plans that were provided are kept confidential. Also included in the table are sketches of the typical RFB connection for each bridge. Similar information on SOBD from the rest of the world are tabulated in Table 3.

The literature review revealed that modern orthotropic decks in North America employed trapezoidal and round-bottom ribs passing continuously through FBs, with or without additional stiffening inside the ribs. In contrast to the Canadian designs, typically the orthotropic decks in the United States employed trapezoidal ribs. Most of the early

SOBDs, built between 1960s to late-1980s, incorporated fitted RFB connections as shown in Figure 7. Opened to traffic in 1964 (Hilton and Hardenberg 1964), the Port Mann Bridge in Vancouver, Canada was the first application of a modern steel orthotropic bridge deck in North America that employed round-bottom ribs continuously passing through matching cutout in the FBs and fillet welded. The first implementation of SOBD for a major bridge in the United States was in the Poplar Street Bridge (Shields 1964), although prototype SOBDs for investigating wearing surface design and verification of orthotropic deck analysis software for the upcoming San Diego-Coronado Bridge were installed on Route 580/680 in Dublin, CA (Bouwkamp and Powell 1967).

An EC in the FB below the rib was introduced in the SOBD in the 1990s, for both new construction and replacement decks. This transition in the RFB connection design may have originated in Europe (Haibach and Plasil 1983) to facilitate fabrication and fit-up for ribs passing continuously through FBs, as significant cracking, (Figure 8) was experienced in Europe (Nunn 1974a, Nunn 1974b, Cunninghame 1987) at RFB connections that employed discontinuous ribs fillet welded to the FB, as shown in Figure 9. With the introduction of an EC came the necessity for internal stiffening, using an internal bulkhead or stiffeners, to prevent cracking at the EC termination in the rib wall (Grundy et al. 1994) as shown in Figure 10.

2.2 Fatigue Testing

Significant literature from foreign sources exist on laboratory fatigue testing of various RFB geometries, however, most of these studies are dedicated to SOBDs with antiquated geometry, for example, with deck plate thickness less than $\frac{1}{2}$ in. (13mm), a fillet welded RDP connection, triangular ribs (Figure 11), or ribs fitted between FB with

fillet-welded connections (Beales 1990a, Beales 1990b, Lehrke 1990, Kolstein 2007). Additionally, these tests often evaluated retrofit details for existing SOBD using small size specimens. These retrofit details are not applicable for the current study as they are case-to-case specific and not readily applicable to a new SOBD design. Additionally, the small size specimens did not accurately capture the effects of boundary conditions that exist in full size decks. A few full scale laboratory fatigue test results of interest are as follows.

Significant literature on domestic full-size laboratory fatigue testing of RFB connections was reviewed. Most notable of these tests were four SOBD tested at the ATLSS Engineering Research Center, Lehigh University, starting in mid-1990's and proceeding through 2015. These tests included realistic boundary conditions, moving loads, and fabrication effects. The RFB connection, with and without an EC below the rib, was of primary interest in all of these studies. All tests were performed for one or two lanes of AASHTO fatigue design load with a series of actuators loaded in sequence. The deck design of all four SOBD employed ribs passing continuously through matching cutout in the FB. The first three tests were replacements decks with limitations on vertical depth, and included an EC in the FB below the rib with some form of internal stiffening, either as a stiffener or a bulkhead plate. For the first three tests, the FB refers to the transverse stiffening element of the SOBD, which was separate from the FB of the bridge floor framing system. The fourth test was for the SOBD for a movable lift bridge where the RFB connection consisted of a fitted FB without an EC below the rib and without any internal stiffening.

Haibach and Plasil (1983)

A significant German study that influenced the development of RFB connections with EC, and has been extensively cited in subsequent studies, was performed by Haibach and Plasil at the Fraunhofer Institute for Structural Durability, Darmstadt. The study evaluated fatigue performance of orthotropic decks for railway bridges with ballasted tracks. The test program consisted of four test series, of which Test series A and C are the most relevant as they dealt with RFB connection details that were developed for improved fatigue resistance. The orthotropic deck specimens had trapezoidal ribs passing continuously through matching cutouts in the FB web. Two forms of RFB connection details, Form I, with an EC below the rib; and Form II, without an EC below the rib, were investigated in each of the test series. In Test series C, the RFB connections were tested under in-plane stresses using a single simply supported FB specimen that consisted of four ribs. In Test series A, the RFB connection was tested under out-of-plane (out of the FB plane) loading using a specimen with a single rib and FB. The cross section of the specimen in Test series C is shown in Figure 12, along with the simulated single-track uniformly distributed railway load. The dimensions of the ribs are shown in Figure 13.

In a preliminary study performed under Test series C, two variations of the Form I RFB connection, Form I.1 and Form I.2 (Figure 14), were investigated, which resulted in fatigue cracks respectively at the edge of the EC and at the EC termination on the rib. Based on preliminary testing, Form I was developed by combining and modifying Form I.1 and I.2 and was tested in the final phase of the test series. The most notable modifications, as show in Figure 15, included increasing the upper radius to 20 mm and introducing a tab of 10 mm ($\frac{3}{8}$ in.) to offset the termination of the upper radius from the face of the rib wall.

The outer termination of the upper radius of Form I (point CI.1 in Figure 15) was identified as the critical point for fatigue cracking. These modifications were intended to prevent the cracking that occurred in Form I.1 and Form I.2 and reduce the geometric stress concentration of the EC on the notch effect of the weld termination at the cutout, thereby increasing the fatigue performance. Form I exhibited the best fatigue performance in subsequent fatigue testing when compared to the performance of Form I.1 and I.2. Due to cracking on the edge of the welded rib, as shown in Figure 16, the Form II RFB connection was only tested in the preliminary stage. It was postulated that this cracking was caused by high residual stresses.

Lehrke (1990)

Subsequent to Haibach and Plasil's study, Lehrke commenced a study to evaluate the fatigue performance of Haibach and Plasil's Form I EC, referred to as the new cutout, in comparison to the commonly used EC for highway bridges. The commonly used EC terminates perpendicular to the rib wall and does not use a tab to offset the upper radius termination from the face of the rib wall. Although Lehrke states the new cutout shape to be that of Haibach and Plasil's work, the upper radius does not end parallel to the rib wall creating a small tab with square ended termination on the rib wall, rather it terminates tangentially on the rib wall. Figures in a subsequent publication (in German) by Lehrke depict the new connection with the square tab, however it is unclear to what extent the square tab was or was not incorporated into the modeling and fatigue testing.

A two-dimensional, in-plane finite element model of a simply supported cross beam with six ribs showed the stress distribution along the edge of the EC for the commonly used shape and new shape differ in regard to the volume of highly stressed material, however

the maximum value of stress is nearly the same in both ECs. The stress at the termination of the new cutout was smaller than that of the common cutout. It is important to note that the values of the stress distribution also had to be verified by test measurements since it was questioned whether the finite element model accurately represented the stress in the vicinity of the weld.

Fatigue testing of both EC geometries was performed. Only the new cutout developed cracking at the cutout termination. Both the commonly used cutout and the new cutout developed cracks at the free edge of the EC. These cracks developed in the new cutout after the number of load cycles reached 3-5 times that of the commonly used shape. Although the new cutout exhibited increased fatigue life compared to the commonly used cutout, it was unclear whether it was attributed to the shape of the cutout, since the weld details were not provided and the EC termination for the new cutout was unclear. As a result, a specific cutout geometry could not be recommended.

Kaczinski et al. (1997), Tsakopoulos and Fisher (2003)

In the first full scale laboratory study in the United States, the replacement deck for the Williamsburg Bridge in New York City was evaluated for fatigue resistance on a prototype and an as-built deck panel in multiple phases carried out between 1995 and 1998. The deck had transverse diaphragms at the FB and intermediate locations, and the rib-to-diaphragm connections are referred to here as RFB connections. The FBs were spaced at 12 ft. (6.1 m). The intermediate diaphragms were spaced at 6 ft. (3 m) and had a 1/2 in. (13 mm) thick web. The RFB connections at the FBs employed partial depth internal bulkhead plates as stiffeners to minimize out-of-plane distortion of the rib wall and to facilitate

transmission of forces in the FB across the rib. Internal bulkheads were not provided at the intermediate diaphragms. Additional dimensions are provided in Figure 17.

In Phase I of this test program (Kaczinski et al. 1997), two variations of the RFB connections, one fillet welded (weld option B) and one a combination of CJP groove weld and fillet weld (weld option A) were investigated on a prototype deck, as shown in Figure 18. The fillet welded connection employed back-to-back welds terminating $\frac{1}{4}$ in. (6 mm) short of the EC termination on the rib, resulting in a crack-like condition between the FB and the rib wall and the unfused root of the fillet welds. The combination weld (weld option A) employed a 4 in. (102 mm) long CJP groove weld with fillet reinforcements along the termination of the EC that transitioned to back-to-back fillet welds continuing above the groove weld. To minimize stress concentrations and weld discontinuities at the EC termination, a 1 in. (25 mm) runoff tab below the EC was provided, which was ground to a smooth radius transition onto the rib wall. Both weld options had the same internal bulkhead weld detail, where back-to-back fillet welds were used and terminated short of the bulkhead edge. The prototype deck was tested for 8.5 million cycles simulating the passage of two trucks side by side, with 1×HS15 fatigue truck in the inner lane and 1.3×HS15 fatigue truck in the outer lane, including impact. Each actuator represented the rear tandem axle, similar to the HS20 truck design. The test results demonstrated that the combination weld (weld option A) performed better than the fillet-welded connection (weld option B), as only one weld option A connection experienced cracking while seven weld option B connections experienced cracking. It may be noted that weld option A required substantial fabrication effort due to joint (plate) preparation, welding from both sides, grinding of the EC termination to a smooth transition radius on the rib wall, and a

strict inspection regimen for the CJP groove welds. Upon completion of Phase I testing, the combination weld detail as well as other improvements were incorporated in the design, which included: increasing the FB diaphragm web thickness from $\frac{5}{16}$ in. (8 mm) to $\frac{1}{2}$ in. (13 mm) to reduce the dominant in-plane stresses without compromising the out-of-plane stresses; making the FB diaphragms of uniform depth and continuous under ribs for a more uniform distribution of shear stresses between ribs, and improved in-plane flexural compliance between the diaphragm and the FB; increasing the thickness of the internal bulkhead plates from $\frac{5}{16}$ in. (8 mm) to $\frac{1}{2}$ in. (13 mm); and extending the bulkhead plate $\frac{3}{4}$ in. (19 mm) below the termination of the EC on the rib wall for a more uniform distribution of stresses at the rib-to-bulkhead connection.

The subsequent Phase IIA and IIB testing (Tsakopoulos and Fisher 2003) was conducted to assess the design improvements derived out of the Phase I study and to more thoroughly assess the fatigue resistance of weld options A and B. A shorter as-built test panel was fabricated, consisting of one internal FB diaphragm and incorporating the design improvement features. The Phase I prototype panel was reconfigured to incorporate the new as-built panel in the middle. The deck was tested for 5 million cycles in Phase IIA, under similar loading as Phase I, simulating the passage of two trucks side by side, but focusing primarily on weld option A. No fatigue cracks were detected from the weld toe in the weld option A RFB connections at the conclusion of Phase IIA testing. One crack was detected in the Phase IIA at the as-built diaphragm, initiating from a notch like defect in the flame cut edge of the cutout adjacent to the RFB weld toe. In Phase IIB, the Phase IIA test panel was tested without modifying the deck configuration. The deck was tested for 2 million cycles under single lane (outer lane) of 2.3×HS15 fatigue truck including impact.

The two RFB connections with weld option B that had developed fatigue cracks at the fillet weld termination, where the built-in crack-like end LOF existed, were refurbished by removing the cracked fillet weld metal and wrapping fillet welds around the termination of the EC, thus eliminating the crack like condition. This repair method was identified as weld option C, as shown in Figure 18.

The test results indicated the combination weld detail (weld option A) was consistent with AASHTO LRFD fatigue category C. The fillet welded connection refurbished with the weld wrapped around the EC termination (weld option C) also exhibited a fatigue resistance of Category C. The extensive testing of the SOBD for the Williamsburg Bridge was influential in subsequent designs of SOBD in the United States, particularly the use of the combination weld detail for RFB connections with an EC in the FB web below the rib. Notable examples of SOBD designed in the United States that referenced the Williamsburg bridge RFB connection detail including the rib internal bulkhead plate are the Triborough Bridge in New York (Abdou et al 2003), the Alfred Zampa Memorial Bridge crossing the Carqinez Straits in California (Spoth et al 2000), and the Third Tacoma Narrows Bridge in Washington (Serzan and Spoth 2008). The same combination weld detail for RFB connections was also used for the replacement SOBDs for the Bronx-Whitestone Bridge, the Verrazano Narrows Bridge, the new SFOBB in California, and has been proposed for the replacement SOBD for the Throgs-Neck Bridge. *Tsakopoulos and Fisher (2002), Tsakopoulos and Fisher (2005)*

In the second study, the replacement deck for the Bronx-Whitestone Bridge in New York City was evaluated for fatigue resistance by testing a prototype deck. The RFB connection included an EC with two internal stiffeners at each FB to reduce the rib

distortion. The design of the SOBD, specifically the development of the EC geometry of the RFB connection, was influenced by the testing and in-service performance of the Williamsburg Bridge as well as a prototype deck panel for the Triborough Bridge (Fanjiang et al 2004). The FBs were spaced at $19\frac{3}{4}$ ft. (6 m) and had a $\frac{3}{4}$ in. (19 mm) thick web. The diaphragms were spaced at $9\frac{7}{8}$ ft. (3 m) and had a $\frac{1}{2}$ in. (13 mm) thick web. Additional dimensions are provided in Figure 19.

In contrast to the Williamsburg Bridge, the Bronx-Whitestone Bridge had a deeper EC with CJP groove weld and back-to-back reinforcement fillet weld along the entire length of the connection. The fatigue design truck loading was applied by three deck actuators spaced at 5 ft. (1.5 m) along the deck, each actuator representing the rear tandem axle of a HS20 truck. In Phase I, the deck was tested for 4.1 million cycles under $3.45\times$ HS15 fatigue loading including impact, where no fatigue cracking was detected. In Phase II, the deck was subjected to an additional 2 million cycles under increased $4.6\times$ HS15 fatigue loading including impact. A crack was discovered at the termination of the test that had developed in the deck plate at the FB intersection under a wheel load print, and extended beyond the load prints on the deck. The test program verified that the RFB connection was a Category C detail.

Roy et al (2012a), Roy et al (2012b)

In the third study, the replacement deck for the Verrazano Narrows Bridge in New York City was evaluated for fatigue resistance by testing prototype decks in two phases. The RFB connection employed an EC and full depth bulkheads inside the ribs at the FB. In contrast to the Williamsburg Bridge and Bronx-Whitestone Bridge, the FBs were integral with the existing stringers, making them load bearing in the transverse direction.

The FBs were spaced at 37 ft. 1 1/2 in. (11.3 m). The intermediate FBs were spaced at 12³/₈ ft. (3.8 m) and had a 7/8 in. (22 mm) thick web. Additional dimensions are provided in Figure 20.

Similar to the weld option A for the Williamsburg Bridge SOBD, the RFB connection employed a CJP weld for a minimum 4 in. (102 mm) from the EC termination on the rib wall, reinforced with back-to-back fillet welds that transitioned to PJP weld reinforced with back-to-back fillet welds. The internal bulkhead plates were fillet welded on both sides.

In Phase I, the deck was tested for 5 million cycles at a load level of 3.45×HS15 including impact. The fatigue design loading was applied by six sequentially loaded above-deck actuators spaced at 4 ft. 1 1/2 in. (1.3 m) along the deck. In contrast to the previous two test programs, each actuator represented one axle of the rear tandem of the fatigue truck. After 3.53×10⁶ cycles, a fatigue crack was detected at a RFB weld termination. The EC geometry was modified to remove the fatigue crack and allow for the continued fatigue testing. The test results showed that the stress ranges at the RFB connection was too high to satisfy the fatigue design requirements of a 75-year service life. Accordingly, design improvements were proposed to reduce the stresses in the SOBD, including: enlarging the EC with an increased termination radius on the rib; increasing the FB web thickness from 5/8 in. (16 mm) to 7/8 in. (22 mm); reducing the FB spacing; and increasing the bulkhead plate thickness from 5/16 in. (8 mm) to 5/8 in. (16 mm).

The design improvements were assessed in the Phase II study. A new deck segment was fabricated incorporating these design improvements, and the Phase I specimen was reconfigured to accommodate the modified FB deck segment. The loading for the Phase II

testing was similar to Phase I, except four above-deck actuators were used to simulate in-plane (symmetric) and out-of-plane (eccentric) loading of the FB. The enhanced RFB connections survived 5 million cycles at a load level of $3.45 \times HS15$ including impact.

Roy et al (2014), Roy et al (2015), Mukherjee (2016)

In the last study, the SOBD for a movable lift bridge, denoted as an unnamed “lift bridge” in this thesis, was evaluated on a prototype deck that was tested in the laboratory. This deck was different than the decks in the previous three studies in several aspects: the FB of the SOBD was integral with the primary load carrying components (i.e., the longitudinal girders) of the superstructure; the FBs has a maximum midspan depth of 4 ft. (1.2 m); and FBs were fitted around the ribs without an EC and without internal stiffening of the ribs at the FB, since sufficient FB depth was available to make the FB sufficiently flexible to accommodate the rib rotations. The FBs were spaced at $11\frac{3}{4}$ ft. (3.6 m) and had a $\frac{1}{2}$ in. (13 mm) thick web. Additional dimensions are provided in Figure 21.

In an initial phase, the required fabrication effort and the fatigue performance of three RFB connection details were investigated. Two of these connection details were fillet welded with target fit-up gaps between the rib and the FB of $\frac{1}{32}$ in. and $\frac{1}{16}$ in., respectively. The third connection detail employed a PJP weld with joint preparation on the FB, but with a larger fit up gap of $\frac{1}{8}$ in. In comparative fatigue testing of small size specimens consisting of a rib and a FB under identical loading, the PJP connection details performed the best.

In the following phase, a full size specimen, including five ribs and three FBs, was fatigue tested. The specimen had a fillet welded RFB connection and a FB depth of 2 ft. $10\frac{1}{2}$ in. (876 mm). The loading was applied by two above-deck actuators spaced at 4 ft. (1.2 m) along the deck simulating the individual axles of the rear tandem of the fatigue

design truck. The deck was tested for 8 million cycles under $3.45 \times HS15$ fatigue truck including impact. No fatigue cracks were detected upon completion of the test program.

2.3 Fabrication

Information on fabrication of RFB connections in published literature are limited, particularly for connections employing an EC in the FB with or without internal stiffening of the rib. In comparison, a few publications on RFB connections with fitted FB from the early orthotropic decks in North America are available, which provided some useful information and possibilities for automated fabrication of these connections. These publications are related to the fabrication of the Port Mann Bridge, the Concordia Bridge, the Mission Bridge, and the Poplar Street Bridge. All of these SOBDS employ a fully fitted RFB connection with ribs passing continuously through a matching cutout in the FB, with a rounded bottom or trapezoidal rib profile. Most of the information indicate that the RFB connections are typically fabricated manually. No evidence of full automated welding of the RFB connections could be found. In order to explore the possibility of automating the fabrication of the RFB connection, the literature review also broadly encompassed welding technology including welding processes suitable for automation, identification of important welding parameters, and the key features of robotic welding. The relevant findings of this literature review are presented in the following.

2.3.1 General Considerations of Arc Welding

Arc welding processes are most commonly used for joining steels. Irrespective of manual or automated welding, the primary arc welding parameters that influence weld quality are current, wire feed speed, contact-tip-to-work distance (CTWD), voltage, electrode diameter, travel speed, and mode of transfer (Linnert 1994).

The welding energy input is a function of the welding current, voltage, travel speed and the efficiency of the particular process. For a given welding process these parameters need to be controlled for quality weld. The parameters in turn depend on several aspects of welding. Arc welding is typically a high current low voltage process. The welding current has the greatest effect on the weld penetration. A decrease in current decreases the penetration and results in a tall, narrow weld bead, while an increase in current increases the penetration and results in a proportional weld bead. Current that is disproportionately high can undercut the base metal and result in a wide, flat irregular weld bead. Wire feed speed, the rate at which the wire is fed into the weld or the weld deposition rate, is directly proportional to current when all other parameters remain constant. Adjustments in wire feed speed can be made to control the weld deposition rate to accommodate the orientation of a work piece, i.e., welding with or against gravity. For the same energy input, the CTWD (Figure 22), the distance from the tip of the nozzle to the top face of the work piece, is inversely proportional to the current. A specific CTWD must be maintained to ensure a consistent weld profile.

The welding voltage has minimal impact on weld penetration but may more noticeably impact the shape of the weld. The voltage is synonymous with arc length, or the distance from the tip of the electrode to the top face of the work piece. The arc length affects the cone width (Figure 22) which is the width of effective area of the arc on the work surface. An increased arc length results in wider cone width and greater voltage. The size or diameter of the electrode contributes to the weld penetration and deposition rate. A smaller diameter electrode provides a more concentrated current and thus increases the penetration, however it is important to note that an unstable arc results from a

disproportionately small electrode. Conversely, a larger diameter electrode will result in less penetration. The travel speed also impacts the penetration and a faster speed will provide less penetration than a slower speed.

Various modes of transfer are available for welding, and their applicability is determined according to the welding process and the geometry of the work piece. These modes of transfer characterize how the metal is transferred from the electrode to the weld pool and include globular, axial spray, pulsed spray, and short circuit. Of these modes of transfer, pulsed spray transfer is promising for the RFB weld as it is applicable to thin and thick sections and can be applied to a work piece in all positions. Pulsed spray transfer is categorized by globules equal to or smaller than the electrode diameter falling across the arc as a result of high spray transfer current and low background current (Linnert 1994).

2.3.2 Available Information on Fabrication of SOBD for Existing Bridges

Literature on manual fabrication, specifically the RFB connection, exists for some early SOBDs in North America and are discussed in the following. The geometric parameters of these SOBDs are shown in Figures 23 through 26. Although other fabrication information for these bridges may be available, particularly for the RDP connection, they are not discussed.

Hilton and Hardenberg (1964), Smylie (1966)

The Port Mann Bridge was the first application of a modern SOBD in North America, and opened to traffic in 1964. This SOBD included ribs passing continuously through the FB and a rounded bottom rib profile. The fabricator, Dominion Bridge Company of Vancouver Production, increased efficiency by adopting significant innovative and automated techniques. A bridge mounted torch that followed an overhead

template was used to burn the rib profiles in the FB webs, as shown in Figure 27. These profiles followed the design cross sections of the ribs and did not consider the cross sectional distortions that occur due to thermal effects of welding the ribs to the deck plate. A design fit-up gap of $\frac{1}{8}$ in. was available, however significant difficulty was experienced in fitting the FB to the ribs. As a result, when the ribs were too tight, the FB webs were ground or trimmed (by burning) for proper fit. Conversely, when the ribs were too loose (i.e., with a gap more than $\frac{5}{32}$ in.), the excessive gap between the rib and FB was filled by manual welding with the aid of a backing bar before final welding of the FB to the ribs. Final welding of the RFB connection was performed after jack-fitting the FB to the ribs in a jig, standing the deck assembly vertical on its end, and continuously welding the connection with a fillet weld in the 2F position.

Gill and Dozzi (1966), Troisky (1987)

The Concordia Bridge was fabricated by the Montreal Branch Dominion Bridge Company in 1964. Fabrication of the orthotropic deck made extensive use of jigs and fixtures developed specifically for the project to expedite the fabrication process. The FBs were made in pairs, as shown in Figure 28, and the profile was cut using a pantograph burning machine, similar to the Port Mann Bridge. The burning tip of the pantograph allowed the remaining U-shaped pieces cut from the FB to be used as end diaphragms for the ribs.

A jig with three stations was designed for the fabrication of the orthotropic deck sections. The first station butt-welded the deck plate on one side, and the second station pneumatically clamped the ribs to the deck plate in the inverted position and welded the RDP connection. The deck section was then moved to the third station where the FB was

fitted to the deck and rib in the inverted position. The rounded portion of the RFB connection was welded with a semi-automatic FCAW-G welding process. Lastly, the deck section was placed in a horizontal rotator, as shown in Figure 29, and the RFB connection was finished by welding the flat wall of the U-shaped rib to the FB.

Shields (1964), Shields (1966), Shields and Schmidt (1969)

The Poplar Street Bridge was the first major SOBD in the United States, with construction completed in 1967. The FBs were cut in pairs from three-plate welded girders then separated at the center to produce the final FB sections. They were then fitted to the deck plate and ribs, and manually welded. Although not noted specifically in the text, it can be inferred from Figure 30 that the RFB weld was made while the deck section was in the inverted position.

Manniche and Ward-Hall (1975)

The Mission Bridge has several similarities to the Port Mann Bridge, however the fabrication approach differed. Canron Limited, Western Bridge Division supplied, fabricated, and erected the structural steelwork. Innovative techniques and equipment for fabrication had to be developed because they lacked prior experience fabricating SOBD. The ribs were formed by bending plate material in a framed jig that applied pressure to the restricted outer edge of the rib plate and allowed the radius to form freely. This rib forming process provided consistent results. A sample orthotropic deck panel was fabricated to accurately represent the deformation and shrinkage experienced during welding. The sample panel was then used as a template for flame-cutting the rib profile in the FB web. A cope was provided in the FB web where the rib, FB, and deck plate intersect to avoid the

intersecting welds. Minimal distortion due to welding was observed in the sample panel, and close fit-up was achieved which resulted in minimal effort in fitting the FB to the rib.

Roy et al. (2014)

The fatigue performance of three RFB connection details were evaluated using three full-scale small-size specimens with varied fabrication parameters. The orthotropic deck specimens employed round bottom ribs with fully fitted FBs without an EC below the rib, and without any internal stiffening of the rib at the FB intersection. The ribs were formed from $\frac{5}{16}$ in. (8 mm) plate and spanned 6 ft. (1.8 m). The FB web thickness was $\frac{1}{2}$ in. (13 mm) with a maximum depth of 36 in. (914 mm). Two RFB connection details were fillet welded with target fit-up gaps of $\frac{1}{32}$ in. and $\frac{1}{16}$ in., to investigate the extent of the fabrication effort and resulting performance. An alternative RFB connection detail was investigated that employed a PJP weld with joint preparation on the FB, but with a larger fit up gap of $\frac{1}{8}$ in. The fabricator of the specimens, High Steel Structures Inc. of Lancaster, PA, reported that the effort required to fit the FB to the rib of the fillet welded specimens was about eight and four times that for the PJP welded specimen, even considering the joint preparation required for the PJP welded detail. The primary reason for the increased effort was the significant grinding of the FB required to achieve the specified fit-up for the fillet-welded connections due to the uncontrolled surface profile of the ribs welded to the deck plate. Under identical fatigue loading conditions, the specimen with PJP welded connection performed the best, and also appeared to be the most cost-effective.

2.3.3 Automated Processes

Of the arc welding processes, it is known that gas metal arc welding (GMAW), flux cored arc welding (FCAW), and submerged arc welding (SAW) are amenable to

automation. GMAW operates at a relatively low heat input while SAW operates at a relatively high heat input. GMAW and gas shielded flux cored arc welding (FCAW-G) are the predominant processes used for automated bridge fabrication around the world, while SAW is the predominant process used for bridge fabrication in the United States (Verma et al 2001). Pulsed gas metal arc welding (GMAW-P), a subcategory of GMAW, could be a viable option for automated fabrication of the RFB connection given the versatility (welding with or against gravity) of pulsed spray transfer. The use of GMAW can result in flaws such as cold lap, porosity, LOF, and lack-of-penetration (LOP), however use of GMAW-P could decrease or eliminate the LOF.

Verma et al. (2001)

A comprehensive overview of steel bridge fabrication in Japan, Italy, Germany, and the United Kingdom was presented from a scanning tour performed by a team of specialists. The objective of the scanning tour was to assess the development of steel bridge manufacturing outside the United States. Of particular interest was steel production, design, innovation, and fabrication.

Laser and plasma cutters were used to mark and cut the steel pieces, with equipment tailored to the type of bridge cross section most commonly produced for a given fabrication shop. Numerically controlled (NC) equipment and robotic welding were used in every fabrication shop visited. International automated and robotic welding methods differed from those implemented in the United States. Submerged arc welding (SAW), predominantly used for bridge fabrication in the United States, was not used frequently in international fabrication shops. International automated welding primarily used gas shielded flux cored arc welding (FCAW-G) or gas metal arc welding (GMAW) with either

solid or metal cored electrode. Other welding processes used less frequently in international fabrication shops included shielded metal arc welding (SMAW) and electro-slag/gas welding. A notable robotic welding method was the high-speed, high-current rotating arc welding system, patented by NKK, which provided a robotic welder with electrical feedback for tracking. None of the fabrication shops appeared to use robotic welding for the RFB connection.

Based on the scanning tour, the highest priority need noted in the report was the need for development and implementation of computer integrated manufacturing (CIM) software. At the time of the tour, all the fabricator shops that were visited used computer aided drawing (CAD) and computer aided manufacturing (CAM), however, none of the software was completely integrated. The use of CIM would allow a 3-D model to be modified according to the fabrication process and to reflect any shrinkage or distortion from one fabrication station to the next, ultimately allowing for virtual assembly verification. This type of CIM process would assist in the fit-up of the RFB connection. Additionally, 3-D measurements could be made to verify the as-built 3-D model to ensure accuracy.

Ryuh and Pennock (2006)

General guidelines were provided for robotic automation capabilities that should be considered for optimum performance and appropriate selection. Considerations for robotic welding include: work envelope, reach of robot tip, number of joints, travel velocity, repeatability, accuracy, and resolution of motion. In general, a robotic welding station is comprised of a robot, a robot controller, welding equipment, work clamp and motion devices, sensors, and safety devices.

The work envelope available at the fabrication facility will dictate the specimen size. The robot is programmed to move the welding torch, attached to the wrist of the robot, along the weld path in a given orientation. Important orientation angles include work angle (angle between the travel plane and the horizontal axis of the work piece), Figure 31, and travel angle (angle between the electrode axis and the vertical axis perpendicular to the work piece), Figure 32. These angles impact weld profile and quality and are particularly important when welding with and against gravity. The welding equipment integrated with the robot generates the power for the welding process as well as provides the appropriate wire feed. The best results will be obtained with a short arc welding process and welding equipment attached closely to the robot for quick response time.

Accurate manipulators and sensors maintain quality control and repeatability of welding. Manipulators hold and move the work piece to allow better access to the joint when the robot cannot move the work piece to a more desirable welding position that will produce better results and increase welding speeds (ultimately productivity). Sensors, either contact or non-contact, transfer information from the robot, peripheral devices, and welding process to a controller. A variety of sensors are available and selected based on applicability and cost. A contact sensor uses a probe to make direct contact with the work piece surface and process information to deduce the location and orientation and thus be able to locate the weld seam. Contact sensors are more economical and easier to use than non-contact sensors, however they cannot be applied to butt joints and thin lap joints. Throughout the welding process, the welding will stop and the contact sensor will touch down to contact multiple surface points. The number of times the welding process is

stopped varies and will be dependent on the complexity of the work piece as well as the required tolerance.

Peripheral equipment enables the use of robotic welding for work pieces that exceed the robot workspace. Peripheral devices are selected based on intended use and include track, gantry, and column configurations. These devices increase productivity and allow for flexibility from one project to the next. A track device mounts the robot to a track, which only allows movement in one direction but nearly eliminates size constraints. A gantry device suspends the robot above the work piece and allows the attachment of multiple robots from a single gantry. A column device suspends the robot from a column and can be fixed, traveling, rotary, or rotary/traveling.

Touran and Ladick (1989)

The benefits of steel bridge deck replacements, specifically SOBDS, to achieve lower life cycle cost, increased load capacity, and minimized traffic disturbance with rapid repairs are investigated. Steel orthotropic bridge decks provide a solution for concrete deck replacement, however implementation is limited due to the cost of production in a traditional fabrication shop. As a result, the potential to increase design economy by applying robotic welding was evaluated by comparing fabrication of a typical SOBDD module by conventional methods with robotic fabrication.

A standard deck module, composed of an 8 ft. x 40 ft. section with trapezoidal ribs, was used for the comparison. Drawings, specification list, and estimation sheets were sent to fabricators recommended by AISC to assess estimated welding man-hours per module, remaining man-hours per module, cost of welding consumables, and the remaining material costs. From the response of five fabricators, average values were calculated, revealing that

the 26.4 man-hours/module for welding time by conventional methods was reduced to 9.0 man-hours/module using robotic welding at 75% efficiency.

ESAB assisted in developing an appropriate robotic welding system which included five degrees of freedom, integral tactile sensing, GMAW welding capabilities, and track and boom system. Two integrated tooling system and positioning tables were also incorporated to facilitate the welding process. The first positioning table would load the module components for tack welding while the second positioning table welded a deck module. An estimated robot maintenance cost for the implemented system was obtained through customer surveys; cycle times and production rates of the robotic system were also estimated. Life cycle economic factors were considered with the estimated cost reported by the fabricators and it was determined that the fabrication cost could be reduced by 5.6% with the implementation of robotic welding.

Based on the economic analysis, it was evident that the fabrication of SOBDS would benefit from robotic welding. Additional benefits of using robotic welding were considered and include reductions in rework and scrap, accident claims, welding consumable cost, and initial equipment investment risk. It was explicitly stated that the RDP and RFB connection welds were performed by continuous robotic welding, however additional detail outlining the weld parameters used for the continuous weld was not provided.

2.4 Performance Review

A performance index, tabulated in Table 4, was developed to evaluate existing SOBDS according to the wearing surface, fatigue performance of the RFB connection, and corrosion. The performance index reflects the in service performance and includes other relevant information, such as bridge location and years in service, that assist in

understanding a given SOBD performance. Publications that were referenced in development of this table include: Wolchuk (1987); Touran and Okereke (1991); Wolchuk (2001); Wolchuk (2002). Anecdotal information was collected through personal communication that supplemented the published documents. The performance index shows that the primary cause for in-service performance issues is inadequate wearing surface rather than fatigue performance.

3 Parameter Evaluation and Connection Types

3.1 Database Evaluation

The databases of SOBD parameters for existing bridges, shown in Tables 2 and 3, were evaluated with respect to the recommended parameter limits provided by the FHWA Manual and the AASHTO LRFD BDS, reproduced in Table 5. Histograms of select parameters from the combined databases are plotted in Figures 33 through 39. Applicable limits for the SOBD parameters were developed considering the limits specified in AASHTO LRFD BDS, FHWA Manual, and the histograms of existing bridge parameters. These limits are defined in Table 6 and are depicted in Figures 33 through 39. An evaluation of the histograms is summarized in Table 7. Figure 33 shows that only 24% of the deck plate thickness from the combined databases of existing SOBD (45 bridges) exceed the recommended minimum deck plate thickness of 16 mm ($\frac{5}{8}$ in.). It may, however, be noted that the remaining 76% of the decks with less than the recommended minimum deck plate thickness were built prior to 1985. Figure 38 shows that the ratio of cutout-to-rib depth for 100% of the bridges in the North America database (6 bridges) exceed the minimum of 0.33. It may be noted that EC information was only available for SOBD in North America. Additionally, RFB connections with an EC are used in less than 30% of the bridges in the North America database. An additional ratio was plotted to assess the relationship between the distance from the rib soffit to the top of the FB bottom flange and the FB web thickness, as shown in Figure 40. This ratio represents the data differently than the rib-to-FB depth ratio, as 80% of the rib-to-FB depth ratios is less than the maximum recommended ratio value, while the histogram depicts a wide spread in the data exists when the FB thickness is considered.

3.2 Connection Type Identification

Generalized RFB connection types were developed based on the database of existing SOBD in North America, as previously discussed. Evaluation of the tabulated information revealed that RFB connections can be categorized into five types. An overview of connection types is shown in Figure 41.

3.2.1 Type 1 Connection

Type 1, Figure 42, is the fully fitted RFB connection. The rib passes continuously through a matching cutout in the FB web without an EC below the rib and without any internal stiffening of the ribs. The Type 1 connection can be further classified as Type 1A (Figure 42a), for a trapezoidal rib, and Type 1B (Figure 42b), for a round-bottom rib. Typically, the rib is joined to the FB by back-to-back fillet welds. An alternate weld that could be applied would use a two-sided PJP weld along the round bottom which transitions to a fillet weld, Figure 43. This connection has been used for both new construction and replacement decks and has been used in approximately 65% of the existing SOBD bridges in North America, mostly built prior to 1985.

3.2.2 Type 2 Connection

Types 2, Figure 44, consists of a continuous rib through the FB web with an EC below the rib. The EC geometry has a shallow, oblong shape with sharper tangential termination on the rib wall. A partial depth bulkhead plate inside the rib is also employed to prevent longitudinal cracking of the rib wall at the cutout termination due to out-of-plane bending from the increased out-of-plane flexibility of the rib wall. This connection type has been employed without the partial depth bulkhead plate when used with intermediate FBs that provide only load distribution in the deck and are not connected to the main

structure. Implementation of this connection type has employed CJP welds at the cutout termination on the rib wall, transitioning to a PJP weld or a fillet weld in the upper region of the connection away from the termination. This connection has been used in approximately 20% of the existing SOBD bridges in North America, both for new construction and replacement decks.

3.2.3 *Type 3 Connection*

The Type 3 connection, Figure 45, consists of a continuous rib through the FB web with an EC below the rib. The EC geometry has a deep, rectangular shape with sharp tangential termination on the rib wall. Internal stiffeners inside the ribs are employed to prevent longitudinal cracking of the rib wall at the cutout termination, due to out-of-plane bending from the increased out-of-plane flexibility of the rib wall and/or the torsional deformation of the ribs (Grundy et al 1994). This connection type has been employed without the internal stiffeners when used with intermediate FBs that provide only load distribution in the deck and are not connected to the main structure. Implementation of this connection type has employed CJP welds at the cutout termination on the rib wall, transitioning to a fillet weld in the upper region of the connection away from the transition. This connection has been used only for replacement decks and has been used in less than 4% of the existing SOBD bridges in North America.

3.2.4 *Type 4 Connection*

The Type 4 connection, Figure 46, consists of a continuous rib through the FB web with an EC below the rib. The EC geometry has a crescent shape with a larger upper radius that terminates tangentially on the rib wall (Figure 47). Two variations, with or without a full depth bulkhead plate inside the rib, have been implemented. A full depth bulkhead

plate has been implemented to prevent longitudinal cracking of the rib wall at the cutout termination, which may arise due to out-of-plane bending from the increased out-of-plane flexibility of the rib wall and/or the torsional deformation of the ribs (Grundy et al 1994), and punching of the FB into the rib wall when the rib is in the shear span of a load bearing floor beam. Implementation of this connection type has employed CJP welds at the cutout termination on the rib wall, transitioning to a PJP weld or a fillet weld in the upper region of the connection away from the termination. This connection was implemented in the early 21st century. It has been used for new construction and replacement decks, and has been used in approximately 7% of the existing SOBD bridges in North America.

3.2.5 Type 5 Connection

The Type 5 connection, Figure 48, consists of a continuous rib through the FB web with an EC below the rib. The EC geometry closely resembles that of Type 4 and has a crescent shape consisting of multiple curves of different radii. The curve adjacent to the rib is of smaller radius and does not terminate tangentially on the rib wall; rather it ends parallel to the rib wall creating a small tab with a square-ended termination on the rib wall (Figure 49). This termination is intended to eliminate the high stress concentration at the cutout termination on the rib wall. The weld is a two-sided fillet weld wrapped around the end. A variation of this connection could include internal stiffeners. This connection has only been used for replacement decks and has been used in less than 4% of the existing SOBD bridges in North America.

3.3 Connection Type Manufacturability

The manufacturability and cost-effective fabrication of SOBDs are influenced by: repeatability and automation possibilities; ability to weld in 3F position (with and against

gravity); discontinuous welding to optimize use of robotic welding capabilities; simplified cutout geometry, weld configuration, and rib bent configuration; lesser joint preparation; and fit-up gaps and their tolerances. Fatigue resistance and manufacturability are inter-related. The factors affecting fatigue resistance include: to joint configuration, such as fillet welds versus PJP or CJP welds; connection geometry and configuration; geometric parameters of the orthotropic deck; and the inherent fabrication parameters such as, fit up gap and tolerances.

Typically orthotropic decks are fabricated in the inverted position (upside down), as it facilitates automatic or semi-automatic welding of the ribs to the deck plate in the 2F position, Figure 50. For improved manufacturability, it is imperative that the RFB connection be welded in the 3F position, without any additional manipulation of the deck (Figure 51). Another consideration when determining the deck configuration is the use of continuous or discontinuous welds. Both types of weld result in a fully welded joint, however continuous welds are performed without starts and stops while discontinuous welds are performed with starts and stops. The fatigue performance of continuously welded joints can be better, as the weld starts and stops, if not properly performed, can introduce local stress concentrations due to change in weld bead section, and weld discontinuities such as cold lap or overlap, incomplete fusion, slag inclusion, crater cracks and undercuts, which would precipitate fatigue cracking under some stress conditions. The success of automated welding of the RFB connection in the 3F position depends on the capability to weld with and against gravity, if the RFB weld is to be made continuous. While this may be possible by changing the weld travel speed on the up and the down stride to maintain uniform weld deposit, welding with gravity (down stride) is not preferred by welding

professionals as it increases the possibility of wash down and affects the weld penetration and weld bead shape (personal communication with ACROW).

Due to the challenges associated with performing a continuous RFB weld in the 3F position, fabricators prefer welding the RFB connection against gravity symmetrically on either side of a rib, along with the deck plate-to-floor beam connection on one side at a time (personal communication with ACROW). The same procedure is also preferred when the welding process is automated to fully utilize robotic welding capabilities. Alternatively, to avoid welding with or against gravity and to avoid weld starts and stops, the RFB weld can be made continuously in the 2F position on one side of the FB at a time by standing the deck module vertically on each end, as shown in Figure 52. This approach, however, introduces additional steps and cost in fabrication.

Possible robotic fabrication procedures for fitted RFB connections include the potential for continuous welding, simultaneous welding from both sides of the FB, welding with and against gravity, wire type, fit up tolerance, joint configuration, programming the sensors and the possible welding sequences. Robotic welding experts recommend discontinuous welding of each RFB weld against gravity, meeting at the rib soffit, and also, welding one side at a time. Set up parameters and welding sequences are tested on a case-to-case basis to ensure adequate quality. If automation is used, a welding sequence that will result in the least distortion should be determined. A possible sequence welds (1) the floor beam to deck, (2) repositions to weld against gravity, and (3) welds up the rib to the rib soffit, as depicted in Figure 53. This sequence would be repeated to complete the entire deck.

The identified RFB connection types each possess distinct qualities that affect manufacturability and cost-effective fabrication, since weld configuration and joint preparation depend on the RFB connection type. The manufacturability of the identified RFB connection types is discussed in the following.

3.3.1 Type 1 Connection

This RFB connection typically employs fillet welds, as they are perceived to be cost-effective without effort for joint preparation. The use of fillet welds requires a tight fit-up and tolerance such that sufficient weld throat is available to prevent fatigue cracking. Due to variability in the as-fabricated rib profile, the fit-up requirements can be achieved only by match cutting the FB web to the as-fabricated rib dimension and/or grinding the FB web. These fabrication steps can impede manufacturability by hindering automation and increasing the time and cost of production. The inherent unfused root of the fillet welds, which is a function of the FB thickness, may affect the fatigue resistance. Alternatively, a RFB connection employing PJP welds with joint preparation on the FB web, but a larger fit up gap, has the potential to eliminate or reduce match cutting and grinding of the FB web, and may be cost-effective with increased possibility of automation. A combination of fillet and PJP welds could be used, which would retain the potential benefit of the PJP weld at the fatigue critical regions of the RFB connection while avoiding joint preparation along the entire length of the RFB connection.

3.3.2 Type 2 Connection

This RFB connection has employed a combination of a CJP weld at the EC termination on the rib wall with a PJP or fillet welds in the upper regions of the RFB connection away from the EC termination. Partial depth internal bulkhead plates have been

used in this connection type with similar welds as the RFB connection. The CJP or PJP welds require joint preparation and non-destructive inspection. Accurate alignment of the internal partial depth bulkhead plate with respect to the FB web hinders manufacturability. Due to the geometry of the EC, significant grinding is required to achieve the EC profile. The weld details, EC geometry, and internal bulkhead plate render this connection labor intensive, and inhibit automation and cost-effective manufacturability.

3.3.3 Type 3 Connection

This RFB connection has employed a combination of a CJP weld at the EC termination on the rib wall with fillet welds in the upper regions of the RFB connection away from the EC termination. Internal stiffening plates have been used in this connection type with a PJP weld. The CJP and PJP welds require joint preparation and non-destructive inspection. Accurate alignment of the internal stiffening plates with respect to the FB web hinders manufacturability. Due to the geometry of the EC, significant grinding is required to achieve the EC profile. The weld details, EC geometry, and internal stiffeners render this connection labor intensive, and inhibit automation and cost-effective manufacturability.

3.3.4 Type 4 Connection

This RFB connection has employed a combination of a CJP weld at the EC termination on the rib wall with a PJP weld or fillet welds in the upper regions away from the EC termination. Full depth internal bulkhead plates have been used in this connection type with a CJP weld in the upper region and transition to fillet welds. The CJP and PJP welds require joint preparation and non-destructive inspection. Accurate alignment of the full depth internal bulkhead plates with respect to the FB web hinders manufacturability.

Due to the geometry of the EC, significant grinding is required to achieve the EC profile. The weld details, EC geometry, and full depth internal bulkhead plates render this connection labor intensive, and inhibit automation and cost-effective manufacturability.

3.3.5 Type 5 Connection

This RFB connection has simpler EC geometry without a tangential termination on the rib wall and employs two-sided fillet or PJP welds wrapped around the termination. A significant reduction in grinding at the EC termination could be realized by using a weld wrapped around the end. This connection could be adequate for fatigue performance, and could lead to improved manufacturability and be amenable to automation.

4 FINITE ELEMENT ANALYSIS

4.1 Analysis Plan

Multi-level 3D linear elastic finite element analyses (FEA) of RFB connection Types 1B, 4B, and 5B were performed using ABAQUS (Dassault Systemes 2013), a commercially available software. These analyses were performed: (a) to understand the behavior of the connections under wheel loads acting on the SOBD; and (b) to identify the most critically stressed regions for a given connection type. The FEA involved three levels of models where the size of the models were progressively reduced at each level, as shown in Figure 54. The first level 3D FEA model, identified as the Global Model (GM), included a lift bridge superstructure that was analyzed for vehicular live loads as specified in the AASHTO LRFD BDS (AASHTO 2012) under a previous study (Roy and Mukherjee 2015, Mukherjee and Roy 2015, Mukherjee 2016). This model consists of three box girders, 27 FBs of uniform depth, and 46 ribs with RFB connection Type 1B. The GM analysis is summarized here for ease of understanding. The second and third level models, hereafter identified as submodels, were analyzed in the current study based on the results of the GM, and are presented in detail. The second level model, identified as Submodel A (SMA), was analyzed to understand the effect of changing the FB depth from $34\frac{1}{2}$ in. (876 mm) (denoted as FB1) to 30 in. (762 mm) (denoted as FB2). Only RFB connection Type 1B was considered in SMA which includes 23 ribs and 5 FBs. The weld features were not included in SMA. The third level model, identified as Submodel B (SMB), includes 13 ribs and 3 FBs and further focuses on the most highly stressed region of the SOBD to determine the critical local stresses for the RFB connection Types 1B, 4B, and 5B. The weld features were included in SMB.

The analysis matrix is shown in Table 8. A total of 13 submodels with various RFB connection types were analyzed.

4.2 Summary of Global Model Analysis

The GM analysis, performed in a previous study (Roy and Mukherjee 2015, Mukherjee 2016), was used to identify the most critically stressed RFB connection and to provide input for the second level submodel, SMA. The GM analysis is work completed in the previous study and the results of GM analysis were not modified in the current study; a discussion of the GM is necessary to understand the FEA results for the current study.

The lift bridge superstructure modeled by the GM consists of all the deck components including the deck plate, the ribs, the FBs, the end FB, and the box girders. The box girders, ribs, and FBs are identified in Figures 54 through 56. The cardinal directions shown in the figures correspond to the onsite orientation of the bridge. Welded connections were considered as integral and the weld features were not modeled in the GM. All components of GM were modelled using doubly curved, thick shell elements with the geometry defined at the middle surface. Typical cross sections of the components are detailed in Figures 57 and 58 with the mid surface identified. Each element had eight nodes and used a quadratic, reduced integration isoparametric formulation. Each element node had 6 degrees of freedom, 3 translational and 3 rotational. This element is identified as S8R in ABAQUS. The GM had an average element size of 7 in. (178 mm) resulting in 891,164 elements, 2,609,646 nodes, and 15,657,876 solution variables or nodal degrees of freedom.

The GM boundary conditions were based on the design drawings for the bridge. The east end FB rested on expansion bearings which were modeled by releasing the longitudinal displacement and restraining the transverse and vertical displacements of

corresponding nodes on the FB soffit (Figure 59). The west end FB rested on fixed bearings which were modeled by restraining the displacements of corresponding nodes on the FB soffit in all three directions.

The GM was analyzed for the rear tandem axle of the AASHTO fatigue design truck and the Fatigue I Limit State loading per AASHTO LRFD BDS. The model was analyzed for five longitudinal positions around the midspan, as shown in Figure 60 subjecting the deck to tandem axles symmetric and eccentric with respect to the FB 14 (the FB at midspan) in the longitudinal direction. For each longitudinal position, several transverse load positions were considered, moving from the south edge of the SOBD to the north edge. A cross section of the GM with the transverse load position T29 is shown in Figure 61, which was determined to be the most critical position, where the wheels nearest to the right web of the outer box girder (BG-1) were placed centrally between the adjacent pairs of ribs in the transverse direction. The critical load position was determined according to the critical stresses normal to the RFB connection on the FB web and rib wall (Mukherjee 2016). The load positions L1T29 and L2T29 were respectively found to produce the maximum symmetric and eccentric responses at FB 14. The eccentric response included the combined effects of in-plane and out-of-plane deformation of the FB due to rib rotation.

4.3 Details of Submodels

The FEA submodels were developed following the submodels analyzed in the previous study (Roy and Mukherjee 2015), which modeled the critically stressed regions of the deck under the AASHTO tandem axle loading. As noted in the previous section, the GM was used to identify the critical RFB connection and the deck global response due to the critical load positions. Under the critical load positions, the response was significant in

three FBs (FB 13 through FB 15), as shown in Figures 62 and 63. The deck deformation in the transverse direction, shown in Figure 64, was localized to where the load was applied and limited to only a few ribs. These observations defined the extent of the critically stressed region of the deck. This insight allowed for the development of two levels of submodels. These levels of submodels, identified as SMA and SMB and shown in Figure 65, were analyzed as described in the following. A partial cross section identifying the SOBD parameters applicable to all submodels is shown in Figure 66.

4.3.1 Submodel A

The purpose of the first level of submodels, denoted SMA, was to investigate the effect of the variation in the FB depth on the response, particularly the response of the RFB connection. For this purpose, the clear depth of the FB, d , between box girders BG-1 and BG-2 was varied to 30 in. (762 mm) from the depth of $34\frac{1}{2}$ in. (876 mm) as modeled in the previous study. When the depth is $34\frac{1}{2}$ in. (876 mm), the notation FB1 is used, and when the depth is 30 in. (762 mm), the notation FB2 is used. In the SMA submodel with FB2, the change in depth to 30 in. (762 mm) was not implemented throughout the SMA (to maintain compatibility with the GM), but was gradually introduced in the FBs within BG-1 and BG-2, over a length of 9 ft. 4 in. (2.8 m) starting from the outer box girder web, as shown in Figure 67.

The SMA submodels included the region of the critically-stressed RFB connection and the related deck components, as previously discussed and identified in Figures 62 and 63. The extent of these submodels was selected to define a boundary sufficiently far from this critical region, such that the results at critically-stressed RFB connection would not be influenced by boundary effects, the change in FB depth has a minimal effect on the analysis

accuracy, and the various SMA submodels have same boundary at the interface. Accordingly, the SMA submodels consist of two box girders (BG-1 and BG-2), 23 ribs (Rib 4 to Rib 26), and 5 FBs (FB 12 to FB 16) which resulted in a submodel which is 58 ft. 9 in. (17.1 m) long and 53 ft. 8 in. (16.4 m) wide (Figure 68). The boundaries in the longitudinal direction extend from the centerline of the outer FBs (identified as FB 12 and FB 16) by 5 ft. 10 1/2 in. (1.8 m), which is half the spacing between two adjacent FBs. The boundaries in the transverse direction extend from the centerline of the outer ribs (Rib 4 and Rib 26) by 14 in. (400 mm), which is half the spacing between two adjacent ribs.

Two SMA submodels were developed, one with the FB depth transitioning from 34 1/2 in. (876 mm) (FB1) to 30 in. (762 mm) (FB2) as discussed earlier, identified as SMA_FB2 (Figure 67), and the other with constant depth of 34 1/2 in. (876 mm) (FB1) as in the GM and identified as SMA_FB1 (Figure 69). SMA_FB1 was analyzed to provide a consistent comparison of the influence of the FB depth. Note that a similar submodel with a smaller extent was analyzed by Mukherjee (2016).

4.3.2 Submodel B

The purpose of the second level submodels, denoted SMB, was to compare the response of the different RFB connection types with the two different FB depths. For this purpose, versions of SMB with connection Types 1B, 4B, and 5B were created. As previously discussed, Types 1B and 5B appeared to be promising in terms of fabrication automation and fatigue performance. The Type 1B connection is the fully fitted RFB connection. The Type 5B is the RFB connection with a simplified EC geometry and weld detail, as shown in Figure 70. Although not identified as promising in terms of fabrication automation, the geometrically similar Type 4B connection, as shown in Figure 71, was

considered to assess the variation of EC termination. The Type 4B connection has the same dimensions as Type 5B, however the upper radius was simply increased from 1 in. to 1¹/₄ in. to eliminate the tab and allow for a tangential termination on the rib wall. Based on previous research (Roy et al. 2012a, Roy et al. 2012b), it was expected that the increase in the termination radius would have a favorable effect on the stresses and fatigue performance, however, this effect was expected to be small for such a small change in radius.

The extent of the SMB submodels were selected based on the critically-stressed RFB connection and the related deck components, as identified from the SMA analyses. The SMB shown in Figure 72 was 30 ft. 4 in. (9.2 m) wide and 35ft. 3 in. (10.7 m) long. The analyses of the GM and SMA submodels showed that the RFB connection adjacent to the box girder web is the most critical. Accordingly, the SMB models included: 13 ribs, Rib 9 adjacent to south web of BG-1 through Rib 21 adjacent to north web of BG-2; 3 FBs, FB 13 to the west through FB 15 to the east of the critical FB 14; and parts of the webs of BG-1 and BG-2 adjacent to ribs 9 and 21 respectively. Similar to SMA, the boundaries in the longitudinal direction extended from the centerline of the outer FBs (identified as FB 13 and FB 15) by 5 ft. 10¹/₂ in. (1.8 m), which was half the spacing between two adjacent FBs. The boundaries in the transverse direction extended half the spacing between two adjacent ribs or 14 in. (400 mm) from the centerline of the outer ribs (Rib 9 and Rib 21).

All deck components were modeled, including the weld features to determine the local stresses at the RFB connection. The welds were modeled as ⁵/₁₆ in. (8 mm) fillet welds with an idealized zero notch radius at the weld toe and complete penetration at the weld root.

Four versions of SMB were developed, incorporating connection Type 4B and 5B with FB1 and connection Type 1B and 5B with FB2. The naming convention distinguishes the level of submodel, the floor beam depth, and the connection type. For example, Submodel B with floor beam depth of 30 in. (762 mm) (FB2) and connection Type 1B is denoted as SMB_FB2_CT1B. Cross sections of SMB with connection Type 1B and 5B are shown in Figures 73 and 74, respectively.

4.4 Details of Element Type and Meshing for Submodels

4.4.1 Choice of Elements

The submodels were meshed using 3D continuum solid hexahedron elements. These elements had twenty nodes and used a second order isoparametric formulation with reduced integration. The element nodes each had 3 translational degrees of freedom. The element, as shown in Figure 75, is identified as C3D20R in ABAQUS. Reduced integration, as opposed to full integration, was used to decrease computational effort as well as provide better accuracy. The C3D20R element has eight integration points while C3D20, the fully integrated element, has 27 integration points (Figure 76). This reduction of integration points reduces the computational effort for C3D20R to less than 30% of the computational effort of C3D20. In addition, reduced integration underestimates the stiffness matrix through the introduction of spurious rigid body modes, resulting in numerical softening and improved solution accuracy. The C3D20R element is preferred for three dimensional stress analyses as it is effective in capturing stress concentration effects (Dassault Systemes 2013).

4.4.2 Details of Meshing

All meshes were generated automatically by ABAQUS using a structured meshing algorithm and was checked for quality in accordance with ABAQUS recommendations (Dassault Ssystems 2013). Element quality was important in obtaining accurate solution, and elements with an aspect ratio greater than 10 or with a small face angle less than 10° or large face angle greater than 160° were avoided, especially at the regions of primary interest in the RFB connection. The average element size for SMA and SMB was approximately $3\frac{1}{2}$ in. (89 mm) and 1 in. (25.4 mm), respectively. Additional information on the FEA of SMA and SMB are tabulated in Table 9. All modeled components were assembled first, then the mesh was propagated on the full extent of each submodel.

4.5 Boundary Conditions

An overview of the progression of submodeling and resulting boundary conditions is shown in Figures 77 and 78.

4.5.1 Submodel A

Analysis of SMA employed shell-to-solid node-based submodeling, where the displacement output from the GM was used as boundary conditions for SMA (Dassault Systemes 2013). The nodes on SMA at the common interface belonged to the solid elements and were driven by the GM nodes that belonged to the shell elements, as shown in Figure 79. The displacement boundary conditions for SMA were determined by projecting the nodes onto the GM boundary at the common interface, calculating displacements at a given driving node from the rotations and displacements, interpolating the displacement, and assigning the value to the appropriate node (Figure 80). ABAQUS automatically selects the driving region field by searching all regions in the GM that lie in

the vicinity of SMA as dictated by a calculated distance that multiplies a prescribed fraction by the average element size in the GM.

4.5.2 Submodel B

Analysis of SMB employed solid-to-solid node based submodeling, where the results from SMA provided the displacement boundary conditions for SMB at the common interface (Dassault Systemes 2013), as shown in Figure 81. The displacement boundary conditions of SMB are determined internally by ABAQUS, by projecting the nodes of SMB onto SMA at the common interface, determining the displacements at the projected points by interpolation from the nodal displacements of SMA, and assigning the values to the appropriate nodes of SMB. ABAQUS automatically determined the relevant nodes of SMA at the interface from the defined boundary of SMB by searching all regions in SMA that lie in the vicinity of SMB as dictated by a calculated distance that multiplies a prescribed fraction by the average element size in the SMA.

4.6 Loading

All submodels were analyzed for the two critical load positions L1T29 and L2T29 that were determined from the previous analysis of the GM (Roy and Mukherjee 2015) and are shown in Figures 60 and 61. Subsequently in this thesis these two load positions are referred to as symmetric loading (SL) and eccentric loading (EL), respectively.

The tandem axle loads was applied as a uniformly distributed pressure over a tire contact area, which according to AASHTO LRFD BDS was 10 in. (254 mm) long and 20 in. (508 mm) wide for each wheel pair of the tandem axle, with the shorter dimension oriented parallel to travel. Each of the tire contact areas was modeled as solid rectangular load patches $\frac{5}{8}$ in. (16 mm) thick that were discretized using C3D20R elements and tied

to the deck models. Node-based surface to surface tie constraints were specified between the bottom surface of the load patch (slave surface) and the top surface of the deck plate (master surface). The patches were assigned very flexible material properties so they only transfer the load from the load patch to the deck surface and do not add to the stiffness of the deck. This modeling technique of using load patches that are separate from the deck model allowed the load to be easily applied in any position.

The load patches were spaced 6 ft. (1.8 m) on centers in the transverse direction and 4 ft. (1.2 m) on centers in the longitudinal direction. The total Fatigue I limit state design load for the rear tandem axle including impact, as specified by the AASHTO LRFD BDS for the deck plate and RFB connection details, was applied to the deck. This resulted in 82.8 kips (368 kN) per rear axle ($3 \times 0.75 \times \text{HS20} + 15\%$ impact), which was distributed as 41.4 kips (184 kN) per axle of the tandem axle or 20.7 kips (92 kN) per load patch. A uniformly distributed pressure load of 0.104 ksi (0.72 MPa) was applied to the top surface of each load patch, as shown in Figure 82.

4.7 Material Properties

Universally accepted linear elastic material properties of steel were used for analysis. The modulus of elasticity and Poisson's ratio of steel were assumed as 29000 ksi (2.0×10^5 MPa) and 0.3, respectively. The modulus of elasticity and Poisson's ratio for the loading patches were assumed as 15 ksi (100 MPa) and 0.5, respectively, to allow the load patches to be flexible and incompressible.

4.8 Analysis

The GM and submodels were analyzed on a distributed memory computer cluster of 4 nodes, each having 16 central processing units. All analyses were linear elastic, used

direct linear equation solver, and were completed in a single increment. The direct linear equation solver used a sparse, direct, Gauss elimination method that found the exact solution of the system of linear equations (Dassault Systemes 2013).

The analysis results are discussed in the following chapter.

5 FINITE ELEMENT ANALYSIS RESULTS

5.1 Discussion of FEA Results

The analysis results for the GM from the previous study (Roy and Mukherjee 2015, Mukherjee 2016) showed high stress concentration in the FB and the rib wall in the shear span adjacent to the box girder web. Since the FBs were integral with the box girder and the wheel loads were transferred to the box girder through the FB by shear, a diagonal tension field resulted in the shear span of the FB from the bottom (tension) flange of FB 14 to the top corner formed by the FB 14 web and the box girder web. The maximum stress occurred in the FB web at the RFB connection (more specifically Rib 10-to-FB 14 connection), where the diagonal tension field deviated around the FB cutout. As such, the discussion of FEA results is focused around this connection location and FB 14 as a whole for both load cases, symmetric loading (SL) and eccentric loading (EL), as described earlier. In addition to the four SMB analyzed within this study, one similar submodel analyzed in the previous study by Roy and Mukherjee (2015) is also discussed. This submodel has the same extent as the SMB discussed earlier with a FB depth $34\frac{1}{2}$ in. (876 mm) (FB1) and has fully fitted connection Type 1B, denoted SMB_FB1_CT1B.

5.1.1 Behavior of the Floor Beam

The vertical displacement of FB 14 along the bottom flange soffit on the axis of symmetry, as obtained from SMB analyses due to SL and EL cases, are shown in Figures 83 and 84, respectively, for RFB connection Types 1B and 5B in FB1 and FB2. Also included in Figure 83 is the result for SMB_FB1_CT4B due to SL. The vertical displacement of FB1_CT4B and FB1_CT5B were nearly identical, as would be expected since the only difference between the two models is the EC termination. The vertical

displacement for FB2_CT1B was comparable to that of FB1_CT5B, suggesting that the increased displacement due to reduction in flexural stiffness of the shallower FB without an EC was comparable to the increased displacement of the deeper FB with an EC due to increased shear deformation. The vertical displacement for FB1_CT1B was noticeably different than FB2_CT5B. The vertical displacement for all the SMB submodels became similar away from the load in the region outside the box girders. These observations are also applicable for the EL condition. The displacement of FB 14 shows a similar trend in all five submodels for a given load condition. This trend was similar to the deflected shape of a propped cantilever where the south web of BG-1 acted as the prop support with support settlement.

The contours of maximum principal stress in the FB web for SL and EL are shown in Figures 85 through 89 for all SMB submodels. Figure 90 shows the two levels of submodels match well for distribution of the principal stress, however the magnitude of the principal stress in SMB is higher than in SMA since welds were modelled in SMB and included the stress raiser of the weld toe notch. The diagonal tension field, identified in the previous study, from the bottom (tension) flange of the FB to the top corner formed by the FB web and the box girder web is evident in these figures. This tensile stress field deviates around the cutouts in the FB web, causing stress concentration at the cutout boundary where the stress fields were approximately tangential. As a result, a high stress concentration develops at the Rib 10-to-FB 14 connection where the tension fields were approximately tangential to the cutout, as shown in Figures 91 through 93 for all five SMB submodels. These figures also show that the stresses are tensile towards the box girder and compressive on the other side of the connection away from the box girder. For connection

Types 4B and 5B with ECs, an additional stress concentration occurred in the rib wall at the EC termination, as shown in Figures 94 through 96, which was higher than the stress concentration in the FB web at the cutout boundary.

The FEA results showed that the stresses produced by symmetric loading were higher than the eccentric loading condition. Symmetric loading produced primarily in-plane (membrane) stresses while EL produced a combination of in-plane and out-of-plane stresses. Out-of-plane bending at the RFB connection of the FB web due to rotation of the rib due to the EL is shown in Figure 97. Eccentric loading would be critical where this rib rotation is restrained and out-of-plane bending is dominant, however in-plane stresses dominated for the cases considered in the study. The response characteristics is consistent with laboratory and field measurements, as well as other analytical studies even when a relatively shallow and thick FB with lesser out-of-plane flexibility was employed (Roy and Mukherjee 2016; Roy et al. 2012; Tsakopoulos and Fisher 2005; Tsakopoulos and Fisher 2003; Connor and Fisher 2001). EL was not critical for any of the submodels. It was known from the previous study that sufficient FB depth for FB1 and connection Type 1B was available to provide out-of-plane flexibility for the FB web when subjected to EL. The out-of-plane stresses were not significant for FB2, even though the shallower FB depth reduced the out-of-plane rotational flexibility of the FB, and reduced the shear area for in-plane stresses. This will be discussed in more detail in the following sections.

5.2 Behavior of the Rib-to-Floor Beam Connection

Fatigue cracking of RFB connections can occur in the base metal or at the welded connections, however the nominal fatigue resistance of the base metal is higher than the welded connections. As such, the stress concentrations present at the welds, in addition to

micro-discontinuities and residual stresses, make these locations more susceptible to fatigue cracking. The stress range normal to the weld toe, where micro discontinuities are expected, is critical for toe cracking, as shown in Figure 98. Fatigue cracking can also occur from the weld root due, as shown in Figure 99, to LOF and volumetric discontinuities such as porosity, propagating normal to the primary stress range. Fatigue cracking in the base metal can initiate from the stress concentrations at the upper and lower radius and propagate normal to the primary (tangential) stress range. The connection types are assessed with respect to these critical stress components in the following sections. The paths the stresses are plotted along and the stress direction are identified by a figure included in each plot.

5.2.1 Connection Type 1B

The circumferential variation of radial stress normal to the weld toe on the FB is shown in Figures 100 through 102 for SL and EL for both FB1 and FB2. The path for the circumferential variation of stress normal to the weld toe originates at the rib soffit, proceeds along the rounding of the rib, and concludes where the rounding of the rib ends (at an angular measure of 75.3°). The maximum radial stress due to SL is approximately 5.5 and 6.5 ksi for FB1 and FB2, respectively. The maximum radial stress due to EL on the west face, the near side of the FB with respect to the load, of the FB is approximately 5 and 6 ksi for FB1 and FB2, respectively. The maximum radial stress due to EL on the east face, the far side of the FB with respect to the load, of the FB is approximately 5.5 and 6.5 ksi for FB1 and FB2, respectively. The maximum stress occurred at approximately 50° from the rib soffit. From the unequal distribution of stresses on the west (near) and the east

(far) faces it is evident that EL produced both in-plane stresses and out-of-plane bending stresses in the FB web.

Figures 103 through 105 show the radial variation of tensile stress normal to the weld toe on the FB surface for both SL and EL. The path originates at the circumferential location of maximum stress previously identified and proceeds radially outward. For both loading conditions, the high tensile stress at the connection gradually became compressive at a distance of approximately 5 in. (127 mm) away from the weld toe. Maximum out-of-plane bending of the FB web due to the rotation of the rib was expected to occur at the RFB connection. Figures 104 and 105 show the out-of-plane bending stresses that occur in the FB web due to EL by comparing the stress on the west (near) and east (far) face of the FB web along the radial path through the maximum radial stress at the weld toe. Although in-plane stresses and out-of-plane bending stresses are produced by EL, the out-of-plane bending stress component is minimal and EL primarily produced in-plane stress in the FB web. Additionally, the out-of-plane stress decreased rapidly away from the connection, as the stresses on the west (near) and east (far) faces became similar.

The circumferential variation of radial stress normal to the weld toe on the rib is shown in Figures 106 through 108 for the SL and EL for both FB1 and FB2. The defined path for circumferential variation of stress originates at the weld toe in the rib wall at the rib soffit, proceeds along the rounding of the rib, and concludes where the rounding of the rib ends (at an angular measure of 75.3°). The maximum radial stress due to SL is approximately 10 and 12 ksi for FB1 and FB2, respectively. The maximum radial stress due to EL on the east and west side of the FB is approximately 8 and 10 ksi for FB1 and FB2, respectively. The maximum stress occurs at approximately 60° from the rib soffit.

Figures 109 through 111 show the radial variation of stress normal to the weld toe in rib 10 for SL and EL. The path originates at the circumferential location of maximum stress previously identified and proceeds longitudinally outward. For both loading conditions, the high tensile stress at the connection quickly became compressive at a distance of approximately $\frac{1}{2}$ in. away from the weld toe.

The circumferential variation of stress tangential to the weld root on the FB is shown in Figures 112 through 114 for SL and EL with both FB1 and FB2. The maximum tensile tangential stress due to SL is approximately 11 and 12 ksi for FB1 and FB2, respectively. The maximum tensile tangential stress due to EL on the west and east face of FB 14 is approximately 10 and 12 ksi for FB1 and FB2, respectively. The maximum stress occurs at approximately 50° from the rib soffit. The variation of stress normal to the weld root is not presented because it is negligible.

5.2.2 Connection Types 4B and 5B

The circumferential variation of tensile stress tangential to the EC lower radius on the FB with connection Types 4B and 5B is shown in Figures 115 and 116 for SL. The defined path for circumferential variation of stress originates at the EC lower radius soffit, proceeds along the rounding of the EC, and concludes where the lower radius intersects the upper radius (at an angular measure of 74.4°). As is evident from the plots, the maximum tensile tangential stress due to SL is approximately 18 and 21 ksi for FB1 and FB2, respectively, for connection Type 5B and is approximately 18 ksi for FB1 for connection Type 4B. The maximum stress occurs at approximately 40° and 55° from the EC lower radius soffit for connection Types 5B and 4B, respectively, although in both cases the variation in stress with circumferential position is small.

The circumferential variation of tensile stress tangential to the EC upper radius on the FB with connection Types 4B and 5B is shown in Figures 117 and 118 for SL. The defined path for circumferential variation of stress originates at the terminus of the EC upper radius (near the rib wall), proceeds along the free edge of the EC, and concludes at the midpoint of the upper radius circumference (at an angular measure of 90°). The maximum tensile tangential stress due to SL is approximately 8 ksi for FB1 and FB2 for connection Type 5B and is approximately 12 ksi for FB1 for connection Type 4B. For connection Type 4B, where the EC was tangential on the rib wall, the maximum stress occurred at the cutout termination on the rib wall. For connection Type 5B, where the cutout termination was not tangential on the rib wall, the maximum stress occurred at approximately 20° from the EC terminus. Thus, the critical location for fatigue cracking from the upper radius of the EC is dependent on EC geometry, particularly the EC upper radius termination and weld type.

The variation of stress normal to the weld toe in the FB web along the path for connection Types 4B and 5B is shown in Figures 119 and 120 for SL. The path originates at the weld toe in the FB web near the EC termination, proceeds along the RFB weld on the FB web, and concludes where the RFB weld intersects the RDP weld. The maximum normal stress is approximately 4 ksi for FB1 and FB2 for connection Type 5B and is approximately 5.5 ksi for FB1 and connection Type 4B. The maximum stress occurs at the origin of the path for both connection Types 5B and 4B.

The variation of stress on Rib 10 (the most critically stressed rib adjacent to the box girder web) normal to the EC termination along the defined path at the EC termination for connection Types 4B and 5B is shown in Figures 121 and 122 for SL. For connection Type

5B, the path originates where the wrap-around weld began to wrap, proceeds along the intersection of the FB tab and rib wall, and concludes where the wrap-around weld begins to travel along the straight path of RFB connection. Paths 1 and 3 were defined by the rounding of the wrap-around weld and path 2 was defined by the straight stretch of the wrap-around weld below the tab. For connection Type 4B, the path originates where the ground-smooth termination begins, proceeds along the ground-smooth termination, and concludes where the ground-smooth termination ends. The maximum stress normal to the EC termination due to SL is approximately 22 and 21 ksi for FB1 and FB2, respectively, for connection Type 5B and is approximately 15 ksi for FB1 for connection Type 4B. The maximum stress in connection Type 5B occurred at the corner, where the round edge met the straight edge of the wrap-around weld. The maximum stress in connection Type 4B occurred halfway along the path from the origin. This shows that the location of maximum stress from the EC termination is dependent on EC geometry and weld type.

The variation of stress normal to the EC termination on the Rib along the defined path on the rib surface initiating at the location of maximum stress for connection Types 4B and 5B is shown in Figures 123 and 124 for SL. For connection Types 4B and 5B, the path originates at the point of maximum stress at the EC termination on the rib and proceeds along the rib profile. Path 1 was defined by the flat profile of the rib and path 2 was defined by the rounded profile of the rib.

The variation of stress normal to the weld toe in the Rib along the path with connection Types 4B and 5B is shown in Figures 125 and 126 for SL. The path originates at the weld toe in the rib wall where the EC terminates, proceeds along the RFB weld on the rib wall, and terminates where it intersects the RDP connection. The maximum normal

stress due to SL is approximately 4.5 ksi for FB1 and FB2 for connection Type 5B and is approximately 4 ksi for FB1 for connection Type 4B. The maximum stress occurs at the origin of the path for connection Type 5B and occurs at a distance less than $\frac{1}{2}$ in. from the origin of the path for connection Type 4B. Thus both maxima occur at or near the EC upper radius termination.

5.3 Critical Location for a Given Connection Type

The FEA results for SMB with FB1 and connection Types 1B, 4B, and 5B and SMB for FB2 and connection Types 1B and 5B showing the stress concentrations were presented in the previous sections. The presence of the cutout in the FB web to allow the ribs to pass continuously through the FB causes regions of stress concentration in the FB web and rib wall. For connection Type 1B, which does not have an EC below the rib, the primary stress concentration occurs at the RFB connection in the FB web and rib wall at the weld toe and the weld root. Figure 127 shows connection Type 1B with potential fatigue crack locations at the toes of the weld in the FB web and the rib wall.

The presence of the EC in connection Types 4B and 5B caused regions of stress concentration in the rib wall at the EC termination and in the FB web at the lower and upper radius of the EC. The stress concentration is the maximum near the EC termination, and is more critical because the location of this stress is adjacent to the welded connection. Similar trend of stress concentration is seen with and without the tab at the EC termination for connection Types 4B and 5B. It is important to note that this location of stress concentration is present in connection Type 4B at the ground-smooth weld termination, while in connection Type 5B, it occurs at the weld toe of the wrap-around weld. This stress concentration is substantially higher in connection Type 5B as the EC termination is not

ground-smooth. Figure 128 shows connection Type 5B with potential fatigue crack locations due to cracks propagating in the rib wall at the EC termination as well as cracks that could propagate in portions of the base metal of the upper and lower radius of the EC.

5.4 FEA Result Comparison

5.4.1 Connection Type 1B

The maximum stress for the shallow FB2 is consistently higher than for FB1, as would be expected, due to the decreased FB area. Although the stresses were higher for FB2, the circumferential variation of radial stress normal to the weld toe was similar for both FB depths and for both critical loading conditions. The same observation is true for the circumferential variation of stress tangential to the RFB welded connection. In addition, the radial and tangential stresses reached their maxima at the same circumferential position (angular measure) regardless of variation in FB depth or loading condition considered in this study. The comparison of normal stress distribution in the FB web along the path at approximately 50° is similar for both FB depths, however the stress decays faster for the shallower depth FB2 than for FB1. The out-of-plane bending stress component due to EL is about the same for both FB1 and FB2, and was much smaller compared to the in-plane stresses.

5.4.2 Connection Types 4B and 5B

The geometry of the EC, particularly the radius and the weld detail at the termination, significantly affects the critically stressed regions. The stress tangential to the EC lower radius and the circumferential variation of this stress are similar for connection Types 4B and 5B, however the local maxima occurred at different locations, as shown in

Figure 129. One difference between connection Types 4B and 5B is that the tangential stresses begin to increase as the defined path approaches the upper radius for connection Type 5B. It is evident that the FB depth influences this stress component, as the maximum tangential stress is found to be higher for FB2 than FB1 for connection Type 5B. Although the maximum stress is higher for FB2, both FB1 and FB2 with connection Type 5B reach a maxima at the same circumferential position (angular measure of 40°). Although the maxima occur at different angular measures from the EC lower radius soffit, the maximum tangential stress is about the same for connection Types 4B or 5B with FB1.

The location of critical stress tangential to the EC upper radius varies between 0° and 20° depending on the EC geometry, as shown in Figure 130. The tangential stress at the EC terminus adjacent to the RFB welded connection was significantly reduced for connection Type 4B, demonstrating that non-tangential termination of EC as in connection Type 5B was effective in reducing the potential for fatigue cracking at the weld to on the FB of the RFB connection. The distribution of tangential stress for the upper radius is noticeably different for connection Types 4B and 5B for an angular measure less than 40° . This difference is due to the presence of the weld for connection Type 4B, which ends at approximately 40° . In the case of connection Type 5B, the EC edge at the termination was protected by the cutout. For an angular measure greater than 40° , the profiles become more similar and the tangential stress at 90° is approximately -4 ksi regardless of EC type or FB depth. The similarity in stress distribution beyond 40° occurs as the location is farther from the influence of EC termination including the weld and upper radius. This shows the EC termination influences the tangential stresses mostly in the range of 0° to 40° around the upper radius, for this particular case, and the influence diminishes as the angular measure

increases. Additionally, the variation in FB depth considered for this study does not appear to significantly influence this stress component as the stress distributions are comparable for FB1 and FB2 with connection Type 5B.

The variation of stress normal to the EC termination on the rib was significantly different for connection Types 4B and 5B, with different locations of maximum stress, and different maxima, although they were essentially symmetric about the FB centerline for SL. The stresses at the weld termination on the rib wall indicated that compared to connection Type 4B, the connection Type 5B is more susceptible to fatigue cracking initiating at the weld toe on the rib, particularly when the out-of-plane bending of the rib wall is not mitigated by internal stiffening. This mode of cracking did not occur in the tests conducted by Haibach and Plasil (1983) with connection similar to Type 5B; however, a fatigue crack in the rib wall was reported in a variation of the connection. Similar cracking in service was also reported by Grundy et al. (1994). It may be noted that with internal stiffening (bulkhead plates), the fatigue resistance of connection Type 5B exhibited similar resistance as type 4B in the laboratory fatigue testing of prototype SOBD for Williamsburg Bridge (Tsakopoulos and Fisher 1999). The variation in stress normal to the EC termination for connection Type 5B has double peaks that occurred where paths 1 and 2 and paths 2 and 3 meet. This result is the same for both FB1 and FB2, and the stresses are slightly higher for FB1, particularly over the straight portion of the weld (path 2). The variation in stress normal to the EC termination for connection Type 4B has a parabolic shape, reaching the maximum at the midpoint of the path. The location of maximum stress is found to vary between $\frac{1}{3}$ and $\frac{1}{2}$ of the path from the origin. It is important to note that the path is only about $1\frac{1}{2}$ in. in length and the weld geometry is idealized, particularly for the wrap-around

weld. The variation of this stress on the rib along the path from the weld at the maximum stress locations is similar for connection Types 4B and 5B, both of which decay rapidly. The maximum stress for connection Type 4B is significantly lower than that of connection Type 5B due to the ground-smooth weld condition which removed the stress raiser of the weld toe for connection Type 4B. Both FB1 and FB2 with connection Type 5B have similar stress profiles along this path. The normal stress converges to approximately 4 ksi at the end of path 1, when the rib profile changes from flat to round, for connection Types 4B and 5B.

The variation of stress normal to the weld toe in the FB web and the rib wall was similar, including locations of maximum stress and maxima, regardless of connection type or FB depth. The stresses rapidly decayed away from the weld toe beyond the influence of the weld toe notch and subsequently varied under the influence of the loads, clearly identifying the regions of local and global stresses. The maximum normal stress in the FB web is higher for connection Type 4B than for connection Type 5B, and the FB depth does not appear to influence this stress component until the upper region of the defined path, near the RDP connection. The maximum stress normal to the weld toe on the rib wall is higher for connection Type 5B than for connection Type 4B, due to different weld details at the EC termination. The tensile stresses at the EC termination were due to the influence of the local effect. Subsequently along the path, the stress was initially compressive which gradually changed to tensile under the influence of the global stress (negative moment in the rib at the FB intersection). Approaching the RDP connection, the stresses again changed to negative under the local effect of the intersecting welds. The variation of FB depth appears to have negligible influence on this stress component in both the rib and the FB.

6 CONCLUSIONS AND RECOMMENDATIONS

6.1 Conclusions

The study identified and evaluated rib-to-floor beam (RFB) welded connections for steel orthotropic bridge decks (SOBDs) that appear to be promising considering fatigue performance and the potential for automated fabrication. An extensive literature review was performed to identify the issues related to fabrication of RFB connections and the connections that would be amenable to automation. Two RFB connections employing round bottom ribs, one with a fitted FB (connection Type 1B) and one with an EC in the FB web under the rib (connection Type 5B) were identified. For the connection Type 5B, the FB at the EC had a square termination on the rib wall. Both details employed all-around fillet welds. Two FB depths were considered. Another RFB connection (connection Type 4B), geometrically similar to connection Type 5B, although not amenable to automated fabrication, was also evaluated with the deeper FB for comparative purposes. FEA results were used to understand and assess the response of the SOBD and the RFB connections. All FBs were integral with the primary load carrying members of the bridge. The analyses were performed using the rear tandem axle of the fatigue design truck as per the AASHTO LRFD BDS (2012). Both symmetric and eccentric loading of the FB in the longitudinal (traffic direction) was considered.

The literature review identified that continuous welding of RFB connections would be a challenge due to welding against and with gravity. Welding against gravity would be the preferable method for depositing welds of acceptable profile and shape. For continuous welding, the deck may have to be manipulated either by standing vertically up or by rotating about an axis. For fitted FBs, match cutting would be necessary if a tight fit-up is

specified. Alternatively, a larger fit-up gap along with PJP welded connection would be more cost-effective.

The RFB connections within the shear span of the FB adjacent to the primary load carrying component, both with and without an EC, experienced significant stress concentrations at the FB cutouts. For the fitted FB, the stress concentrations occurred at the cutout edge on the rib soffit. For the FB with EC, the stress concentrations occurred on the edge of the cutout under the soffit and near the termination on the rib, and also on the rib wall at the EC termination. Without an internal stiffening, the connection Type 5B with a square termination on the rib wall and wrapped-around fillet welded connection, although amenable to automated fabrication, exhibited greater stress concentration compared to the connection Type 4B that employed a CJP connection and tangential termination on the rib wall. The stresses in the FB were primarily in-plane, and the contribution of the out-of-plane stress component was negligible. For the depth of the FBs considered in this study, no appreciable effect of the FB depth could be discerned.

The RFB connection Type 1B can be applied with a relatively shallow FB depth without experiencing unreasonably high stresses normal to the weld toe in the FB web or rib wall due to out-of-plane bending of the FB web. The critical stress normal to the weld toe in the rib wall at the EC termination for connection Types 4B and 5B appears to be too high, particularly for connection Type 5B for either FB1 or FB2. The stress in the base metal of the EC lower radius, although not as large as the stresses at the RFB connection welds at the EC termination, is notable for connection Types 4B and 5B.

6.2 Recommendations

This research identified the critical locations for potential fatigue cracking in fillet welded RFB connections with fitted FBs and ECs. For RFB connections without internal stiffening and EC, wrapped around fillet-welded detail may be used for situations where the stresses are not too high, such as interior RFB connections. Further refined analyses need to be performed to assess the fatigue performance of each connection type based on local stresses. Additionally, different geometric parameters may need to be investigated, particularly the EC parameters for the Type 5B connection. Different boundary conditions for the submodels, for example, for the SOBD for a different bridge may need to be considered. The potential for automated fabrication of the RFB connection using robotic welding needs further work to understand the possibilities and limitations for the connection types studied in this thesis. This work should qualitatively assess whether the connection types considered here may ultimately decrease fabrication costs while maintaining acceptable fatigue performance when compared to connection types not amenable to automated fabrication but having fatigue performance already proven to be acceptable. Finally, the fatigue performance of the connection Type 5B should be experimentally evaluated.

TABLES

Table 1 Steel Orthotropic Bridge Deck Parameters

Symbol	Definition	Reference
a	Out-to-out width of a closed rib at deck plate	Figure 3, Figure 4
b	Width at the base of a trapezoidal rib (distance between working points)	Figure 4, Figure 6
	Width at the bottom of the flat portion of a round bottom rib web	Figure 3
b_f	Flange width of members transverse to ribs	Figure 5
c	Vertical distance of rib soffit from extended cutout termination on the rib	Figure 6
c_e	Vertical distance from rib soffit to the lowest point of extended cutout	Figure 6
d	Depth of members transverse to ribs	Figure 3, Figure 4, Figure 5
e	Clear spacing in between ribs at deck plate	Figure 3, Figure 4
h	Depth of deck	Figure 3, Figure 4, Figure 5
h'	Length of the flat portion of rib web	Figure 3, Figure 4
h_r	Depth of rib	Figure 3, Figure 4, Figure 5
L	Span length center-to-center of supports	Figure 5
r	Inner bend radius of trapezoidal rib	Figure 4
R	Inner bend radius of round-bottom rib	Figure 3
r_l	Lower radius of extended cutout	Figure 6
r_u	Upper radius of extended cutout	Figure 6
s	Center-to-center rib spacing	Figure 3, Figure 4
t	Thickness of deck plate	Figure 3, Figure 4, Figure 5
t_c	Web thickness of members transverse to ribs	Figure 5
t_f	Flange thickness of members transverse to ribs	Figure 3, Figure 4, Figure 5
t_r	Thickness of rib web	Figure 3, Figure 4
w_t	Width of tab perpendicular to rib web at the termination of extended cutout	Figure 6

Table 2 Database of North American Steel Orthotropic Bridge Decks

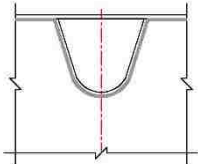
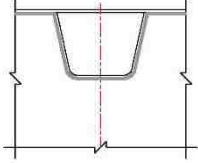
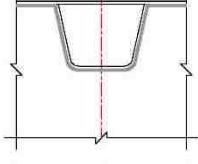
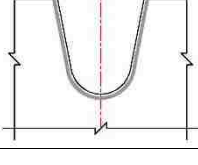
SI. No.	Year Built, Country	Min.	Rib Details					Floor Beam Details			RFB Detail	Weld Details	
		t , in. (mm)	b , in. (mm)	t_r , in. (mm)	h_r , in. (mm)	a , in. (mm)	s , in. (mm)	t_c , in. (mm)	d , in. (mm)	L , in. (mm)		RFB	RDP
1	1964 CA	$7/16$ (11)	N/A	$5/16$ (8)	10 (254)	12 (305)	24 (610)	$5/16$ (8)	42 (1067)	75 (1905)		Fillet	Fillet
2	1965 US	$3/8$ (10)	6 (152)	$1/4$ (6)	$8\frac{1}{2}$ (216)	12 (305)	24 (610)	$7/16$ (11)	24 (610)	180 (4572)		N/A	N/A
3	1965 US	$7/16$ (11)	6 (152)	$5/16$ (8)	$8\frac{1}{2}$ (216)	12 (305)	24 (610)	$7/16$ (11)	$25\frac{11}{16}$ (653)	180 (4572)		N/A	N/A
4	1967 US	$7/16$ (11)	N/A	$5/16$ (8)	13 (330)	12 (305)	24 (610)	$5/16$ (8)	30 (762)	180 (4572)		Fillet	90% PJP

Table 2 Database of North American Steel Orthotropic Bridge Decks continued

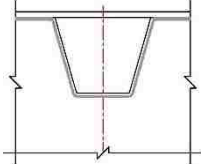
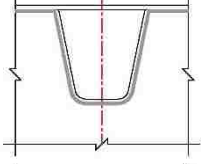
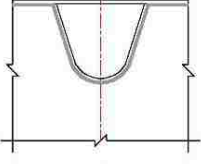
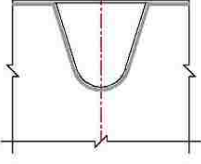
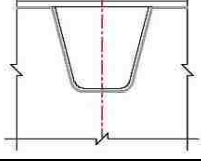
SI. No.	Year Built, Country	Min. t , in. (mm)	Rib Details					Floor Beam Details			RFB Detail	Weld Details	
			b , in. (mm)	t_r , in. (mm)	h_r , in. (mm)	a , in. (mm)	s , in. (mm)	t_c , in. (mm)	d , in. (mm)	L , in. (mm)		RFB	RDP
5	1967 US	$\frac{9}{16}$ (14)	$6\frac{1}{2}$ (165)	$\frac{5}{16}$ (8)	10 (254)	13 (330)	26 (660)	$\frac{3}{8}$ (10)	33 (838)	180 (4572)		Fillet	80% PJP
6	1969 US	$\frac{3}{8}$ (10)	6 (152)	$\frac{1}{4}$ (6)	9 (230)	12 (305)	24 (610)	$\frac{3}{8}$ (10)	39 (991)	180 (4572)		Fillet	PJP
7	1969 CA	N/A	N/A	N/A	N/A	N/A	N/A	N/A	N/A	180 (4572)		N/A	N/A
8	1970 CA	$\frac{3}{8}$ (10)	N/A	$\frac{1}{4}$ (6)	11 (279)	12 (305)	24 (610)	$\frac{5}{16}$ (8)	21 (533)	190 (4826)		Fillet	90% PJP
9	1971 US	$\frac{1}{2}$ (13)	$6\frac{1}{2}$ (165)	$\frac{5}{16}$ (8)	11 (279)	13 (330)	26 (660)	$\frac{3}{8}$ (10)	36 (914)	180 (4572)		Fillet	80% PJP

Table 2 Database of North American Steel Orthotropic Bridge Decks continued

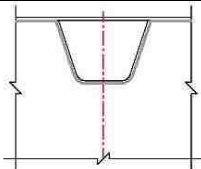
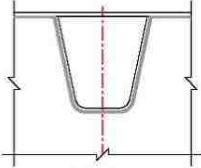
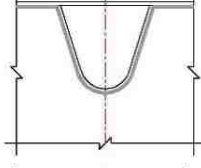
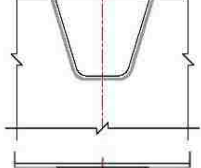
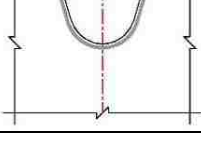
SI. No.	Year Built, Country	Min. t , in. (mm)	Rib Details					Floor Beam Details			RFB Detail	Weld Details	
			b , in. (mm)	t_r , in. (mm)	h_r , in. (mm)	a , in. (mm)	s , in. (mm)	t_c , in. (mm)	d , in. (mm)	L , in. (mm)		RFB	RDP
10	1972 US	$\frac{3}{8}$ (10)	6 (152)	$\frac{1}{4}$ (6)	8 (203)	12 (305)	24 (610)	$\frac{3}{8}$ (10)	24 (610)	132 (3353)		20% PJP	Fillet
11	1973 US	$\frac{1}{2}$ (13)	6 (152)	$\frac{5}{16}$ (8)	12 (305)	12 (305)	24 (610)	$\frac{7}{16}$ (11)	$50 \frac{9}{16}$ (1284)	$134 \frac{1}{2}$ (3416)		Fillet	80% PJP
12	1975 CA	$\frac{1}{2}$ (13)	N/A	$\frac{5}{16}$ (8)	11 (279)	12 (305)	24 (610)	$\frac{7}{8}$ (22)	36 (914)	144 (3658)		Fillet	80% PJP
13	1975 US	N/A	$6 \frac{1}{2}$ (165)	$\frac{3}{8}$ (10)	8 (203)	$11 \frac{1}{2}$ (292)	34 (864)	$\frac{5}{16}$ (8)	30 (762)	N/A		Fillet	PJP or Fillet
14	1976 CA	$\frac{1}{2}$ (13)	N/A	$\frac{5}{16}$ (8)	9 (229)	12 (305)	24 (610)	$\frac{3}{8}$ (10)	N/A	N/A		N/A	90% PJP

Table 2 Database of North American Steel Orthotropic Bridge Decks continued

SI. No.	Year Built, Country	Min.	Rib Details					Floor Beam Details			RFB Detail	Weld Details	
		t , in. (mm)	b , in. (mm)	t_r , in. (mm)	h_r , in. (mm)	a , in. (mm)	s , in. (mm)	t_c , in. (mm)	d , in. (mm)	L , in. (mm)		RFB	RDP
15	1982 US	$1/2$ (13)	$6\frac{1}{2}$ (165)	$7/16$ (11)	12 (305)	14 (356)	$25\frac{1}{2}$ (648)	$3/8$ (10)	27 (686)	240 (6096)		Fillet	80% PJP
16	1983 US	$7/16$ (11)	$6\frac{1}{2}$ (165)	$5/16$ (8)	9 (229)	12 (305)	24 (610)	$3/8$ (10)	$44\frac{7}{8}$ (1140)	172 (4369)		Fillet	80% PJP
17	1985 US	$5/8$ (16)	6 (152)	$3/8$ (10)	11 (279)	14 (356)	$28\frac{1}{2}$ (724)	$1/2$ (13)	12 (305)	300 (7620)		Fillet	80% PJP
18	1986 US	1 (25)	10 (254)	$7/16$ (11)	12 (305)	$19\frac{1}{8}$ (486)	$38\frac{1}{8}$ (968)	N/A	N/A	246 (6248)		N/A	N/A
19	1993 CA	$5/8$ (16)	8 (203)	$5/16$ (8)	15 (381)	13 (330)	$25\frac{3}{4}$ (654)	N/A	N/A	384 (9754)		N/A	80% PJP

Table 2 Database of North American Steel Orthotropic Bridge Decks continued

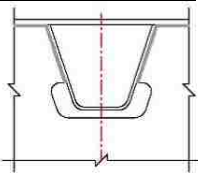
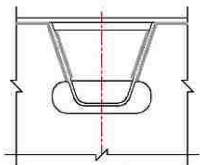
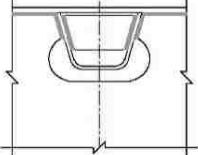
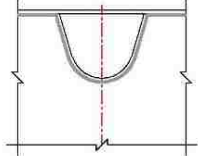
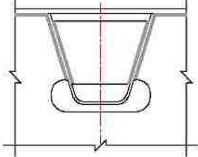
SI. No.	Year Built, Country	Min.	Rib Details					Floor Beam Details			RFB Detail	Weld Details	
		t , in. (mm)	b , in. (mm)	t_r , in. (mm)	h_r , in. (mm)	a , in. (mm)	s , in. (mm)	t_c , in. (mm)	d , in. (mm)	L , in. (mm)		RFB	RDP
20	1997 US	$\frac{5}{8}$ (16)	N/A	N/A	N/A	14 (356)	26 (660)	$\frac{3}{4}$ (19)	$88 \frac{3}{8}$ (2245)	N/A		N/A	80% PJP
21	1999 US	$\frac{5}{8}$ (16)	6 (152)	$\frac{3}{8}$ (10)	11 (279)	14 (356)	$28 \frac{1}{2}$ (724)	$\frac{1}{2}$ (13)	N/A	120 (3048)		Fillet/ CJP	80% PJP
22	1999 US	$\frac{5}{8}$ (16)	6 (152)	$\frac{7}{16}$ (11)	$7 \frac{3}{8}$ (187)	11 (279)	$20 \frac{5}{8}$ (524)	$\frac{3}{4}$ (19)	22 (559)	204 (5182)		Fillet/ CJP	80% PJP
23	2002 CA	$\frac{9}{16}$ (14)	N/A	$\frac{5}{16}$ (8)	N/A	12 (305)	24 (610)	$\frac{3}{8}$ (10)	N/A	N/A		N/A	90% +/-5% PJP
24	2003 US	$\frac{5}{8}$ (16)	N/A	$\frac{5}{16}$ (8)	12 (305)	14 (356)	$28 \frac{1}{2}$ (724)	$\frac{1}{2}$ (13)	N/A	198 (5029)		Fillet/ CJP	80% PJP

Table 2 Database of North American Steel Orthotropic Bridge Decks continued

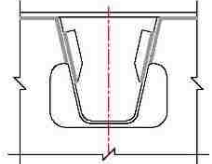
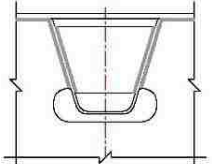
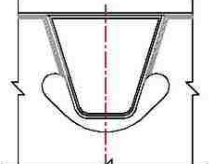
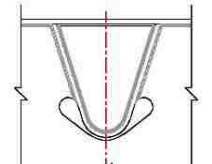
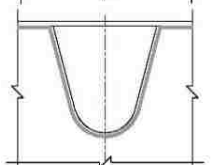
SI. No.	Year Built, Country	Min.	Rib Details					Floor Beam Details			RFB Detail	Weld Details	
		t , in. (mm)	b , in. (mm)	t_r , in. (mm)	h_r , in. (mm)	a , in. (mm)	s , in. (mm)	t_c , in. (mm)	d , in. (mm)	L , in. (mm)		RFB	RDP
25	2007 US	$5/8$ (16)	5 (127)	$5/16$ (8)	$13\ 1/2$ (343)	N/A	26 (660)	$5/8$ (16)	$18\ 7/8$ (479)	$118\ 1/2$ (3010)		CJP	80% PJP
26	2007 US	$5/8$ (16)	N/A	$5/16$ (8)	12 (305)	N/A	N/A	$3/8$ (10)	$66\ 1/2$ (1689)	240 (6096)		N/A	80% PJP
27	2012 US	$5/8$ (16)	$6\ 1/2$ (165)	$5/16$ (8)	12 (305)	14 (356)	25 (635)	$7/8$ (22)	22 (559)	198 (5029)		PJP/ CJP	80% PJP
28	2014 US	$9/16$ (14)	N/A	$1/2$ (13)	$13\ 1/2$ (343)	12 (305)	24 (610)	$9/16$ (14)	$29\ 1/2$ (749)	198 (5029)		PJP/ CJP, Fillet/ CJP	80% PJP
29	2016 CA	$9/16$ (14)	N/A	N/A	N/A	12 (305)	24 (610)	N/A	N/A	198 (5029)		N/A	N/A

Table 3 Database of International Steel Orthotropic Bridge Decks

SI. No.	Year Built	Rib Details						Floor Beam Details			EC
		Min. t , in. (mm)	b , in. (mm)	t_r , in. (mm)	h_r , in. (mm)	a , in. (mm)	s , in. (mm)	t_c , in. (mm)	d , in. (mm)	L , in. (mm)	
1	1954	$1/2$ (13)	12 (305)	$1/4$ (6)	12 (305)	12 (305)	24 (610)	N/A	N/A	93 (2362)	No
2	1954	$9/16$ (14)	N/A	$5/16$ (8)	11 (279)	N/A	24 (610)	N/A	N/A	81 (2057)	No
3	1964	$9/16$ (14)	N/A	$1/4$ (6)	N/A	N/A	N/A	N/A	N/A	120 (3048)	No
4	1970	$1/2$ (13)	$11 \frac{1}{3}$ (287)	$1/4$ (6)	9 (229)	$5 \frac{5}{8}$ (143)	(598)	$5/16$ (8)	$117 \frac{5}{8}$ (2988)	$118 \frac{1}{8}$ (3000)	Yes
5	1974	$3/8$ (10)	N/A	$5/16$ (8)	$9 \frac{7}{8}$ (251)	$12 \frac{7}{8}$ (327)	$25 \frac{3}{4}$ (654)	$3/8$ (10)	$39 \frac{3}{8}$ (1000)	$196 \frac{7}{8}$ (5000)	No
6	1975	$3/8$ (10)	N/A	$1/4$ (6)	$5 \frac{5}{8}$ (143)	N/A	N/A	N/A	N/A	84 (2134)	No
7	1985	$1/2$ (13)	$5 \frac{7}{8}$ (148)	$1/4$ (6)	$11 \frac{1}{8}$ (282)	$11 \frac{1}{4}$ (287)	$24 \frac{1}{2}$ (622)	$3/8$ (10)	$127 \frac{1}{2}$ (3238)	$157 \frac{1}{2}$ (4000)	Yes
8	1994	$1/2$ (13)	$7 \frac{5}{8}$ (193)	$5/16$ (8)	9 (231)	$11 \frac{1}{2}$ (293)	24 (610)	$5/8$ (16)	$117 \frac{1}{2}$ (2985)	$154 \frac{3}{4}$ (3930)	Yes
9	1996	$1/2$ (13)	6 (152)	$1/4$ (6)	$11 \frac{1}{8}$ (282)	$11 \frac{1}{4}$ (287)	24 (610)	$3/8$ (10)	157 (3988)	$157 \frac{1}{2}$ (4000)	Yes

Table 3 Database of International Steel Orthotropic Bridge Decks continued

SI. No.	Year Built	Min. t , in. (mm)	Rib Details					Floor Beam Details			EC
			b , in. (mm)	t_r , in. (mm)	h_r , in. (mm)	a , in. (mm)	s , in. (mm)	t_c , in. (mm)	d , in. (mm)	L , in. (mm)	
10	1998	$1/2$ (13)	6 (152)	$1/4$ (6)	$11\ 1/8$ (282)	$11\ 1/4$ (287)	24 (610)	$1/2$ (13)	31 (788)	$157\ 1/2$ (4000)	Yes
11	1998	$1/2$ (13)	6 (152)	$1/4$ (6)	$11\ 1/8$ (282)	$11\ 1/4$ (287)	24 (610)	$9/16$ (14)	35 (888)	$158\ 3/8$ (4022)	Yes
12	2002	$9/16$ (14)	$8\ 1/8$ (208)	$5/16$ (8)	$9\ 3/4$ (248)	$12\ 3/4$ (324)	$24\ 3/4$ (628)	N/A	N/A	$157\ 1/2$ (4000)	No
13	2004	N/A	$7\ 7/8$ (200)	$5/16$ (8)	12 (305)	$11\ 3/4$ (298)	24 (610)	$3/4$ (19)	$23\ 5/8$ (600)	N/A	Yes
14	2008	$9/16$ (14)	$6\ 1/2$ (164)	$5/16$ (8)	11 (279)	$11\ 1/4$ (287)	24 (610)	$3/4$ (19)	157 (3986)	$157\ 1/2$ (4000)	Yes
15	2008	$9/16$ (14)	$7\ 1/4$ (184)	$5/16$ (8)	11 (279)	$11\ 1/4$ (287)	24 (610)	$1/2$ (13)	$66\ 1/4$ (1682)	$157\ 1/2$ (4000)	Yes
16	2009	$3/4$ (19)	6 (152)	$3/8$ (10)	$12\ 5/8$ (321)	$11\ 3/4$ (298)	24 (610)	$1/2$ (13)	N/A	$149\ 5/8$ (3800)	Yes
17	2009	$9/16$ (14)	$7\ 1/2$ (189)	$5/16$ (8)	$9\ 11/16$ (246)	12 (305)	24 (610)	$7/16$ (11)	$117\ 1/2$ (2985)	$147\ 5/8$ (3750)	Yes
18			$4\ 3/4$ (120)	$5/16$ (8)	$13\ 1/2$ (343)	$15\ 3/4$ (400)	N/A	N/A	N/A	$157\ 1/2$ (4000)	Yes

Table 4 Performance of Existing Steel Orthotropic Bridge Decks

Bridge Location	Year Built	Adequate Wearing Surface Performance	Adequate Fatigue Performance	Corrosion
British Columbia, Canada	1964	0	1	0
Livermore, California	1965	0	1	0
Long Beach, California	1971	1	1	0
San Diego, California	1969	1	1	0
Portland, Oregon	1973	1	1	0
San Francisco, California	1985	1	1	0
St. Louis, Missouri	1967	0	1	0
Lansing, Michigan	1968	0	1	0
New York, New York	1986	0	1	0

Table 5 Limits of Steel Orthotropic Bridge Deck Parameters per FHWA Manual and AASHTO LRFD BDS

Detailing Dimension	Limits ¹ , in. (mm)	
	FHWA Manual	AASHTO LRFD BDS
Deck plate thickness	$t_d > 5/8$ ($t_d > 14$)	$t \geq 5/8$ ($t \geq 16$)
Rib thickness	$1/4 < t_r < 1/2$ ($6 < t_r < 12$)	$t_r \geq 1/4$ ($t_r \geq 6$)
Rib spacing – directly under wheel path	$24 < s < 30$ ($600 < s < 762$)	N/A
Rib spacing – not directly under wheel path	$24 < s < 40$ ($600 < s < 1000$)	N/A
Floorbeam spacing	$L < 236$ ($L < 6000$)	N/A
Ratio of rib-to-floorbeam depth	$\frac{h_{rib}}{h_{FB}} < 0.4$	N/A
Floorbeam web thickness	$3/8 < t_{FB} < 3/4$ ($10 < t_{FB} < 20$)	N/A
Ratio of cut-out to rib depth	$\frac{h_{cutout}}{h_{rib}} > 0.33$	N/A

¹ Parameter symbols shown are consistent with respective documents

Table 6 Range of Existing Steel Orthotropic Bridge Deck Parameters

Parameter	Range, in. (mm)
Deck plate thickness	$5/8 \leq t \leq 3/4$ (16 ≤ t ≤ 19)
Rib plate thickness	$1/4 \leq t_r \leq 1/2$ (6 ≤ t _r ≤ 13)
Rib spacing – directly under wheel path	24 ≤ s < 30 (610 ≤ s < 762)
Floorbeam spacing	140 ≤ L < 240 (3556 ≤ L < 6096)
Floorbeam web thickness	$3/8 \leq t_c \leq 3/4$ (10 ≤ t _c ≤ 19)
Ratio of cut-out to rib depth	$\frac{c}{h_r} \geq 0.33$

Table 7 Evaluation of Histograms

Parameter	Range, in. (mm)	Percentage of Parameter		Median Dimension, in. (mm)
		Within Range	Exceed Range	
t	$5/8 \leq t \leq 3/4$ (16 ≤ t ≤ 19)	24%	76%	$1/2$ (13)
t _r	$1/4 \leq t_r \leq 1/2$ (6 ≤ t _r ≤ 13)	100%	0%	$5/16$ (8)
s	24 ≤ s < 30 (610 ≤ s < 762)	91%	9%	24 (610)
L	140 ≤ L < 240 (3556 ≤ L < 6096)	68%	32%	180 (4572)
t _c	$3/8 \leq t_c \leq 3/4$ (10 ≤ t _c ≤ 19)	81%	19%	$7/16$ (11)
$\frac{c}{h_r}$	$\frac{c}{h_r} \geq 0.33$	100%	0%	N/A

Table 8 Submodel Analysis Matrix

Floor Beam Details			Loading			
			SL		EL	
FB ID	t _c , in.	d, in.	SMA	SMB	SMA	SMB
Connection Type 1B						
FB1	1/2	34 1/2	SMA_FB1_SL	SMB_FB1_CT1B_SL*	SMA_FB1_EL	SMB_FB1_CT1B_EL*
FB2	1/2	30	SMA_FB2_SL	SMB_FB2_CT1B_SL	SMA_FB2_EL	SMB_FB2_CT1B_EL
Connection Type 4B						
FB1	1/2	34 1/2	SMA_FB1_SL	SMB_FB1_CT4B_SL		
Connection Type 5B						
FB1	1/2	34 1/2	SMA_FB1_SL	SMB_FB1_CT5B_SL	SMA_FB1_EL	SMB_FB1_CT5B_EL
FB2	1/2	30	SMA_FB2_SL	SMB_FB2_CT5B_SL	SMA_FB2_EL	SMB_FB2_CT5B_EL

* These submodels were developed in a previous study (Roy and Mukherjee 2015, Mukherjee 2016)

Table 9 **Details of FEA Models**

Model	No. of elements	No. of nodes	No. of degrees of freedom	Desired length of element (in.)
GM	891,164	2,609,646	15,657,876	7
SMA_FB1	260,900	1,629,360	4,888,080	3 1/2
SMA_FB2	224,860	1,402,896	4,208,688	3 1/2
SMB_FB1_CT1B	1,602,188	8,227,602	24,682,806	1
SMB_FB2_CT1B	1,590,956	8,163,168	24,489,504	1
SMB_FB1_CT4B	1,711,244	8,831,803	26,495,409	1
SMB_FB1_CT5B	1,683,800	8,686,949	26,060,847	1
SMB_FB2_CT5B	1,781,348	9,122,989	27,368,967	1

FIGURES

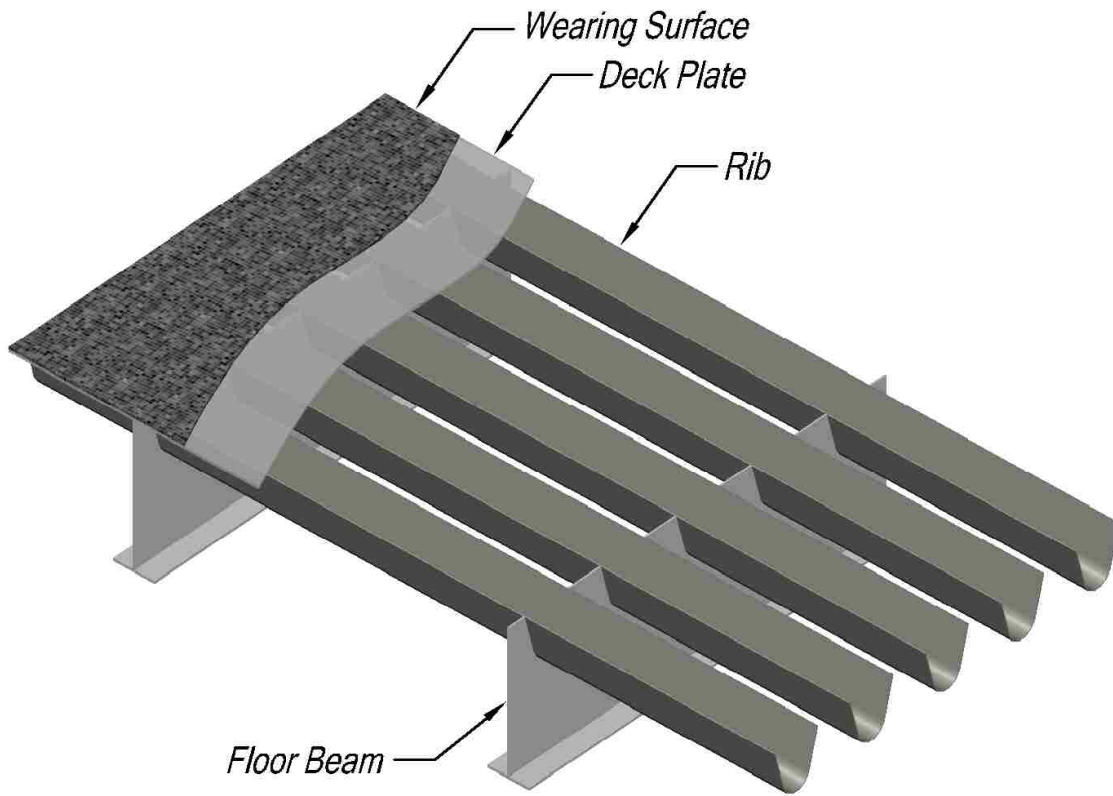


Figure 1 Closed rib orthotropic deck

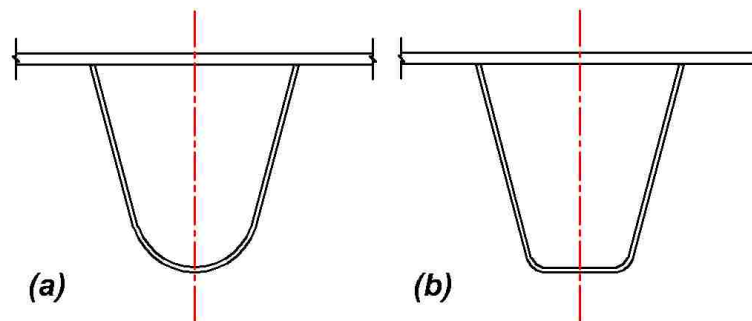


Figure 2 Torsionally stiff closed rib profiles: (a) Round-bottom; (b) Trapezoidal

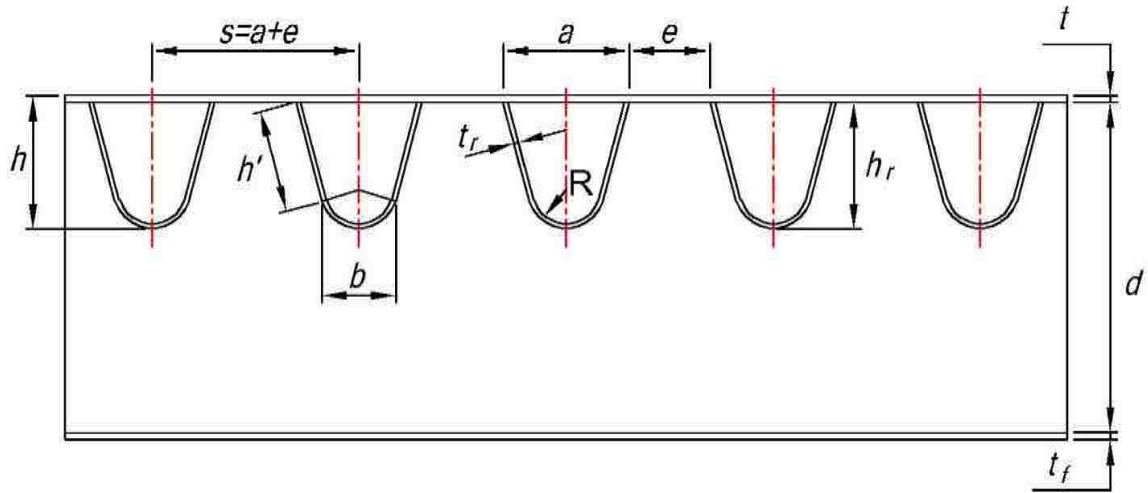


Figure 3 Parameters of a steel orthotropic bridge deck with rounded bottom rib profile

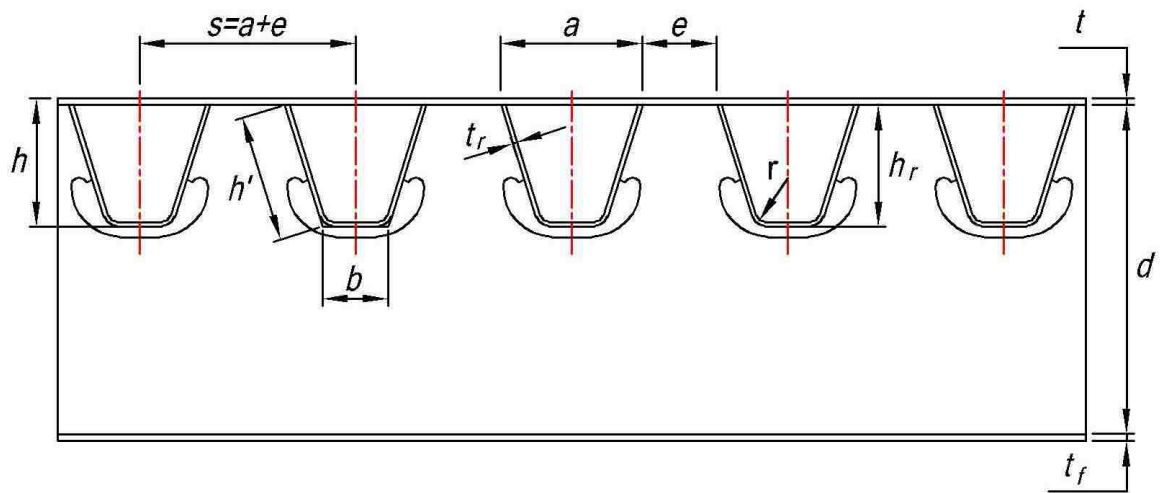


Figure 4 Parameter of an orthotropic deck with trapezoidal rib profile

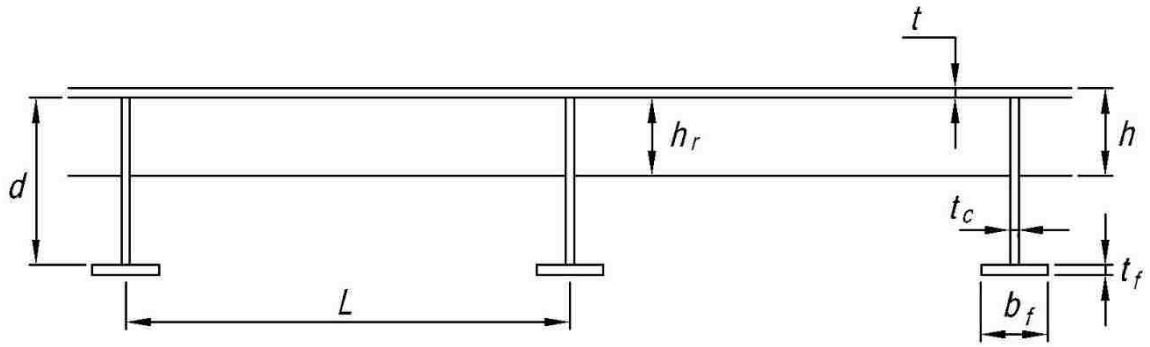


Figure 5 Common parameters of steel orthotropic bridge deck for all rib-to-floor beam connection types

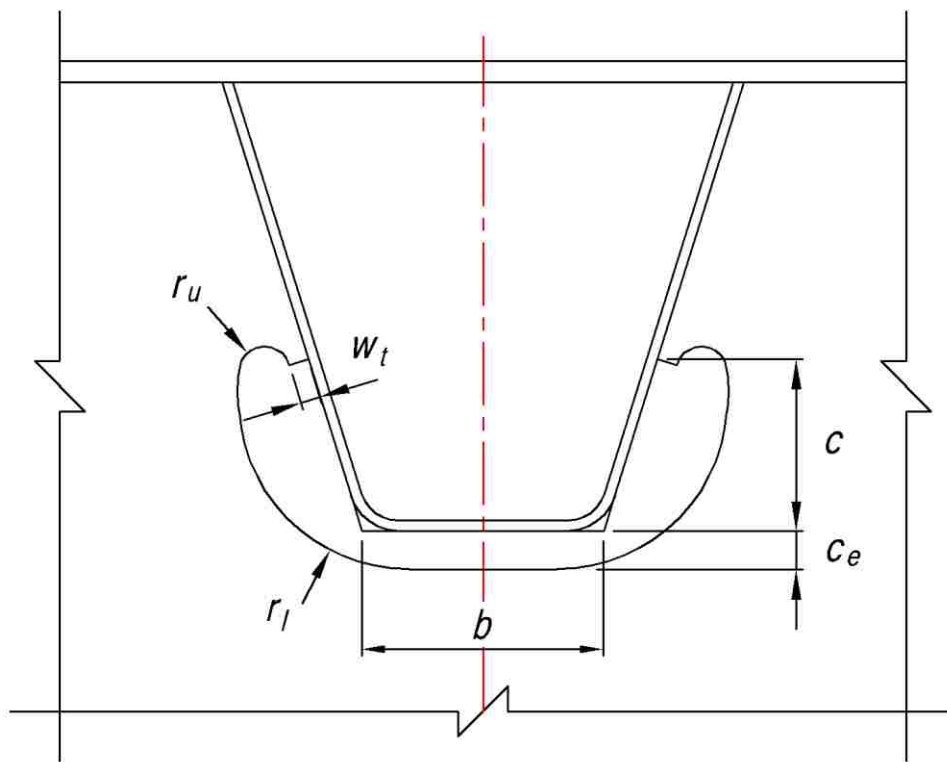


Figure 6 Parameters of the extended cutout in the rib-to-floor beam connection with trapezoidal rib profile

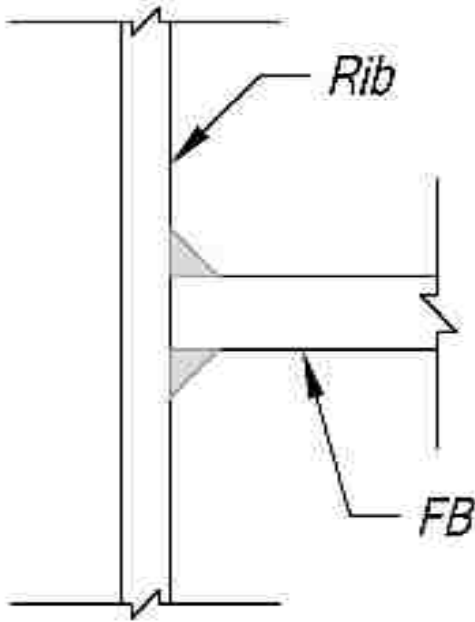


Figure 7 Rib-to-floor beam connection with continuous ribs passing through cutout in the floor beam

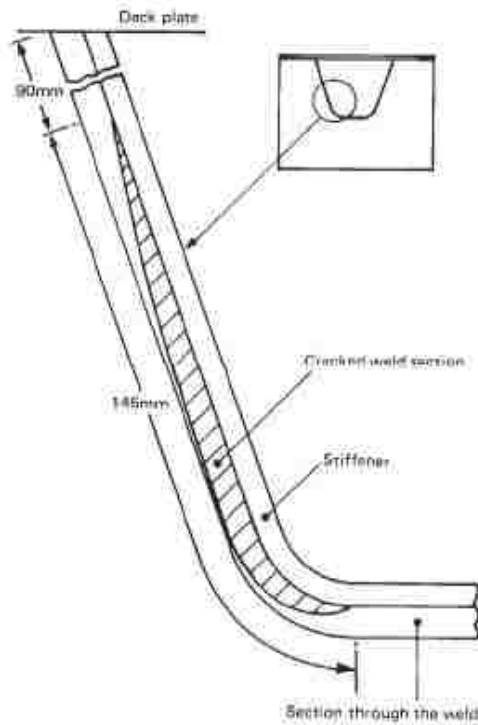


Figure 8 Weld throat failure in rib-to-floor beam connection with ribs fitted between floor beams (reproduced from Kolstein 2007)

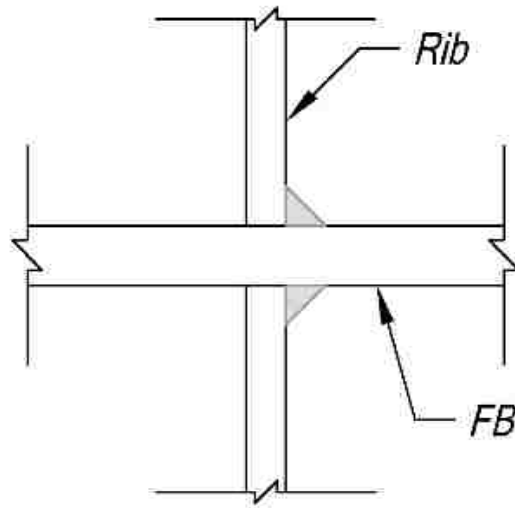


Figure 9 Rib-to-floor beam connection with discontinuous ribs fitted between floor beams

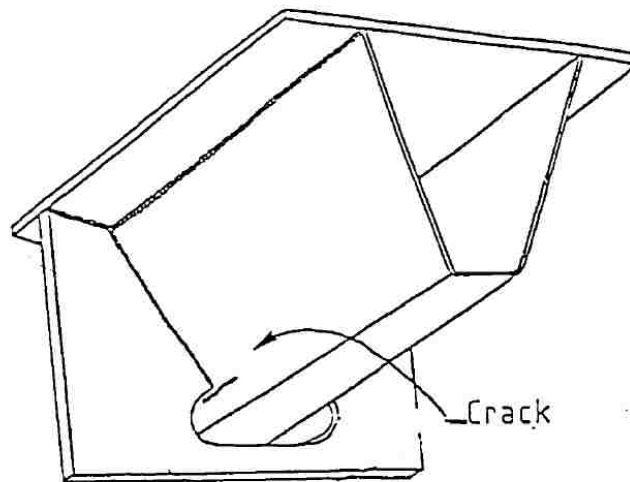


Figure 10 Fatigue crack at extended cutout termination in the rib wall (reproduced from Dexter and Fisher 1997)

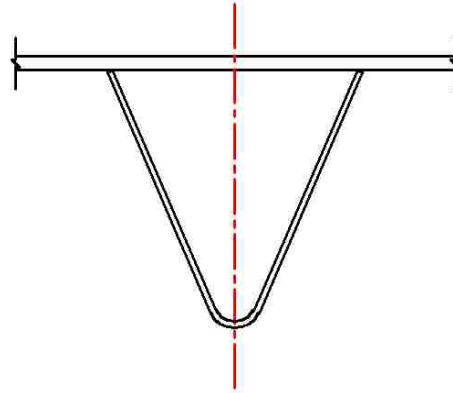


Figure 11 Triangular rib profile

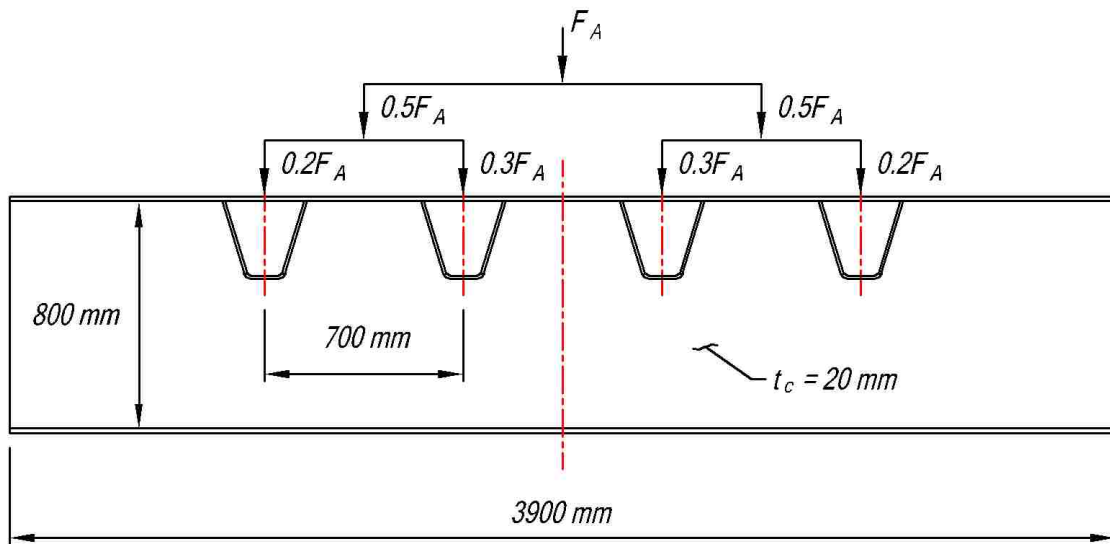


Figure 12 Cross section of experimental arrangement (reproduced from Haibach and Plasil 1983)

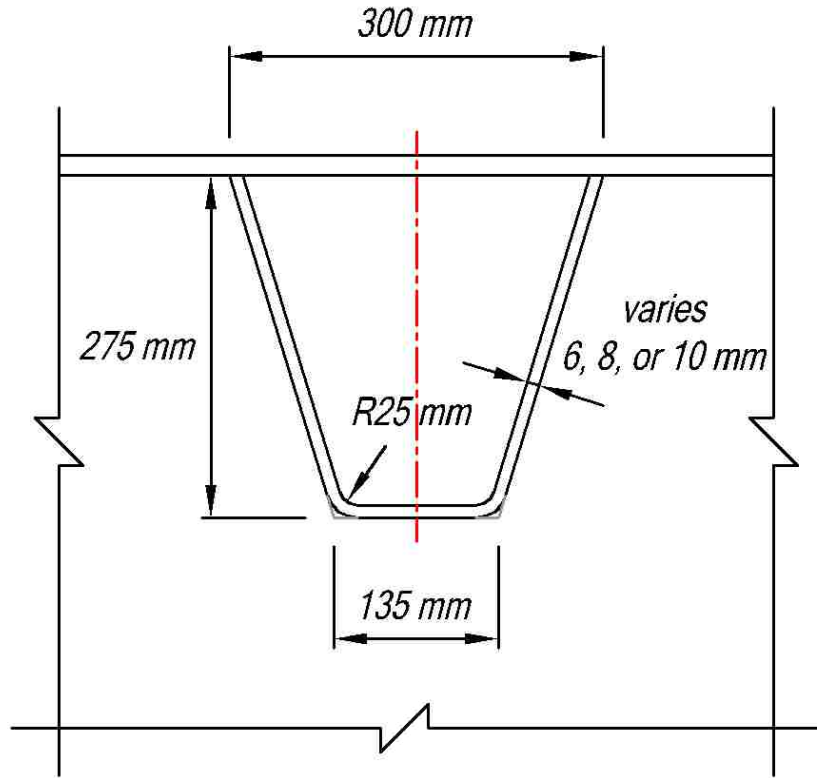


Figure 13 Rib dimensions

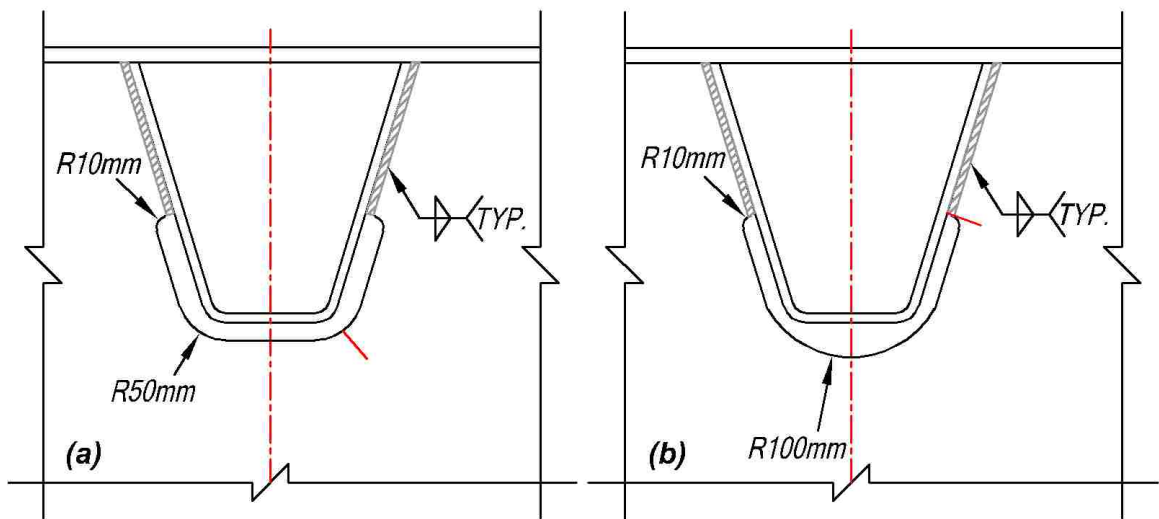


Figure 14 Preliminary forms of extended cutout: (a) Form I.1; (b) Form I.2 (reproduced from Haibach and Plasil 1983)

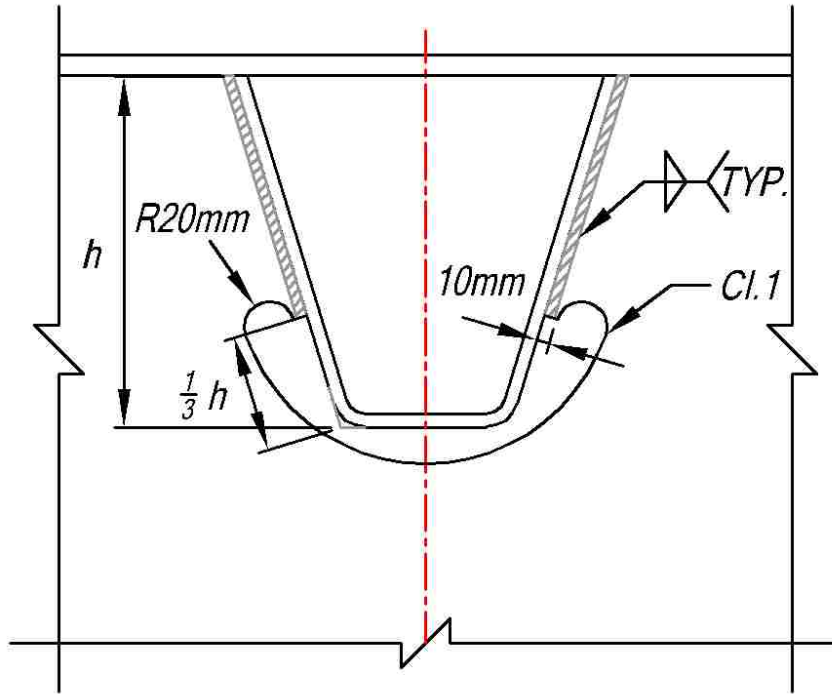


Figure 15 Form I (reproduced from Haibach and Plasil 1983)

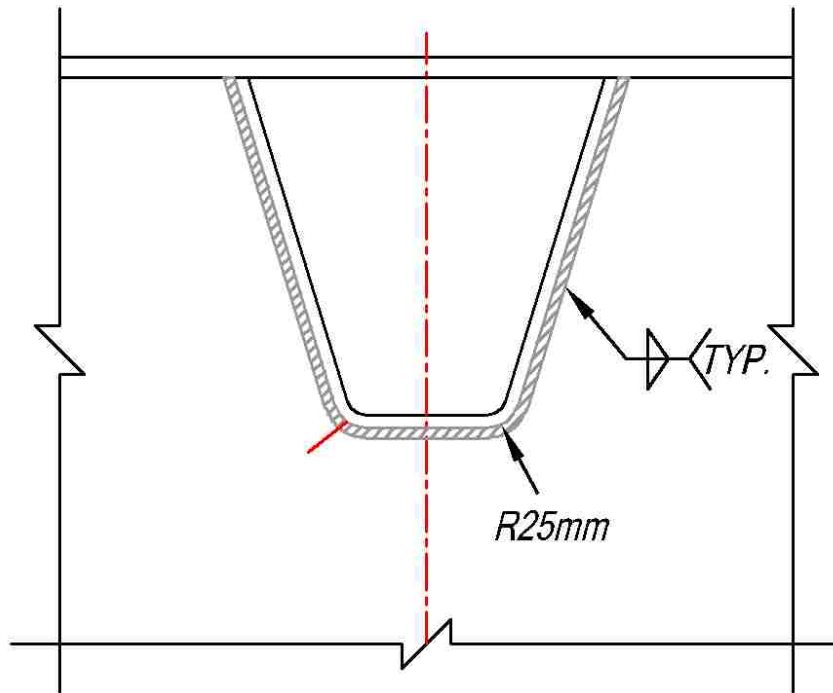


Figure 16 Form II (reproduced from Haibach and Plasil 1983)

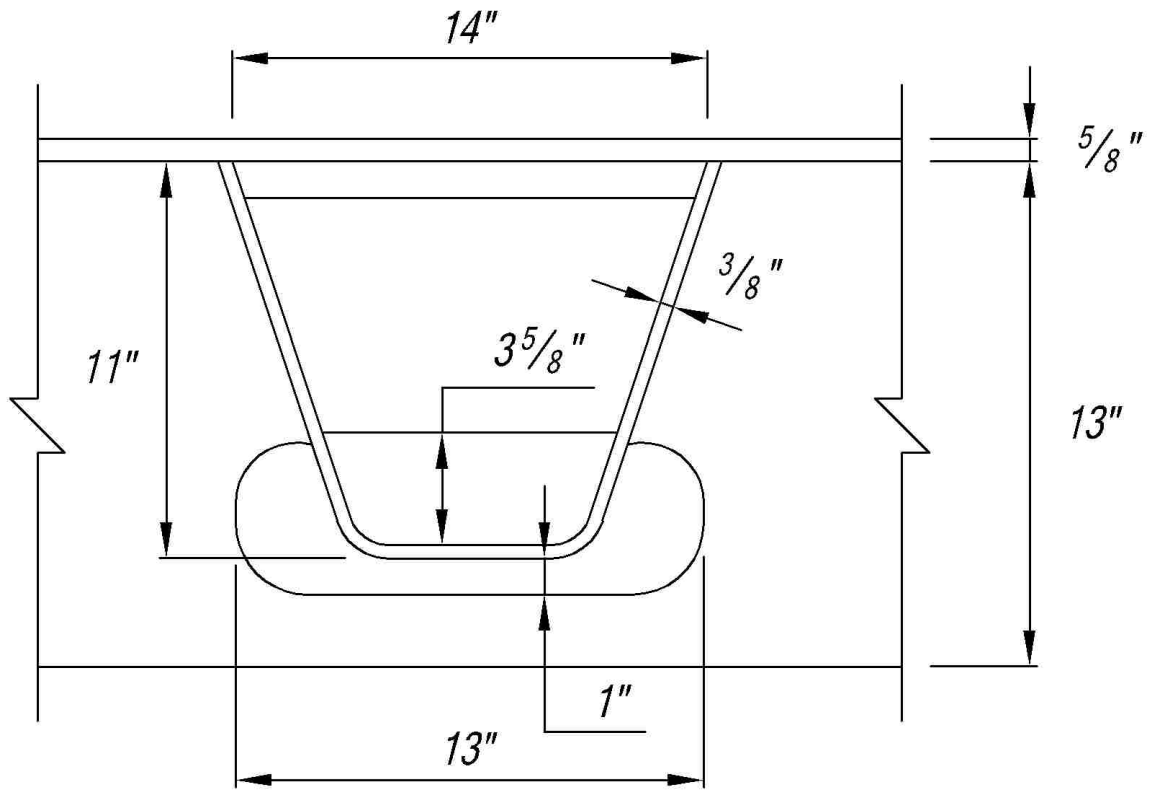


Figure 17 **Dimensions of the Williamsburg Bridge rib-to-floor beam connection**

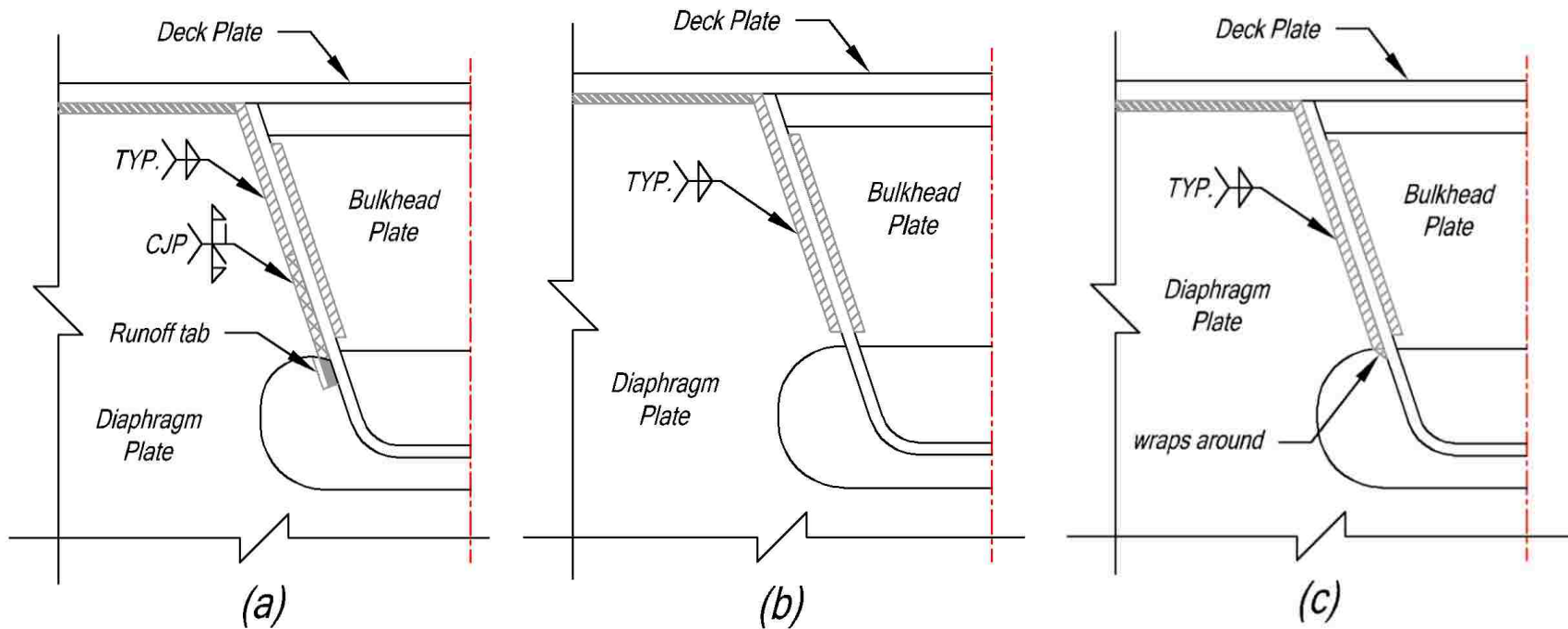


Figure 18 Weld options for the rib-to-floor beam connection in the Williamsburg Bridge fatigue testing: (a) Weld Option A; (b) Weld Option B; (c) Weld Option C (reproduced from Tsakopoulos and Fisher 2003)

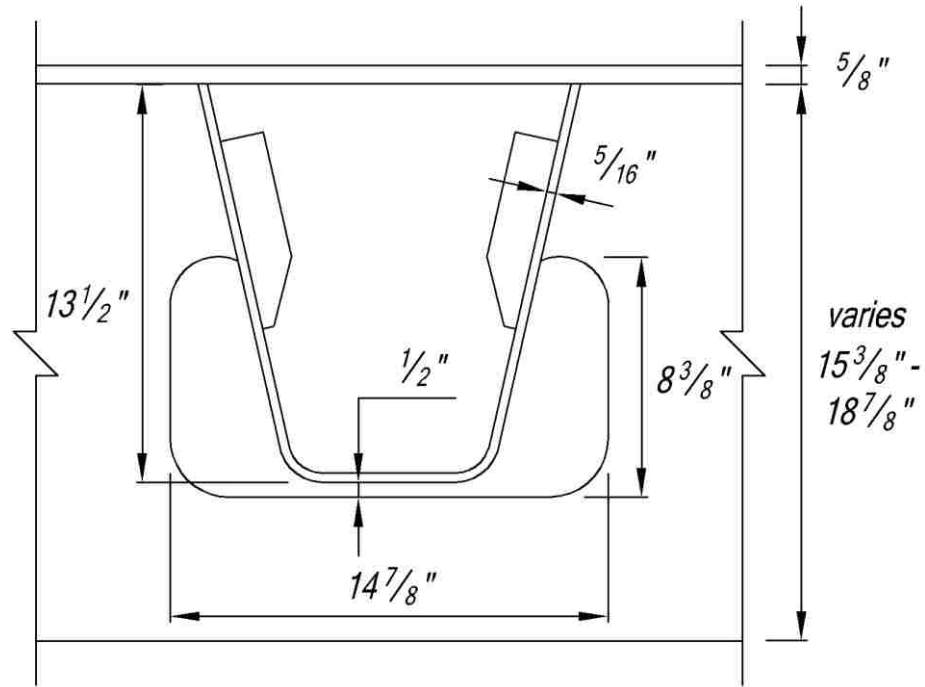


Figure 19 Dimensions of the Bronx Whitestone Bridge rib-to-floor beam connection

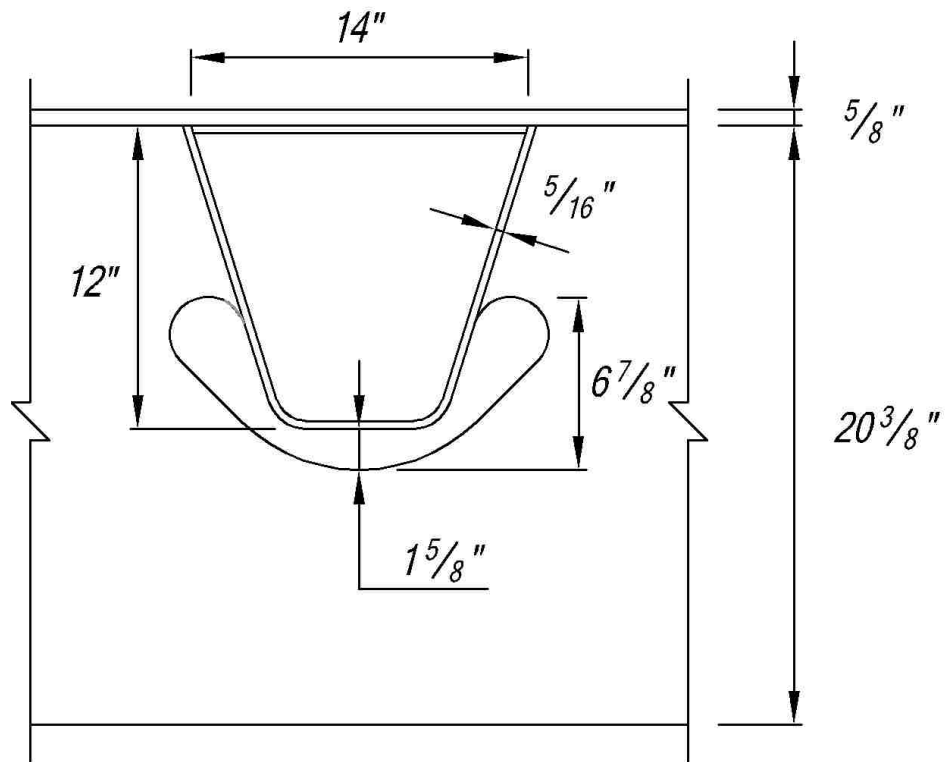


Figure 20 Dimensions of the Verrazano Narrows Bridge rib-to-floor beam connection

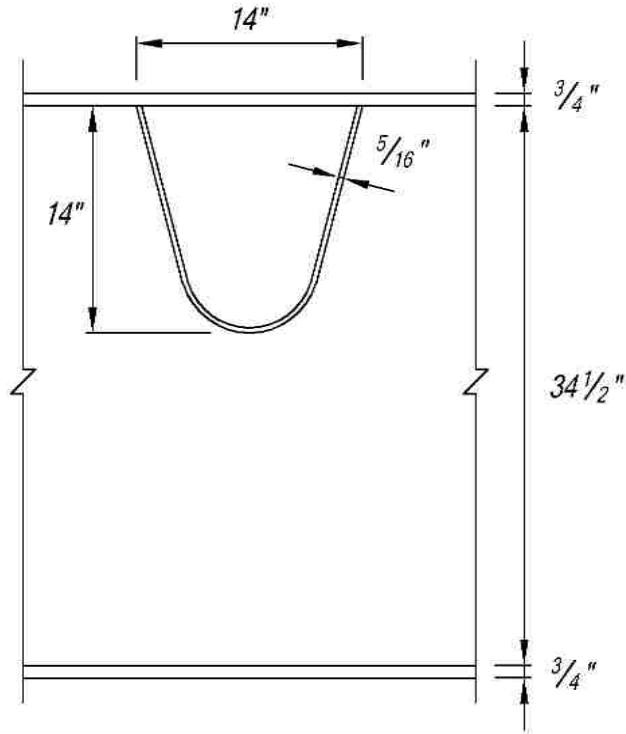


Figure 21 Dimensions of the rib-to-floor beam connection of SOBD for unnamed lift bridge

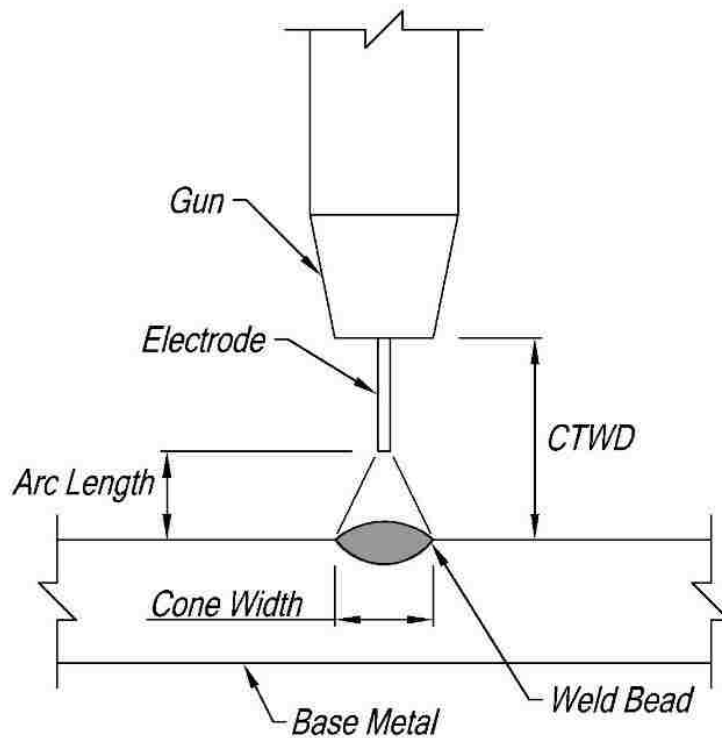


Figure 22 Welding terminology (reproduced from Linnert 1994)

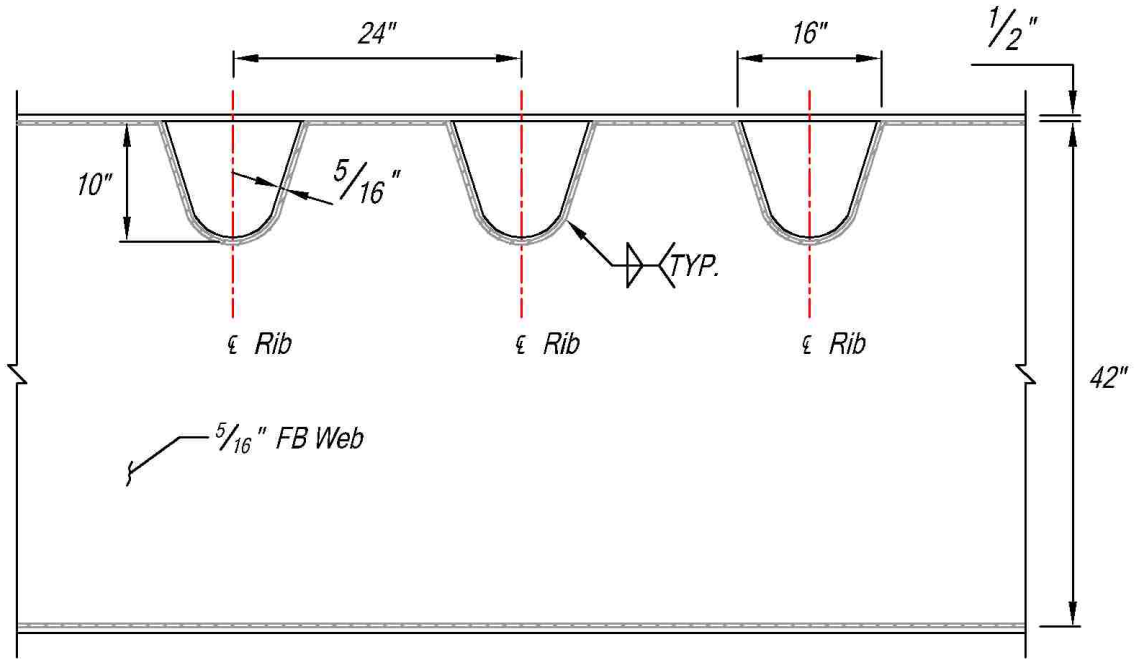


Figure 23 Port Mann Bridge Cross Section

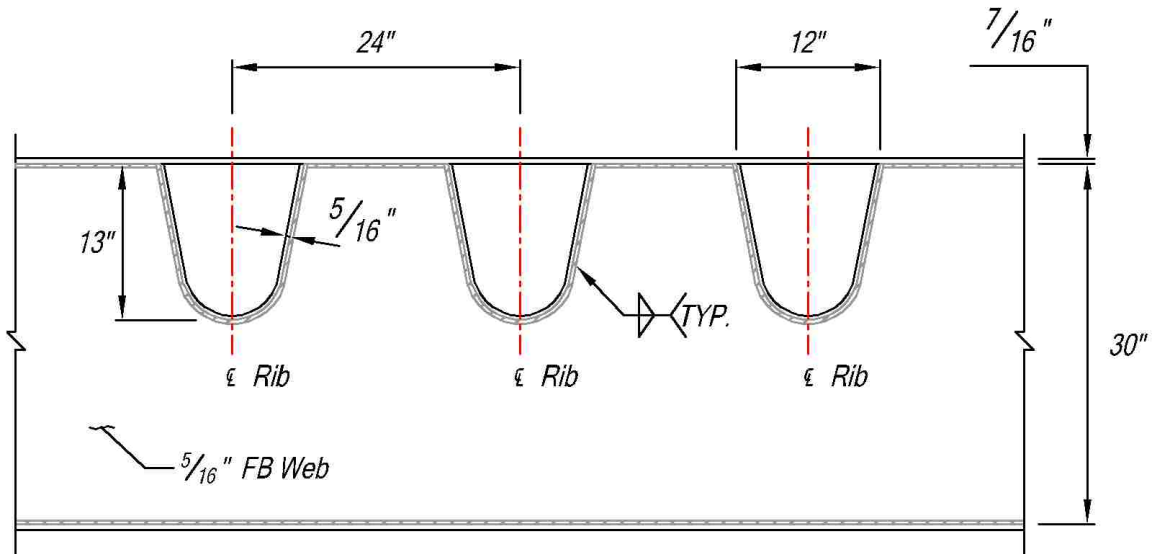


Figure 24 Concordia Bridge Cross Section

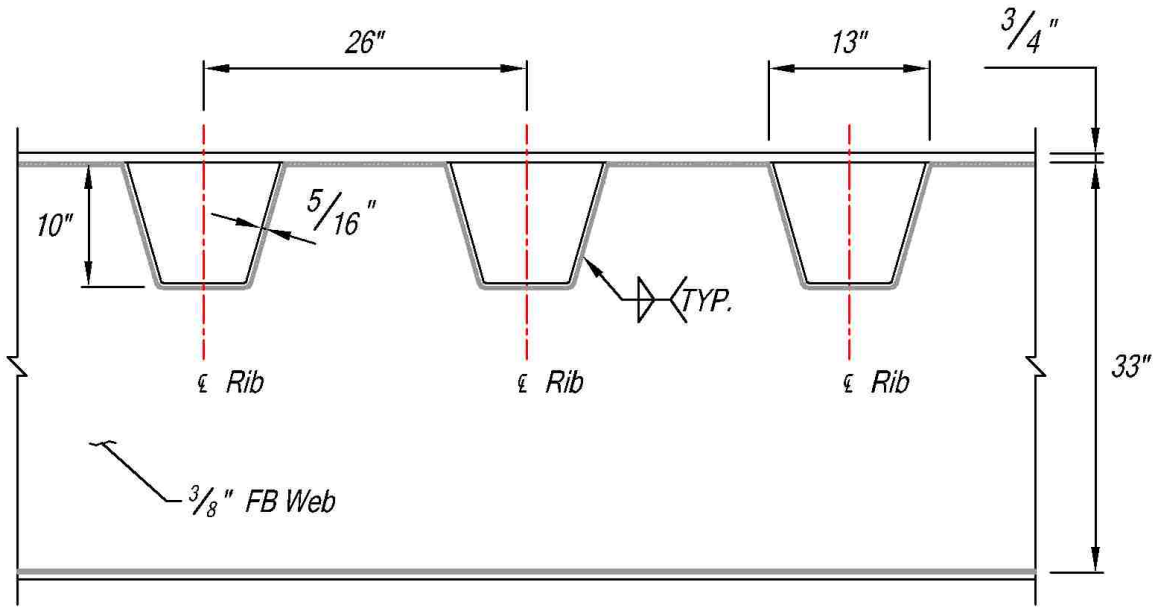


Figure 25 Poplar Street Bridge Cross Section

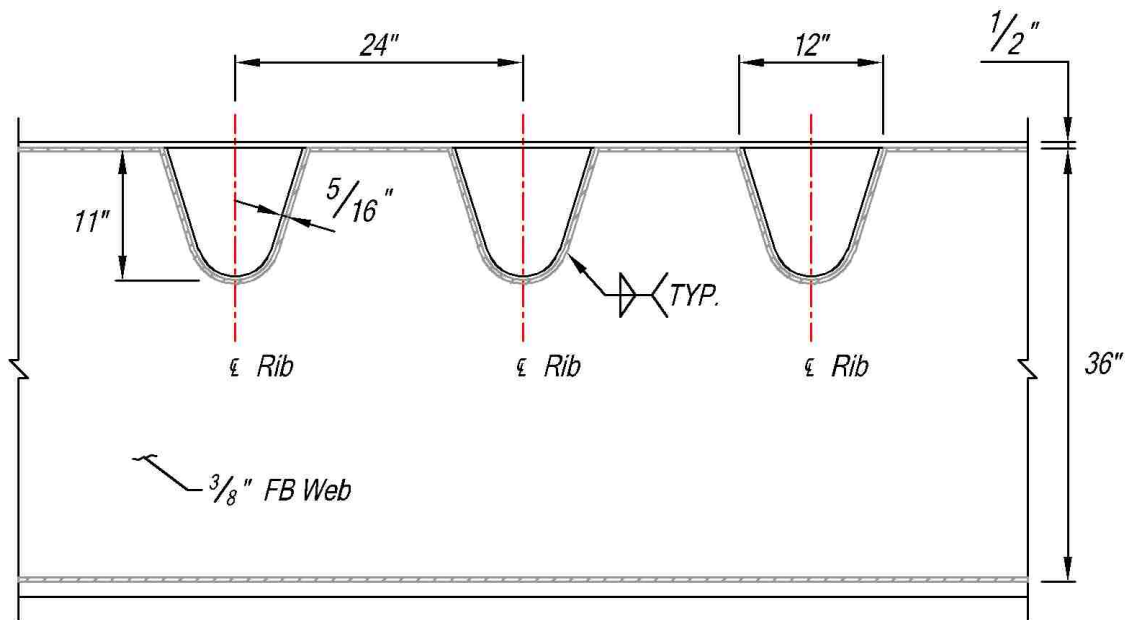


Figure 26 Mission Bridge Cross Section



Figure 27 Burning of rib profiles in floor beam web (reproduced from Gerritt Hardenberg)

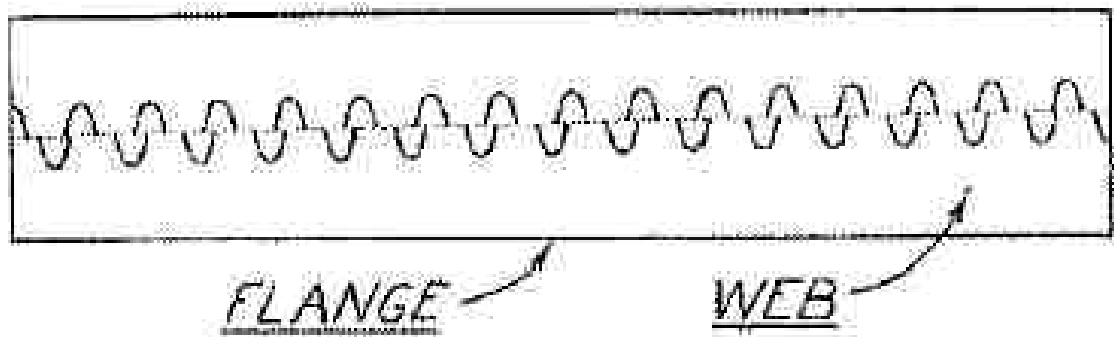


Figure 28 Cutting rib profile in floor beam web to produce pair of floor beams (reproduced from Smylie, 1966)



Figure 29 **Horizontal rotator (reproduced from Gill and Dozzi, 1966)**

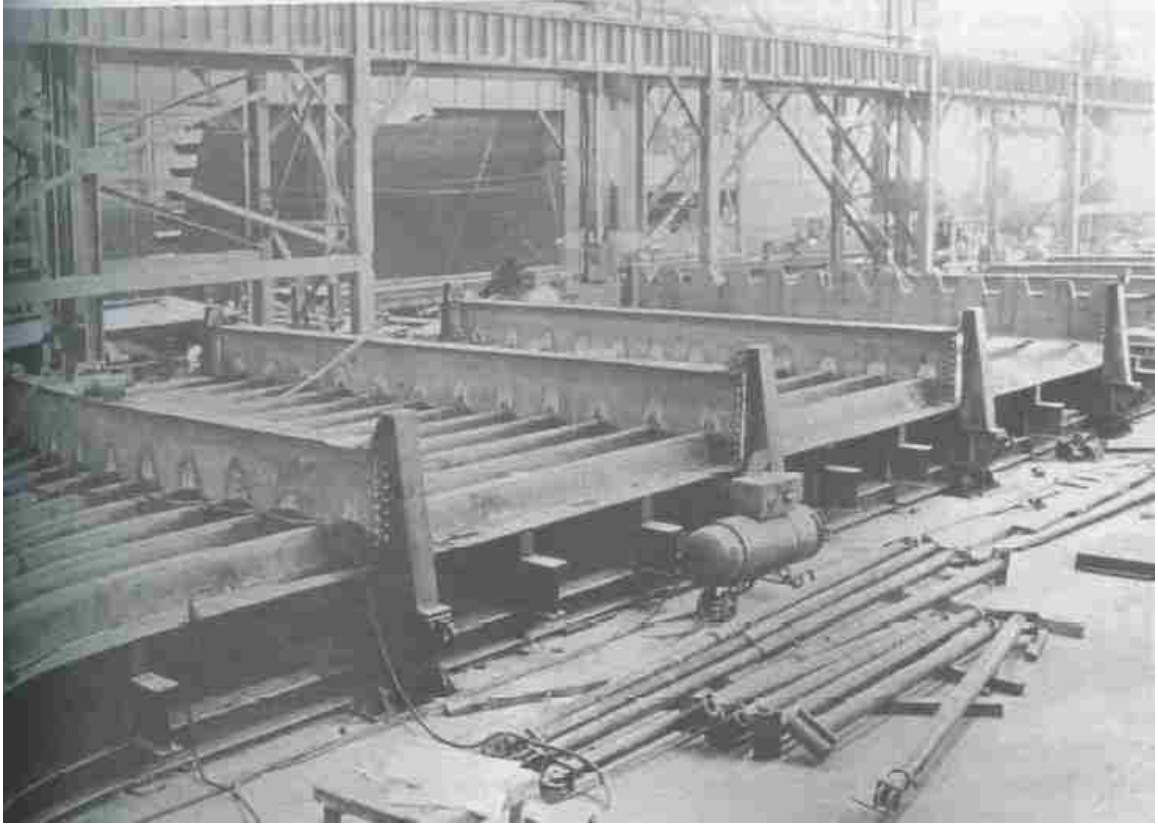


Figure 30 Assembly of the floor beams and deck units (reproduced from Shields and Schmidt, 1969)

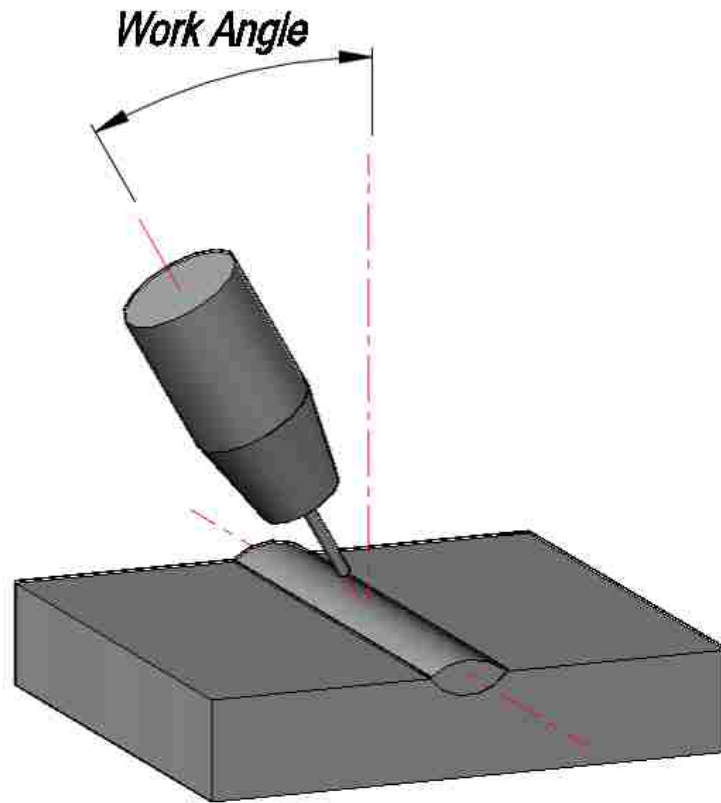


Figure 31 Welding work angle (reproduced from Linnert 1994)

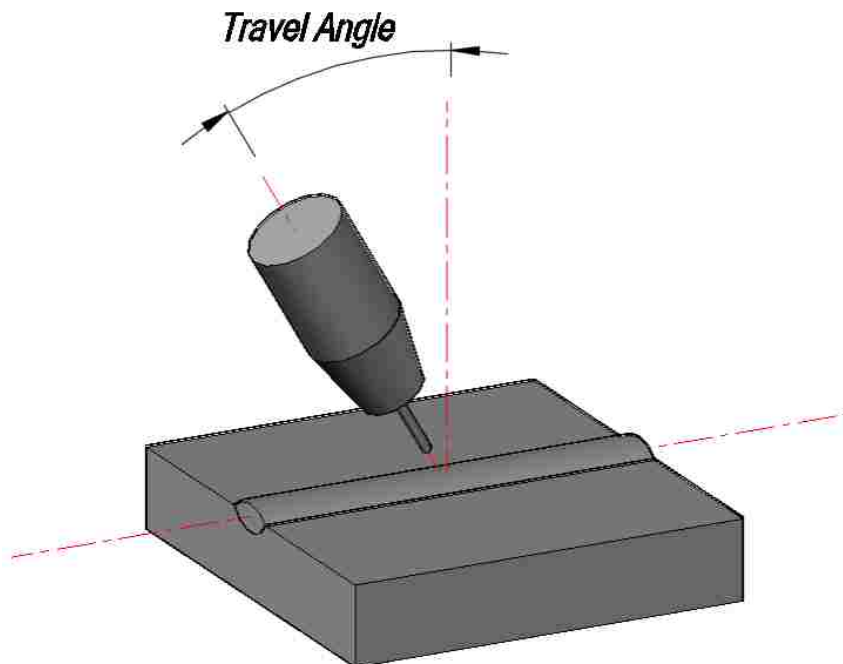


Figure 32 Welding travel angle (reproduced from Linnert 1994)

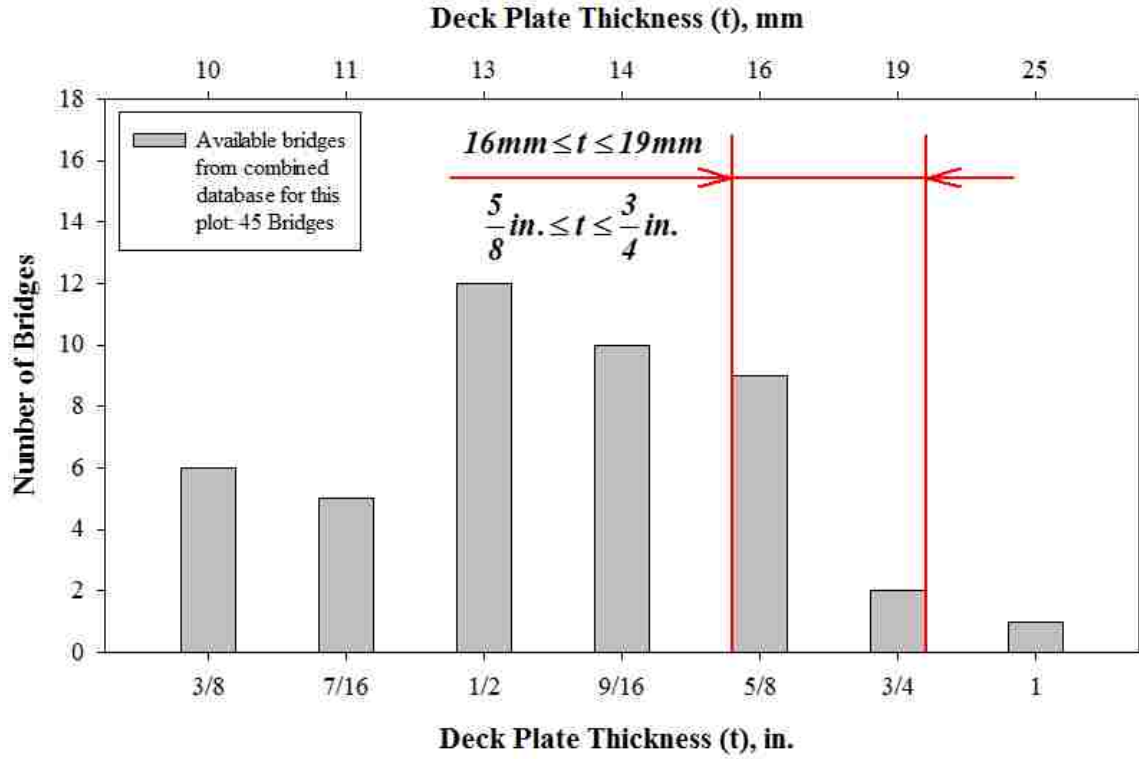


Figure 33 Existing deck plate thickness

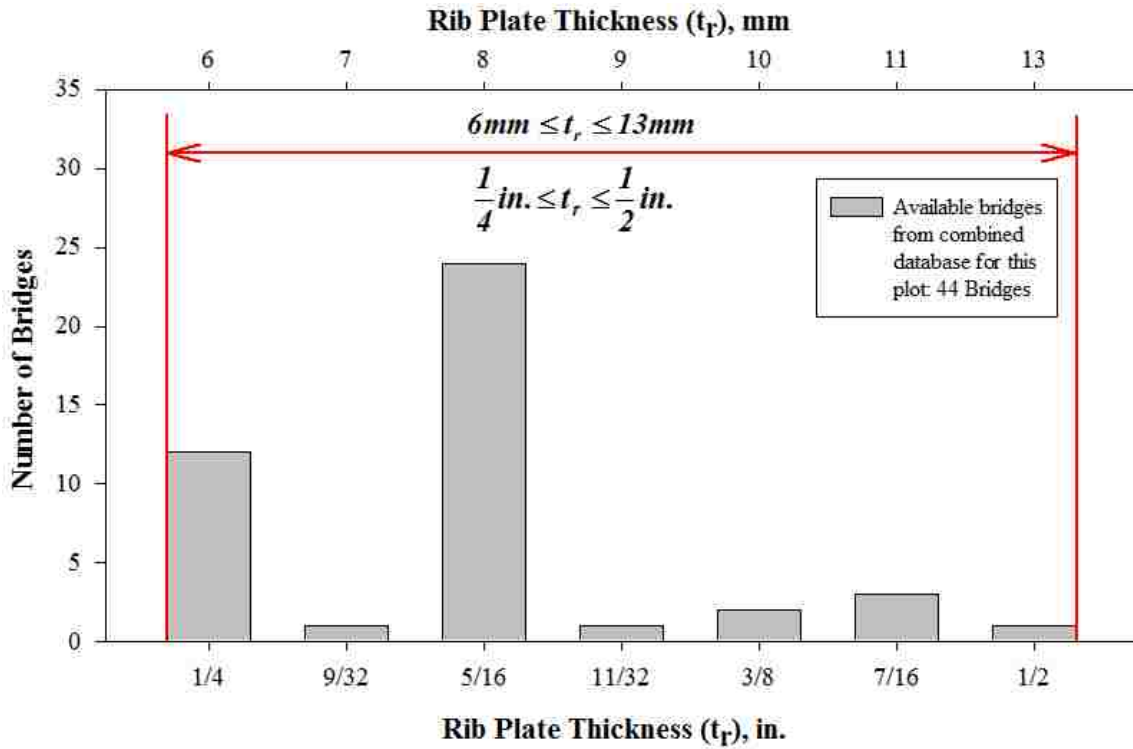


Figure 34 Existing rib plate thickness

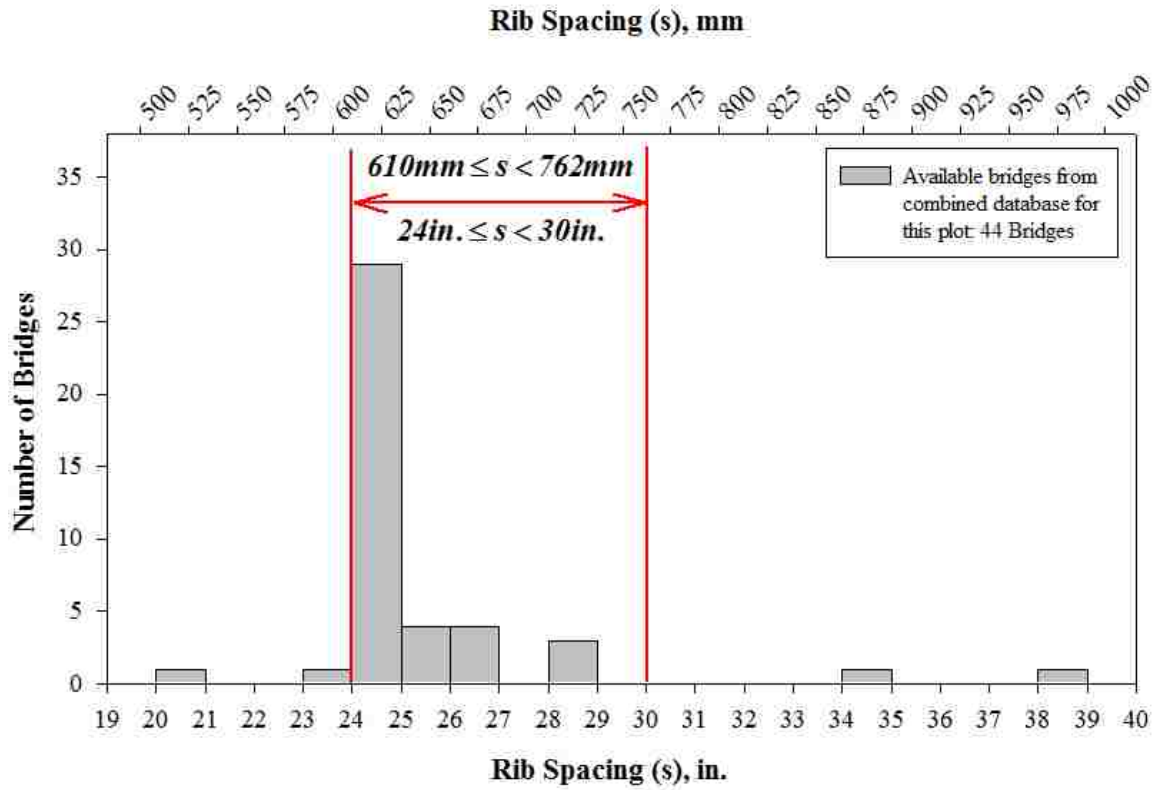


Figure 35 Existing rib spacing

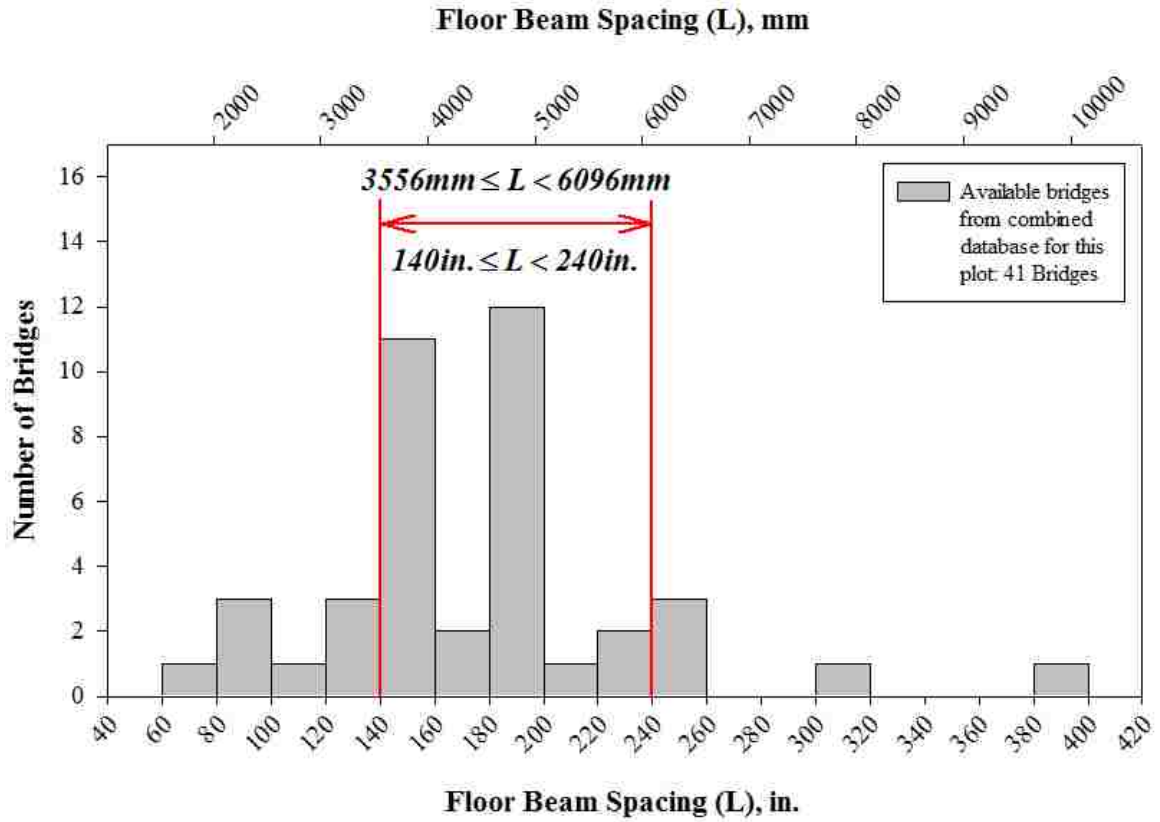


Figure 36 Existing floor beam spacing

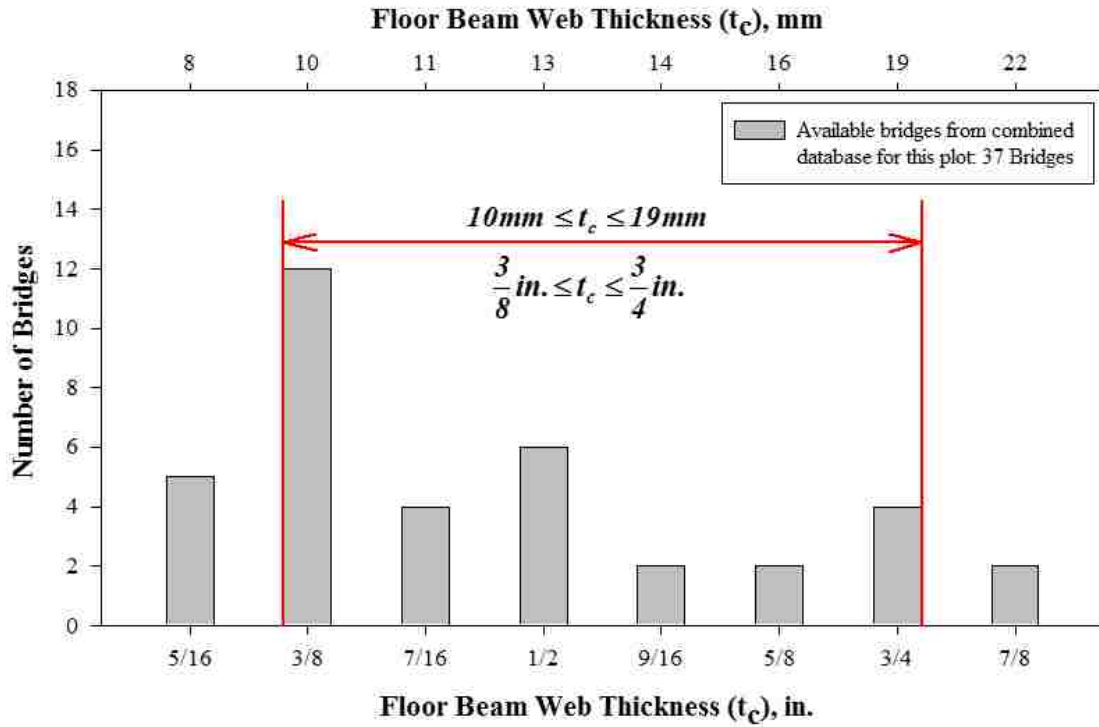


Figure 37 Existing floor beam web thickness

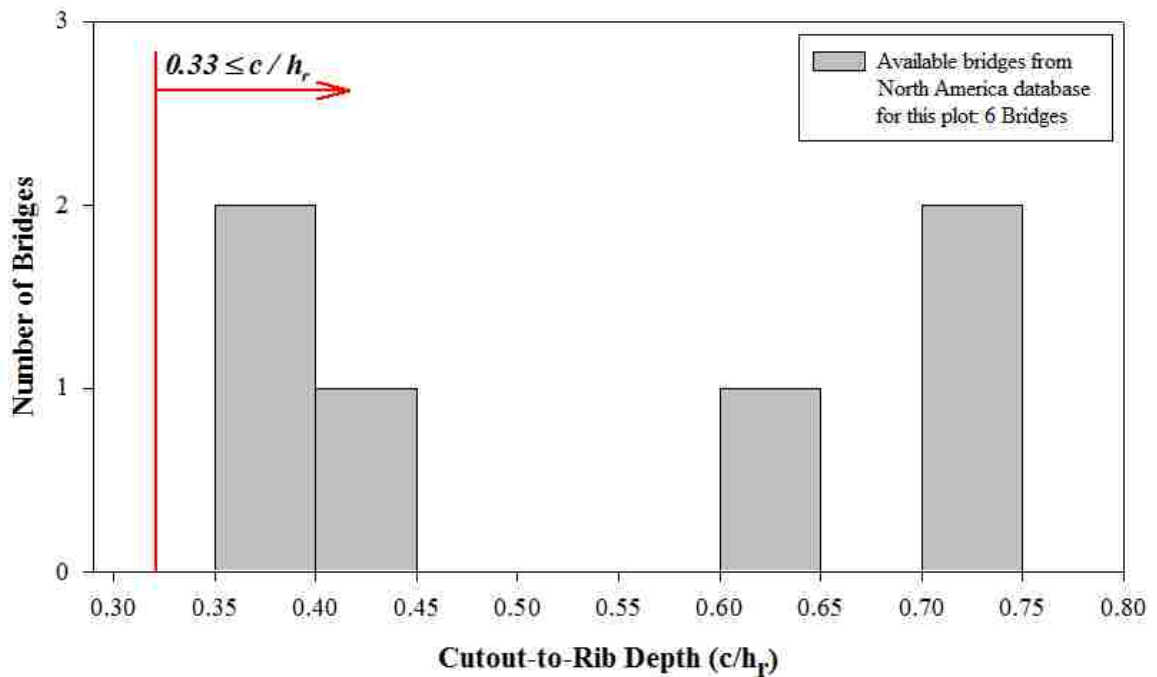


Figure 38 Existing cutout-to-rib depth

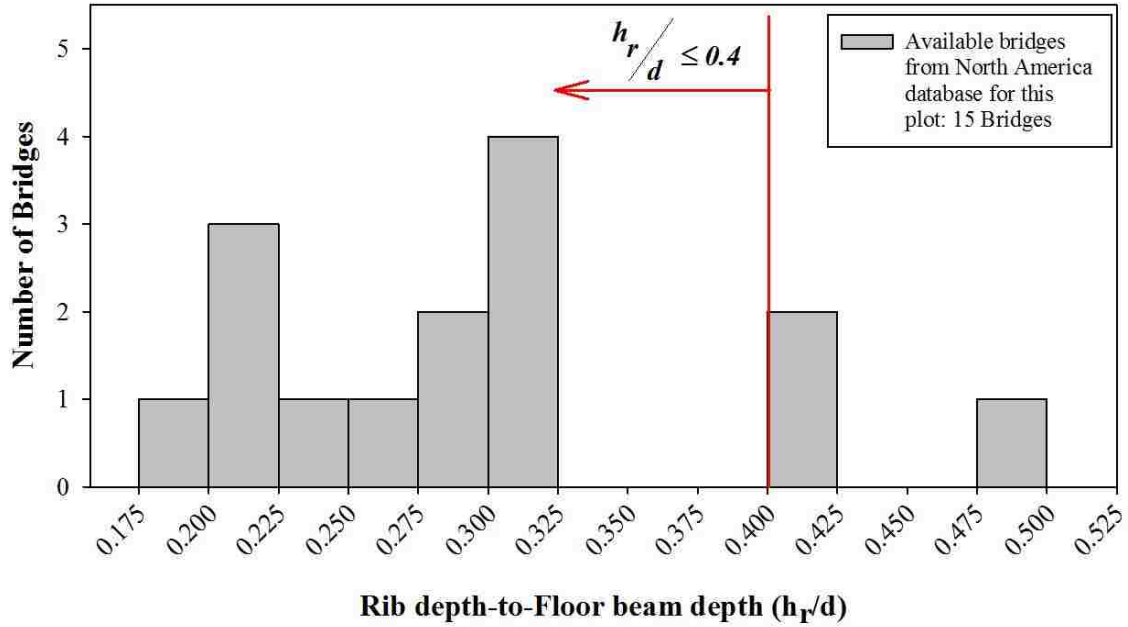


Figure 39 Existing rib depth-to-floor beam depth

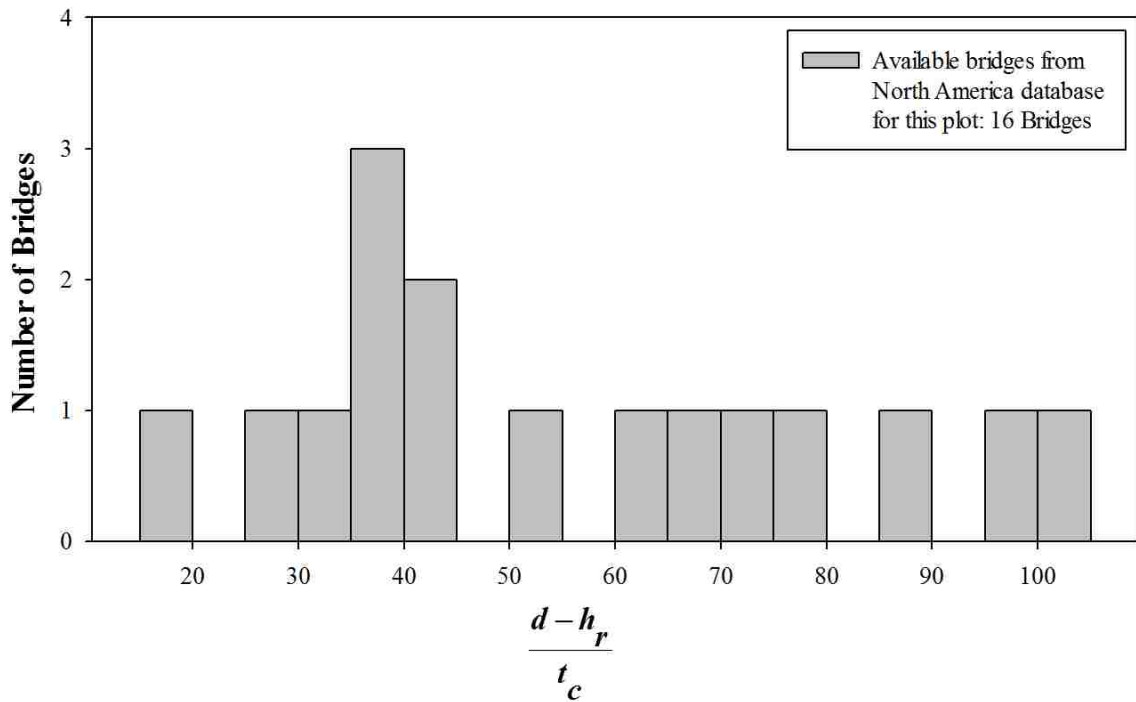


Figure 40 Existing portion of floor beam depth-to-floor beam thickness

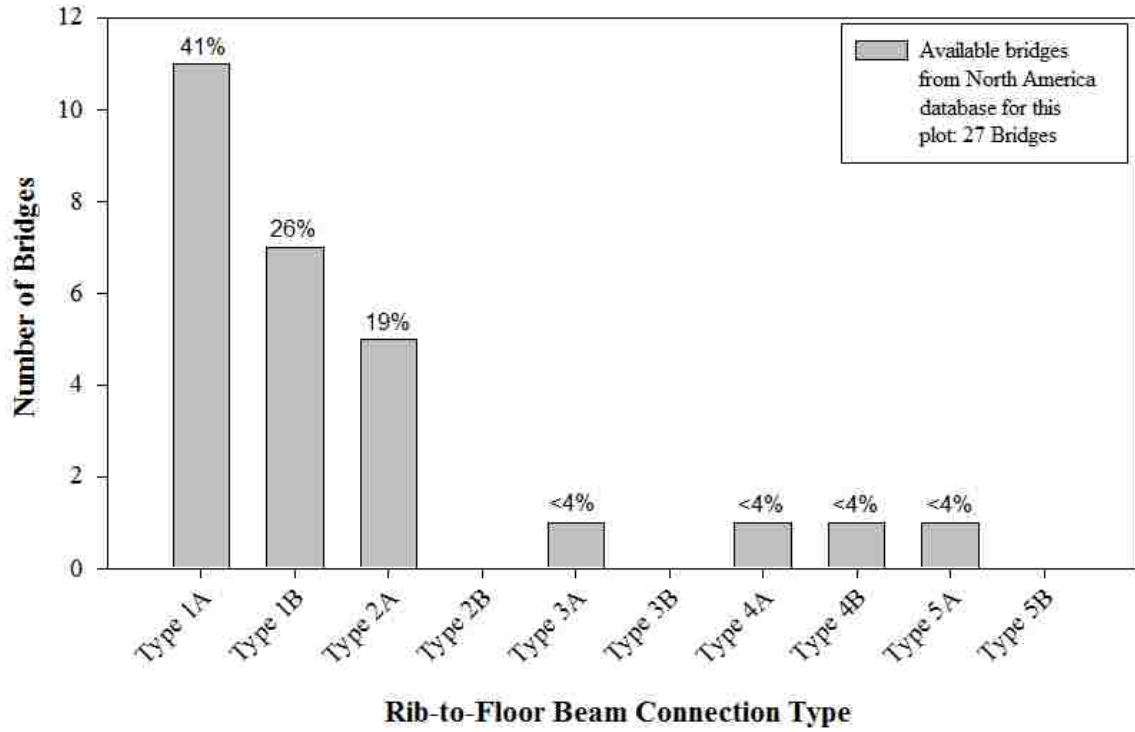


Figure 41 Existing rib-to-floor beam connection types

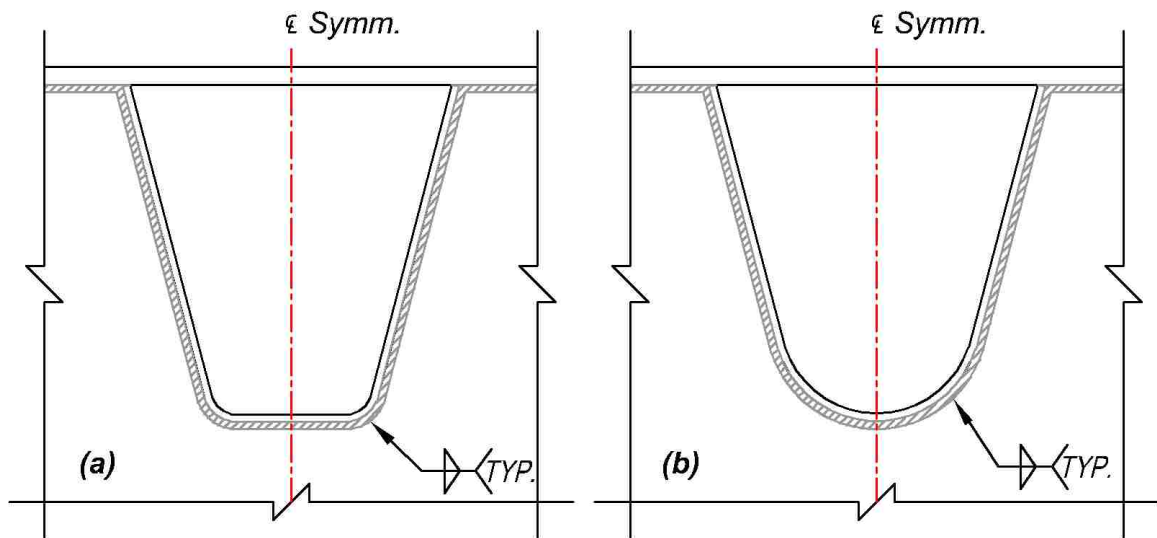


Figure 42 Type 1 rib-to-floor beam connection: (a) Type 1A with trapezoidal rib; (b) Type 1B with round-bottom rib

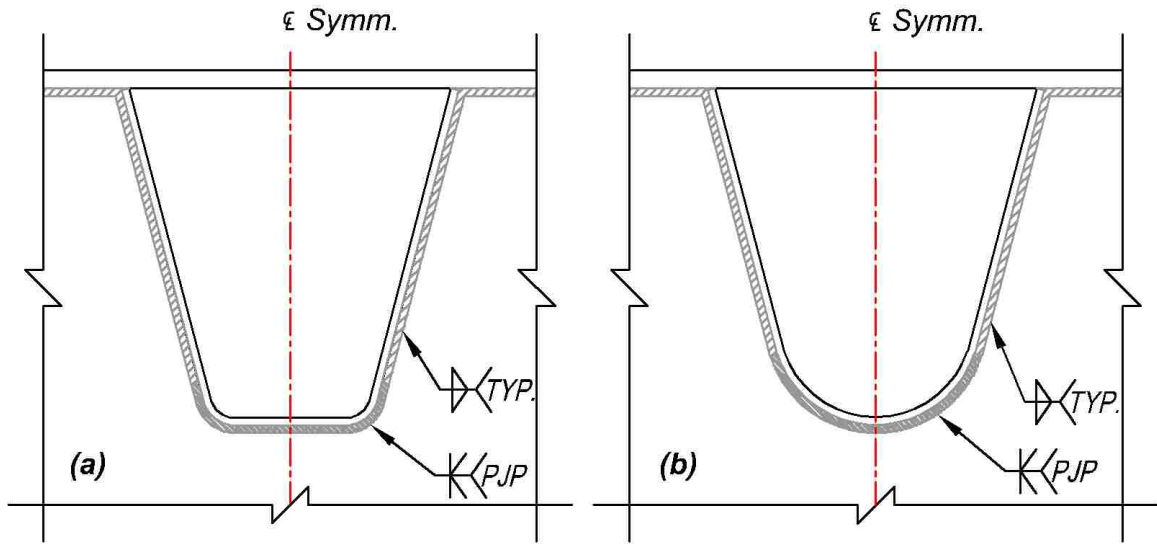


Figure 43 Type 1 rib-to-floor beam connection with alternate weld detail: (a) Type 1A with trapezoidal rib; (b) Type 1B with round-bottom rib

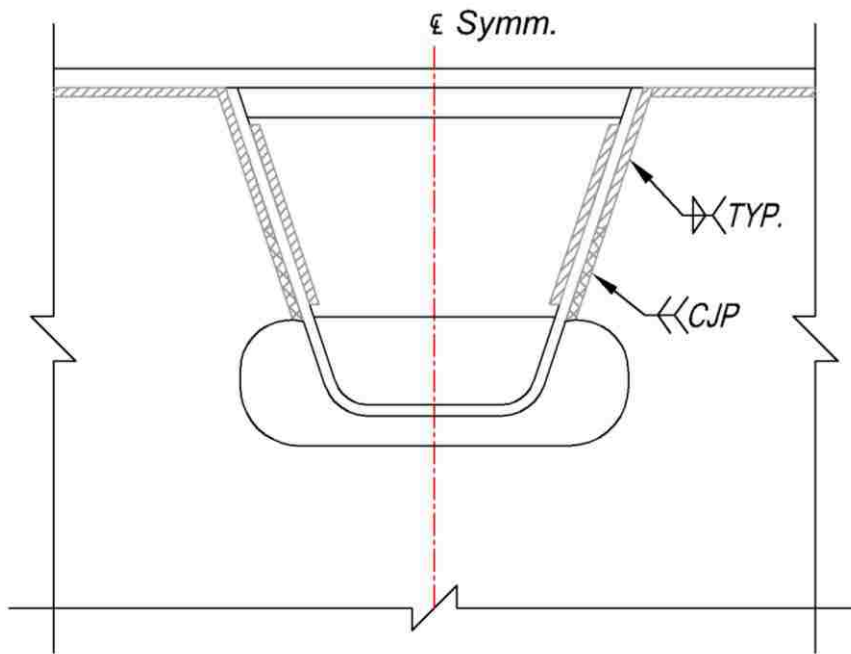


Figure 44 Type 2A rib-to-floor beam connection

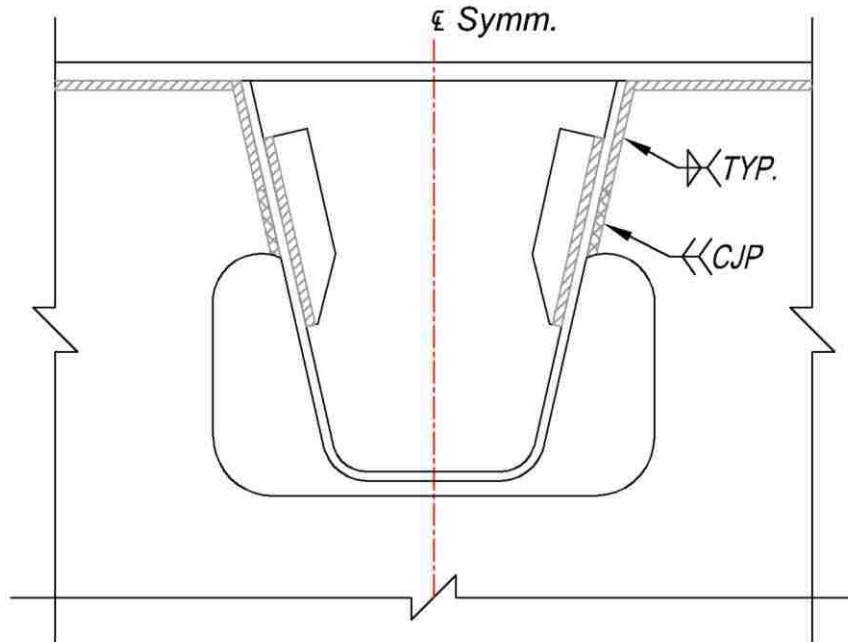


Figure 45 Type 3A rib-to-floor beam connection

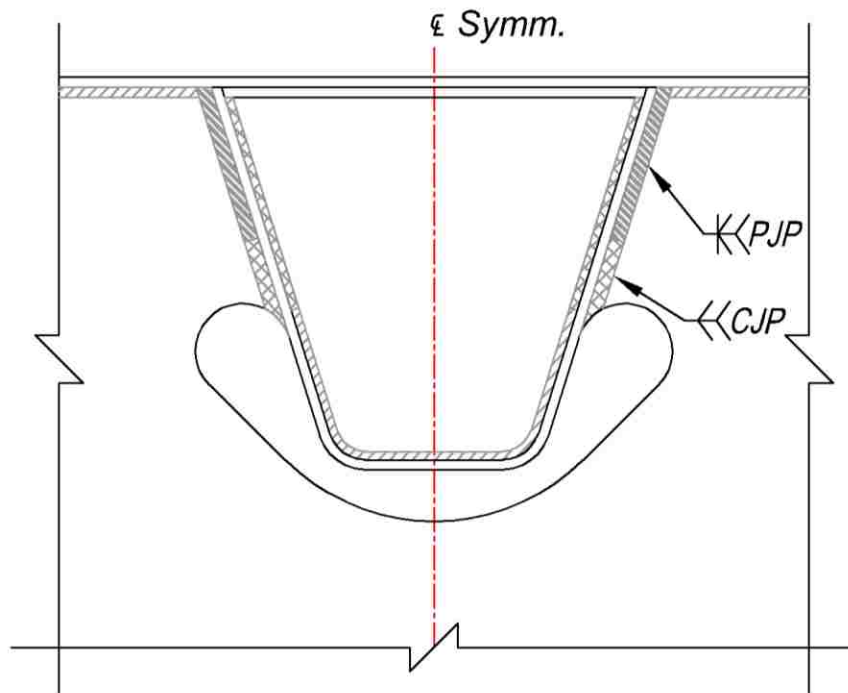


Figure 46 Type 4A rib-to-floor beam connection

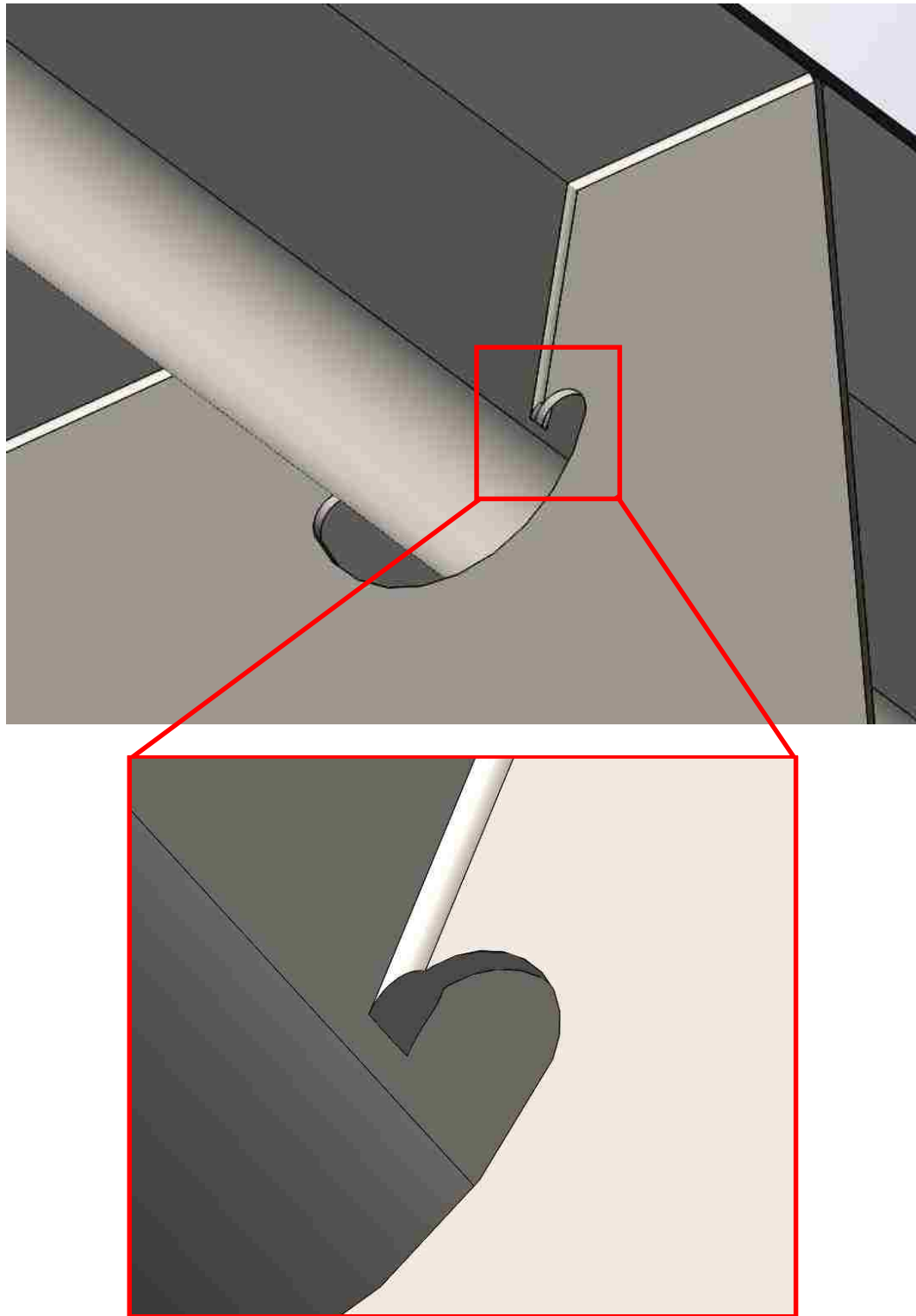


Figure 47 **Type 4B weld detail**

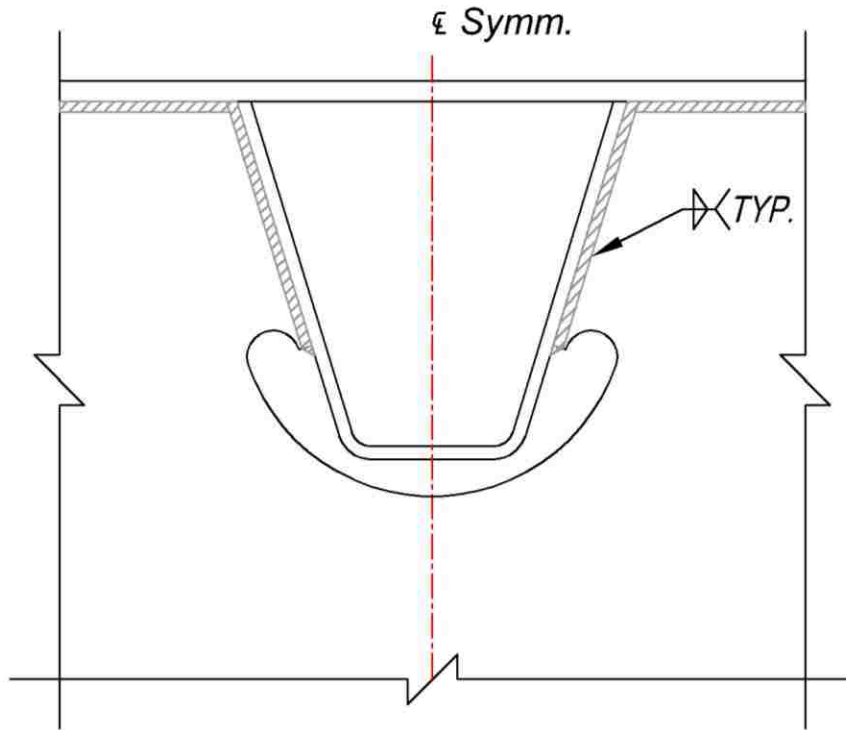


Figure 48 **Type 5A rib-to-floor beam connection**

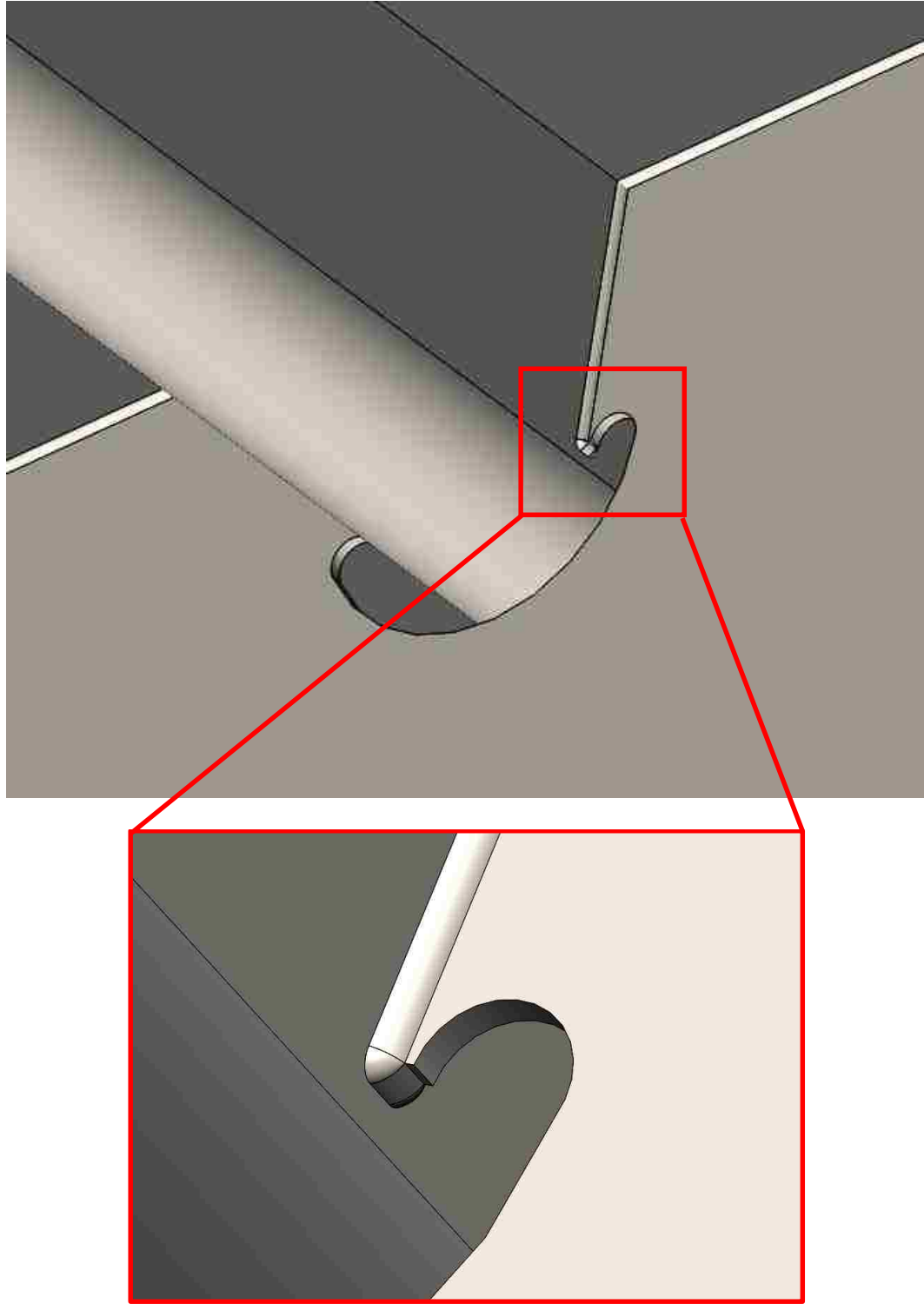


Figure 49 **Type 5B weld detail**

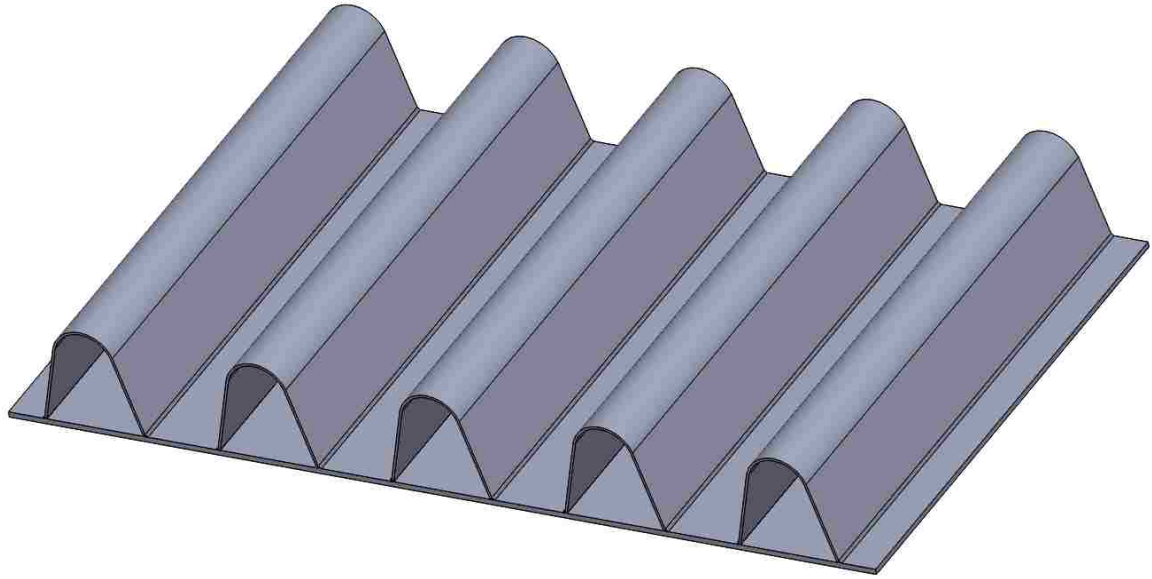


Figure 50 Assembly of ribs and deck plate in the inverted position

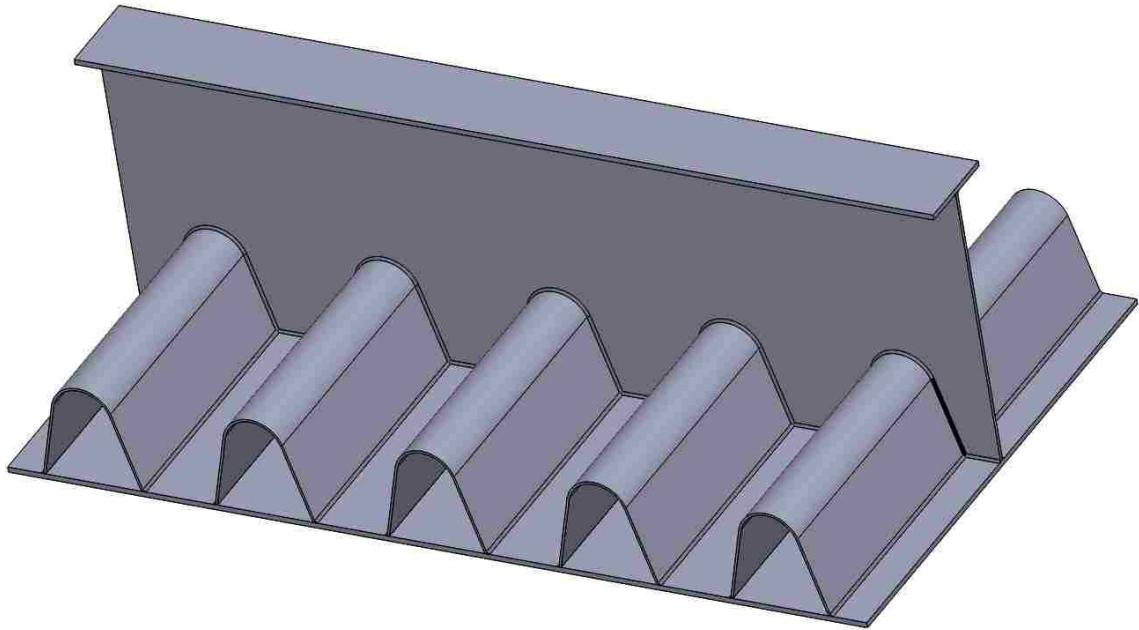


Figure 51 Assembly of floor beam, ribs, and deck plate in the inverted position

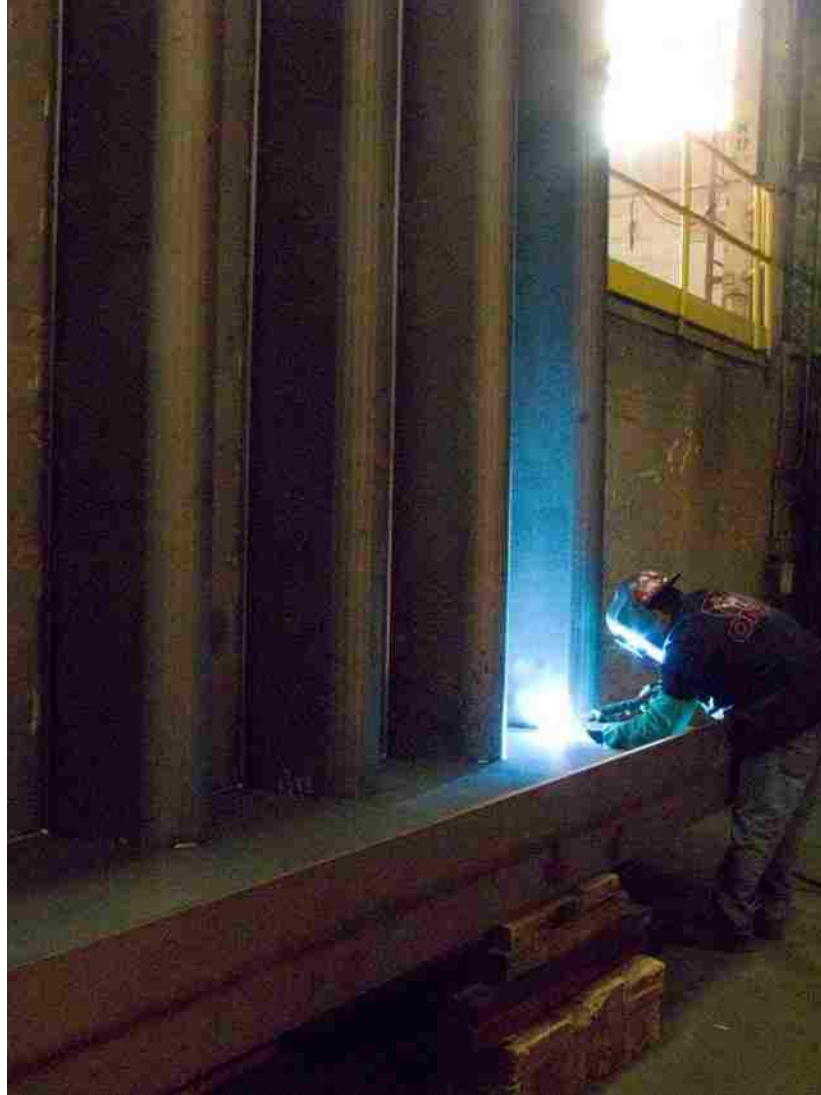


Figure 52 Manual welding rib-to-floor beam connection (reproduced from Mukherjee 2016)

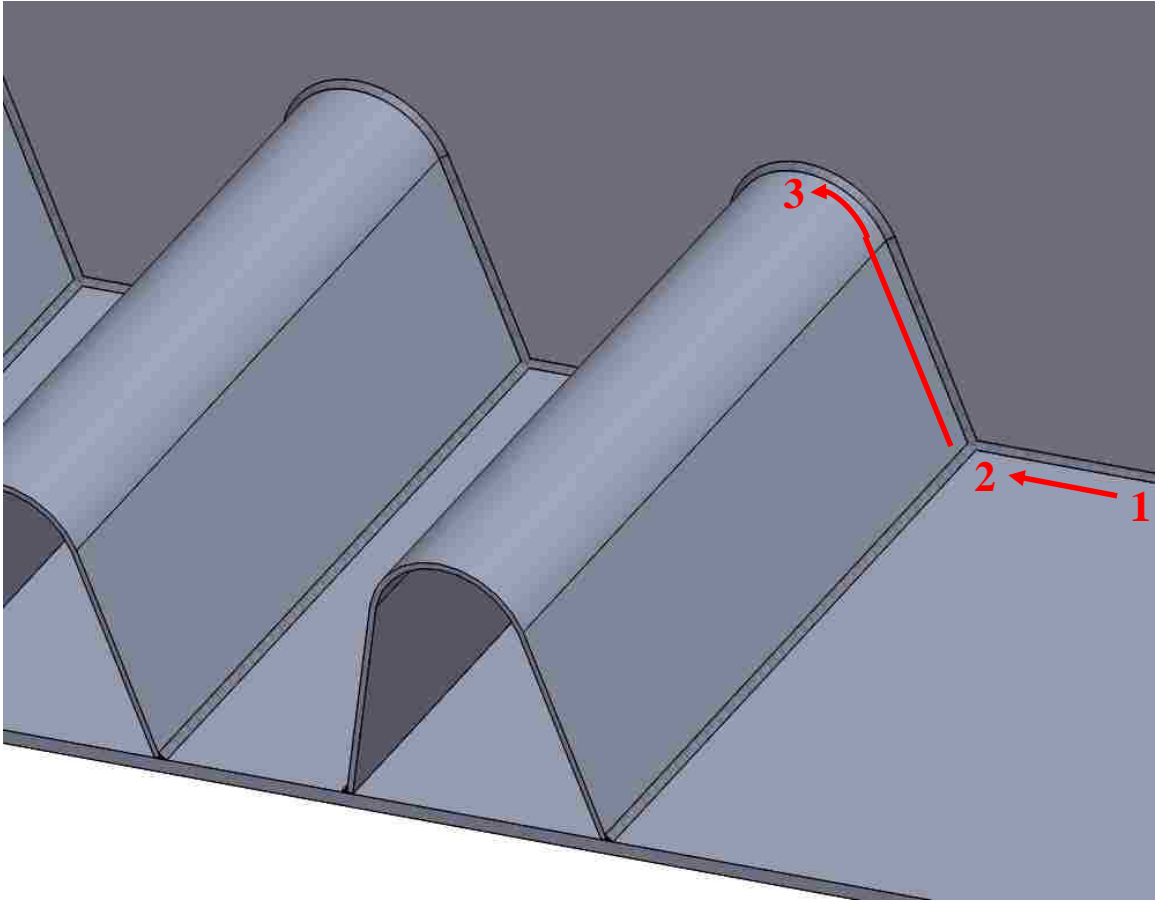


Figure 53 Possible robotic floor beam welding sequence

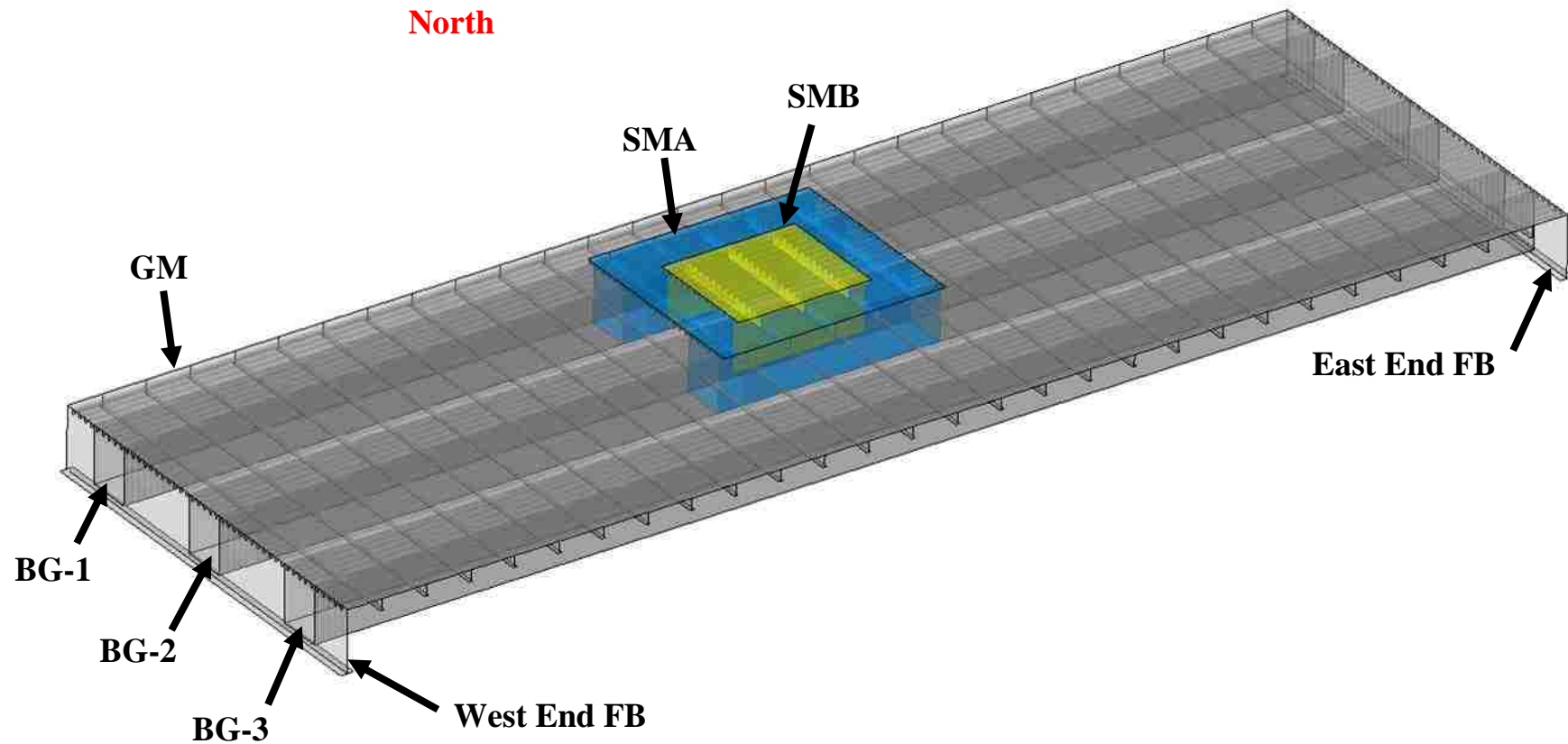


Figure 54 Top view of the Global Model showing extent of Submodel A and Submodel B

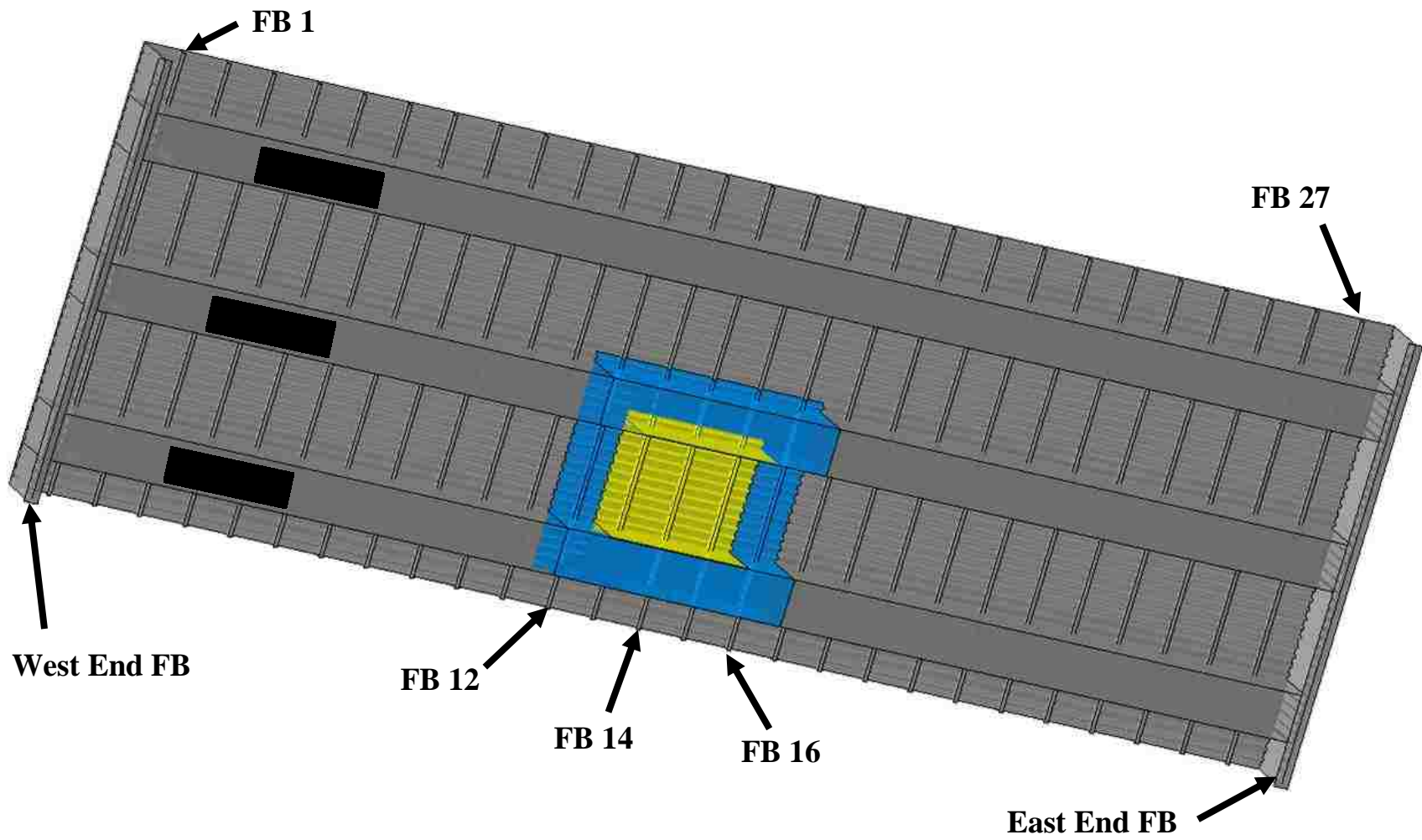


Figure 55 Bottom view of the GM showing extent of Submodel A and Submodel B and global details

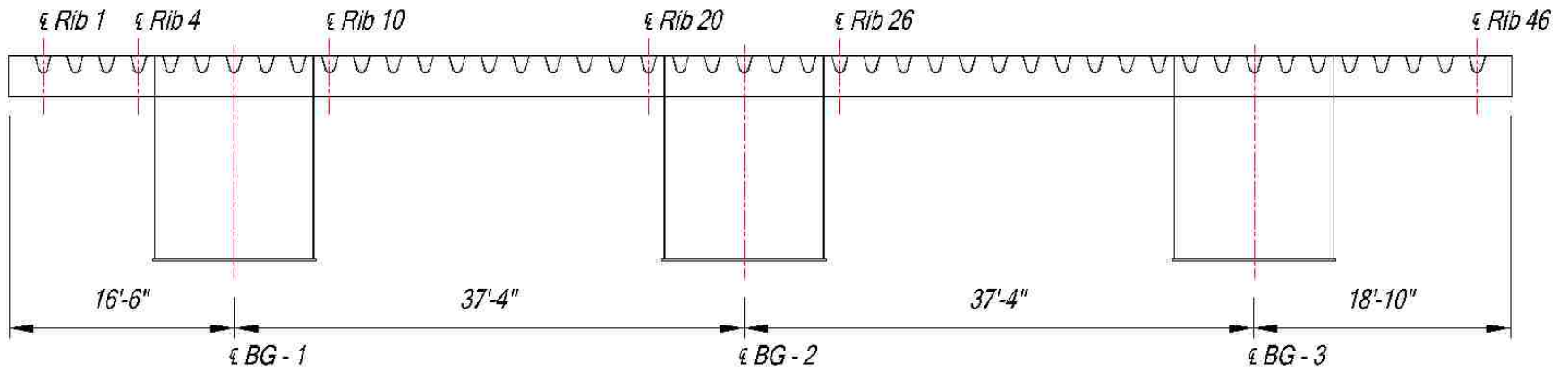


Figure 56 Cross section of the deck (reproduced from Mukherjee 2016)

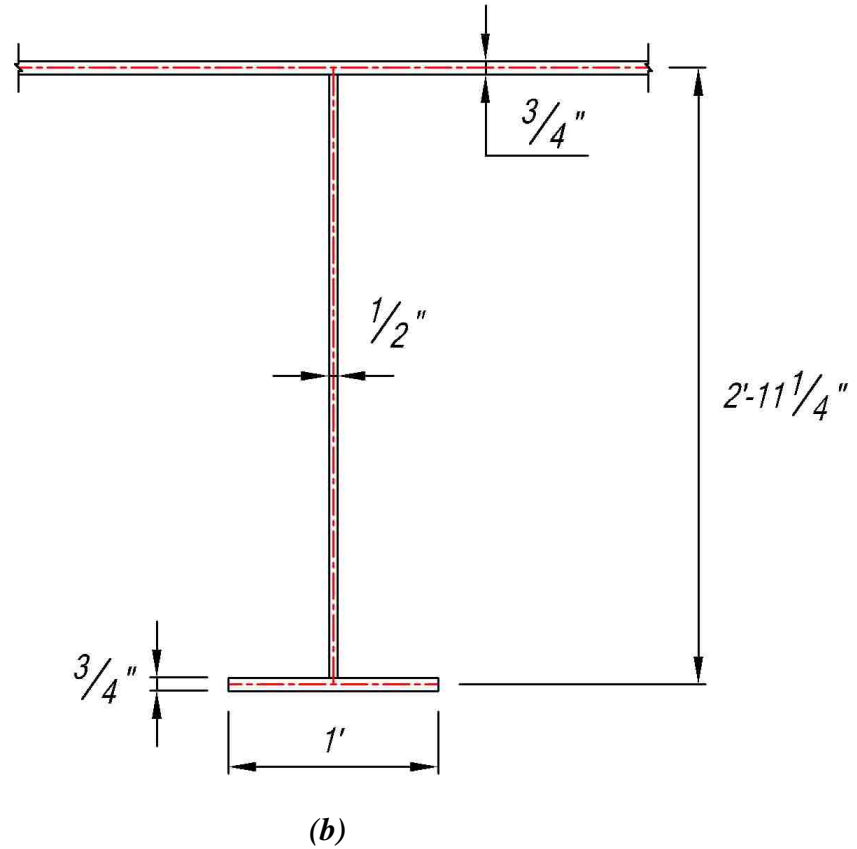
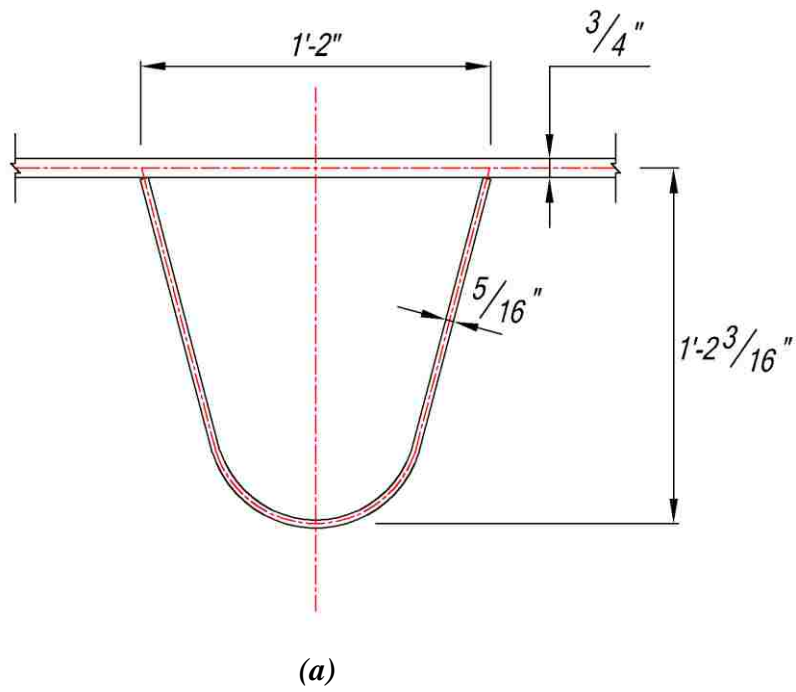


Figure 57 Details of global model: (a) rib; (b) floor beam (reproduced from Mukherjee 2016)

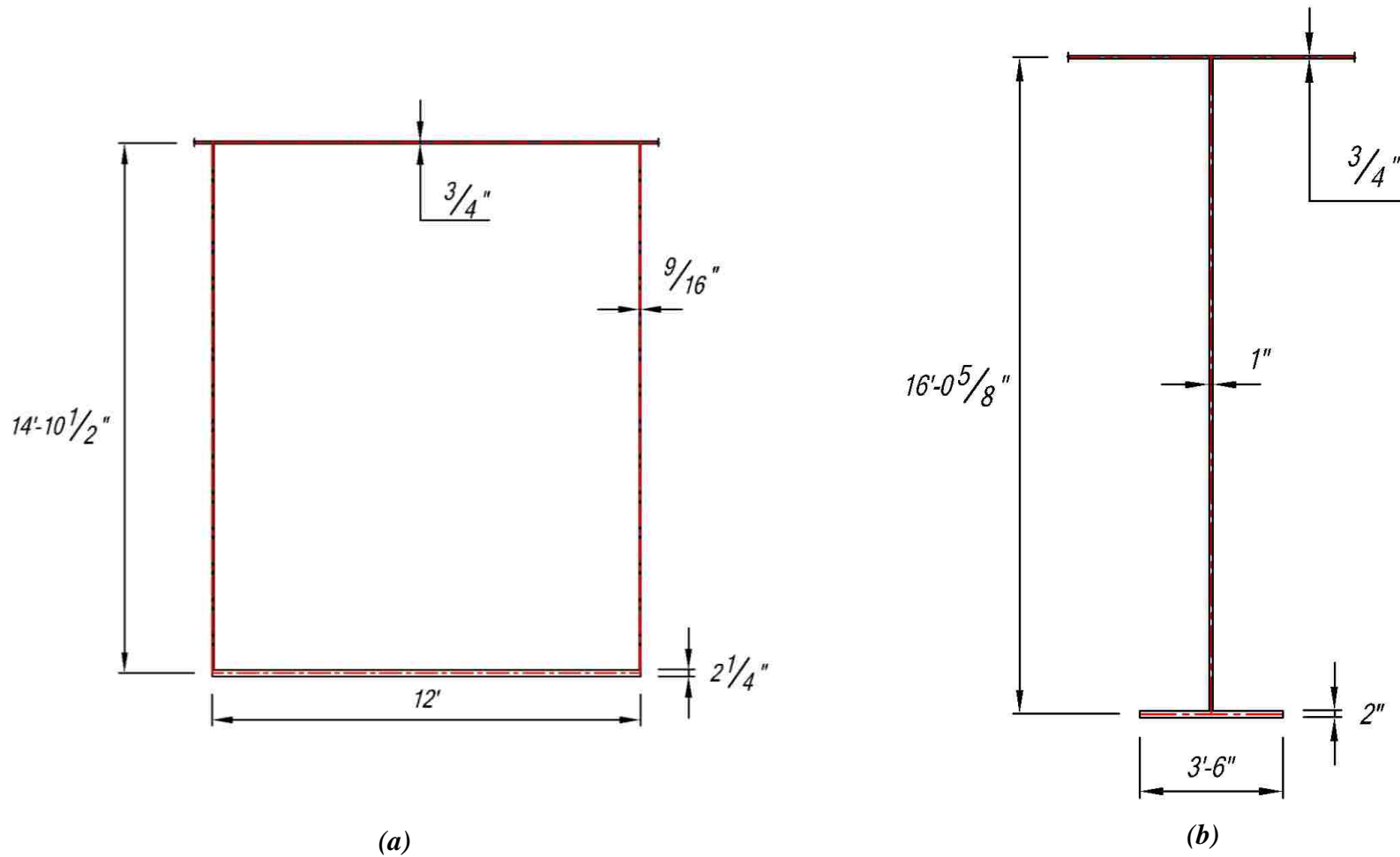


Figure 58 Details of Global Model: (a) Box Girder; (b) End Floor Beam (reproduced from Mukherjee 2016)

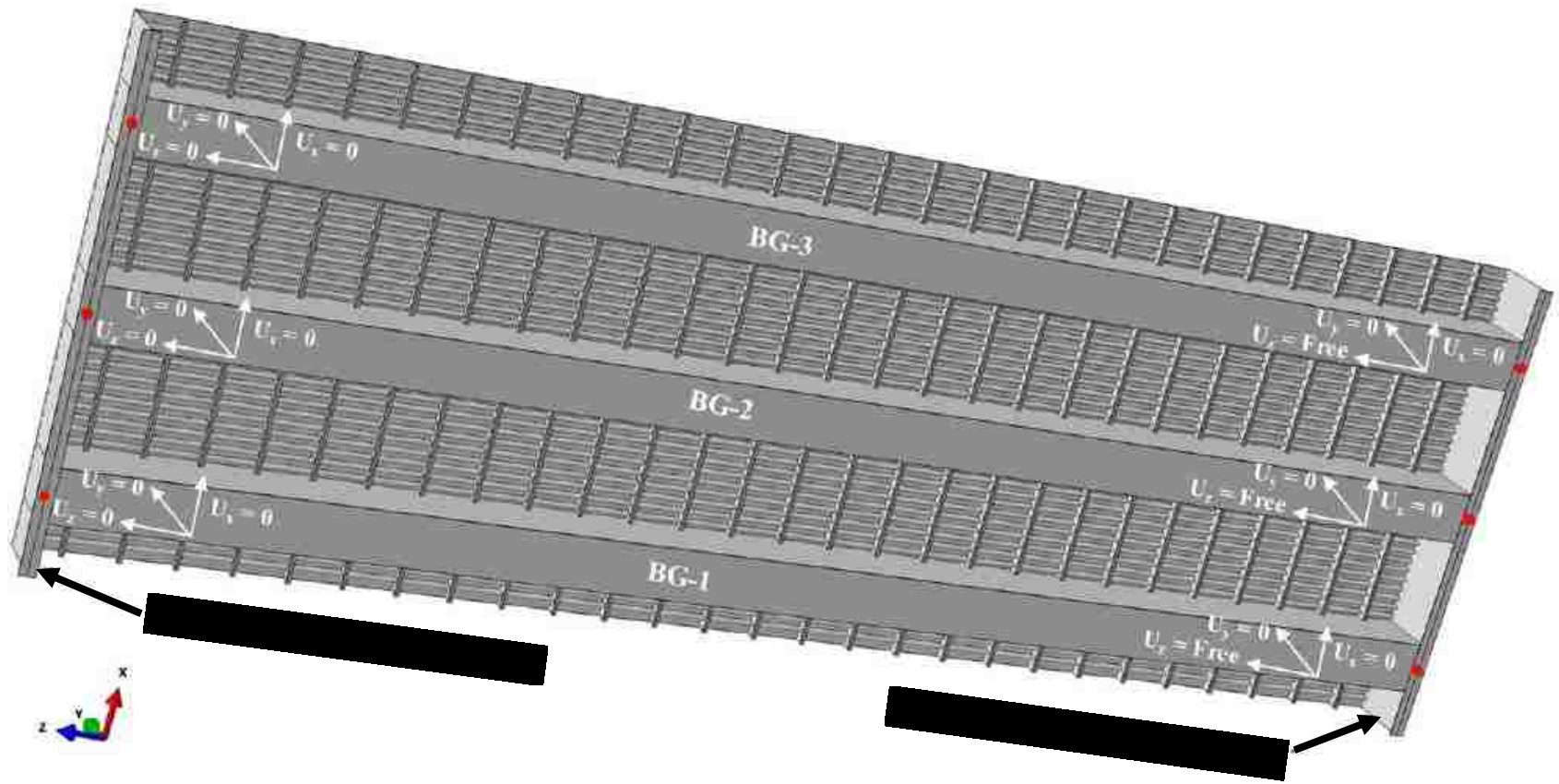


Figure 59 Underside view of the GM showing the boundary conditions specified at the soffit of the end floor beams at locations identified as dots (reproduced Mukherjee 2016)

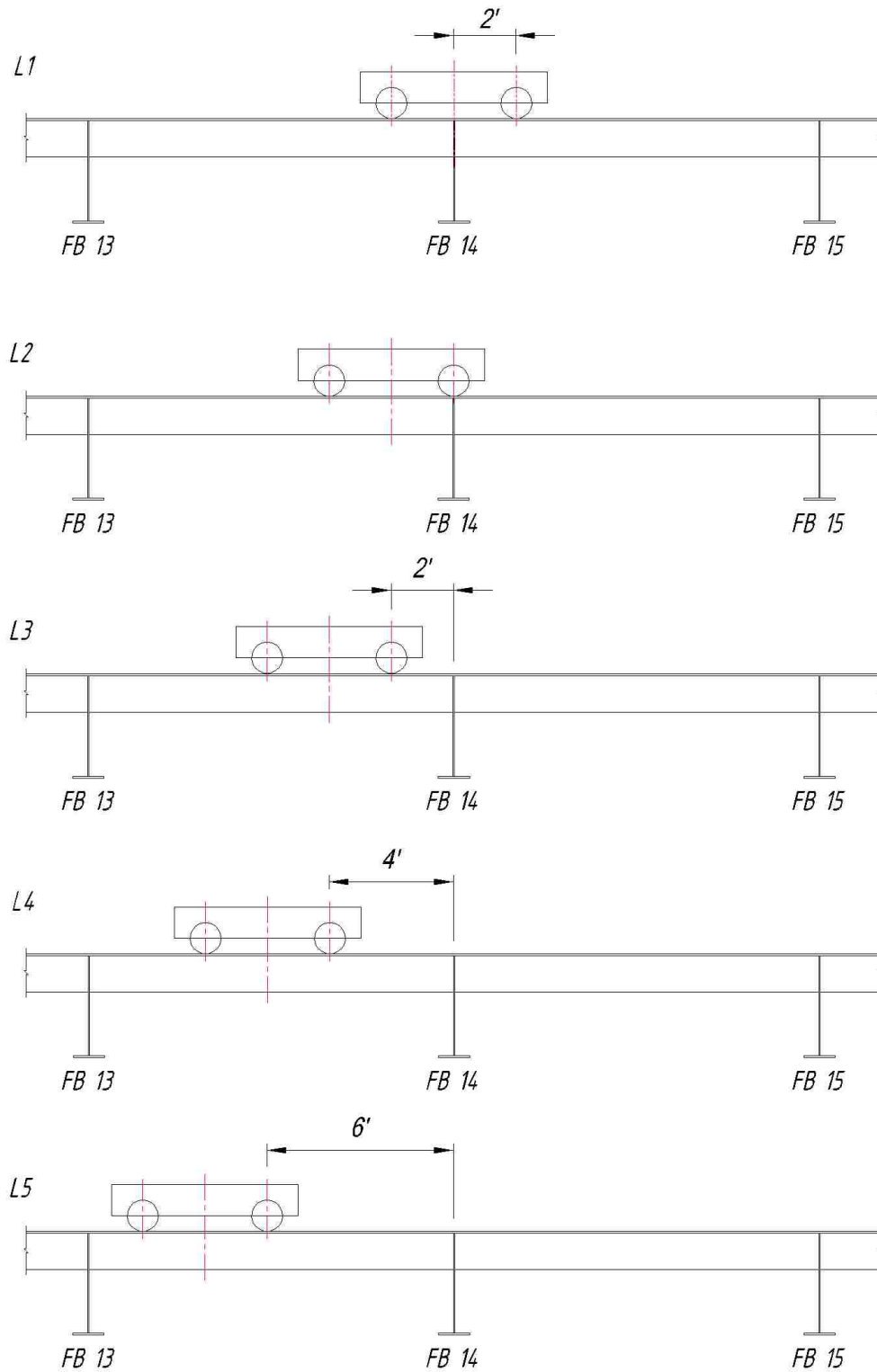


Figure 60 Longitudinal position of AASHTO tandem axles (reproduced from Mukherjee 2016)

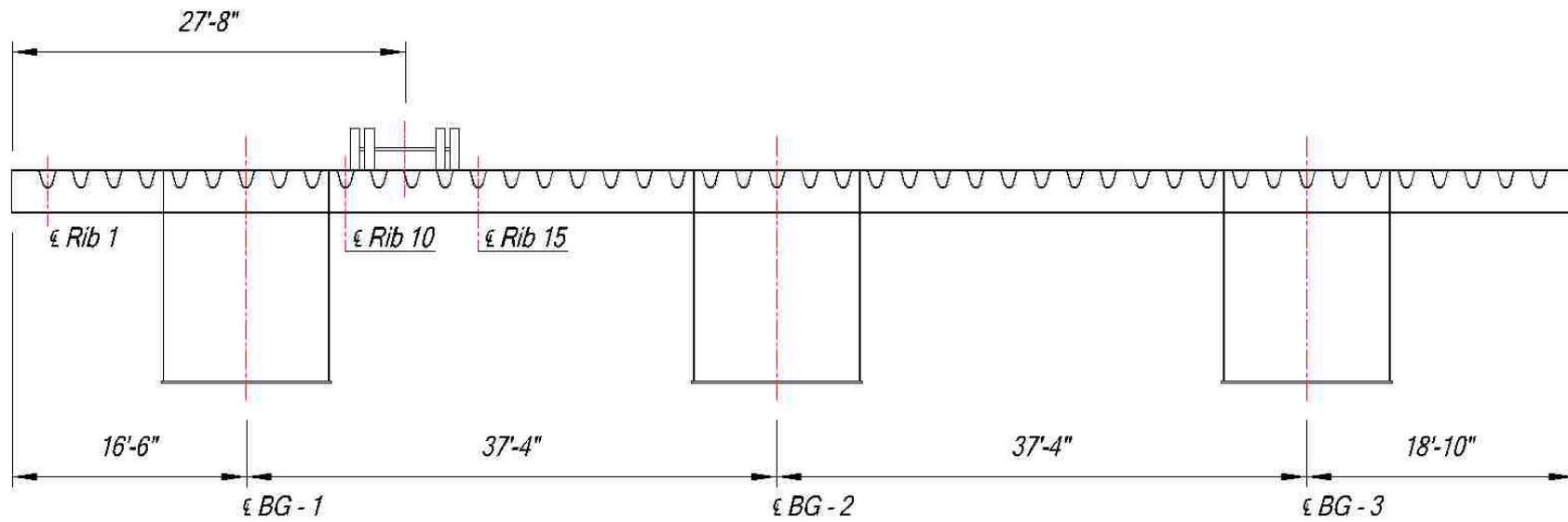


Figure 61 Transverse load position considered for FEA of bridge deck (reproduced from Mukherjee 2016)

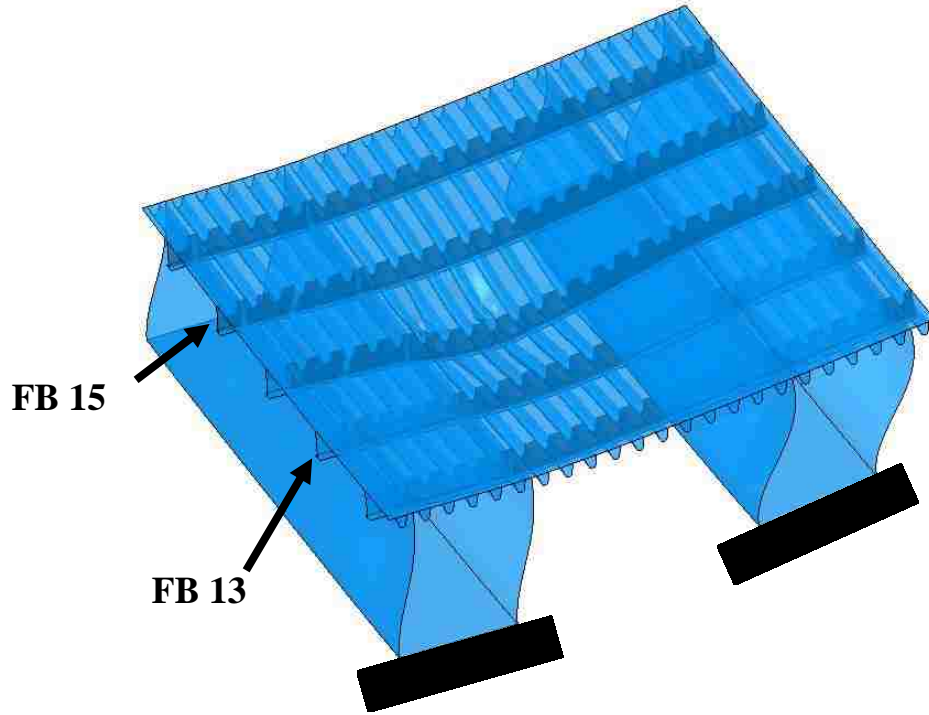


Figure 62 Top view of deformed global model (reproduced from Mukherjee 2016)

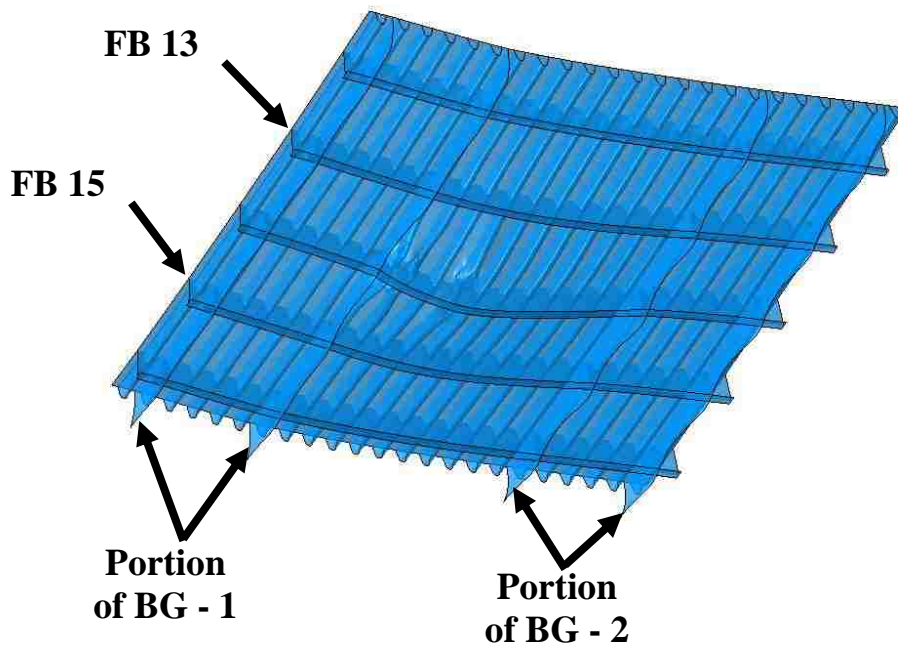


Figure 63 Bottom view of deformed global model (reproduced from Mukherjee 2016)

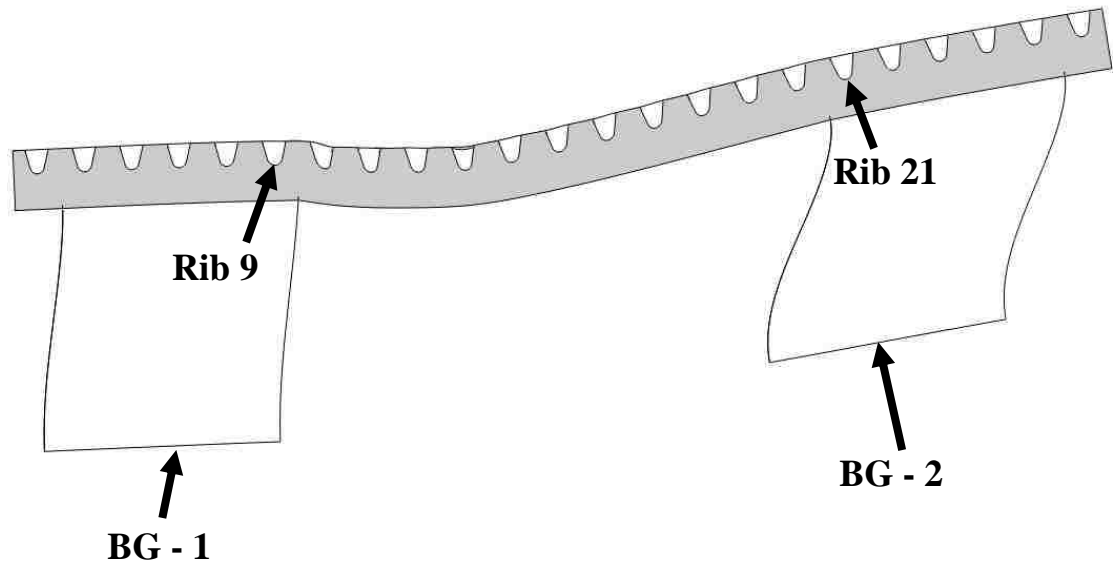


Figure 64 Deformed global model due to critical load position (reproduced from Mukherjee 2016)

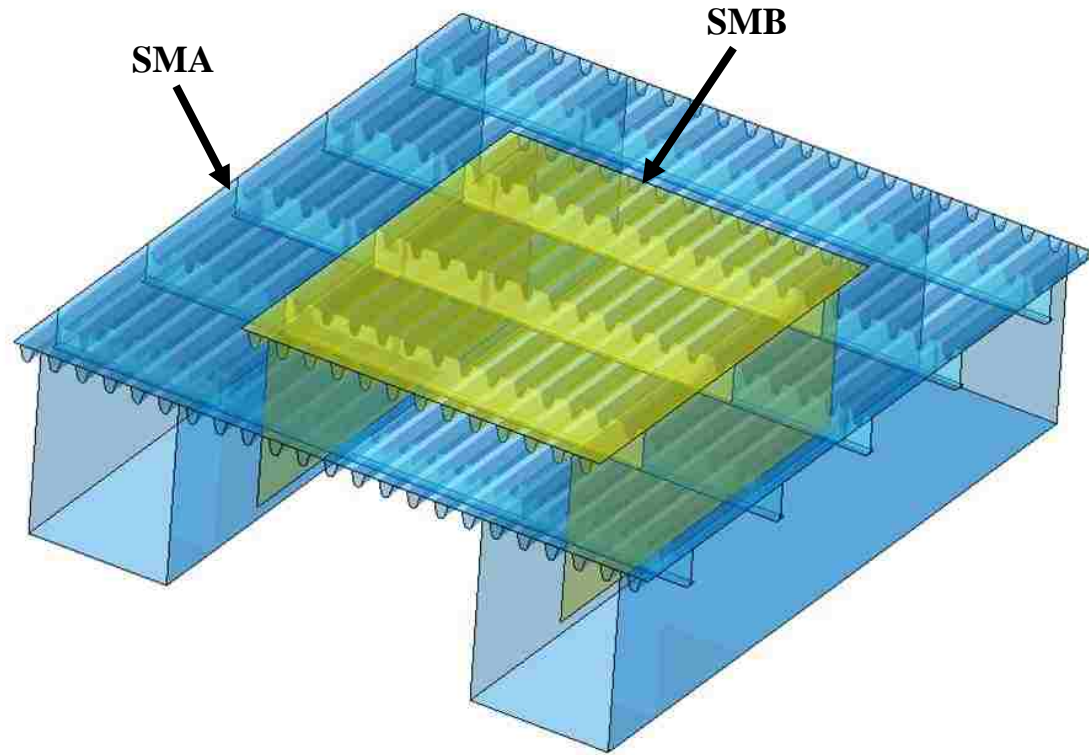


Figure 65 Top view showing the extent of Submodel A and Submodel B

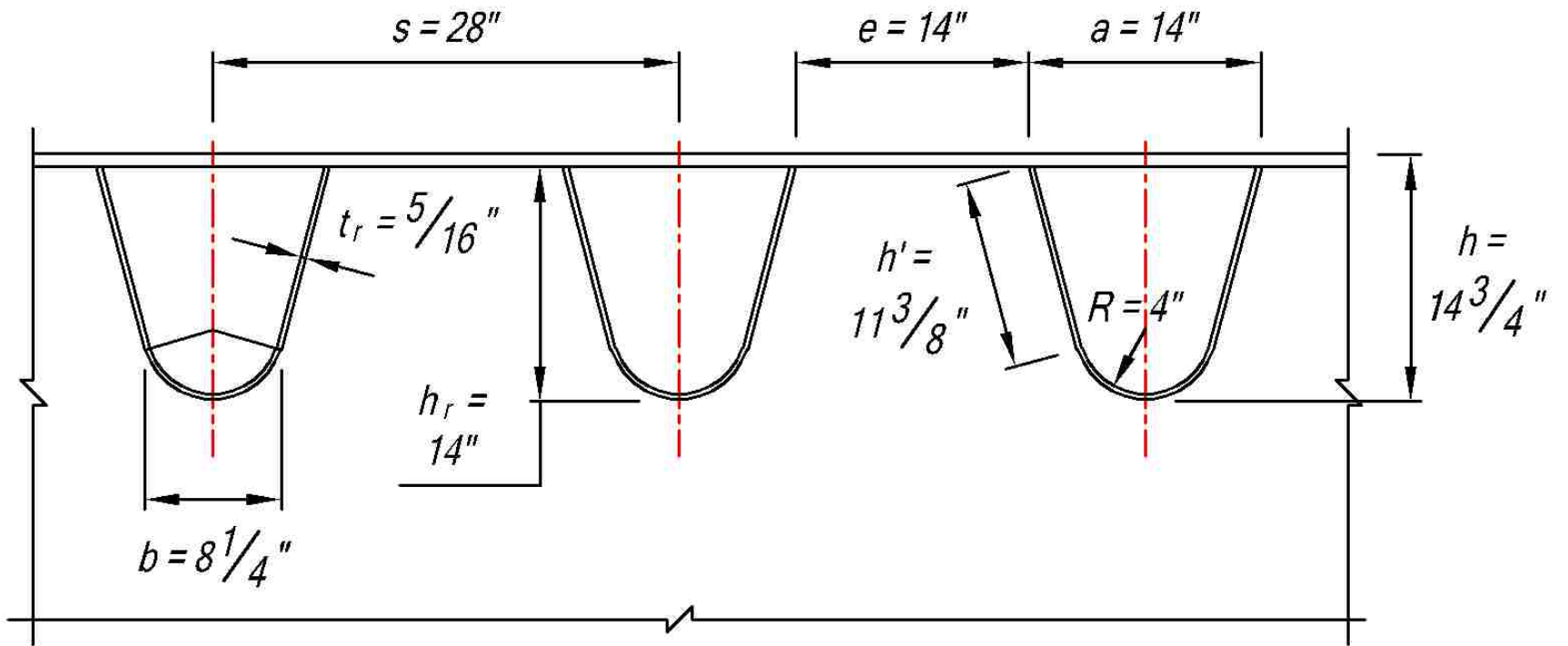


Figure 66 Partial cross section with parameters and dimensions applicable to all submodels

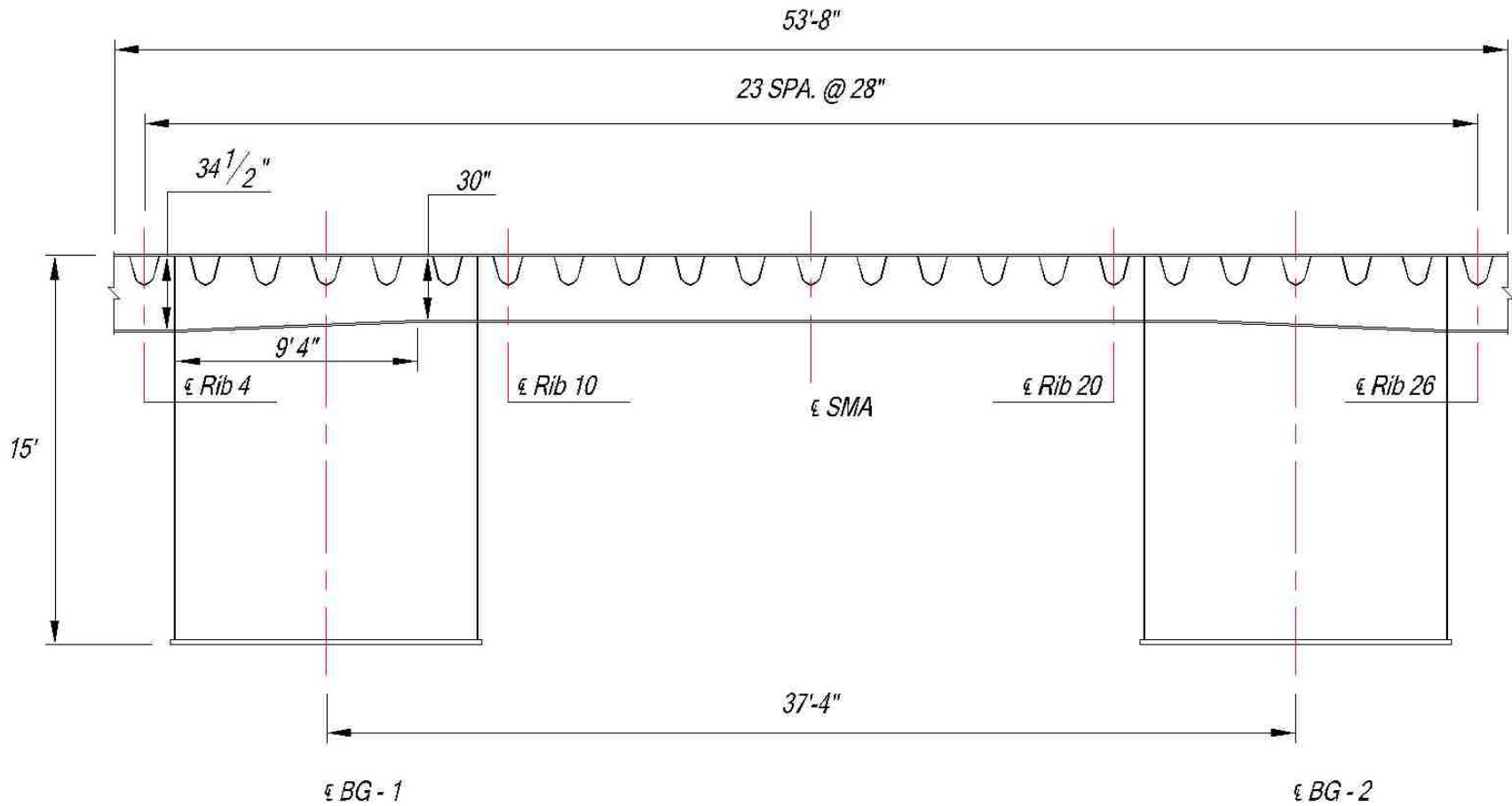


Figure 67 Cross section of Submodel A with floor beam FB2

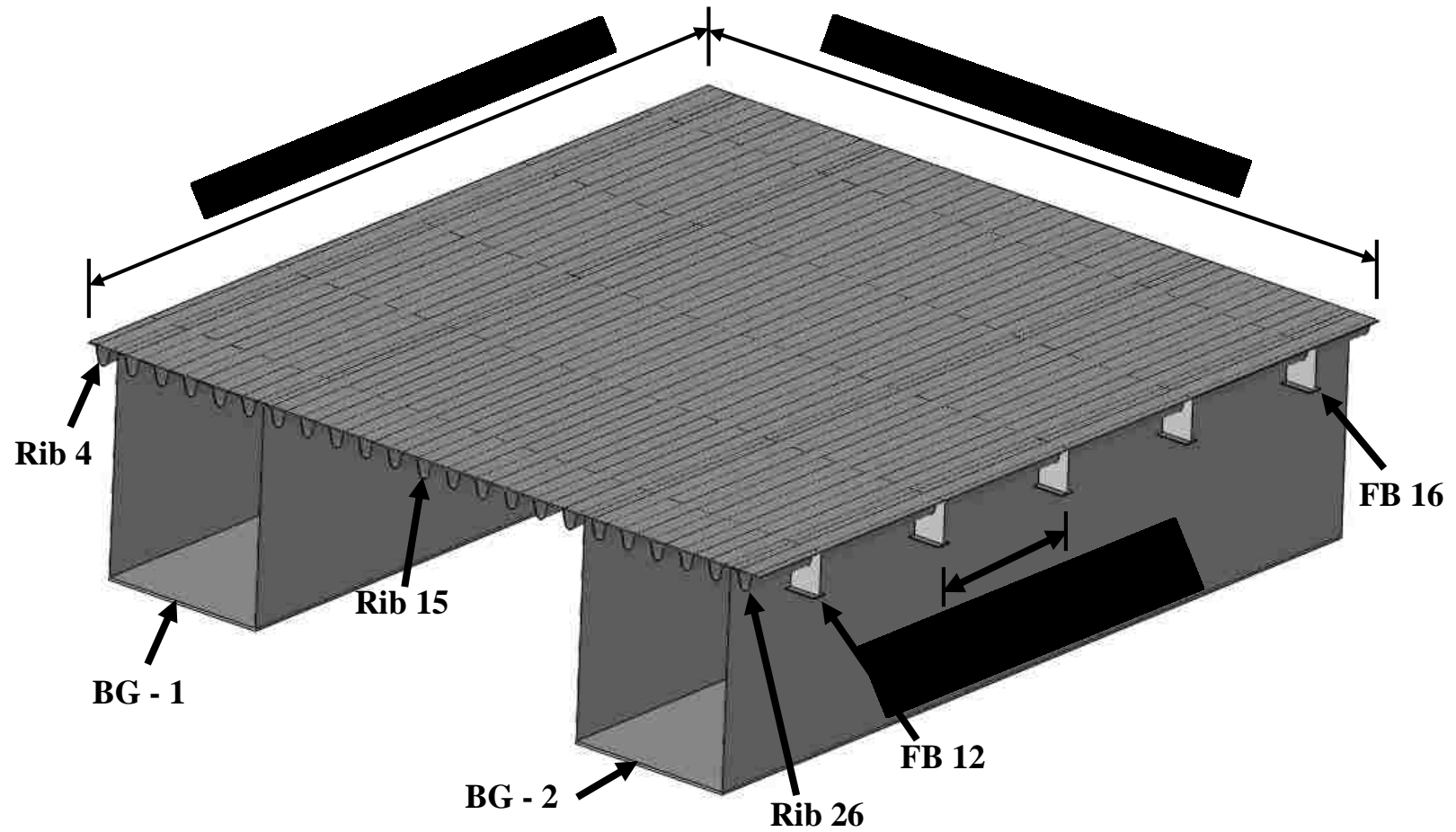


Figure 68 Extent of Submodel A

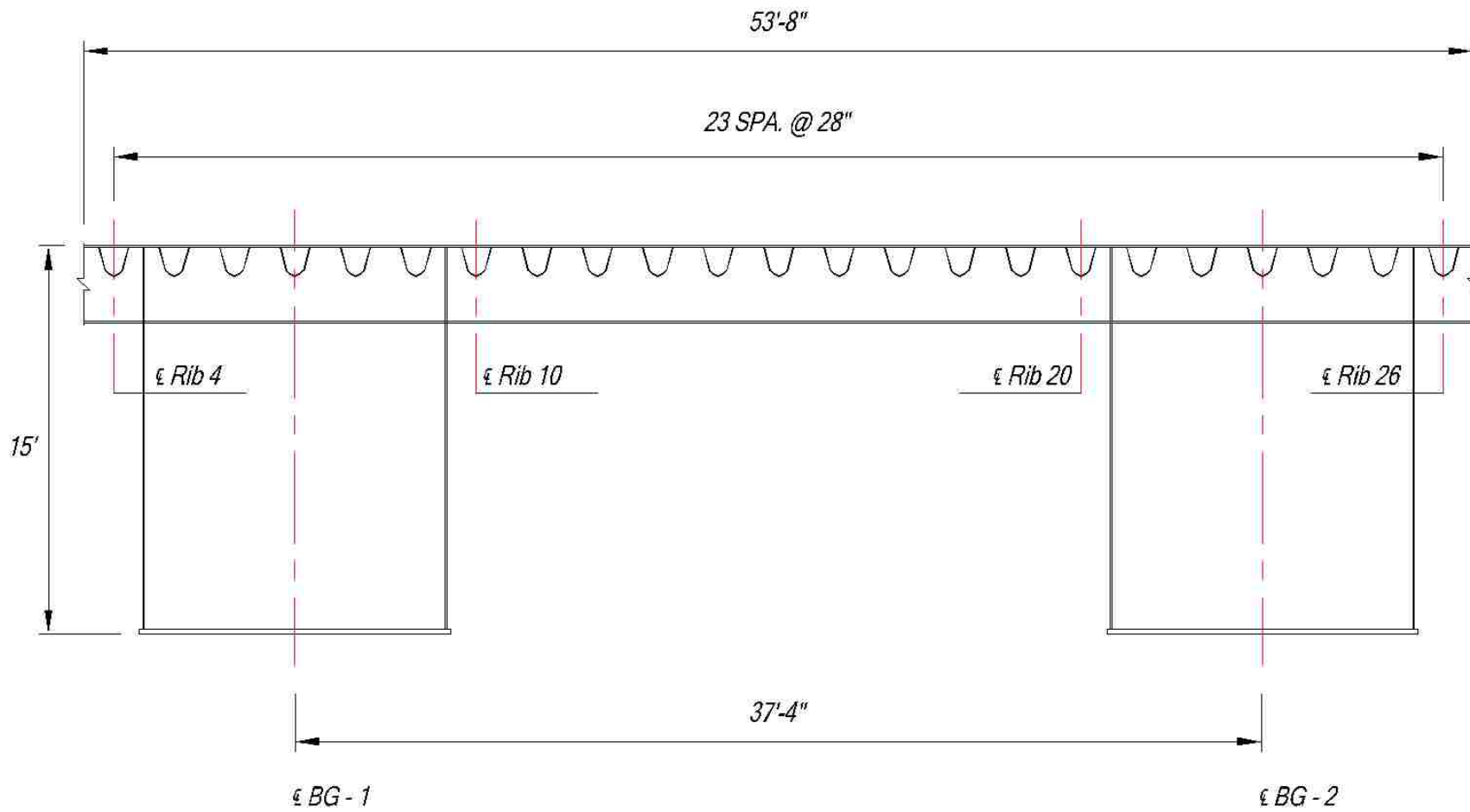


Figure 69 Cross section of Submodel A with floor beam FB1

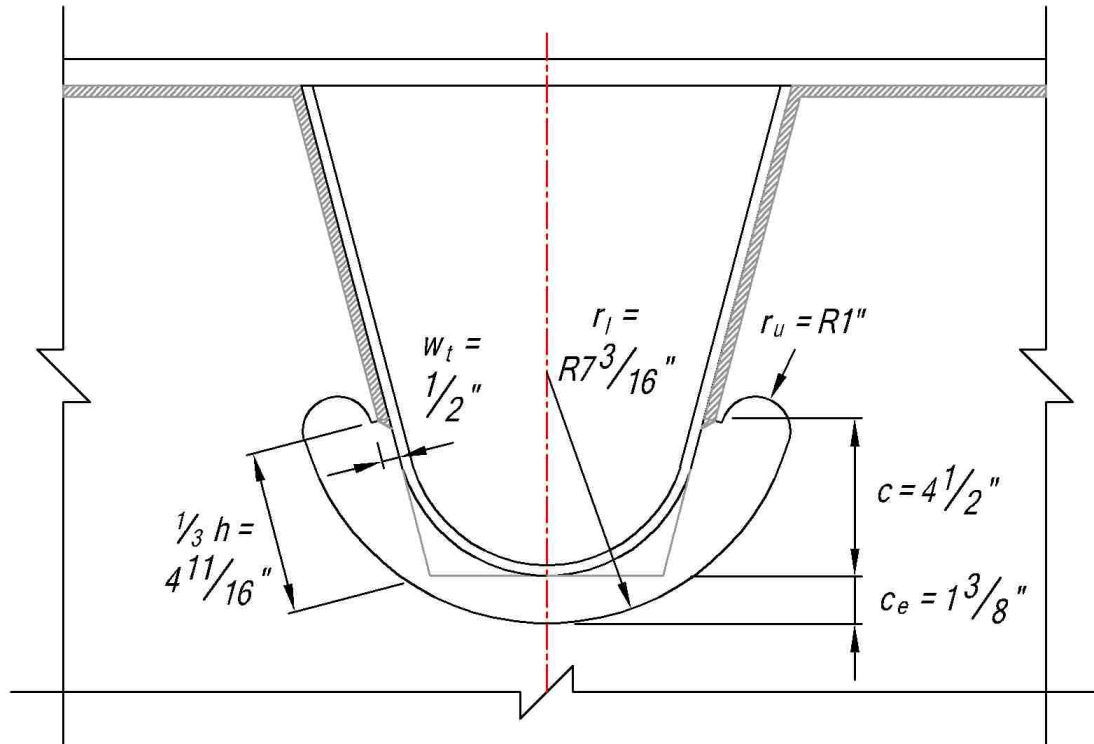


Figure 70 Extended cutout details of connection Type 5B used in FEA

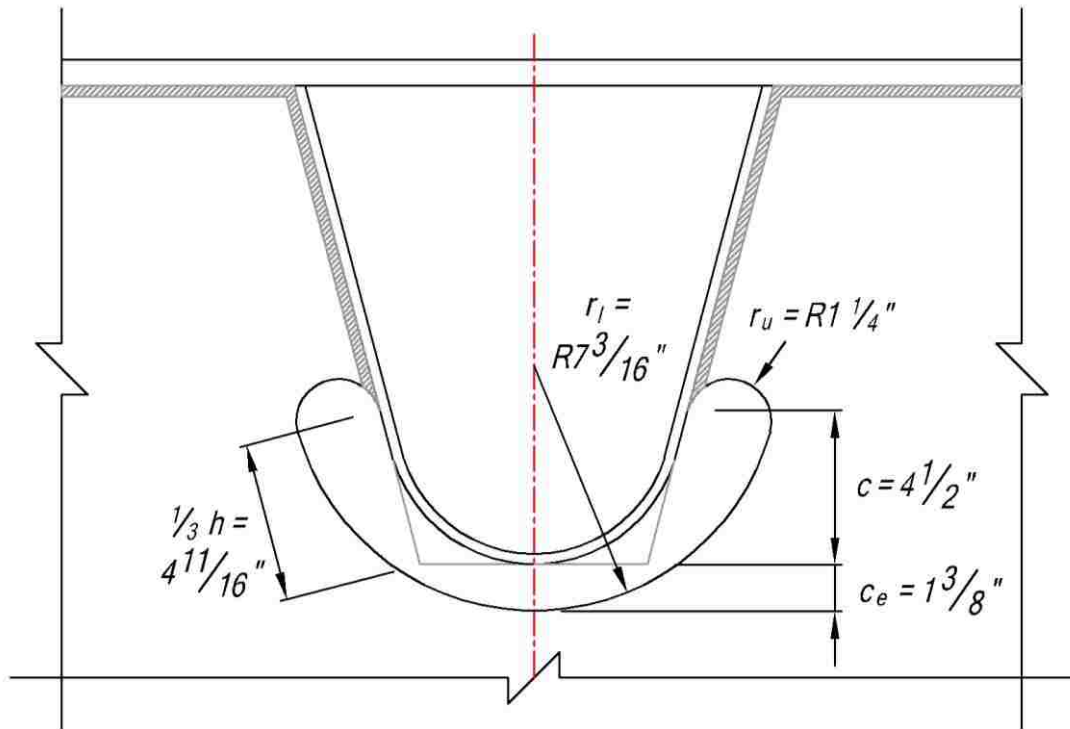


Figure 71 Extended cutout details of connection Type 4B used in FEA

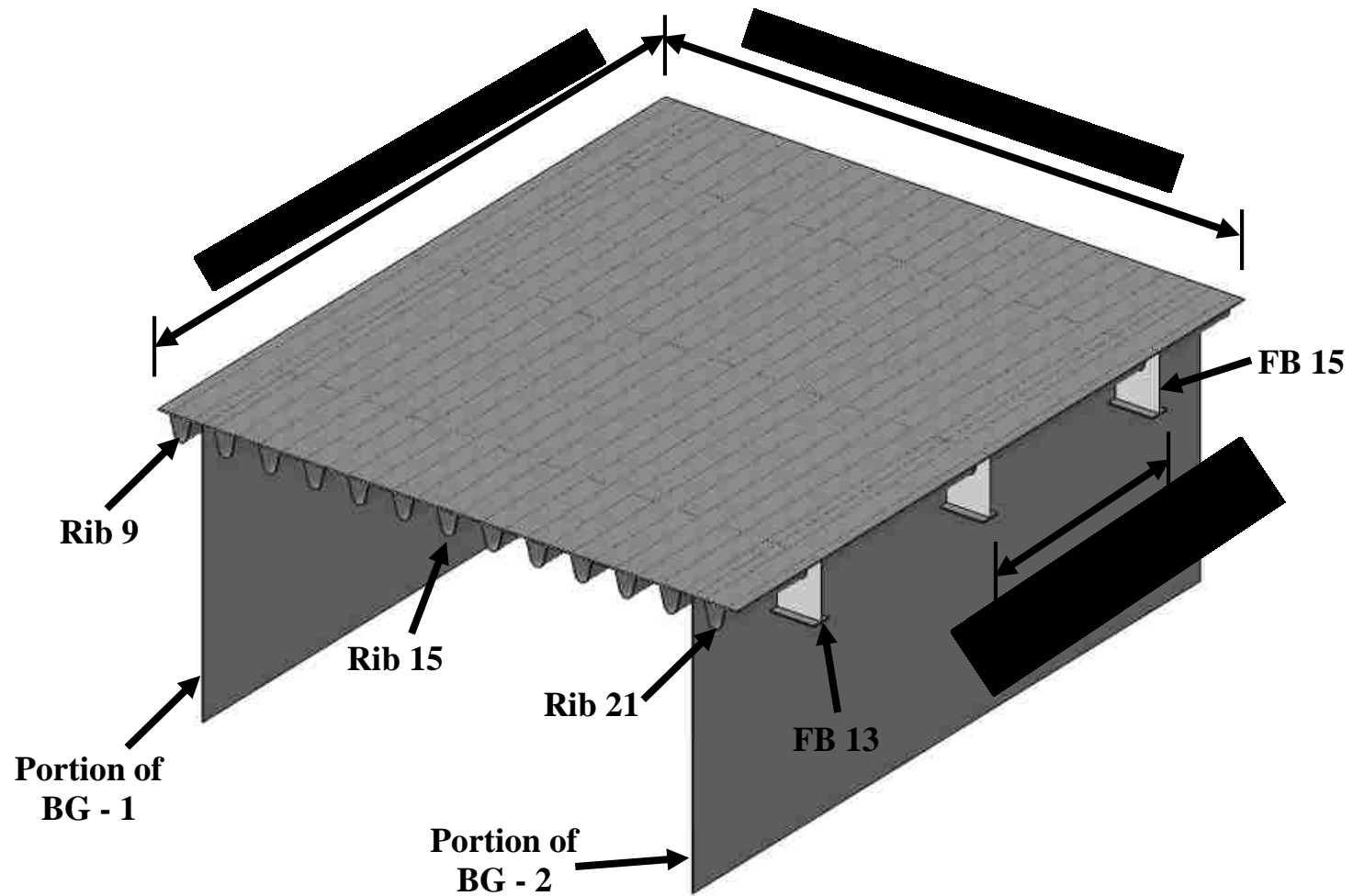


Figure 72 Extent of Submodel B

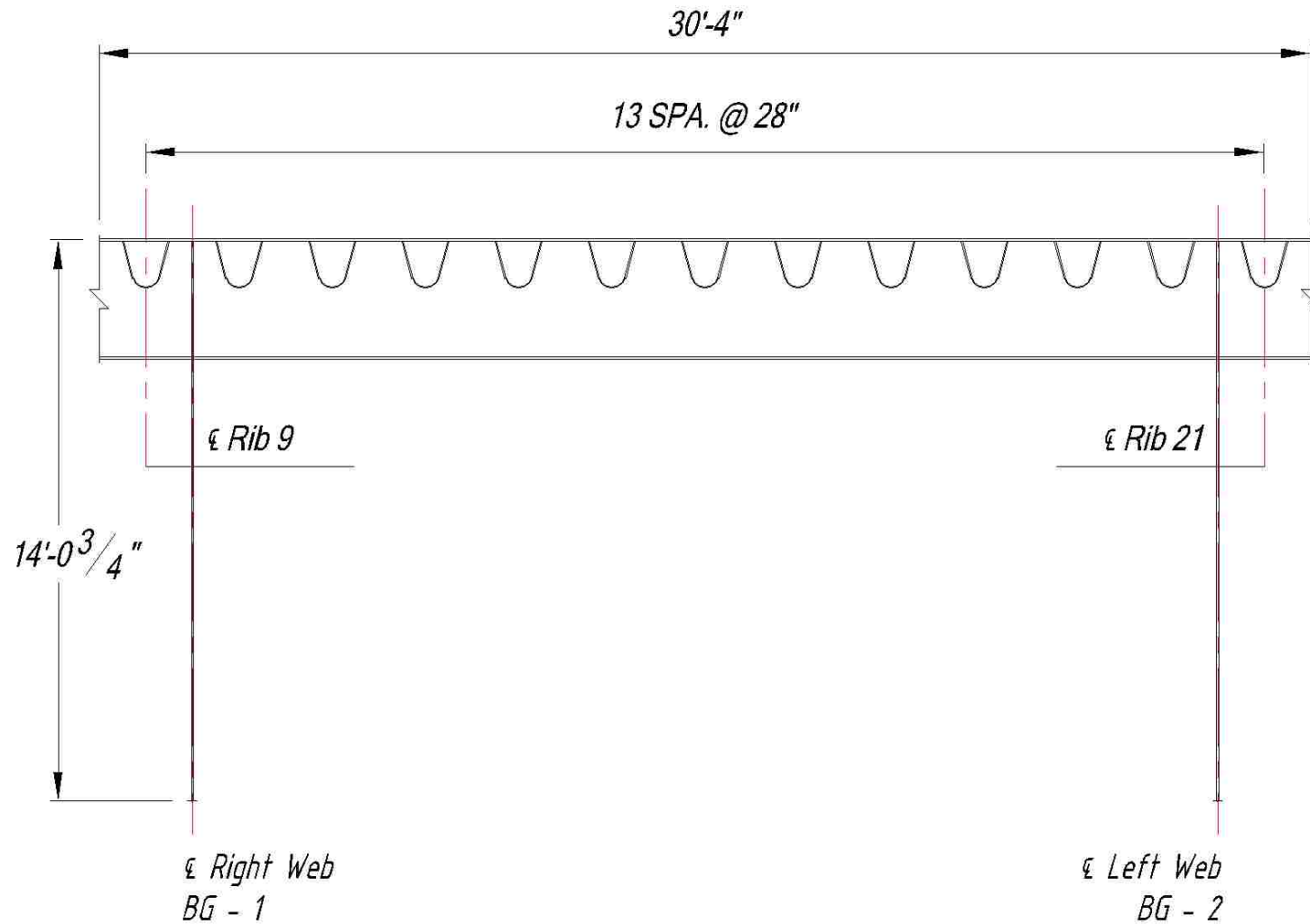


Figure 73 Cross section of Submodel B with connection Type 1B looking east

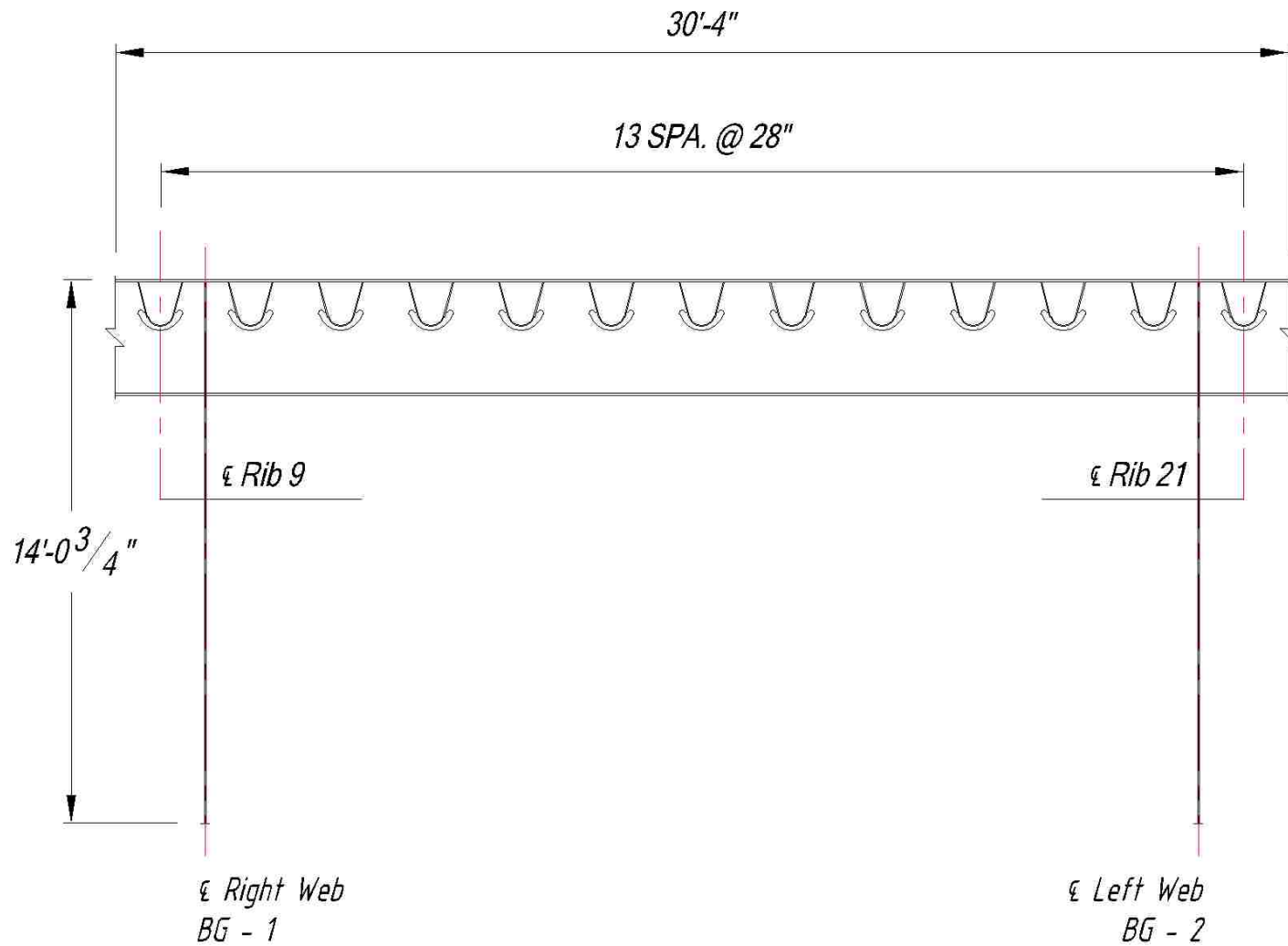


Figure 74 Cross section of Submodel B with connection Type 5B looking east

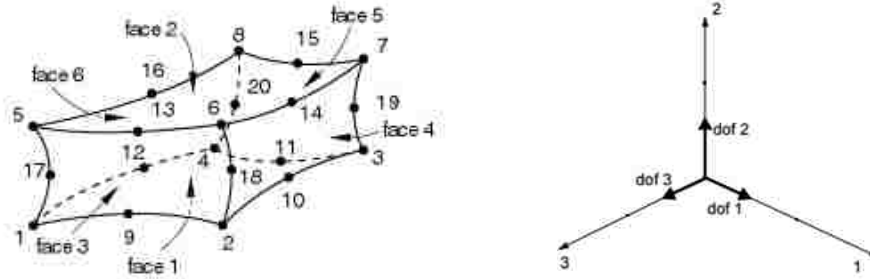


Figure 75 Solid Element, C3D20R, and degrees of freedom (reproduced from Dassault Systemes 2013)

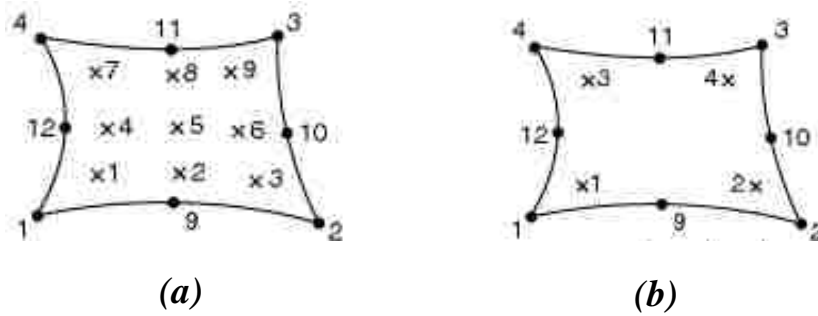


Figure 76 Face of solid element showing DOF and integration points: (a) C3D20; (b) C3D20R (reproduced from Dassault Systemes 2013)

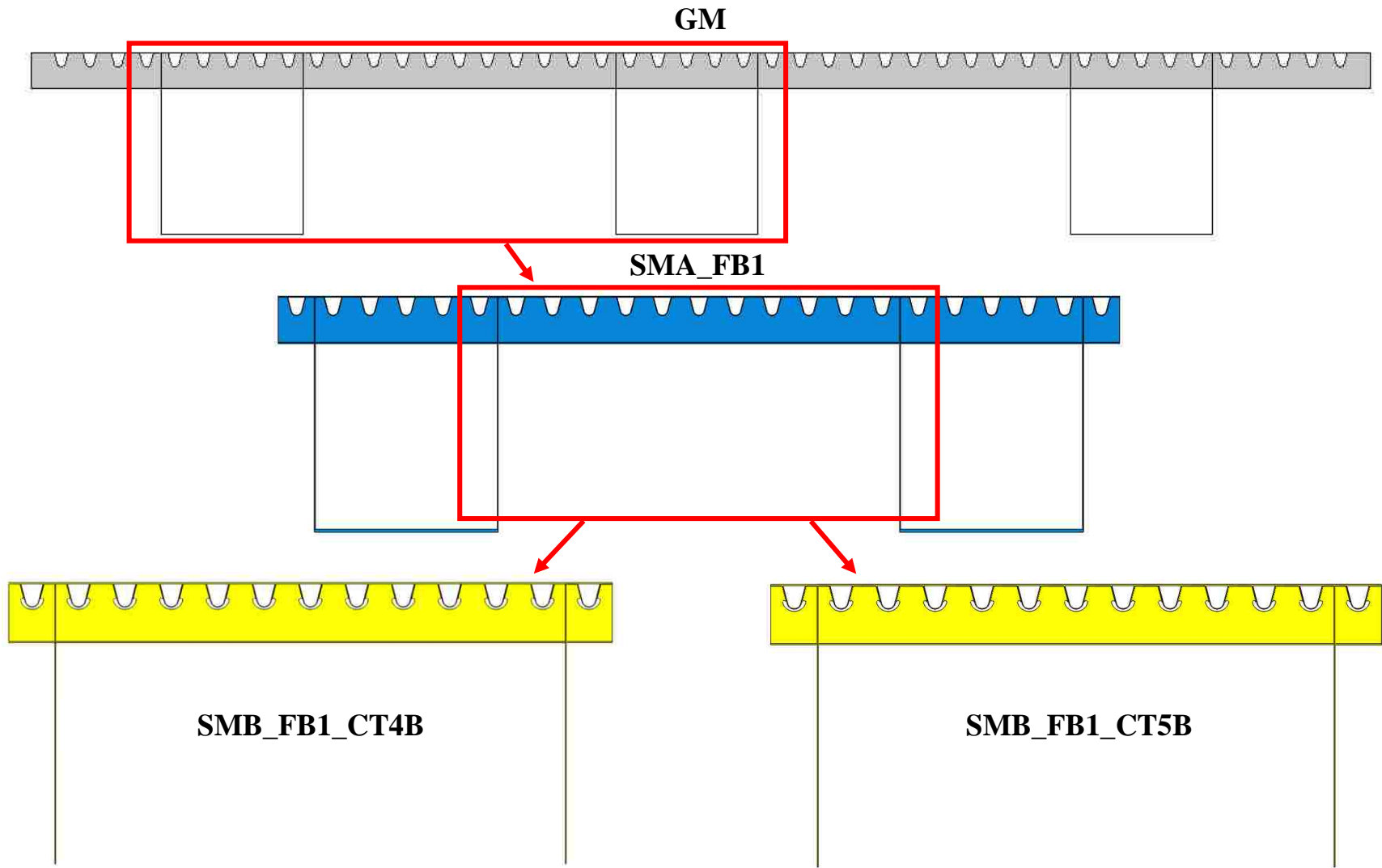


Figure 77 Submodeling progression with floor beam FB1

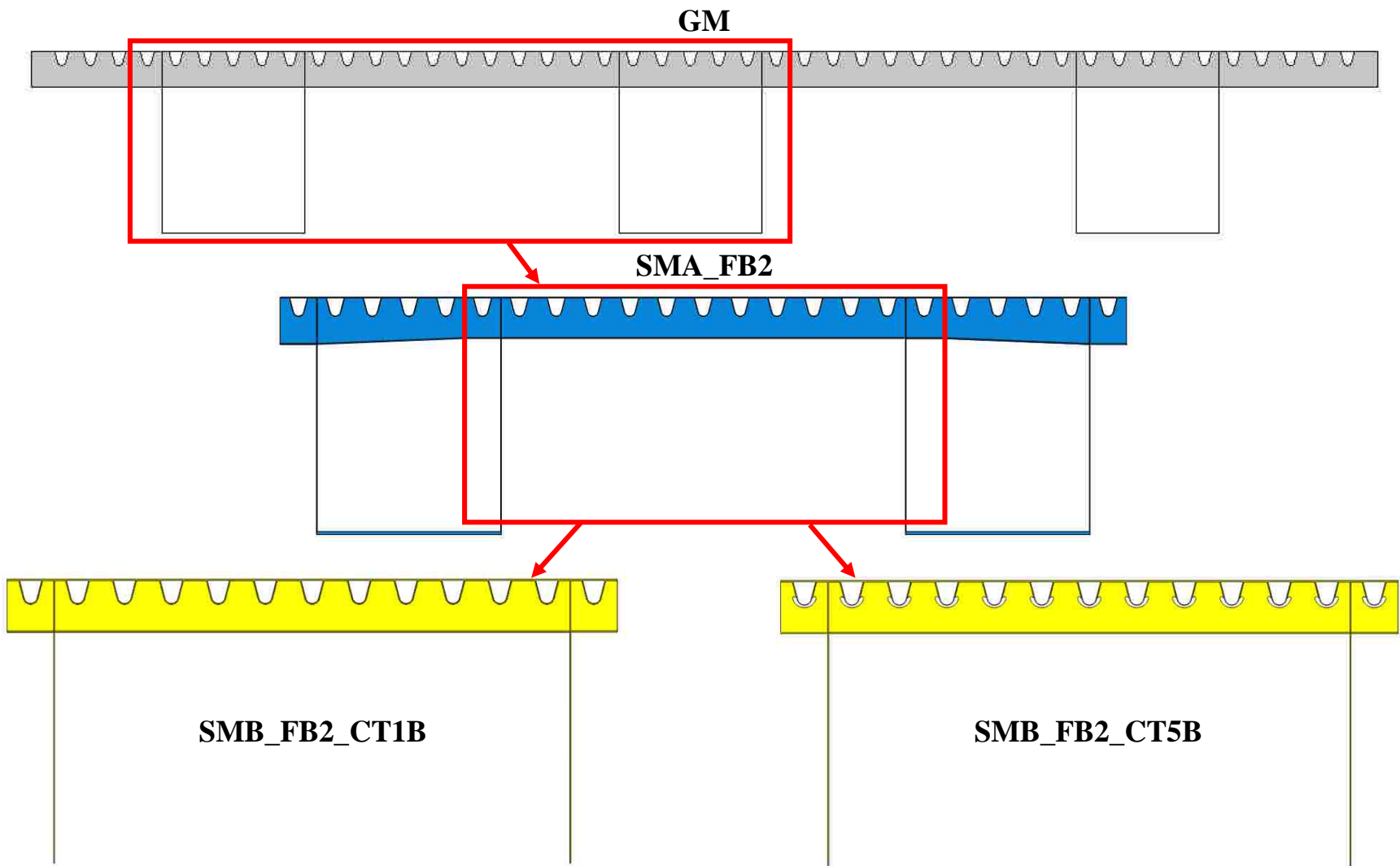


Figure 78 Submodeling progression with floor beam FB2

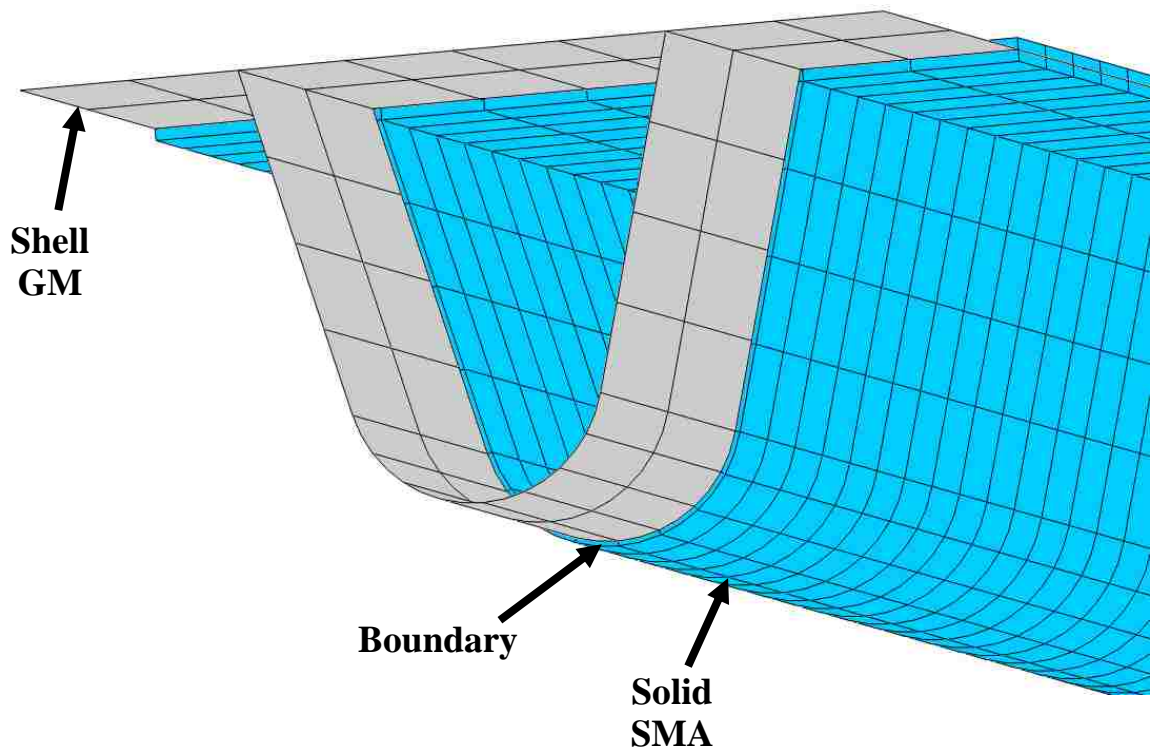


Figure 79 Shell-to-solid submodeling of the Global model to Submodel A

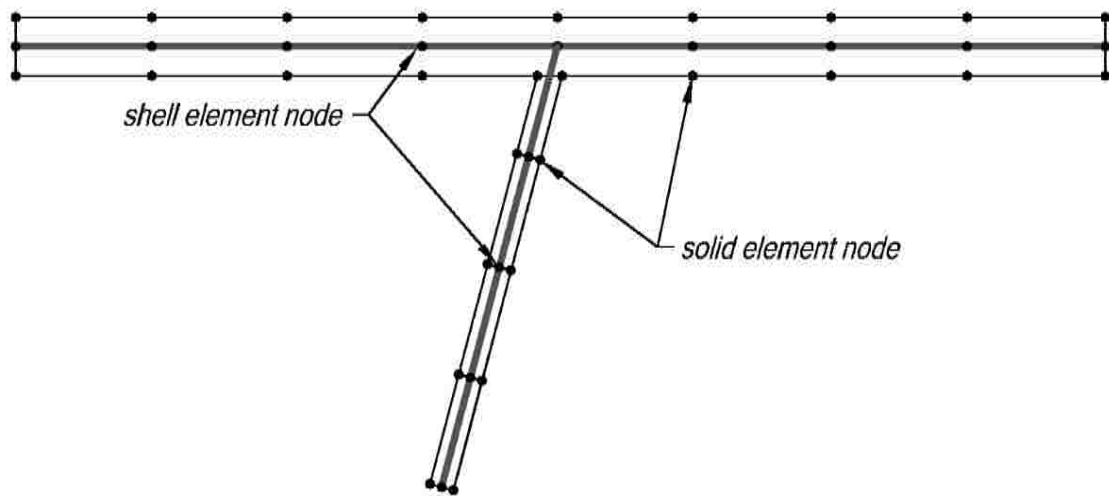


Figure 80 Shell-to-solid submodeling

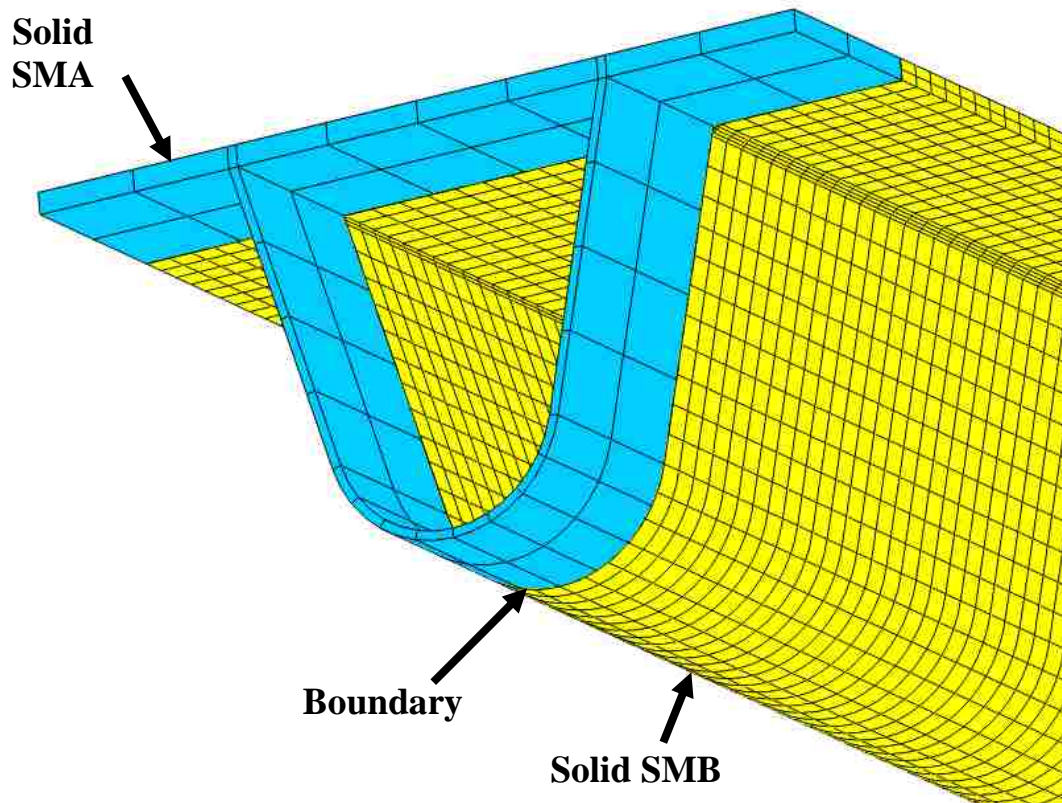


Figure 81 Solid-to-solid submodeling of Submodel A to Submodel B

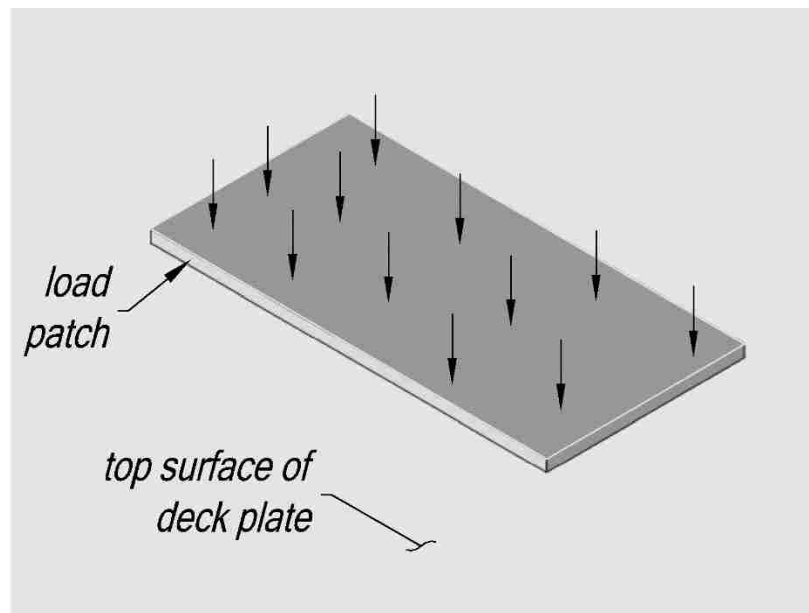


Figure 82 Uniformly distributed load on top surface of load patch

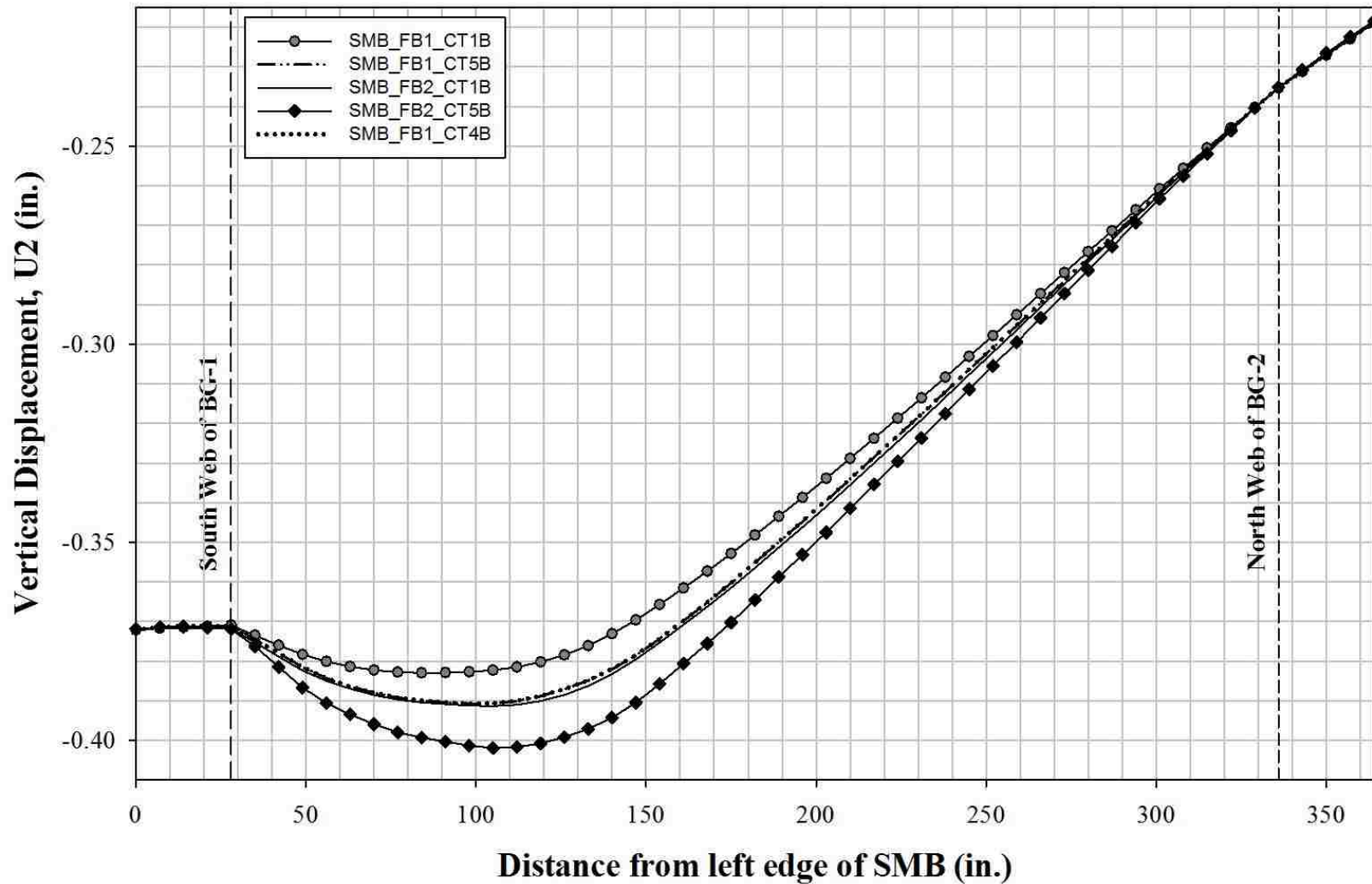


Figure 83 Vertical displacement of floor beam 14 due to symmetric loading (SL)

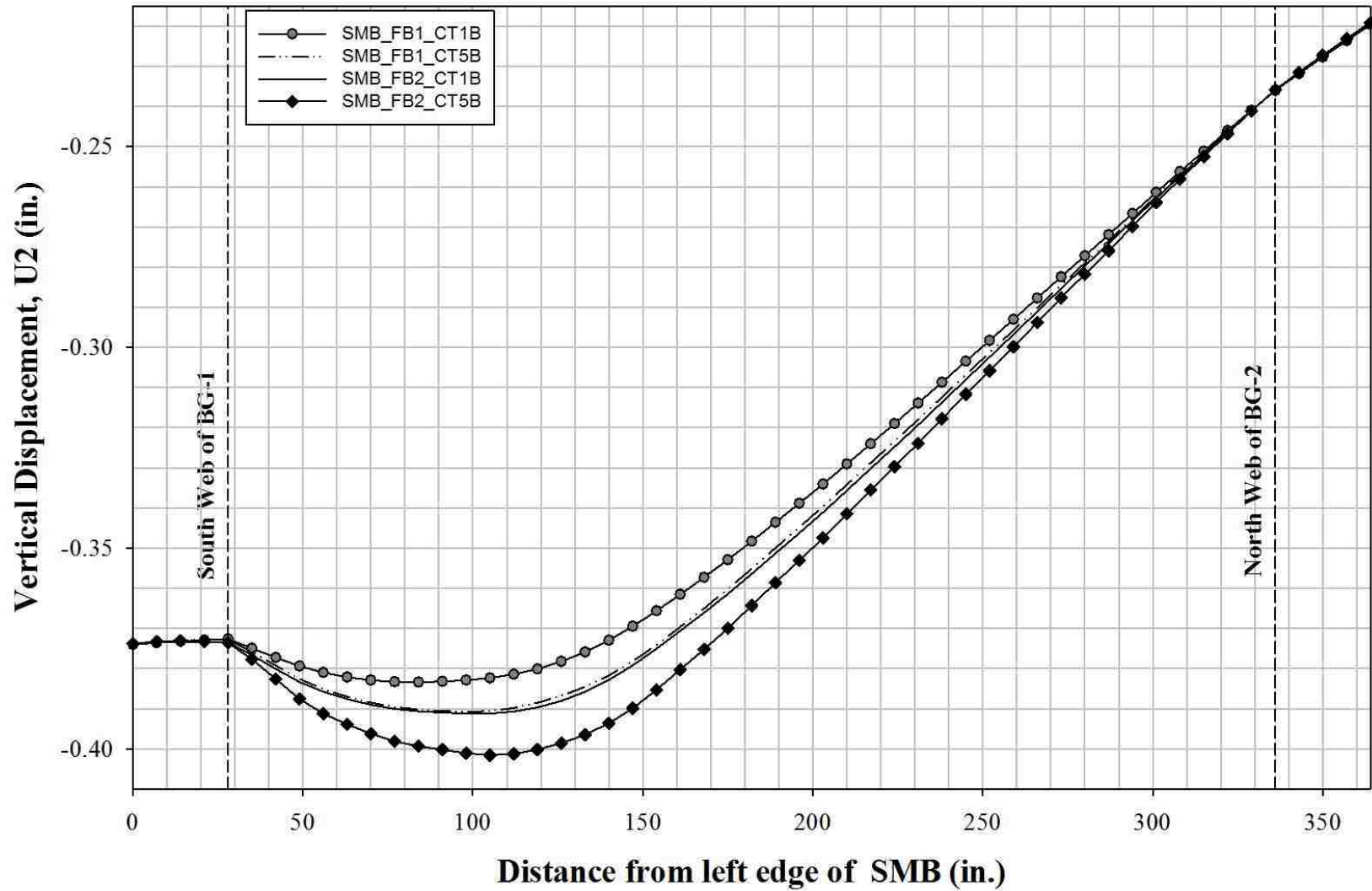
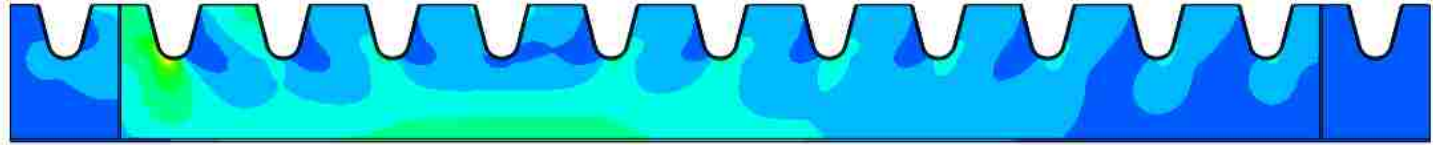
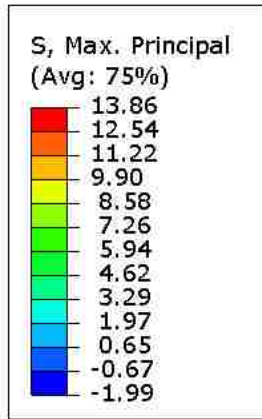
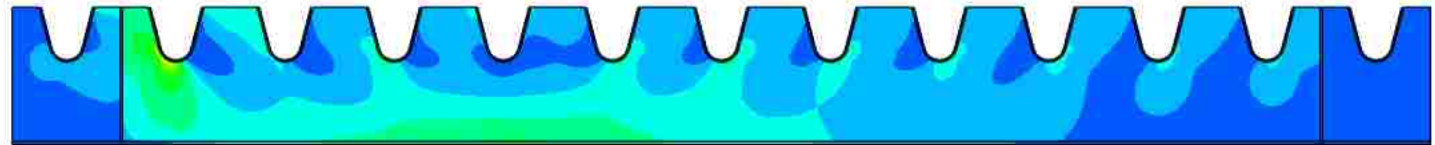
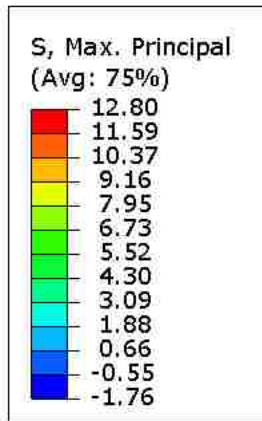


Figure 84 Vertical displacement of floor beam 14 due to longitudinally eccentric loading (EL)

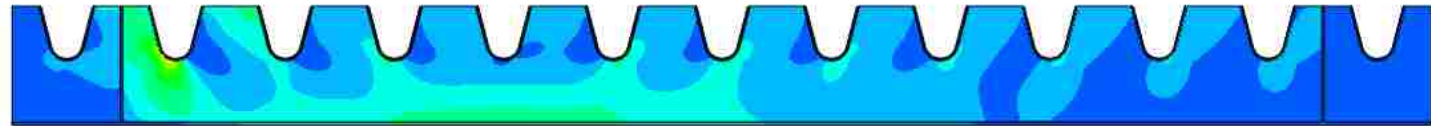
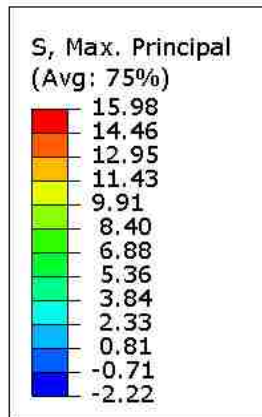


(a)

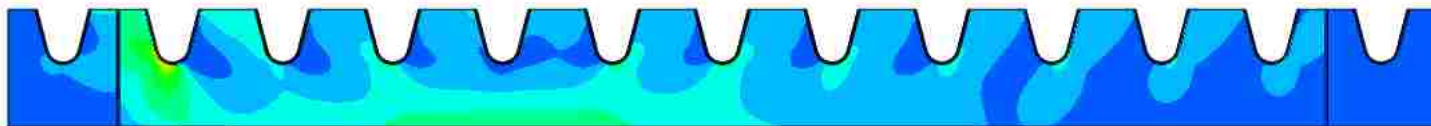
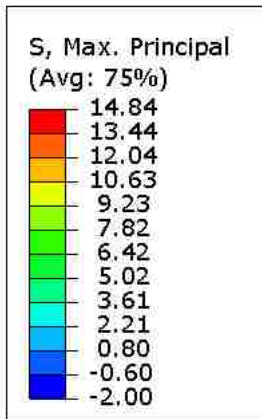


(b)

Figure 85 Principal stress contour on the west face of floor beam 14 for Submodel B with floor beam FB1 and connection Type 1B: (a) symmetric loading (SL) (b) longitudinally eccentric loading (EL)

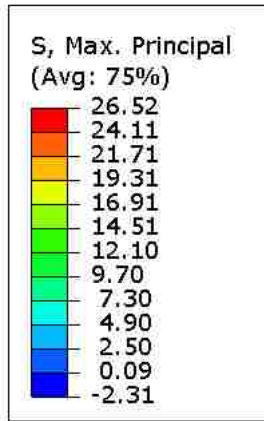


(a)

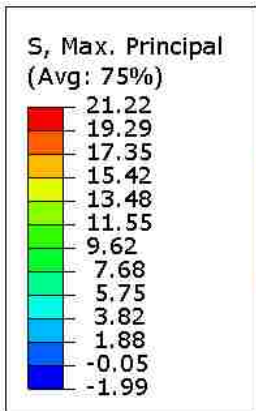


(b)

Figure 86 Principal stress contour on the west face of floor beam 14 for Submodel B with floor beam FB2 and connection Type 1B: (a) symmetric loading (SL) (b) longitudinally eccentric loading (EL)

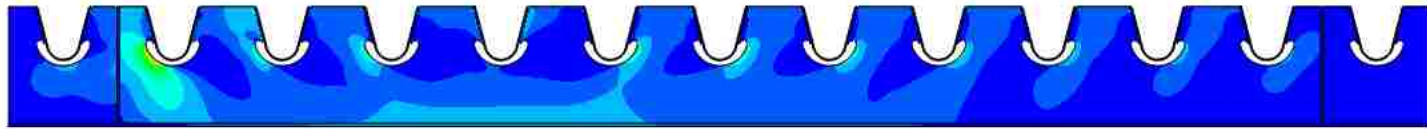
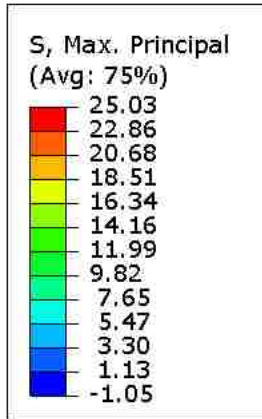


(a)

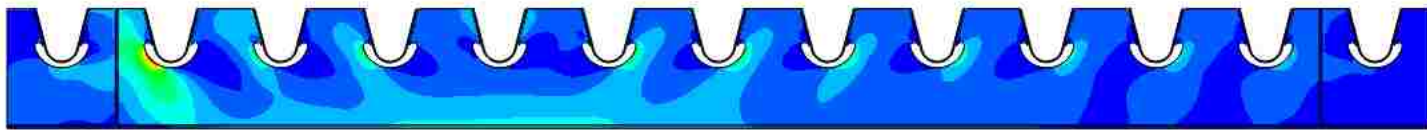
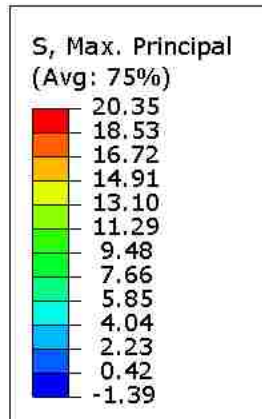


(b)

Figure 87 Principal stress contour on the west face of floor beam 14 for Submodel B with floor beam FB1 and connection Type 5B: (a) symmetric loading (SL) (b) longitudinally eccentric loading (EL)



(a)



(b)

Figure 88 Principal stress contour on the west face of floor beam 14 for Submodel B with floor beam FB2 and connection Type 5B: (a) symmetric loading (SL) (b) longitudinally eccentric loading (EL)

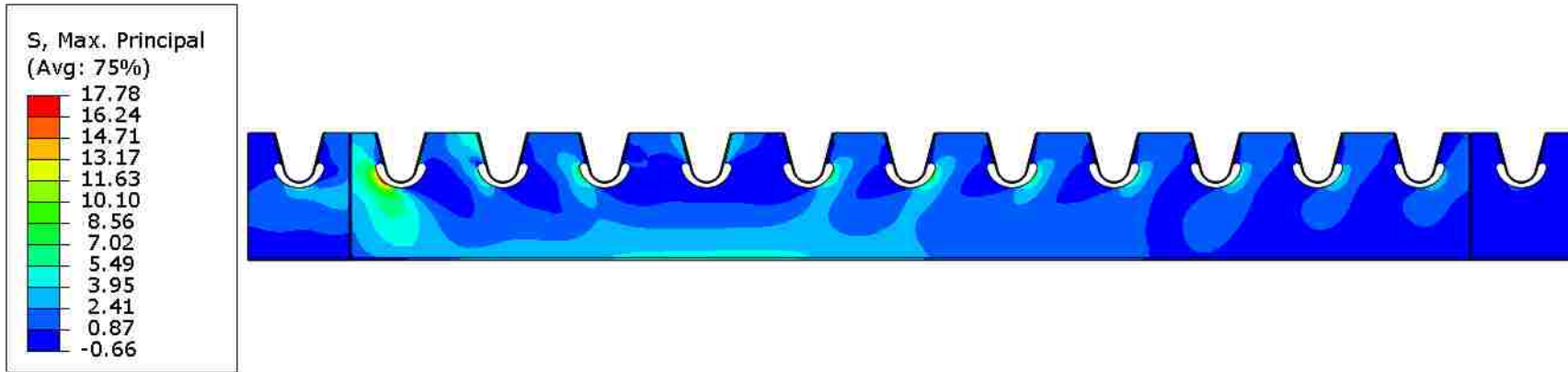


Figure 89 Principal stress contour on the west face of floor beam 14 for Submodel B with floor beam FB1 and connection Type 4B due to symmetric loading (SL)

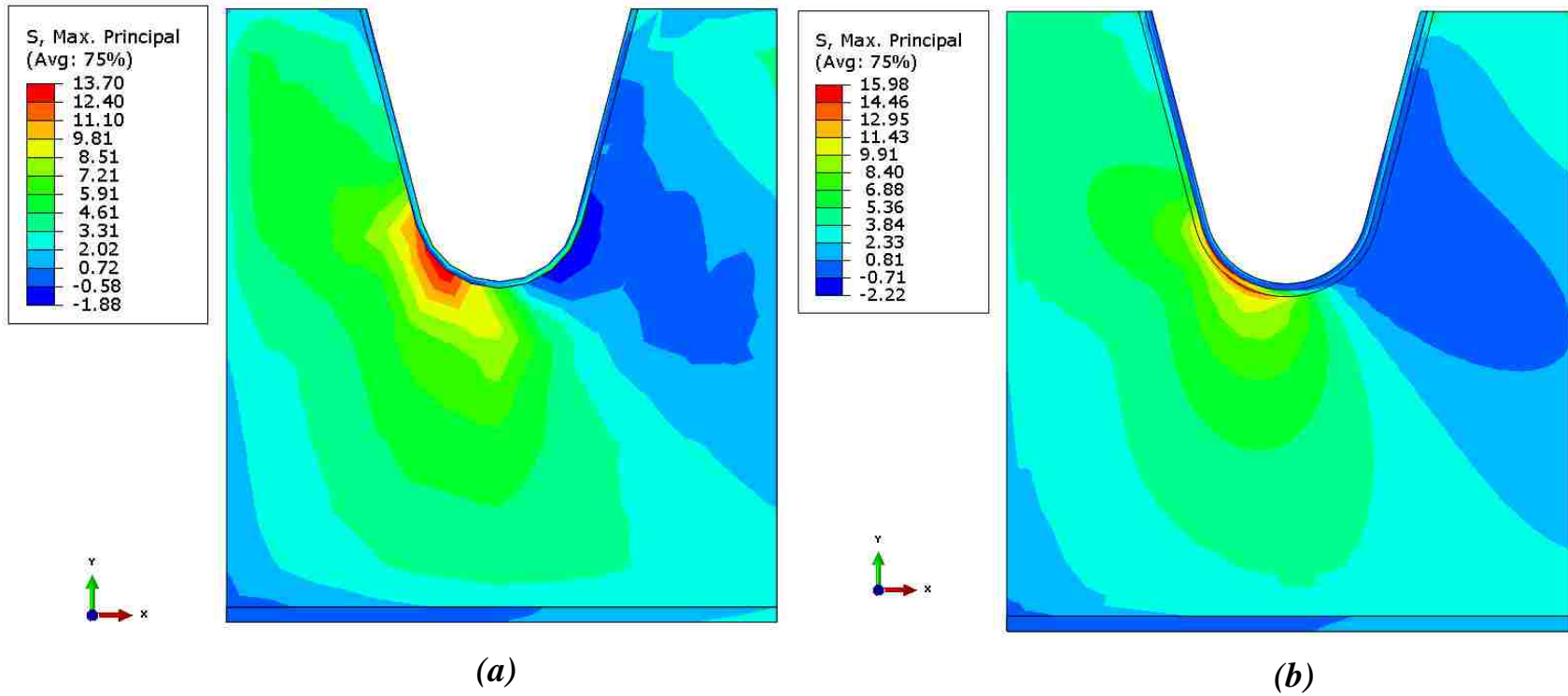


Figure 90 Comparison of principal stress contour in floor beam 14 with floor beam FB2 and connection Type 1B due to symmetric loading: (a) Submodel A; (b) Submodel B

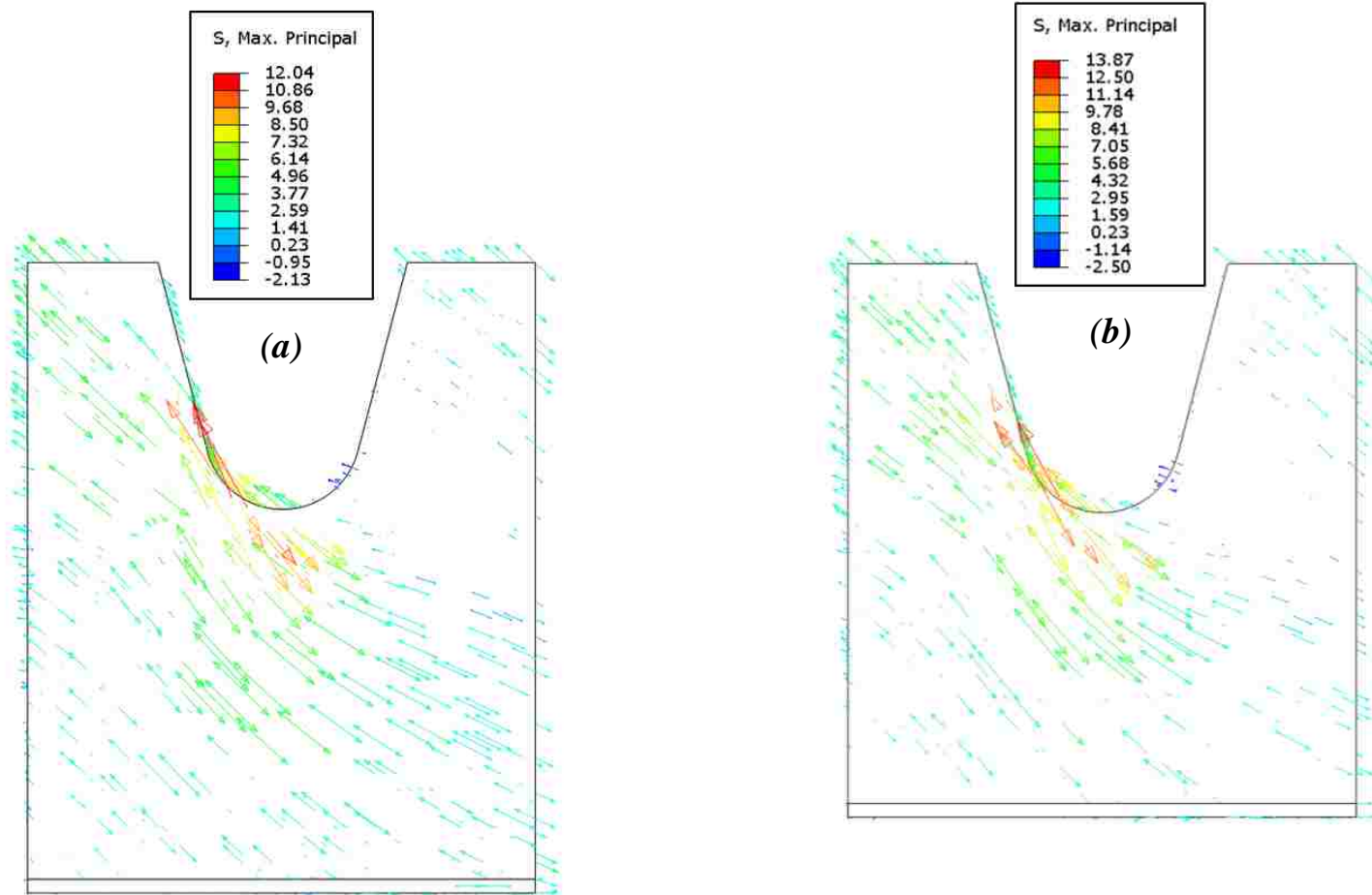


Figure 91 Direction of maximum principal stress in floor beam 14 for Submodel B with connection Type 1B for symmetric loading (SL): (a) floor beam FB1; (b) floor beam FB2

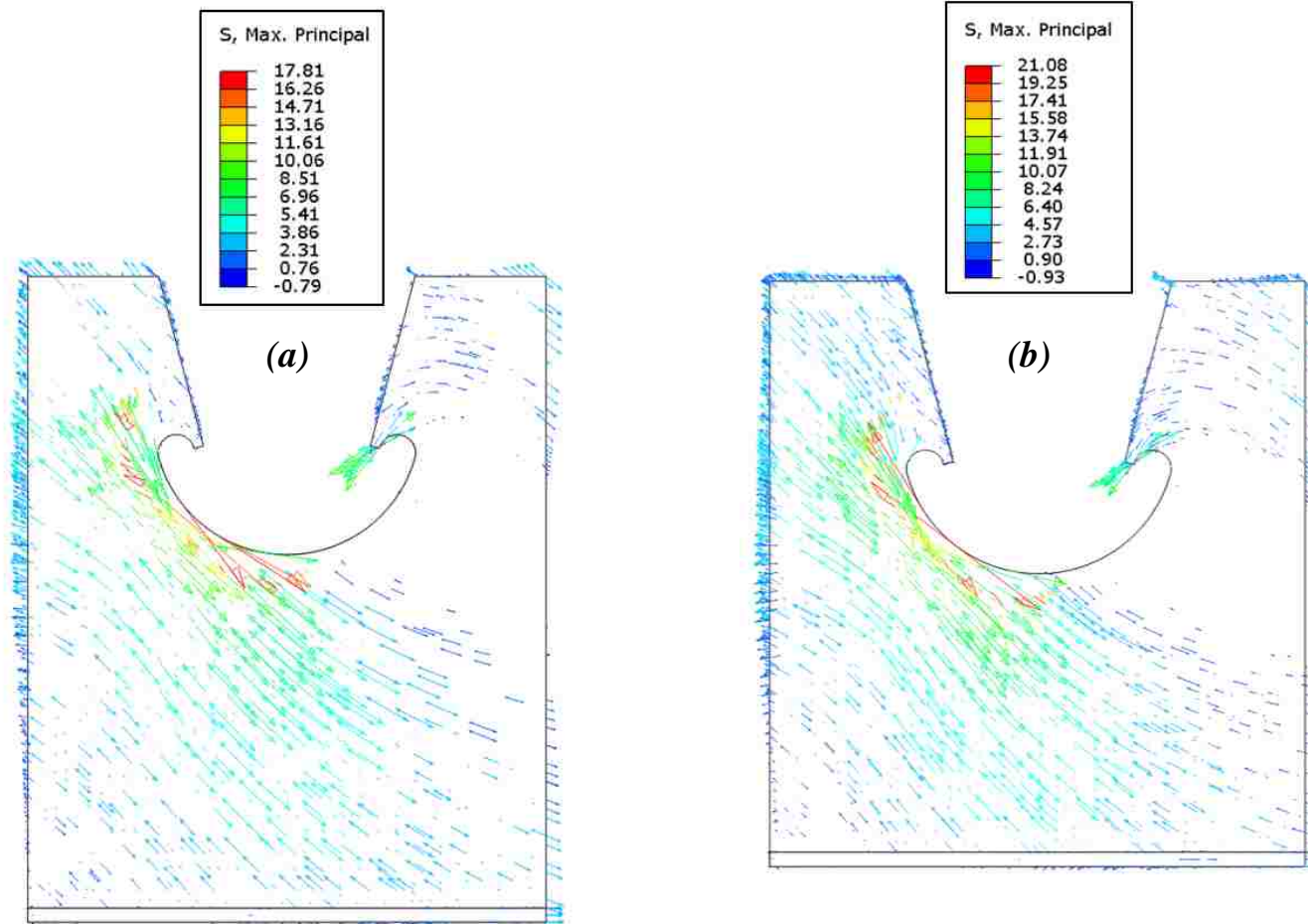


Figure 92 Direction of maximum principal stress in floor beam 14 for Submodel B with connection Type 5B for symmetric loading (SL): (a) floor beam FB1; (b) floor beam FB2

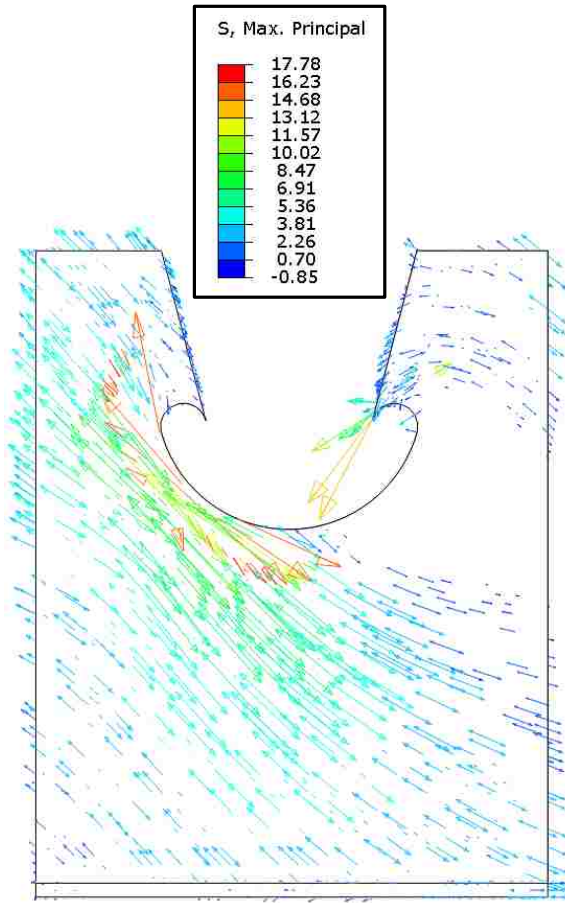


Figure 93 Direction of maximum principal stress in floor beam 14 for submodel B with connection Type 4B for symmetric loading (SL) with floor beam FB1

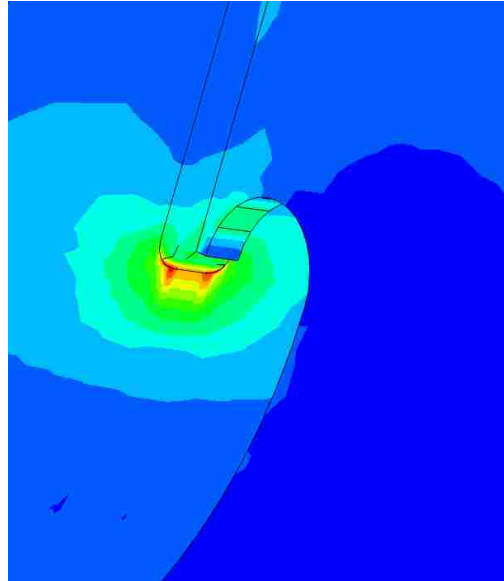
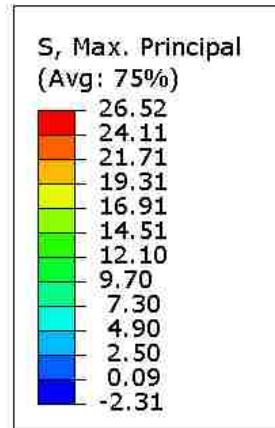


Figure 94 Stress distribution at the extended cutout termination for FB1 and connection Type 5B due to symmetric loading (SL)

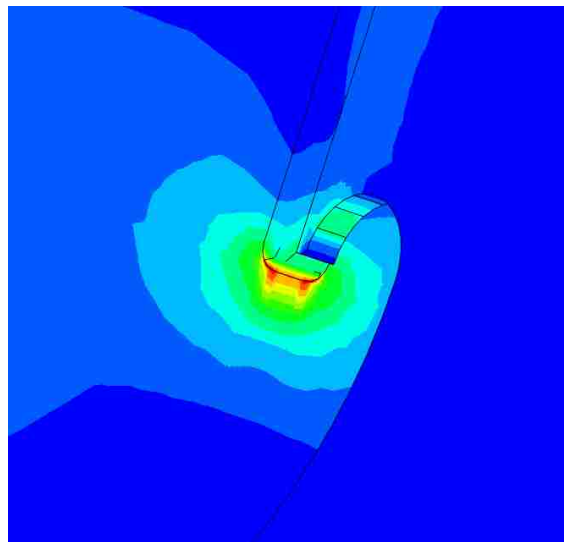
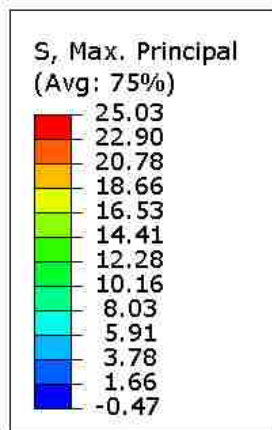


Figure 95 Stress distribution at the extended cutout termination for FB2 and connection Type 5B due to symmetric loading (SL)

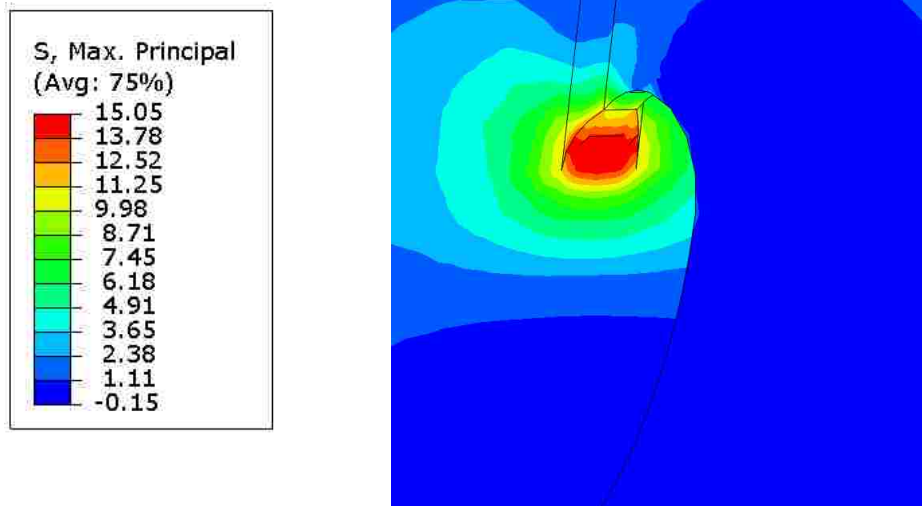


Figure 96 Stress distribution at the extended cutout termination for FB1 and connection Type 4B due to symmetric loading (SL)

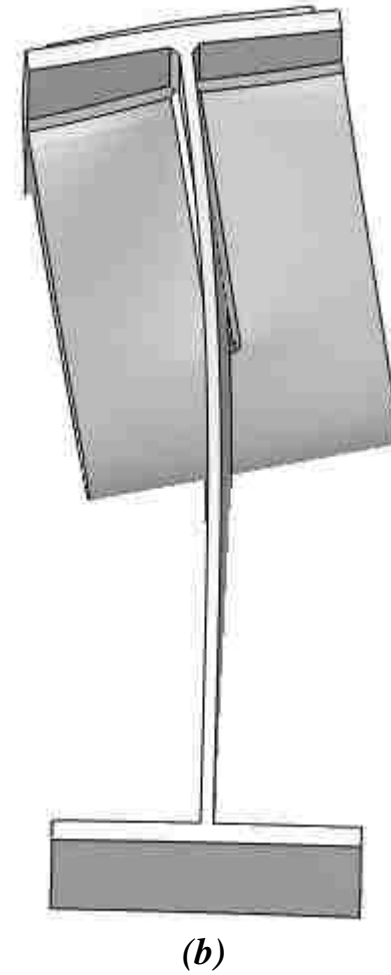
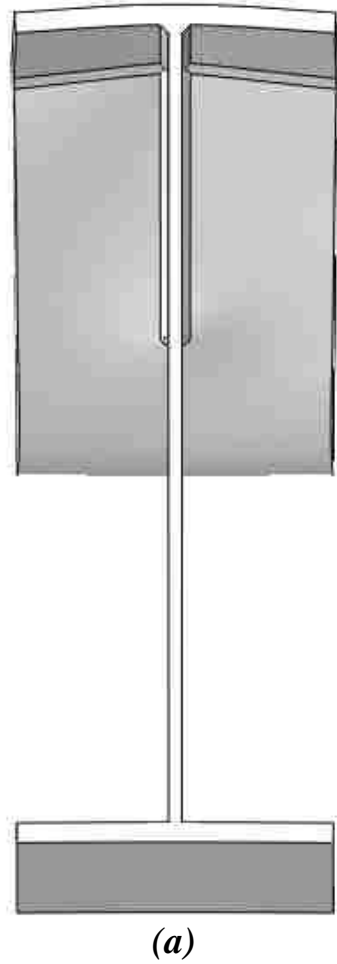


Figure 97 Elevation view of a section of rib-to-floor beam connection due to: (a) symmetric loading (SL); (b) longitudinally eccentric loading (EL)

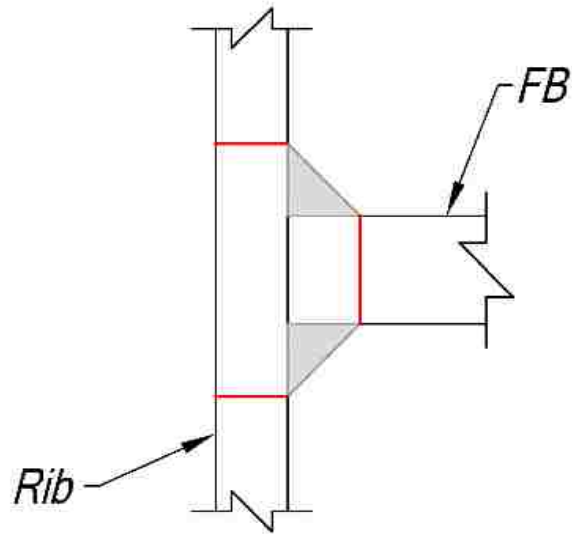


Figure 98 Potential modes of toe cracking shown on a cross section of a typical rib-to-floor beam connection

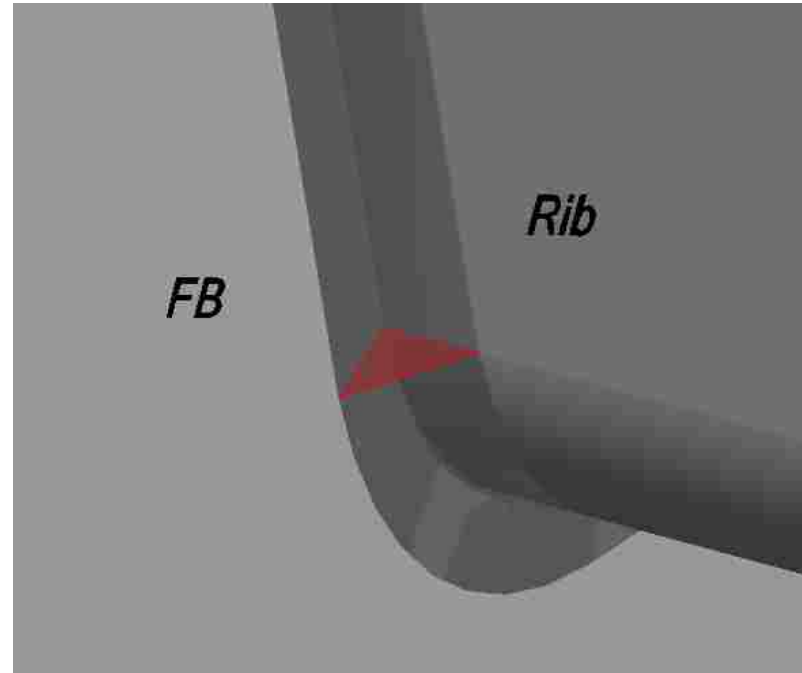
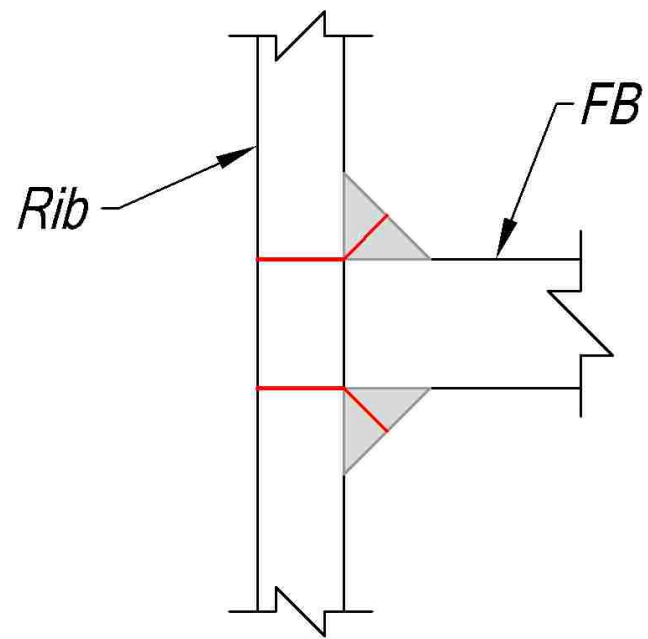


Figure 99 Potential modes of root cracking shown on typical rib-to-floor beam connections

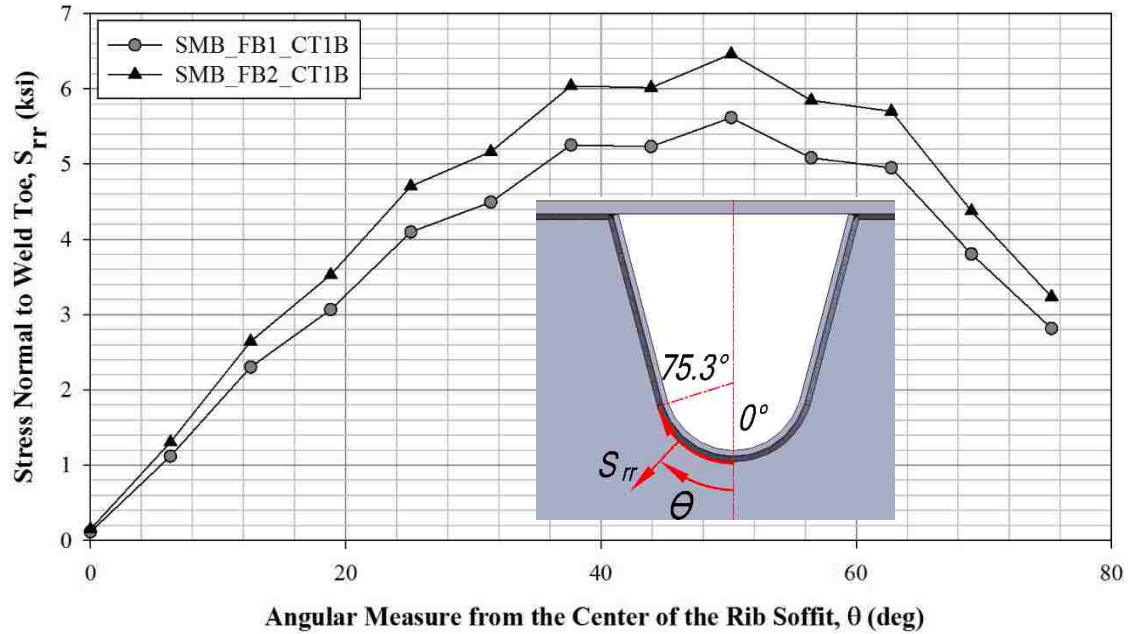


Figure 100 Comparison of tensile stress normal to the weld toe on floor beam 14 web due to symmetric loading (SL)

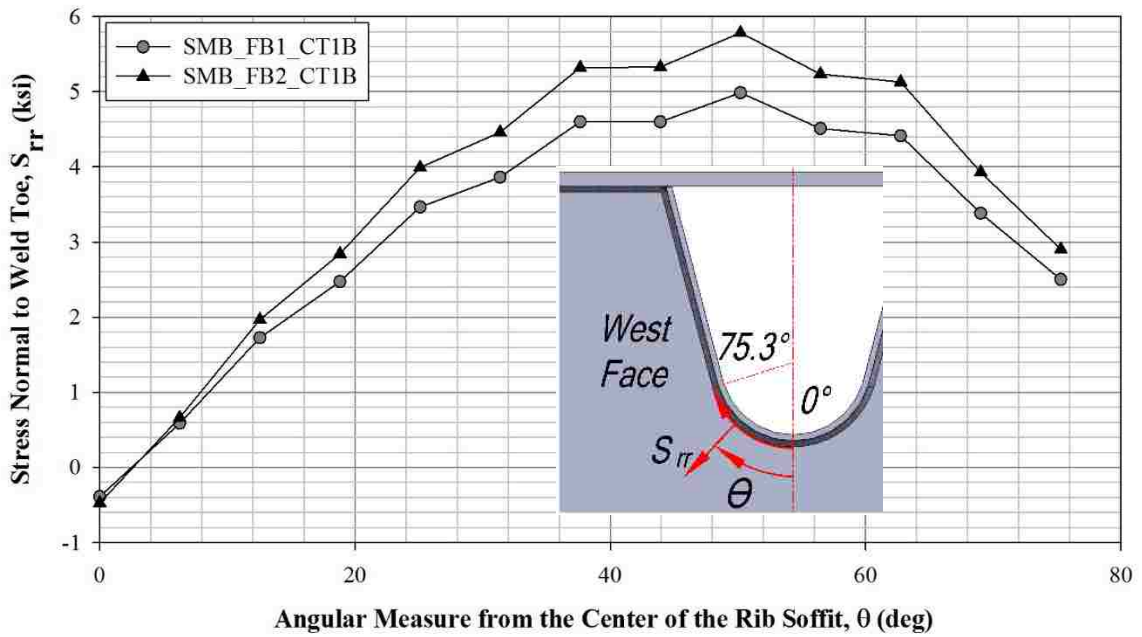


Figure 101 Comparison of tensile stress normal to the weld toe on the west face of floor beam 14 due to longitudinally eccentric loading (EL)

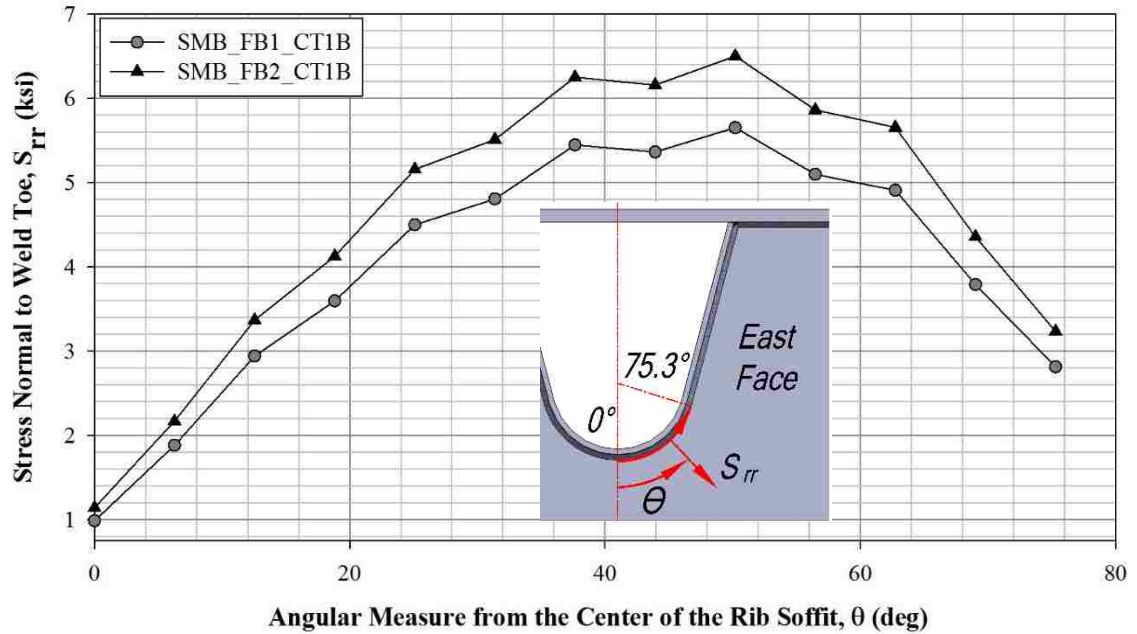


Figure 102 Comparison of tensile stress normal to the weld toe on the east face of floor beam 14 due to longitudinally eccentric loading (EL)

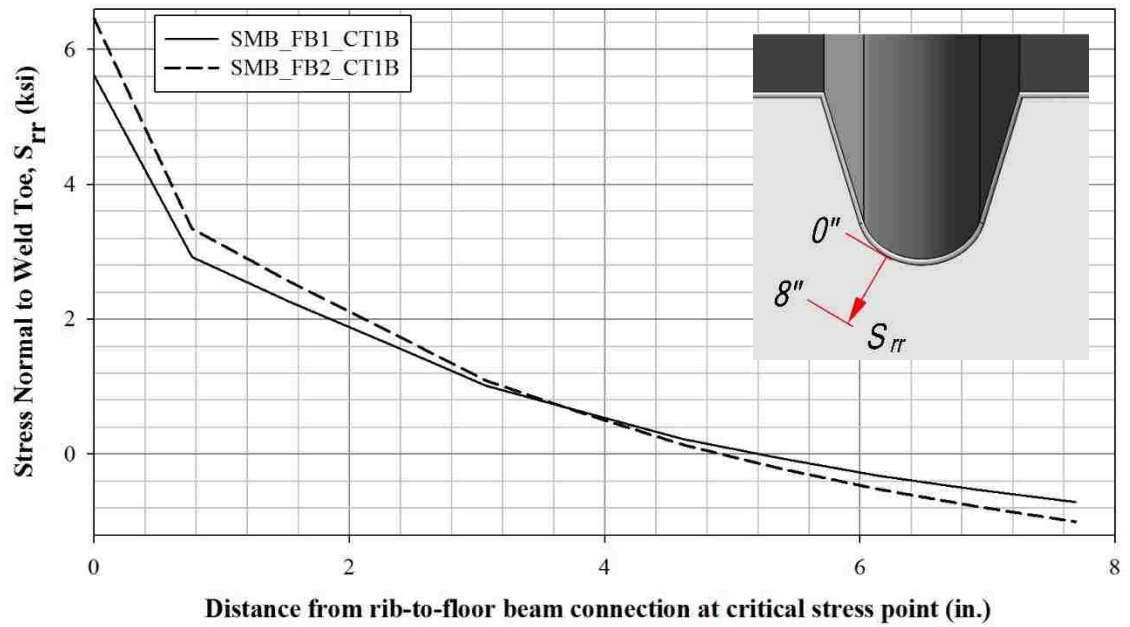


Figure 103 Comparison of radial stress in floor beam 14 along the critical path due to symmetric loading (SL)

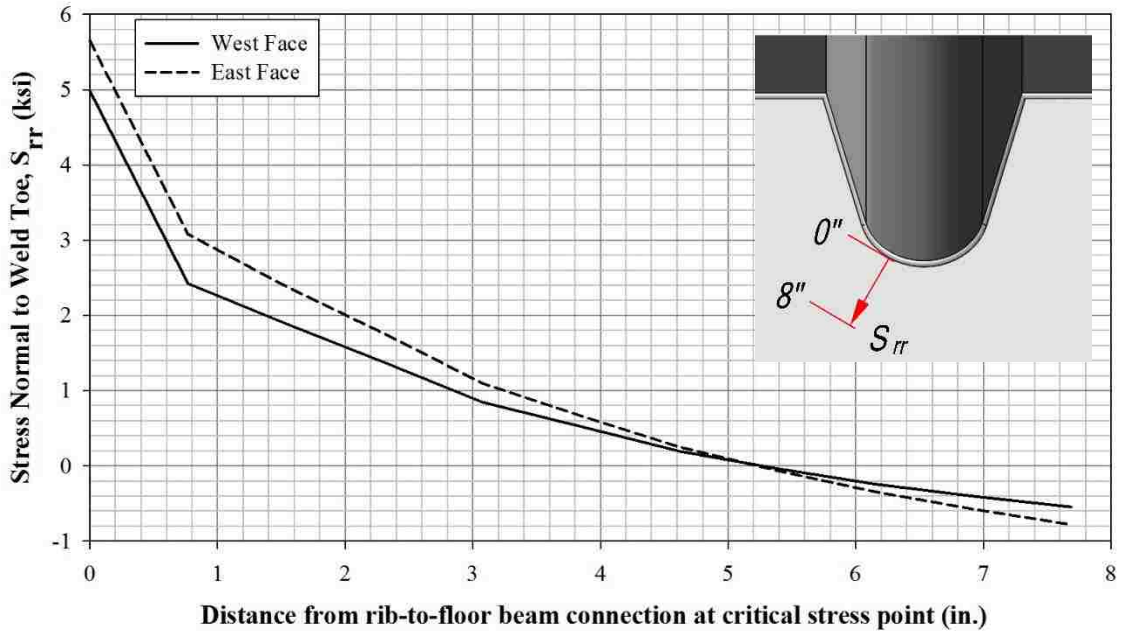


Figure 104 Radial stress showing out-of-plane bending of floor beam 14 web with floor beam FB1 due to longitudinally eccentric loading (EL)

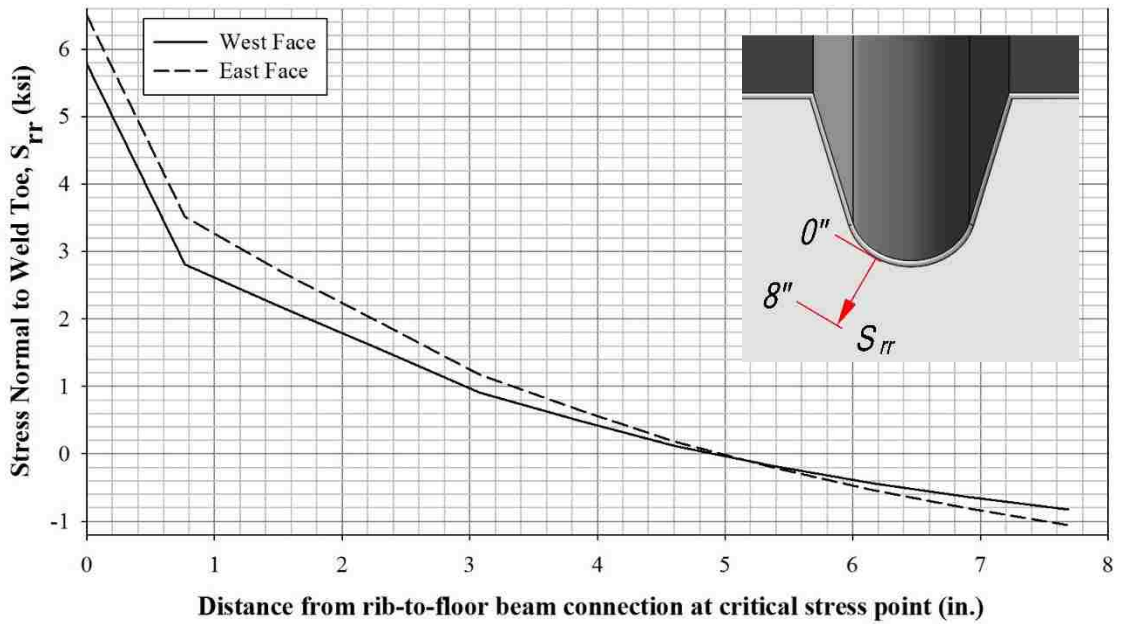


Figure 105 Radial stress showing out-of-plane bending of floor beam 14 web with floor beam FB2 due to longitudinally eccentric loading (EL)

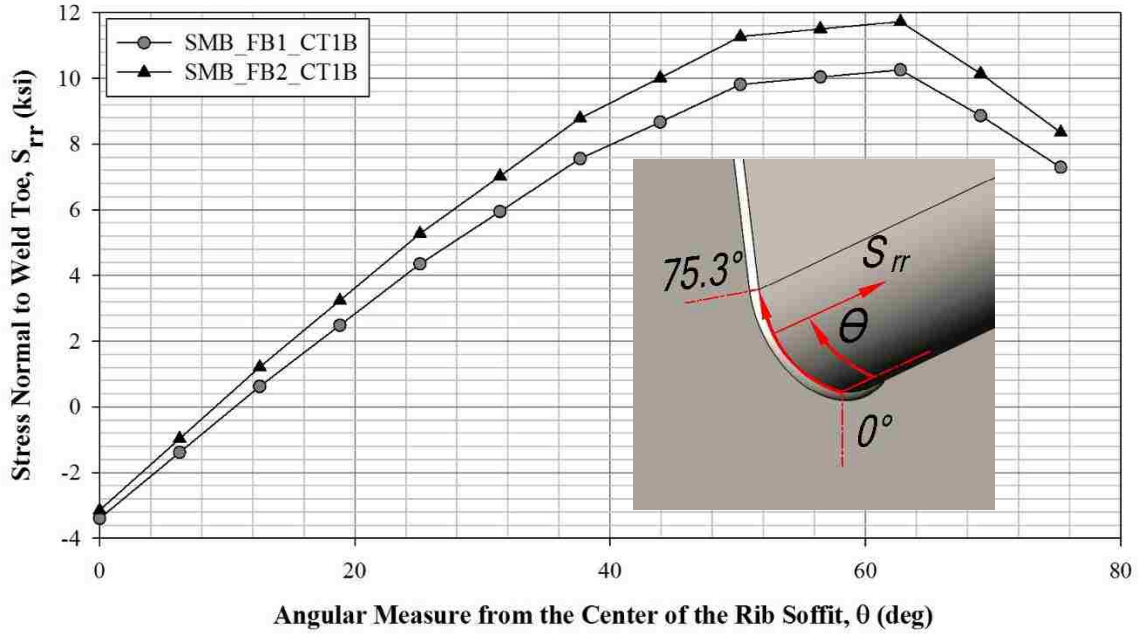


Figure 106 Comparison of tensile stress normal to the weld toe in rib 10 due to symmetric loading (SL)

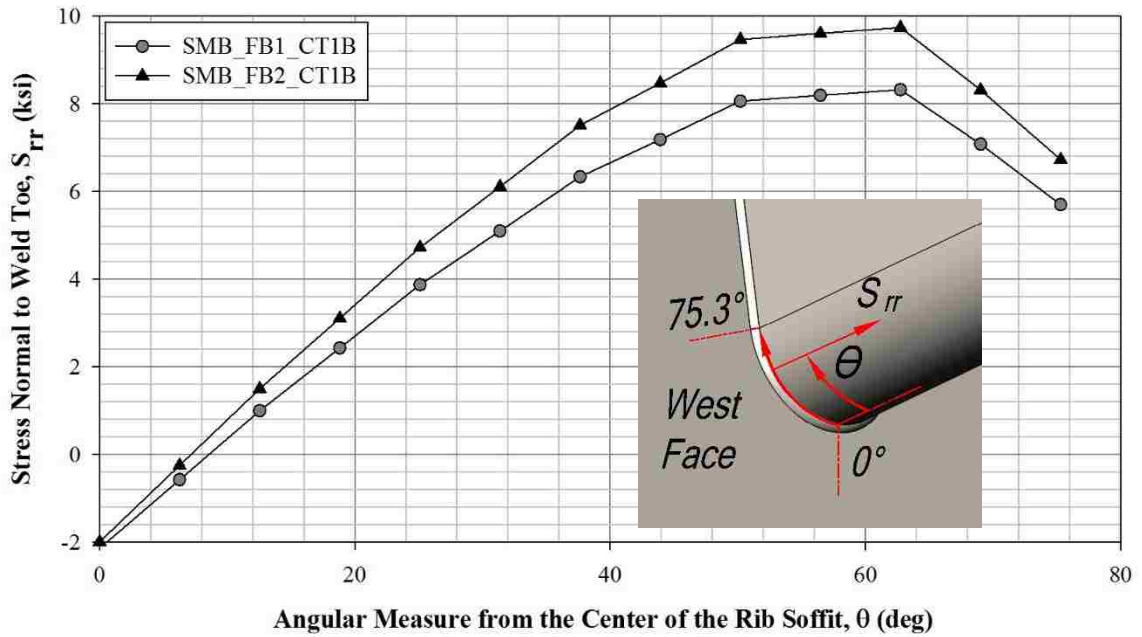


Figure 107 Comparison of stress normal to the weld toe on the west face of rib 10 due to longitudinally eccentric loading (EL)

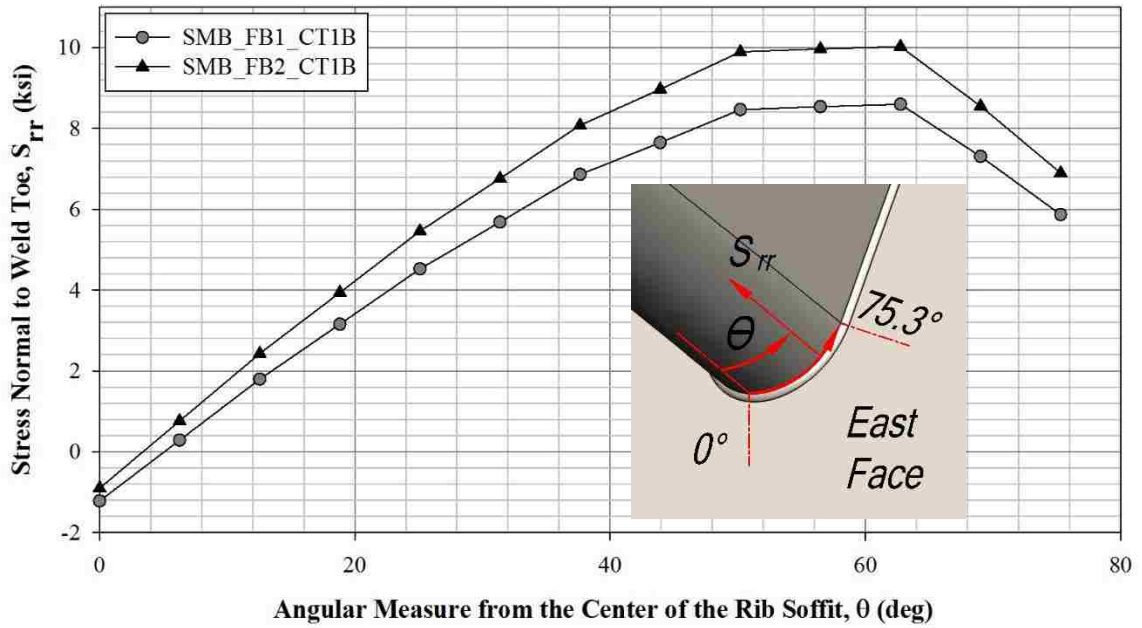


Figure 108 Comparison of tensile stress normal to the weld toe on the east face of rib 10 due to longitudinally eccentric loading (EL)

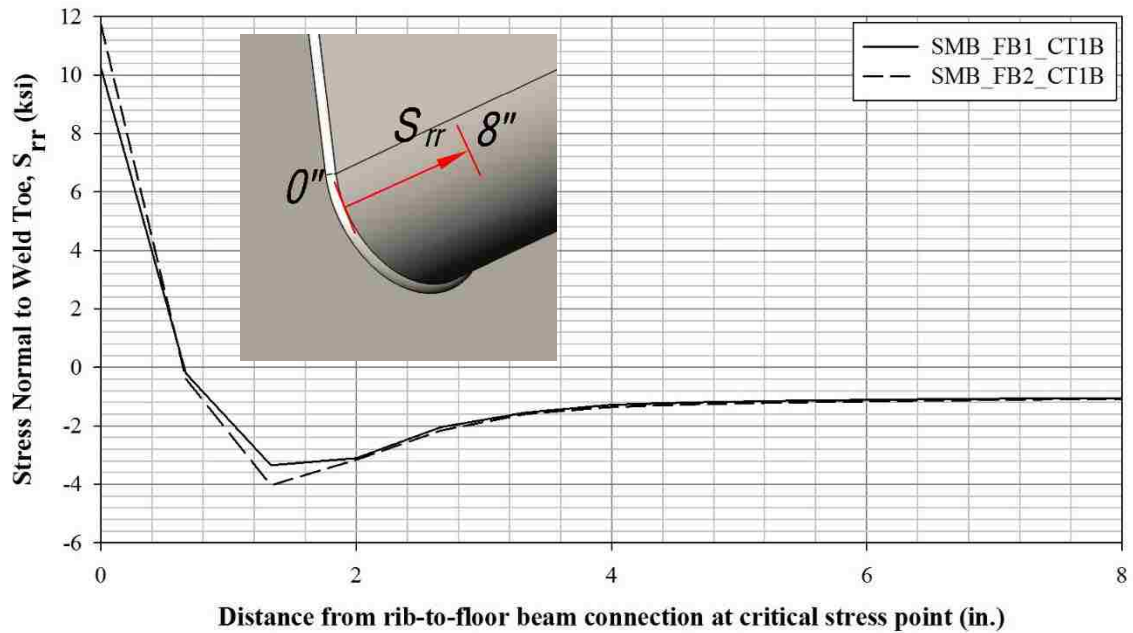


Figure 109 Comparison of radial stress in rib 10 along the critical path due to symmetric loading (SL)

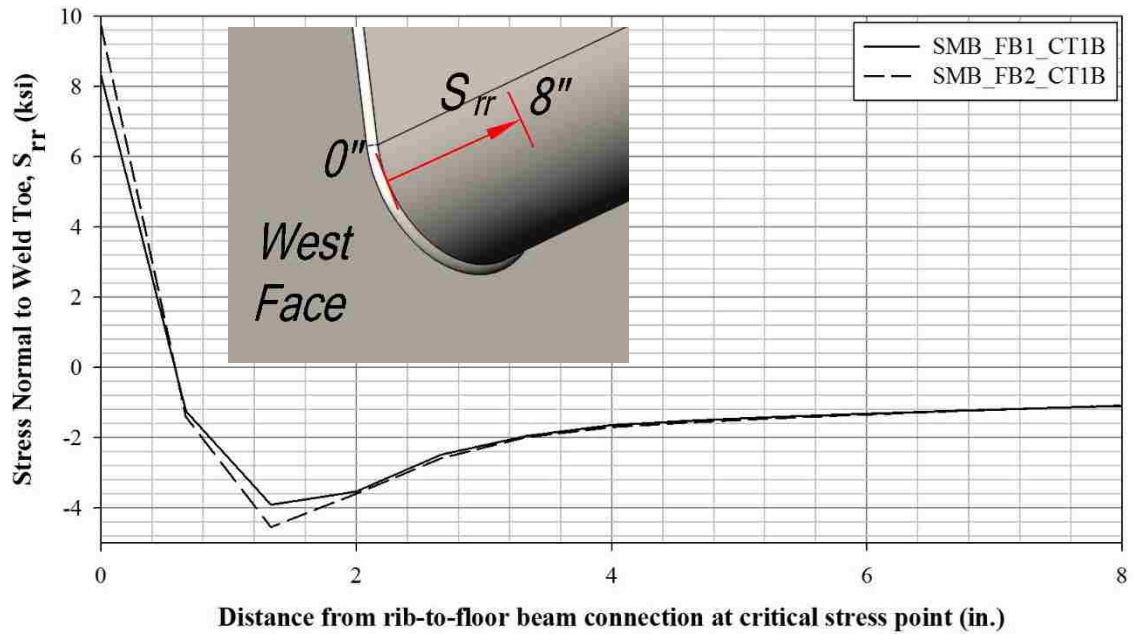


Figure 110 Comparison of radial stress on the west side of floor beam 14 in rib 10 along the critical path due to longitudinally eccentric loading (EL)

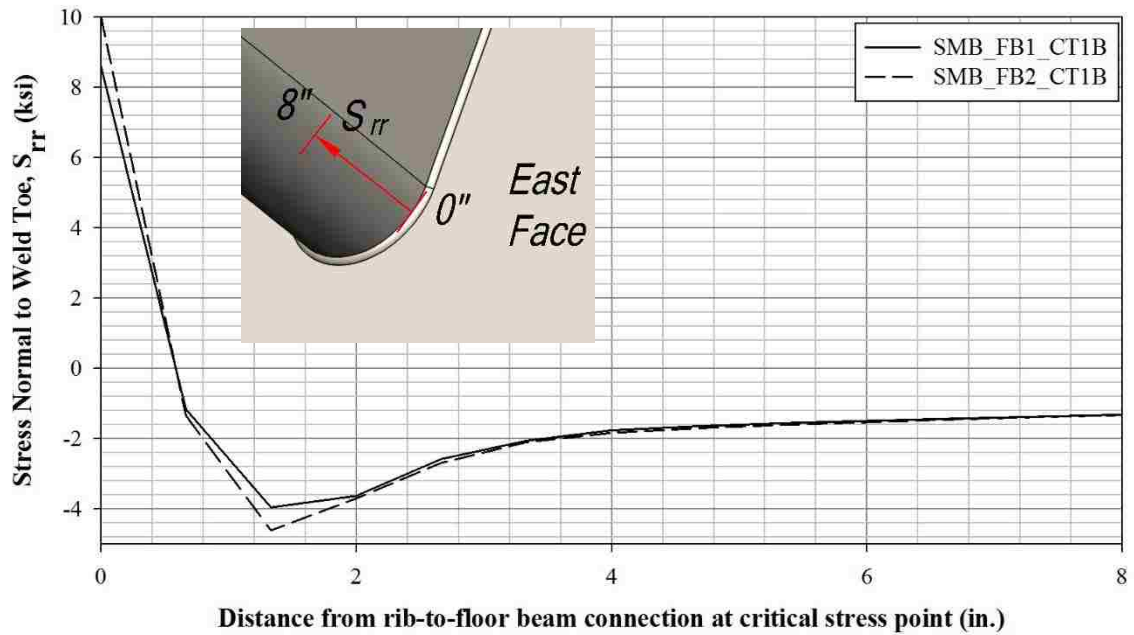


Figure 111 Comparison of radial stress range on the east side of floor beam 14 in rib 10 along the critical path due to longitudinally eccentric loading (EL)

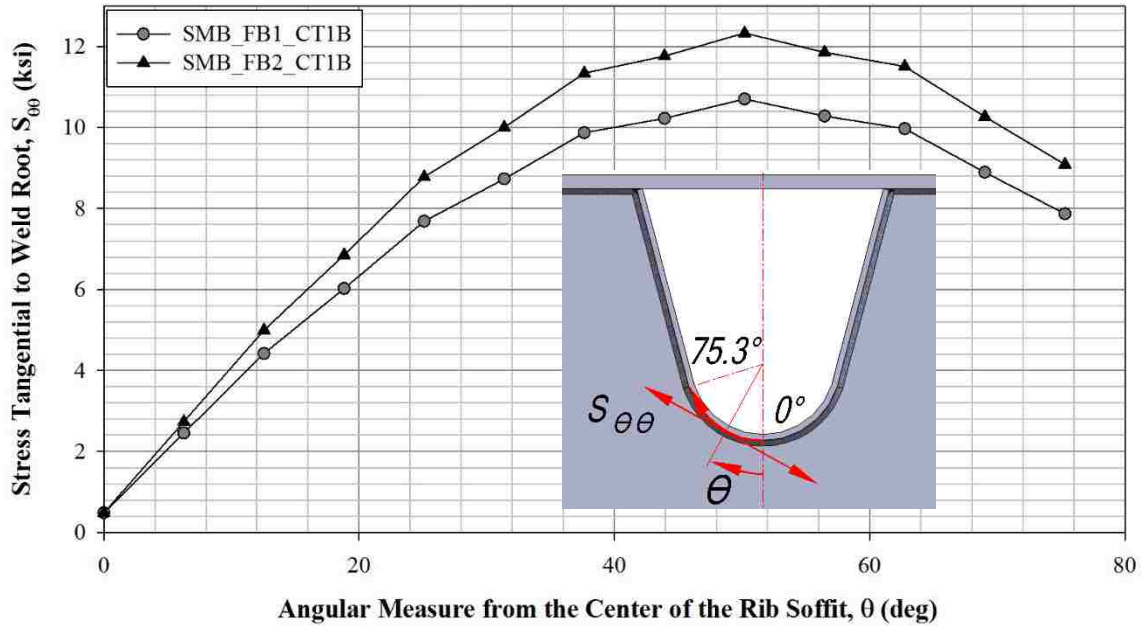


Figure 112 Comparison of tensile stress tangential to the rib-to-floor beam connection at the weld root in floor beam 14 due to symmetric loading (SL)

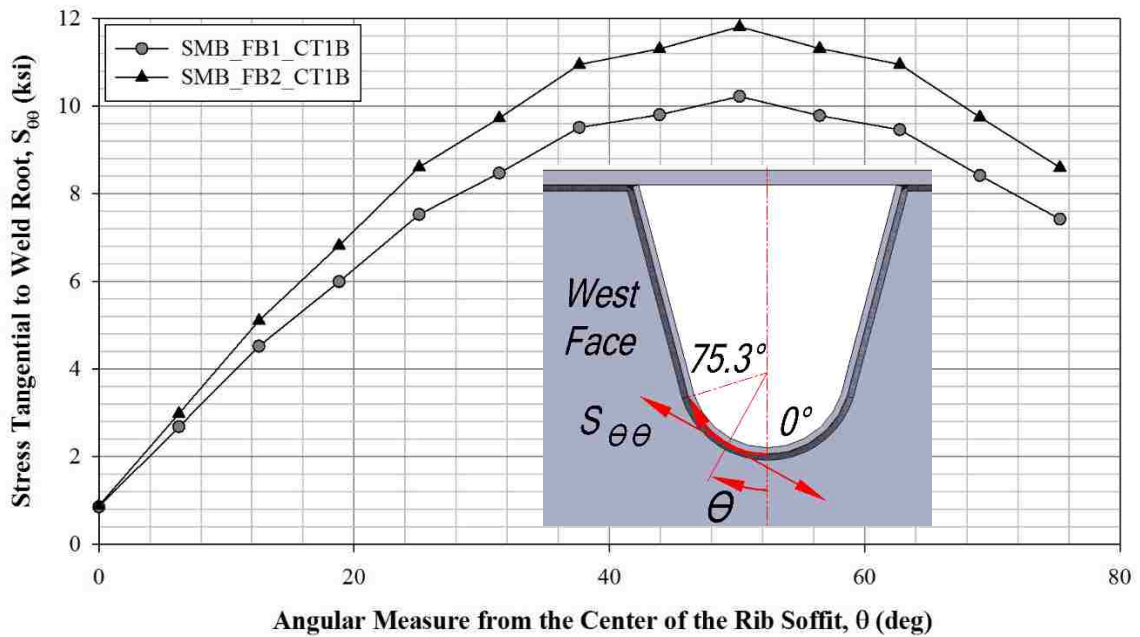


Figure 113 Comparison of tensile stress tangential to the rib-to-floor beam connection at the weld root on the west face of floor beam 14 due to longitudinally eccentric loading (EL)

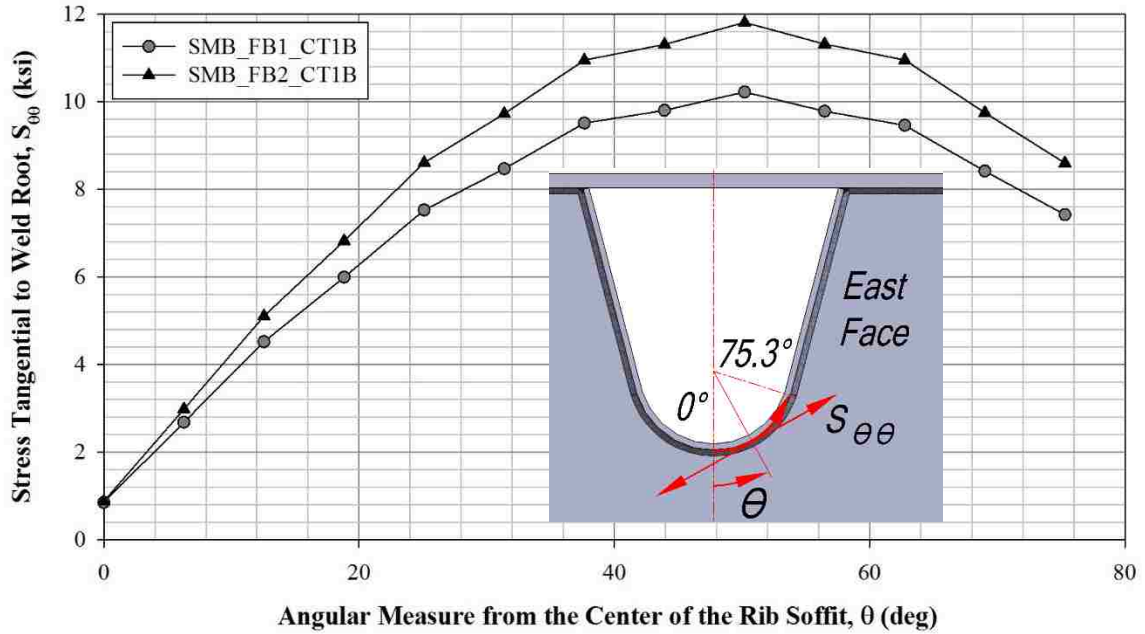


Figure 114 Comparison of tensile stress tangential to the rib-to-floor beam connection at the weld root on the east face of floor beam 14 due to longitudinally eccentric loading (EL)

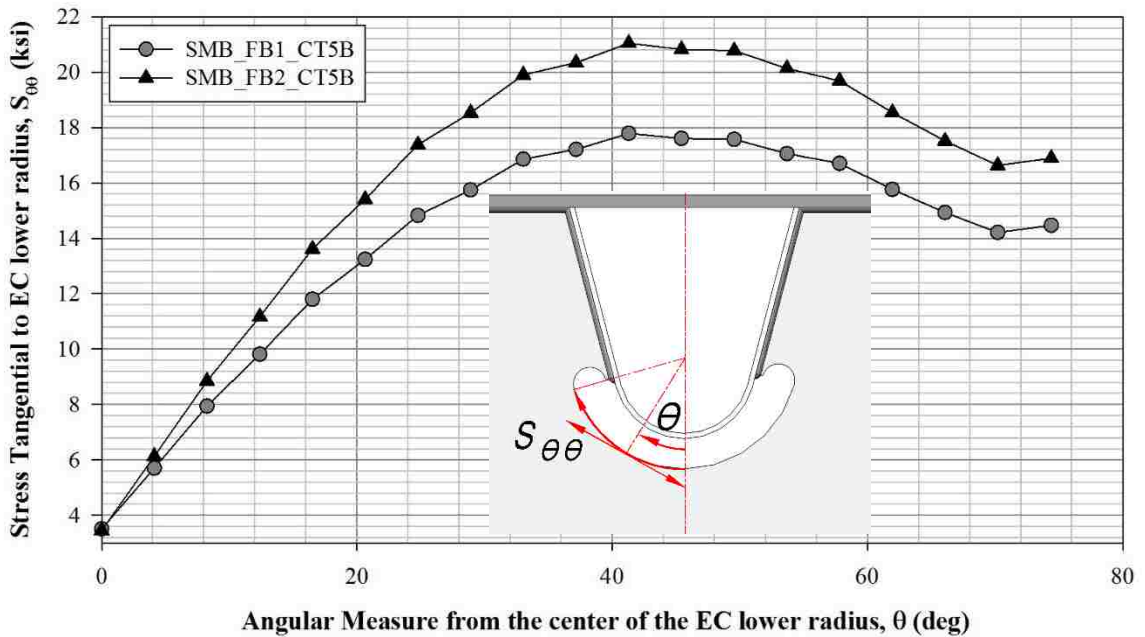


Figure 115 Comparison of tensile stress tangential to lower radius of extended cutout in floor beam 14 with connection Type 5B due to symmetric loading (SL)

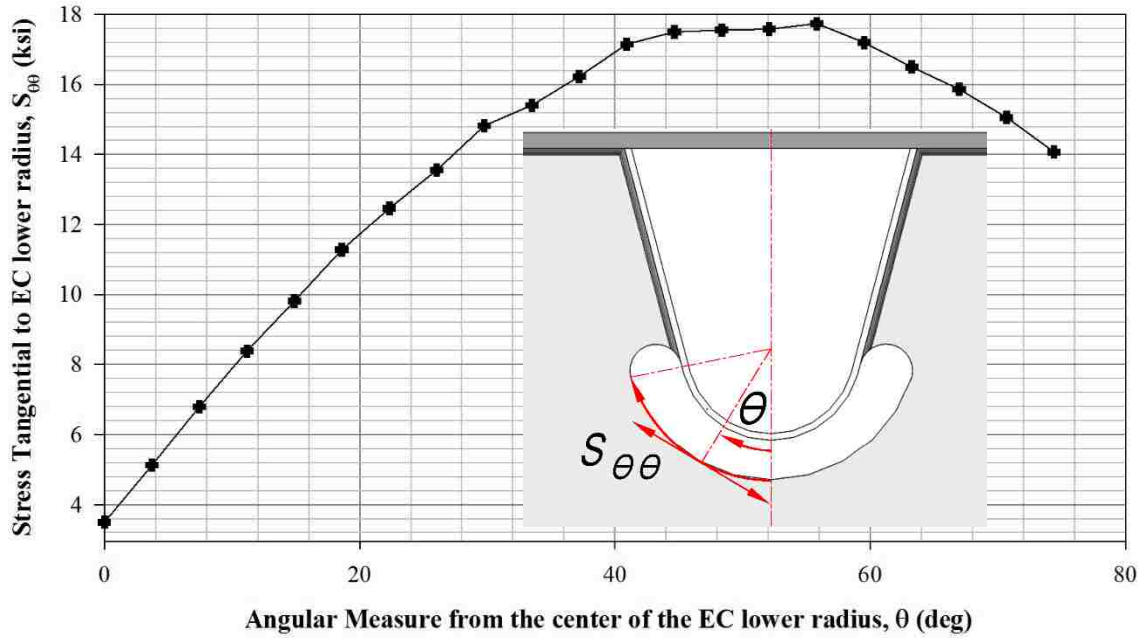


Figure 116 Comparison of tensile stress tangential to lower radius of extended cutout in floor beam 14 with connection Type 4B due to symmetric loading (SL)

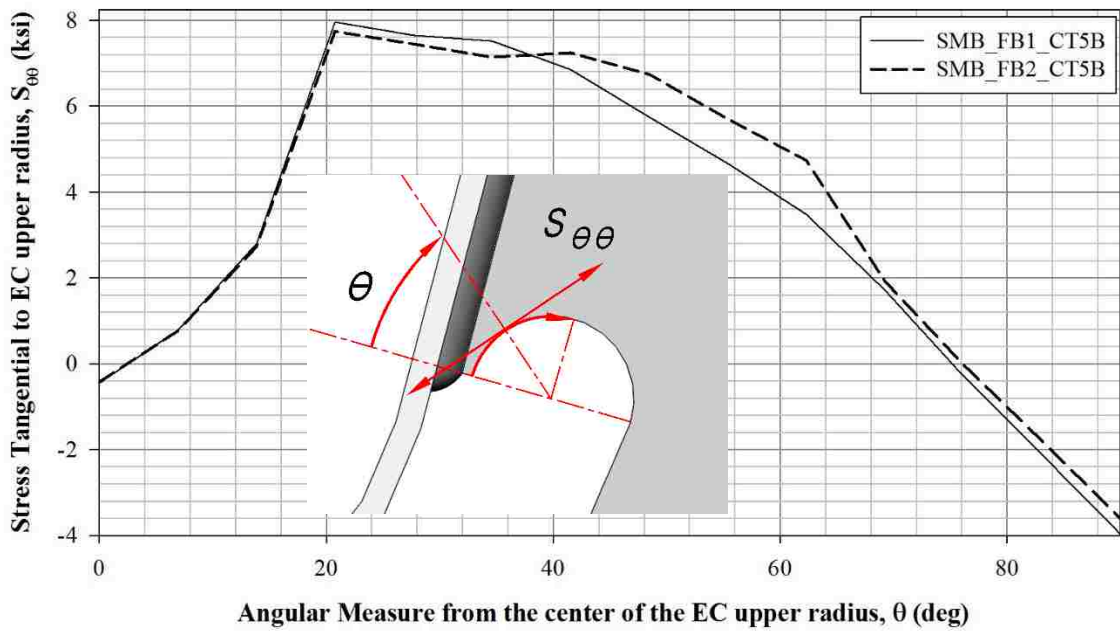


Figure 117 Comparison of tensile stress tangential to upper radius of extended cutout in floor beam 14 with connection Type 5B due to symmetric loading (SL)

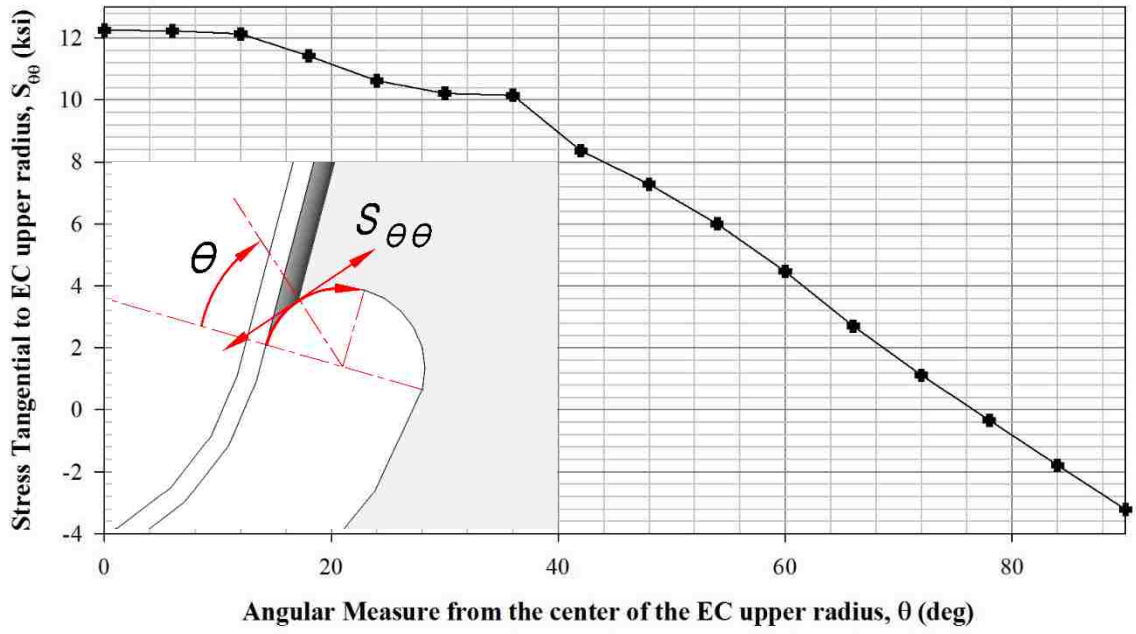


Figure 118 Comparison of tensile stress tangential to upper radius of extended cutout in floor beam 14 with connection Type 4B due to symmetric loading (SL)

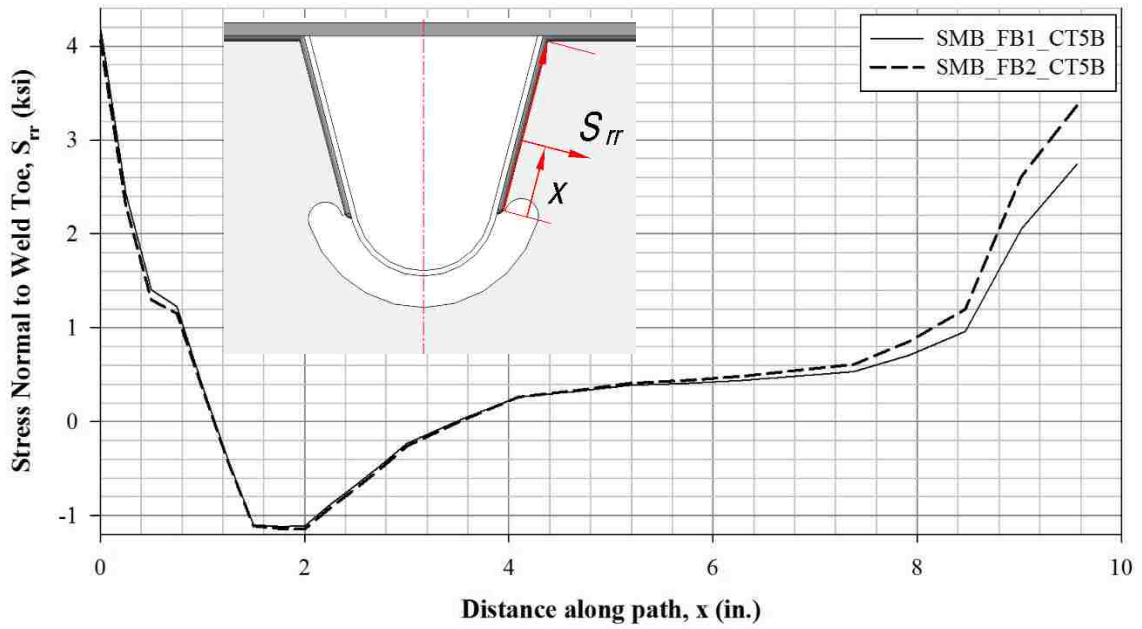


Figure 119 Comparison of stress normal to the weld toe in floor beam 14 for with connection Type 5B due to symmetric loading (SL)

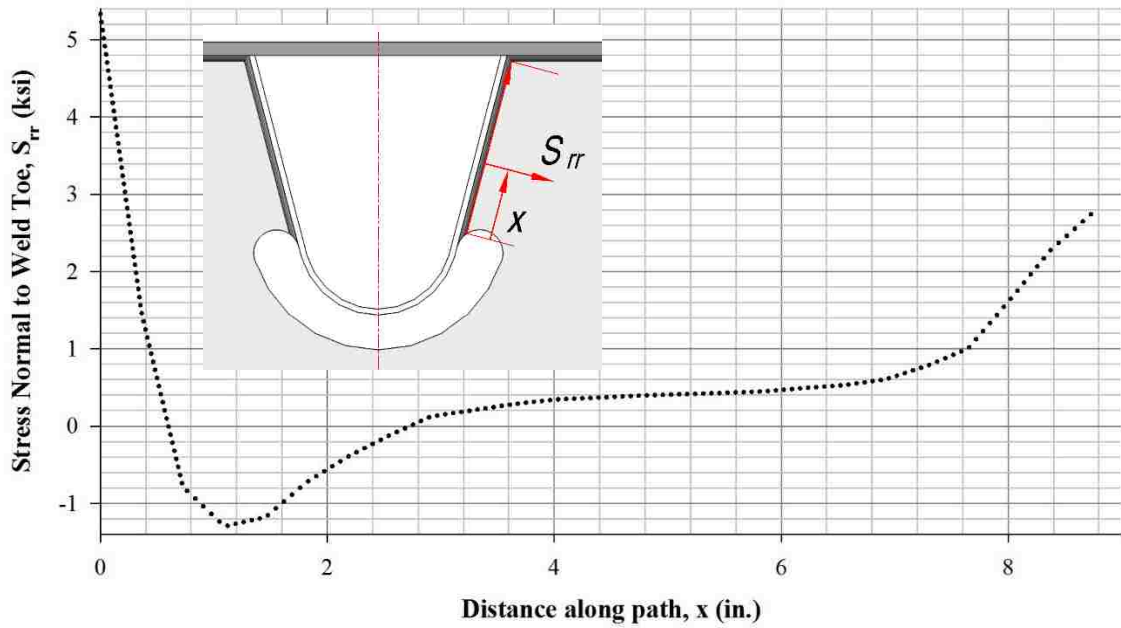


Figure 120 Comparison of stress normal to the weld toe in floor beam 14 with connection Type 4B due to symmetric loading (SL)

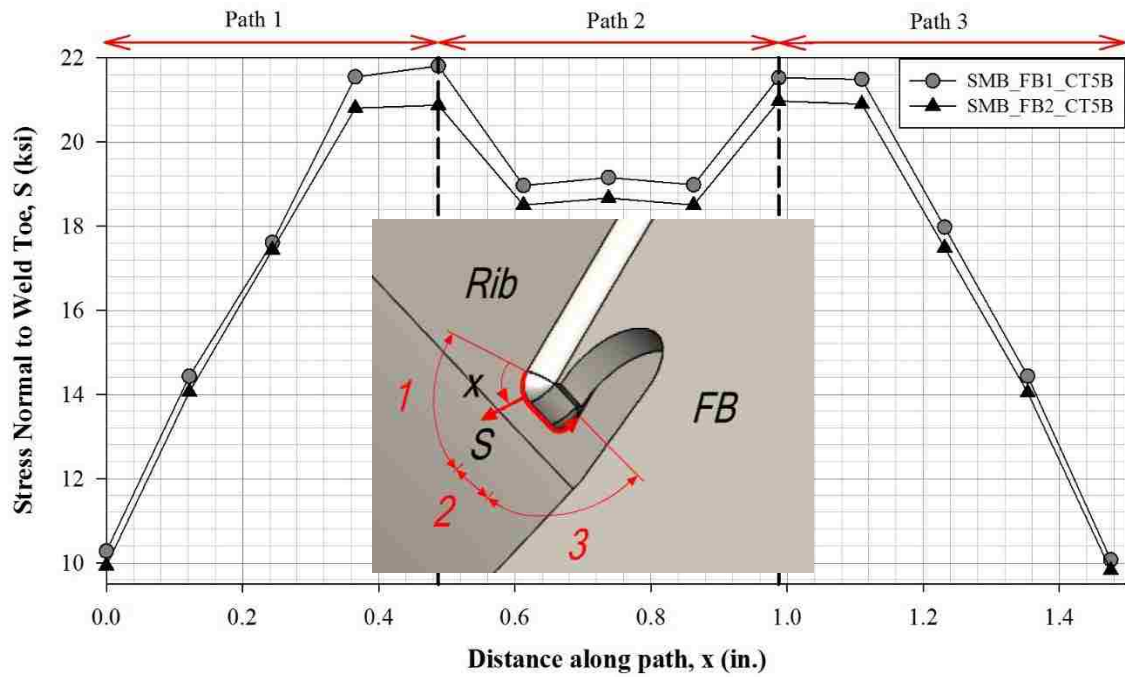


Figure 121 Comparison of tensile stress normal to rib-to-floor beam connection at the weld toe of the extended cutout on the face of rib 10 with connection Type 5B due to symmetric loading (SL)

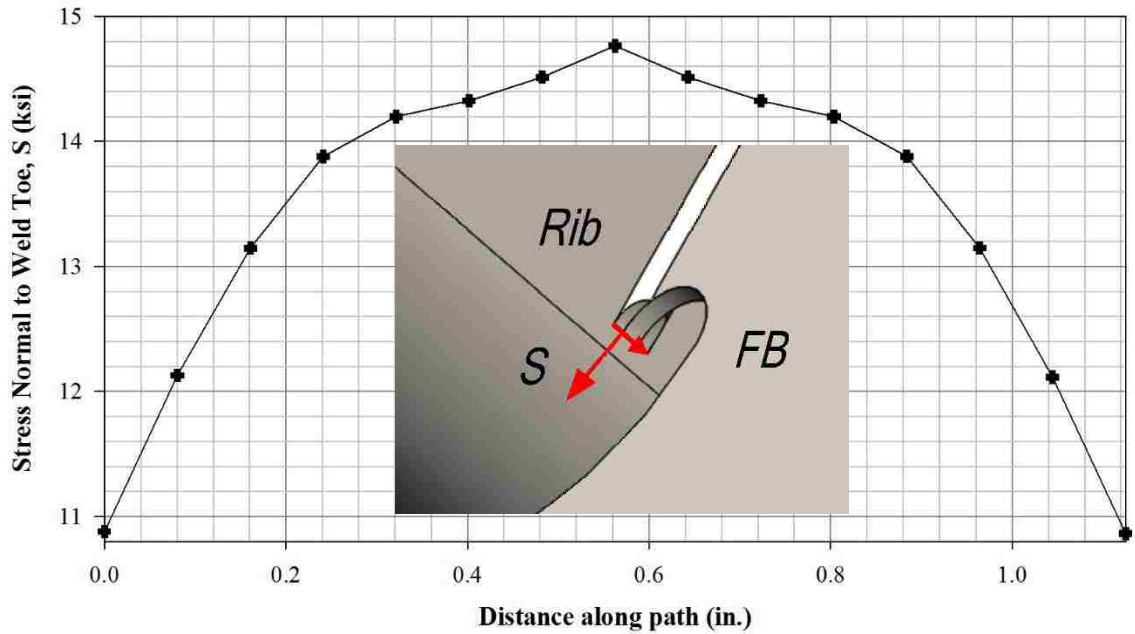


Figure 122 Tensile stress normal to rib-to-floor beam connection at extended cutout termination on the face of rib 10 with connection Type 4B due to symmetric loading (SL)

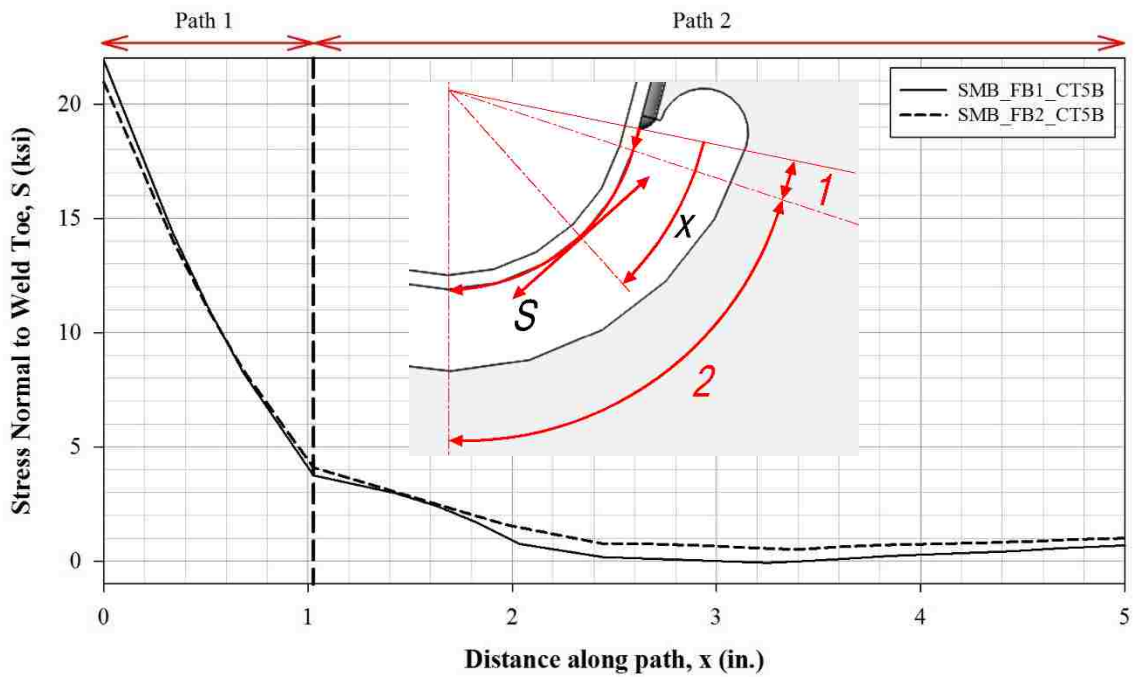


Figure 123 Stress normal to extended cutout termination in rib 10 with connection Type 5B due to symmetric loading (SL)

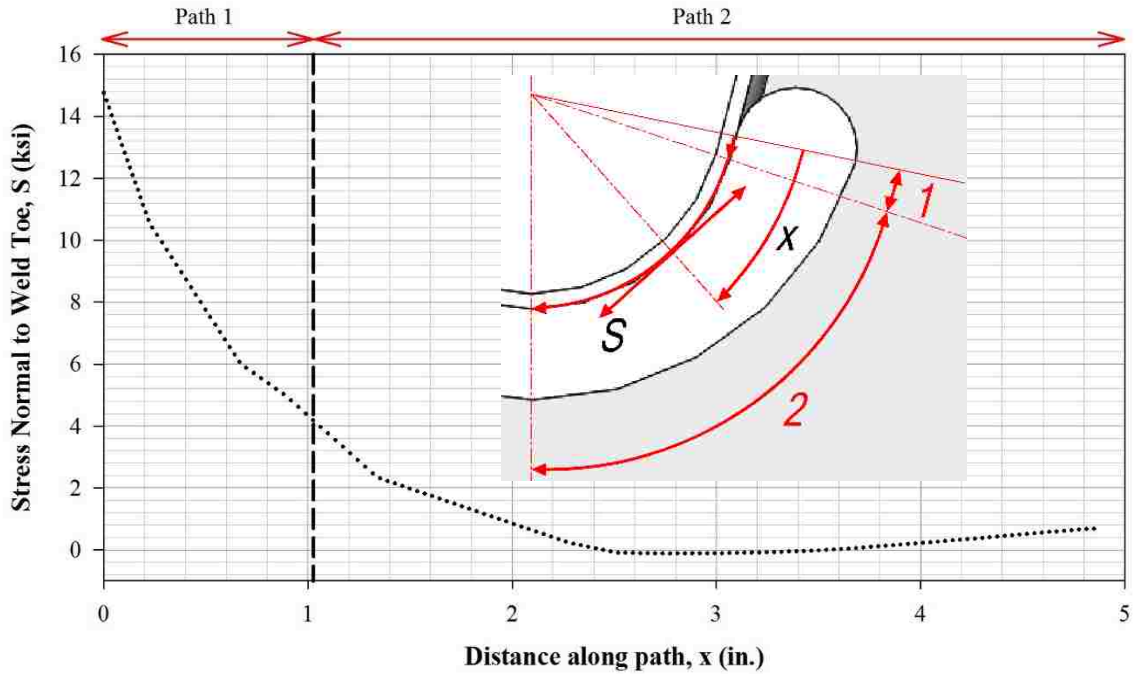


Figure 124 Stress normal to extended cutout termination in rib 10 with connection Type 4B due to symmetric loading (SL)

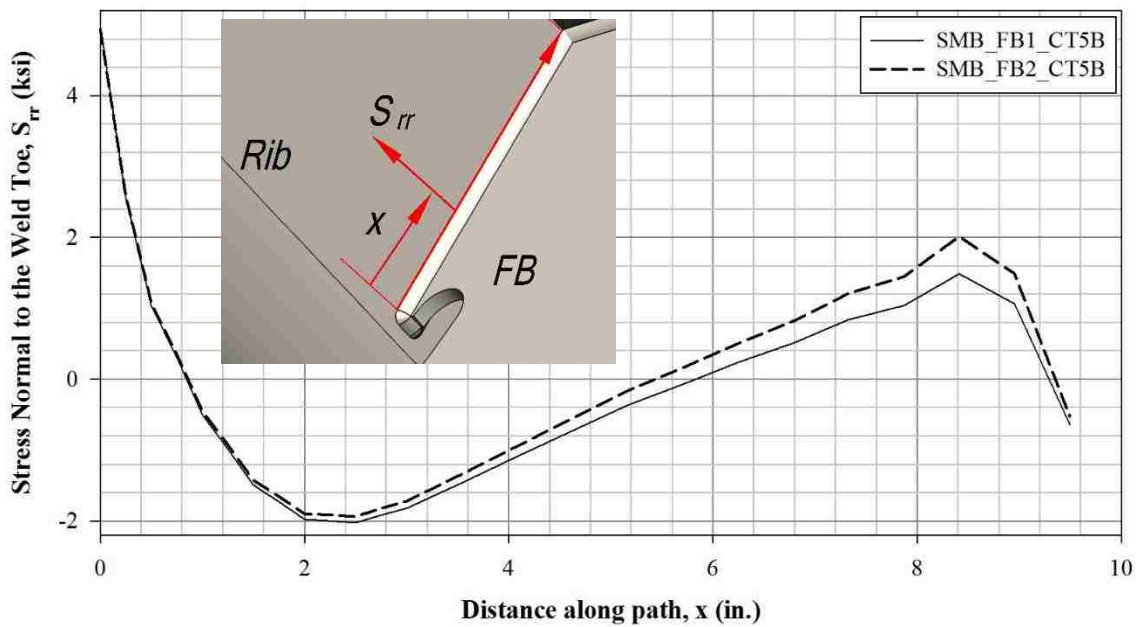


Figure 125 Comparison of stress normal to weld toe in rib 10 with connection Type 5B due to symmetric loading (SL)

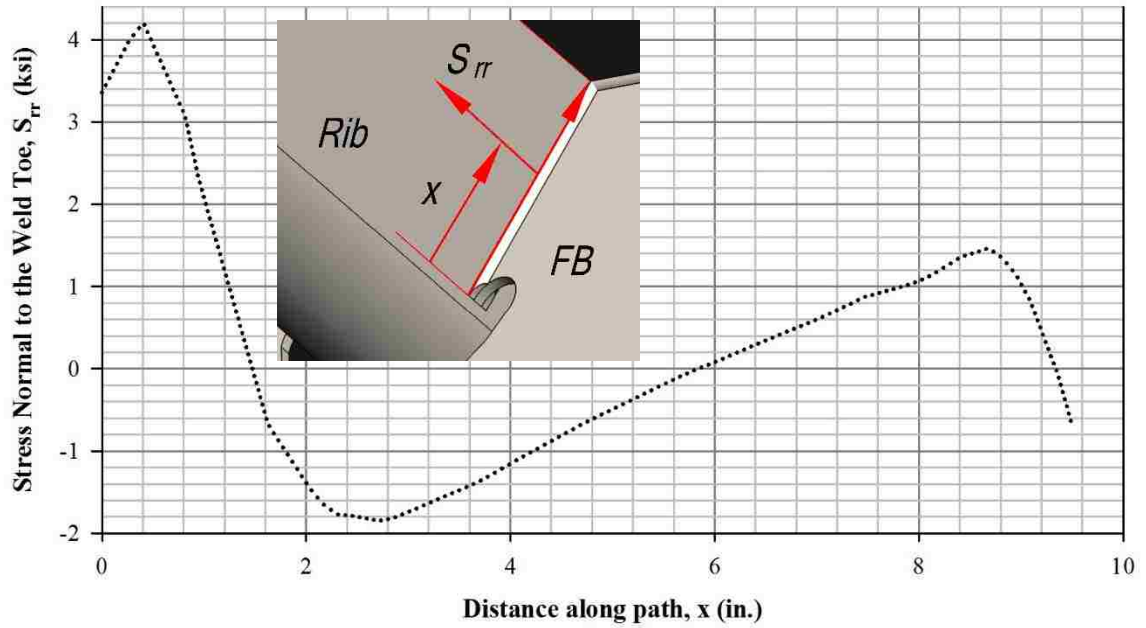


Figure 126 Comparison of stress normal to weld toe in rib 10 with connection type 4B due to symmetric loading (SL)

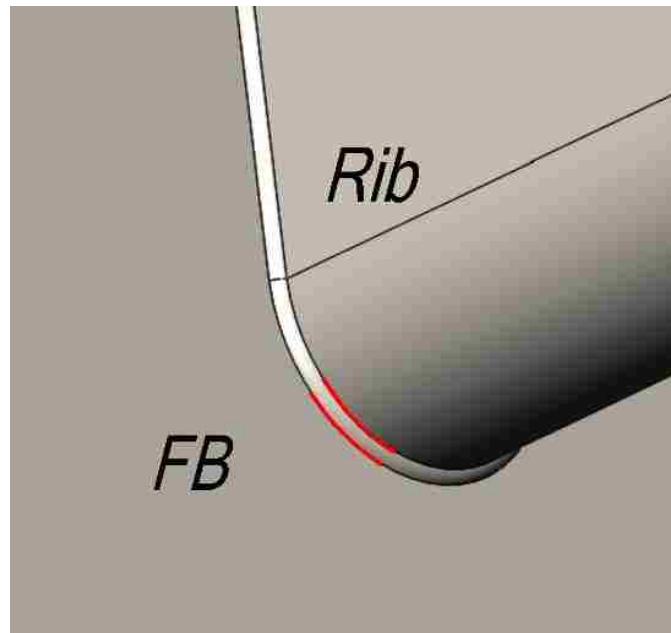


Figure 127 Potential modes of cracking for connection Type 1B

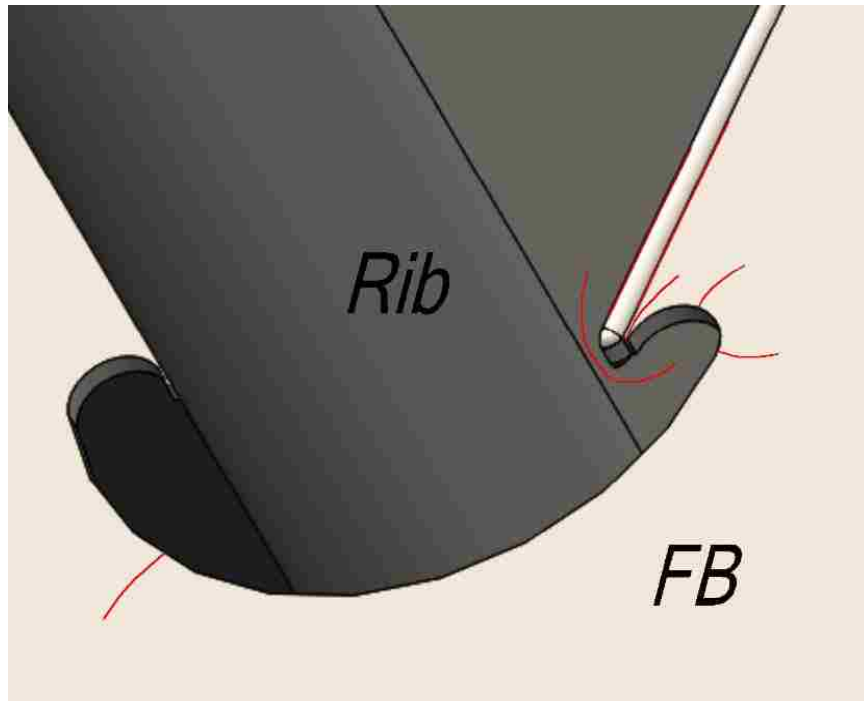


Figure 128 Potential modes of cracking for connection Type 5B

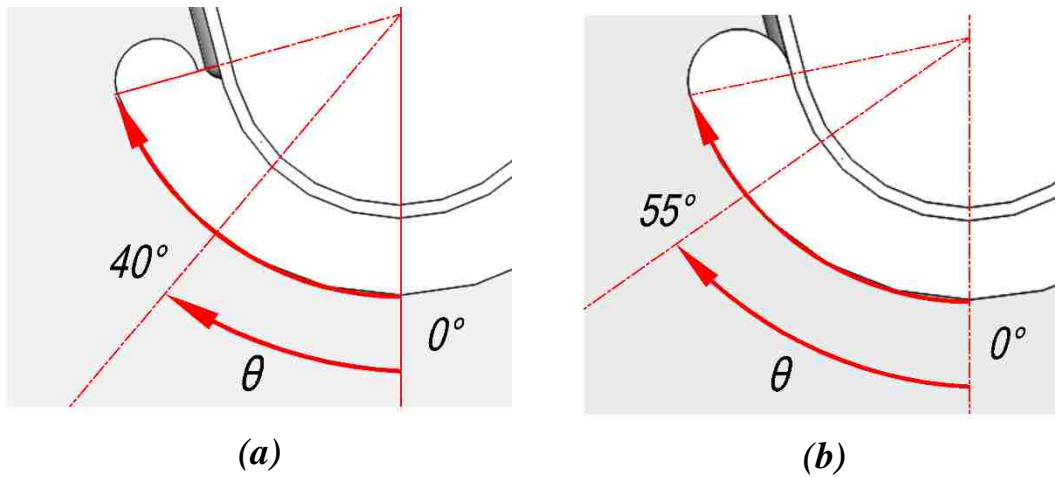


Figure 129 Location of critical tangential stress for extended cutout lower radius for: (a) connection Type 5B; (b) connection Type 4B

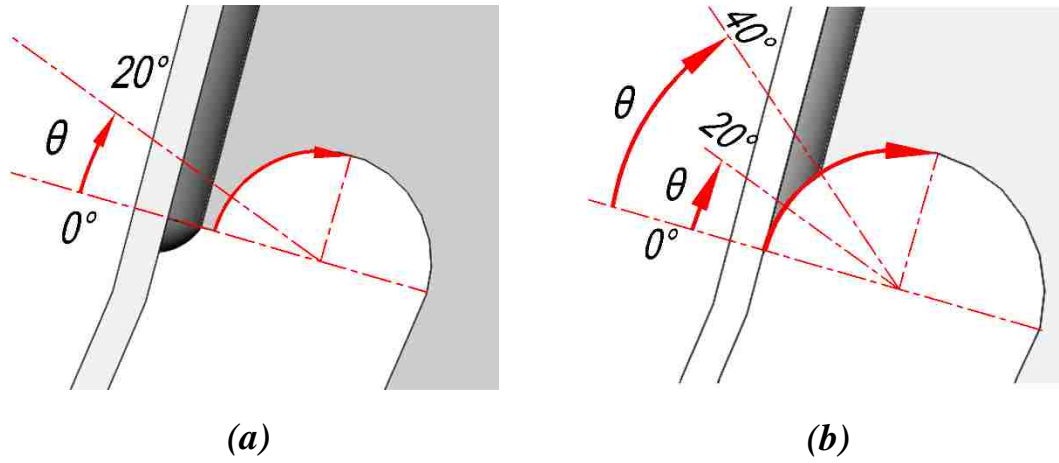


Figure 130 Location of critical tangential stress for extended cutout upper radius with: (a) connection Type 5B; (b) connection Type 4B

REFERENCES

- Abdou, S., Zhang, W., & Fisher, J. W. (2003). Orthotropic Deck Fatigue Investigation at Triborough Bridge, New York. *Transportation Research Record*, (1845), 153-162.
- ACROW. (2015).
- American Association of State Highway and Transportation Officials. (2012). *AASHTO LRFD Bridge Design Specifications* (6th ed.). Washington D.C.:
- Battista, R. C., Pfeil, M. S., & Carvalho, E. M. L. (2008). Fatigue Life Estimates for a Slender Orthotropic Steel Deck. *Journal of Constructional Steel Research*, 64(1), 134-143.
- Beales, C. (1990). *Assessment of Trough to Crossbeam Connections in Orthotropic Steel Bridge Decks*. Crowthorne, Berkshire: Transport and Road Research Laboratory.
- Beales, C. (1990). *Measurements and Interpretation of Dynamic Loads on Bridges - Phase 3: Fatigue Behavior of Orthotropic Steel Decks of Road Bridges* No. Agreement Number 7210-KD/807). Luxembourg: Commission of the European Communities.
- Bouwkamp, J. G. (1967). *Analysis of the Orthotropic Steel Deck of the San Diego-Coronado Bridge* No. Report No. 67-20). Berkeley, CA: University of California College of Engineering.
- Bouwkamp, J. G., & Powell, G. H. (1967). *Structural Behavior of an Orthotropic Steel Deck Bridge, Volume 2 - Figures* No. Report No. 67-27). Berkeley, CA: University of California College of Engineering.
- Bouwkamp, J. G., & Powell, G. H. (1967). *Structural Behavior of an Orthotropic Steel Deck Bridge, Volume 1 - Text* No. Report No. 67-27). Berkeley, CA: University of California College of Engineering.

- Buckland, P. G. (1981). The Lion's Gate Bridge - Renovation. *Canadian Journal of Civil Engineering*, 8, 484-508.
- Carlin, G. P., & Mirza, M. S. (1996). Replacement of Reinforced Concrete Deck of Champlain Bridge, Montreal, by Orthotropic Steel Deck. *Canadian Journal of Civil Engineering*, 23(6), 1341-1349.
- Connor, R. J. (2002). A Comparison of the In-Service Response of an Orthotropic Steel Deck with Laboratory Studies and Design Assumptions. (Doctor of Philosophy in Civil Engineering, Lehigh University), 423.
- Connor, R. J., Fisher, J. W., Gatti, W., Gopalaratnam, V. S., Kozy, B. M., Leshko, B., et al. (2012). *Manual for Design, Construction, and Maintenance of Orthotropic Steel Deck Bridges* No. FHWA-IF-12-027) US Department of Transportation Federal Highway Administration.
- Connor, R. J., & Fisher, J. W. (2000). In-Service Response of an Orthotropic Steel Deck Compared with Design Assumptions. *Transportation Research Record*, (1696), 100-108.
- Connor, R. J., & Fisher, J. W. (2004). *Results of Field Measurements Made on the Prototype Orthotropic Deck on the Bronx-Whitestone Bridge, Final Report* No. ATLSS Report No. 04-03). Bethlehem, PA: Advanced Technology for Large Structural Systems.
- Cunningham, J. R. (1987). Strengthening Fatigue Prone Details in a Steel Bridge Deck. *International Conference on Fatigue of Welded Constructions*, pp. 127-133.
- Cunningham, R. O., Erzurumlu, H., & Leber, R. A. (1968). Construction of the Fremont Bridge. *ASCE National Structural Engineering Meeting*, San Francisco, California.

- Curtis, G. N. (1980). Design of the Queen's Way Bridge. *Modern welded structures* (pp. A-34-A-35). Cleveland, OH: The James F. Lincoln Arc Welding Foundation.
- Dassault Systemes Simulia Corp. (2013). *ABAQUS/Standard version 6.13*. Providence, RI: Dassault Systemes, Inc.
- Davis, R. E., & Bender, O. (1964). California Builds Experimental Orthotropic Plate Bridge. *Civil Engineering*, 62-63.
- De Jong, Foppe B. P., Kolstein, M. H., & Bijlaard, F. S. K. (2004). Research Project tu delft; Behavior Conventional Bridge Decks & Development of Renovation Techniques. Sacramento, CA. pp. 595-615.
- Dexter, R. J., & Fisher, J. W. (1997). Fatigue Cracking of Orthotropic Steel Decks. *Structural Engineering International: Journal of the International Association for Bridge and Structural Engineering (IABSE)*, 203-212.
- Fisher, J. W., & Roy, S. (2011). Fatigue of Steel Bridge Infrastructure. *Structure and Infrastructure Engineering: Maintenance, Management, Life-Cycle Design and Performance*, 7(7-8), 457-475.
- Gajer, R. B., Patel, J., & Khazem, D. (1996). Orthotropic Steel Deck for the Williamsburg Bridge Reconstruction. *Building an International Community of Structural Engineers*, Chicago, IL, USA, pp. 491-498.
- Gill, R. J., & Dozzi, S. (1966). Concordia Orthotropic Bridge: Fabrication and Erection. *Engineering Journal*, (May), 10-18.
- Grundy, P., Burkitt, G., & Stevens, L. K. (1994). Fatigue Studies of Westgate Bridge. *Australasian Structural Engineering Conference*, Sydney. pp. 81-87.

- Haibach, E., & Plasil, I. (1983). Untersuchungen zur betriebsfestigkeit von stahlleichtfahrbahne mit trapezhohlsteifen im eisenbahnbrückenbau. [Studies on the fatigue resistance of lightweight steel decks with trapezoidal hollow stiffeners in Railway Bridge] *Der Stahlbau*, (9), 269-274.
- Haight, R., Chang, S., & Kushmock, R. (2005). Orthotropic Deck Rehabilitation at the Throgs Neck Bridge. *Structures Congress 2005*, pp. 10.
- Hardenberg, G. (1961). Design of the Superstructure of the Port Mann Bridge. *Engineering Journal*, 44(7), 35-45.
- Hilton, N., & Hardenberg, G. (1964). Port Mann Bridge, Vancouver, Canada. *Institution of Civil Engineers*, 29(4), 677-712.
- Kaczinski, M. R., Stokes, F. E., Lugger, P., & Fisher, J. W. (1997). *Williamsburg Bridge Orthotropic Deck Fatigue Test* No. ATLSS Report No. 97-04). Bethlehem, PA: ATLSS Engineering Research Center, Lehigh University.
- Kolstein, M. H. (2007). Fatigue Classification of Welded Joints in Orthotropic Steel Bridge Decks. (Ph. D., T.U. Delft), 461.
- Lally, A., & Wolchuk, R. (1979). American Design Practice for Steel Box Girder Bridges. *International Conference on Steel Plated Structures*, pp. 35.
- Lehrke, H. P. (1990). *Fatigue Tests of Stiffener to Cross Beam Connections* Structural Engineering International.
- Linnert, G. E. (1994). *Welding Metallurgy: Carbon and Alloy Steels*
- Mangus, A. R. (2005, France's Millau Orthotropic Steel Viaduct, State of the Art Bridge Launching. *Structure Magazine*,
- Mangus, A. R. (2014). *Data Base Template*. Unpublished manuscript.

- Mangus, A. R., & Sun, S. (2000). Chapter 14: Orthotropic Deck Bridges. In W. Chen, & L. Duan (Eds.), *Bridge Engineering Handbook* (pp. 46). Boca Raton, FL: CRC Press LLC.
- Manniche, K., & Ward-Hall, G. (1975). Mission Bridge - Design and Construction of the Steel Box Girder. *Canadian Journal of Civil Engineering*, (2), 169-192.
- Marquez, T., Williams, J., Huang, C., Benoit, M., Lowe, L., & Mangus, A. R. (1998). Unique Steel Curved Orthotropic Bridge for the I-880 Replacement Project. *International Steel Bridge Symposium*, pp. 30.
- Matson, D. D. (2000). Lions' Gate Suspension Bridge Deck and Stiffening Truss Replacement. *The 18th Annual International Bridge Conference and Exhibition*, Pittsburgh, PA. pp. 247-253.
- Matson, D. D. (2001). Piece by Piece. *Civil Engineering*, 71(5), 40-45.
- Miki, C., & Sukanuma, H. (2014). Chpt. 17: Rehabilitation of Strengthening of Orthotropic Steel Bridge Decks. In W. Chen, & L. Duan (Eds.), *Bridge Engineering Handbook: Construction and Maintenance* (Second Edition ed., pp. 489-536)
- Mukherjee, S. (2016). Laboratory Fatigue Evaluation of a Full Scale Steel Orthotropic Bridge Deck with Round Bottom Ribs and Fitted Floor Beams. (Master of Science, Lehigh University).
- Mukherjee, S. & Roy, S. (2015). Fatigue Evaluation of Steel Orthotropic Deck for a Lift Bridge by Laboratory Testing of Full Scale Prototype. *Structures Congress*
- Nottingham, D. (1980). Yukon River Bridge an Orthotropic Pipeline-Highway Bridge. *Modern Welded Structures, vol. IV* (pp. A-24-A-26). Cleveland, OH: The James F. Lincoln Arc Welding Foundation.

- Nunn, D. E. (1974). *An Investigation into the Fatigue of Welds in an Experimental Orthotropic Bridge Deck Panel* No. Report 629). Crowthorne, Berkshire: Transport and Road Research Laboratory.
- Nunn, D. E. (1974). *Trials of Experimental Orthotropic Bridge Deck Panels Under Traffic Loading* No. Report 627). Crowthorne, Berkshire: Transport and Road Research Laboratory.
- Radojevic, D., Eppell, J., Kirkwood, K. F., & Buckland, P. G. (2014). Deck Replacement of the Angus L. Macdonald Suspension Bridge. *Structures Congress 2014*, pp. 516-527.
- Roberts, J. E., Marquez, T., Huang, C., Mangus, A. R., Williams, J., & Benoit, M. (2000). California's First Curved Orthotropic Bridge. *Structural Engineering International: Journal of the International Association for Bridge and Structural Engineering (IABSE)*, (2), 124-127.
- Roy, S., Alapati, R. S. D., Manandhar, N. K., & Molina, M. A. (2012). *Fatigue Resistance Investigation for the Replacement Orthotropic Deck at the Verrazano Narrows Bridge: Phase 1* No. ATLSS Report No. 12-01). Bethlehem, PA: Advanced Technology for Large Structural Systems (ATLSS).
- Roy, S., Manandhar, N. K., & Molina, M. A. (2012). *Fatigue Resistance Investigation for the Replacement Orthotropic Deck at the Verrazano Narrows Bridge: Phase 2* No. ATLSS Report No. 12-01). Bethlehem, PA: Advanced Technology for Large Structural Systems (ATLSS).
- Roy, S., & Mukherjee, S. (2015). *Design and Fabrication of Orthotropic Deck Details*. Bethlehem, PA:

- Roy, S., Mukherjee, S., & Zhao, X. (2014). Cost-effective Connections for Enhanced Life Cycle Performance of Steel Orthotropic Bridge Decks. Shanghai, China. pp. 5.
- Serzan, K. P., & Spoth, T. (2008). Advancements of New Narrows Suspension Bridge Design in Tacoma, Washington. *Transportation Research Record: Journal of the Transportation Research Board*, (2050), 59-66.
- Shields, E. J. (1964). The Poplar Street Bridge. *AISC Engineering Journal*, 55-65.
- Shields, E. J. (1966). Poplar Street Bridge: Design and Fabrication. *Civil Engineering*, (February), 52-55.
- Shields, E. J., & Schmidt, A. E. (1969). Fabrication and Erection of Poplar Street Orthotropic-Plate Deck Girder Bridge. *Highway Research Record*, 87-98.
- Sim, H., & Uang, C. (2007). *Effects of Fabrication Procedures and Weld Melt-Through on Fatigue Resistance of Orthotropic Steel Deck Welds* No. CA08-0607). Sacramento, CA: California Department of Transportation.
- Smylie, R. G. (1966). Fabrication of Orthotropic Deck Sections for Port Mann Bridge., 36-42.
- Spoth, T., Serzan, K. P., & Condell, S. (2005). The New Tacoma Narrows Suspension Bridge - Design of the Suspended Superstructure. *Structures Congress 2005*
- Spoth, T., Khazem, D., & Orsolini, G. I. (2000). New Carquinez Bridge, Northeast of San Francisco, California: Technological Design Advancements. *Transportation Research Record*, (1740), 40-48.
- Stahl, F. L. (1990). Orthotropic Steel Plates for Bridge Deck Replacement. *Extending the Life of Bridges, ASTM STP 1100*, pp. 109-120.

- Suganuma, H., & Miki, C. Full Size Fatigue Tests of the New Orthotropic Steel Deck System. *IIW Doc. XIII-2164-07*, 28.
- Touran, A., & Okereke, A.(1991). Performance of Orthotropic Bridge Decks. *Journal of Performance of Constructed Facilities*, 5(2), 134-148.
- Troitsky, M. S. (1987). *Orthotropic Bridges - Theory and Design*. Cleveland, OH: The James F. Lincoln Arc Welding Foundation.
- Tsakopoulos, P. A., & Fisher, J. W. (1999). *Williamsburg Bridge Replacement Orthotropic Deck as-built Full Scale Fatigue Test, Final Report on Phase II* No. ATLSS Report No. 99-02). Bethlehem, PA: Advanced Technology for Large Structural Systems.
- Tsakopoulos, P. A., & Fisher, J. W. (2002). *Fatigue Resistance Investigation for the Orthotropic Deck on Bronx-Whitestone, Final Report* No. ATLSS Report No. 02-05). Bethlehem, PA: Advanced Technology for Large Structural Systems.
- Tsakopoulos, P. A., & Fisher, J. W. (2003). Full-scale Fatigue Tests of Steel Orthotropic Decks for the Williamsburg Bridge. *Journal of Bridge Engineering*, 8(5), 323-333.
- Tsakopoulos, P. A., & Fisher, J. W. (2005). Full-scale Fatigue Tests of Steel Orthotropic Deck Panel for the Bronx-Whitestone Bridge Rehabilitation. *Bridge Structures*, 1(1), 55.
- Verma, K., Frank, K., Wright, W., Medlock, R., McEleney, B., Loftus, P., et al. (2001). *Steel Bridge Fabrication Technologies in Europe and Japan* No. FHWA-PL-01-018). Washington, D.C.: Federal Highway Administration, US Department of Transportation.
- Wolchuk, R. (1968). Part 2. Steel-Plate-Deck Bridges. In E. H. Gaylord, & C. N. Gaylord (Eds.), *Structural Engineering Handbook* (pp. 106-124) McGraw-Hill, Inc.

Wolchuk, R. (1987). Applications of Orthotropic Decks in Bridge Rehabilitation.

Engineering Journal of the American Institute of Steel Construction, 24(3), 113-121.

Wolchuk, R. (1992). Orthotropic Redecking of Bridges on the North American Continent.

Structural Engineering International: Journal of the International Association for Bridge and Structural Engineering (IABSE), 2, 125-130.

VITA

Katelyn Jeanine Kitner, the daughter of Michael Kitner and Kathleen Kitner, was born on July 7, 1990 in Pittsburgh, PA. Katelyn received her Bachelors of Science degree in Civil Engineering from the University of Akron, Akron, Ohio in May 2014. Katelyn joined ATLSS Research Center, Lehigh University as a Graduate Research Assistant in Fall 2014. Katelyn began graduate studies in the Department of Civil and Environmental Engineering at Lehigh University in Bethlehem, PA in August 2014. She will receive her Master of Science in Structural Engineering from Lehigh University, Bethlehem, PA in May 2016.